Numerical Modelling of the Rapid Depressurisation and Outflow of High Pressure Containments in the Framework of Carbon Capture and Sequestration

A thesis submitted to University College London for the degree of Doctor of Philosophy

By

Wentian Zheng

Department of Chemical Engineering
University College London
Torrington Place
London WC1E 7JE

April 2018

I, Wentian Zheng confirm that the work presented in this thesis is my own. Where information has been derived from other sources, I confirm that this has been indicated in the thesis.

List of publications

1. W. Zheng, H. Mahgerefteh, D. Jamois, J. Hebrard, C. Proust, Modelling of Depressurization-Induced Superheating for Compressed Liquefied Gases, Industrial & Engineering Research Chemistry, Issue 56, 2017, Page 5432-5542

2. W. Zheng, H. Mahgerefteh, S. Brown, S. Martynov, Integral multiphase turbulence compressible jet expansion model for accidental releases from pressurized containments, Industrial & Engineering Research Chemistry, Issue 55, 2016, page 7558–7568

3. W. Zheng, H. Mahgerefteh, S. Martynov, S. Brown, Modelling of CO_2 decompression across the triple point, Industrial & Engineering Research Chemistry, Issue 37, 2017, page 10491–10499

4. S. Martynov, W. Zheng, H. Mahgerefteh, S. Brown, J. Hebrard, D. Jamois, C. Proust, Computational and experimental study of solid phase formation during the decompression of high pressure CO_2 pipelines, Industrial & Engineering Research Chemistry, In press

5. S. Martynov, W. Zheng, S. Brown, H. Mahgerefteh, Numerical simulation of CO_2 flows in pipes with phase transition across the triple point, 12^{th} International Conference of Heat Transfer, Fluid Mechanics & Thermodynamics, Malaga, Spain, 2016

6. W. Zheng, S. Brown, S. Martynov, H. Mahgerefteh, Analytical modelling and validation of the expansion of a CO_2 jet released from a ruptured pipeline, 8^{th} International Conference of Turbulence, Heat and Mass Transfer, Sarajevo, Bosnia and Herzegovina, 2015

Abstract

The internationally agreed global climate deal reached at the Paris Climate Conference (COP21) in December 2015 is intended to limit the increase in global average temperature to less than 2°C above pre-industrial levels by 2050. Achieving this goal requires a 50 – 80% reduction in CO_2 emissions. Alongside renewable energy sources, CO_2 Capture and Sequestration (CCS) is widely considered as a key technology for meeting this target, potentially reducing the cost of inaction by some $2 trillion over the next 40 years.

It is estimated that transporting the predicted 2.3 - 9.2 Gt of captured CO_2 to its point of storage will require the use of a global network of between 95000 - 550000 km pipelines by 2050.

The economic pipeline transportation of such large amounts of CO_2 will require operation in dense or supercritical phase. In Europe, this will likely mean pipelines at line pressures above 100 bar, some passing through or near populated areas. Given that CO_2 is increasingly toxic at concentrations higher than 7%, the safe operation of CO_2 pipelines is of great importance and indeed pivotal to the public acceptability of CCS as a viable means for tackling the impact of global warming.

The accurate prediction of the discharge rate of the escaping inventory in the event of accidental pipeline rupture is central to the safety assessment of such pipelines. This information forms the basis for determining the minimum safe distances to populated areas, emergency response planning and the optimum spacing of isolation valves. In addition, in an emergency situation, the controlled depressurisation of CO_2 pipeline is critically important given the unusually high Joule-Thomson cooling of CO_2. Too rapid depressurisation poses the risk of embrittlement of the pipe wall causing pipeline running fracture, solid CO_2 formation leading to blockage of pressure relief valves in the event of crossing the triple point temperature (216.7 K) or a Boiling Liquid Expanding Vapour Explosion (BLEVE) due to the superheating of liquid phase CO_2.

This thesis presents the development, testing and validation of various transient flow models taking account of the above phenomena. These include a Homogeneous Equilibrium Mixture (HEM) pipe flow model, a Homogeneous Relaxation Mixture

(HRM) pipe flow model, a Two-Fluid Mixture (TFM) pipe flow model, and an integral jet expansion model.

The HEM model employing Computational Fluid Dynamics (CFD) techniques is developed for predicting solid CO_2 formation during pipeline decompression. The pertinent vapour-liquid or vapour-liquid-solid multi-phase flow is modelled by assuming homogeneous equilibrium. The flow model is validated against pressure and temperature data recorded during the Full Bore Rupture (FBR) decompression of an extensively instrumented 144 m long, 150 mm i.d. CO_2 pipe initially at 5.25 °C and 153.3 bar. For the conditions tested, the simulated results indicate CO_2 solid mass fractions as high as 35% at the release end, whose magnitude gradually decreases with distance towards the pipe intact end.

Turning to the HRM model, in its development, thermodynamic non-equilibrium between the constituent fluid phases during pipeline decompression is considered for both pure fluids and multi-component mixtures. The validation of the HRM model is carried out by comparing its predictions of a number of CO_2-rich mixtures pipeline FBR decompression experiments against the corresponding measurements. For reference, the HEM model predictions (where thermodynamic non-equilibrium is ignored) for the same tests are also included in the comparison. The results show that improved agreement with the measured data can be obtained by the present model as compared to the HEM model.

The last pipeline decompression model presented in this thesis is the TFM model, where the conservation equations are solved separately for each constituent fluid phases during decompression, unlike in the case of the HEM and HRM models. Fluid/fluid interface interactions are accounted for and modelled using appropriate closure relations. Furthermore, a new puncture outflow boundary condition is presented. For the numerical solution of the conservation equations, modifications towards previous schemes are introduced for improved accuracy and numerical stability. Model validation is carried out by comparing its predictions of two CO_2 pipeline puncture decompression tests against the corresponding measurements, showing excellent agreement. The experimentally observed heterogeneous flow behaviour, that is, the significant temperature difference between the vapour and liquid phases, is captured by the present model.

The final part of this thesis deals with the accurate prediction of the conditions of a pressurised jet upon its expansion to atmospheric pressure, where the simulated outflow data from the decompression flow models is used as the input conditions. Such prediction is of fundamental importance in assessing the consequences associated with accidental releases of hazardous fluids from pressurised vessels and pipes. An integral jet expansion model which for the first accounts for turbulence generation is presented. By the use of accidental release of two-phase CO_2 from a pressurised vessel as an example, the proposed model is shown to provide far better predictions of the fully expanded jet momentum flux as compared to the existing integral model where the impact of turbulence generation is ignored.

Impact statement

This thesis investigates the rapid depressurisation and outflow of high pressure CO_2 mixture pipelines undergoing puncture or full bore rupture failure. Four different mathematical depressurising flow models were developed, dealing with complex physical processes including solid-vapour-liquid phase transitions, non-equilibrium phenomenon, and transport process involved during pipeline decompression. The modelling methodology is partly novel, and where possible, the model predictions are carefully validated against experimental data.

As Carbon Capture and Sequestration being continuously developed as a key solution to combat global warming, significant amounts of CO_2 will be transported via high pressure pipeline networks across the globe. Their safe operation is thus of paramount importance. The models developed can be directly applied for the quantitative failure consequence assessment of the transmission pipelines, hence providing guidelines for emergency planning and mitigation measures.

In addition, the models can be easily extended to simulate the failure consequences of other important process fluids such as hydrogen and hydrocarbons.

Last but not the least, the numerical scheme introduced in this study for solving the flow model governing equations have brought improved accuracy and computational efficiency over the conventional methods, which, in and of itself, is beneficial to the further development of computational fluid dynamics in chemical process engineering.

Acknowledgements

I wish to thank the following people who have contributed so much in many ways to facilitate the completion of this thesis

To my supervisor, Professor Haroun Mahgerefteh for giving me the unique opportunity to study in this field and your excellent supervision.

To my parents: Thank you for your unconditional love.

To my wife Jiaxi Wang: Thank you for staying by my side no matter what.

To my dear friends, Mr. Jianhao Yu and Kaiqiao Wu, and to my office mates, Ms. Nor Daud and Mr. Revelation Samuel. It has been a pleasure.

To the technical and admin. staff of the Department of Chemical Engineering, UCL.

Finally, to Dr. Sergey Martynov and Dr. Solomon F. Brown. Thank you for your patience and guidance through the course of my time at UCL.

Table of Contents

Chapter 1:
Introduction

According to International Energy Agency (2011), with the exponential growth of the energy market, the world is entering 'a golden age of gas'. Indeed, hydrocarbon fuel gases are becoming a significant part of the world energy mix (International Energy Agency 2015), producing over 11000 MWh energy (mainly in the form of electricity) which accounts for 25% of the energy mix in 2014. As the fuel gas production sites are usually not collocated with the power plants, transportation is required. By far, the most prevalent method of transporting the significant amounts of hydrocarbon fuel gases is via high-pressure (usually over 100 bar) transmission pipelines given its superior operation safety and economic viability over other transportation modes (Transportation Research Board 2004). As a result, there are currently over 32000 km of newly built pipelines per year (Linnitt 2013).

Ironically, the intensive application of fuel gases has produced abundant CO_2 emissions, which in turn leads to global warming and climate change. The estimated total carbon emissions reached 35.7 billion tonnes in 2014 (Olivier et al. 2015) and were kept at the same level in the following two years (Conti et al. 2016; International Energy Agency 2017). One of the key mitigation strategies to combat global warming is Carbon Capture and Sequestration (CCS) which involves the transportation of the captured CO_2 from the capture points to the sequestration sites. As expected, high-pressure pipelines are again adopted as the major transportation mode. Although compared to hydrocarbon pipelines, the current CO_2 pipeline network is of a much smaller scale (total length of approximately 7000 km mainly located in USA and Canada) (Knoope et al. 2014), given CCS' great potential in mitigating global warming, it is estimated that there will be over 100000 km of CO_2 pipelines carrying the captured CO_2 across the globe by 2030 (International Energy Agency 2010).

In both the cases, pipeline routing through populated areas cannot be completely avoided in order to keep it economically viable (Koornneef et al. 2010; Vianellob et al. 2013). Given the fact that hydrocarbons are highly flammable, and CO_2 is aspyhxiant at high concentrations (considered to be increasingly toxic above 7% v/v; Harper et al. 2011), pipeline failures often lead to catastrophic consequences, including loss of valuable inventory, damage to property, environmental pollution and fatalities. For

example, on March 12, 2014, a violent explosion of a natural gas pipeline owned by Edison's Gas situated at 1644 and 1646 Park Avenue, New York, the U.S.A. completely destroyed two adjacent five-story buildings (National Transportation Safety Board 2015). 8 fatalities and 46 injuries were reported. The cause of the explosion was identified as natural gas leak resulting from pipeline corrosion. On July 31, 2014, a buried propylene pipeline failure led to a string of explosions in Kaohsiung, Taiwan, causing severe damage to the neighbourhood including several kilometres of the road surface and hundreds of vehicles (Liaw 2016). The explosion itself and the subsequent fire also resulted in 30 fatalities. Estimate shows that, on average, there are 250 pipeline failure incidents per year across the globe (Linnitt 2013). Given the above, the quantitative failure consequence assessment of high-pressure transmission pipelines is essential.

Central to the above is the accurate prediction of the outflow and the decompression characteristics including the in-pipe fluid temperature, pressure and phase composition variations as a function of time in the event of failure (Molag & Dam 2011; Pham & Rusli 2016; Munkejord et al. 2016). The outflow data serve as the source terms for determining the consequences of fire, explosion, dispersion of the emerging toxic cloud (of CO_2) and hence minimum safety distances to populated areas (Mahgerefteh et al. 2007; Mahgerefteh et al. 2008; Brown et al. 2013). With regards to the fluid temperature, pressure and phase composition variations during decompression, such data are central to the determination of fracture propagation behaviour along the pipe wall (Mahgerefteh & Atti 2006; Cosham & Eiber 2008; Aursand et al. 2016; Martynov et al. 2017). In the case of CO_2, there are also the risks associated with solid CO_2 or 'dry ice' formation upon surpassing its triple point (216 K) (DNV 2010; Pham & Rusli 2016). The formation of any significant amounts of solid CO_2 within the pipeline may result either in its blockage (especially along restrictions such as bends), or more likely, the blockage of the emergency pressure relief valves, leading to over-pressurisation and possible pipeline rupture.

Given the above, the development of accurate, robust and computationally efficient mathematical models for predicting the outflow and the decompression characteristics in the event of pipeline failure, or during scheduled maintenances has been the focus of considerable attention (see (Mahgerefteh et al. 2008; Munkejord et al. 2010; Brown

et al. 2013; Brown et al. 2014; Munkejord & Hammer 2015; Nouri-Borujerdi & Shafiei Ghazani 2017) for example). The success of such models invariably depends on the accurate modelling of the fluid dynamics and thermodynamics during decompression. This necessitates careful consideration of fluid/wall interactions including friction and heat transfer, and fluid/fluid interface interactions in terms of mass, momentum and energy exchange.

The most simplistic flow model is the Homogeneous Equilibrium Mixture (HEM) model. In its literal sense, the multiphase mixture formed during pipeline decompression is assumed to be at homogeneous equilibrium, which means instantaneous interface mass, momentum and energy exchange. As such, the constituent fluid phases are assumed to remain at the same pressure, temperature and velocity. The corresponding fluid flow can be described using a single set of the mass, momentum and energy conservation equations. For fluid/wall friction and heat exchange, empirical correlations are usually adopted.

Despite its simplicity, in the case of pipeline Full Bore Rupture (FPR) failure where fully dispersed bubbly flow is observed to occur, its relatively good performance in predicting the decompression process has been reported through several studies. For example, Mahgerefteh et al. (2008) applied the HEM for predicting the decompression characteristics of both high pressure hydrocarbon (mainly LPG) and CO_2 pipelines. A real-fluid Equation of State (EoS) was employed for the prediction of the required thermal properties and phase equilibrium data. In both cases, comparisons against the available experimental data such as the pressure and temperature variations as a function of time during pipeline decompression indicated reasonably good agreement with the model predictions. More recently, Teng et al. (2016) studied the pipeline FBR decompression characteristics for vapour, liquid and supercritical CO_2 using the HEM model. Reporting good agreement between the model predictions and the measured data of the pressure variation as a function of time during decompression, the decompression rate was found to be the highest in liquid phase CO_2 followed by the supercritical phase, vapour-liquid two-phase and finally vapour phase. However, their flow models are not capable of handling solid phase CO_2.

In the case where delayed phase transition occurs during pipeline decompression, metastable fluid states (e.g. superheated liquid phase) may be expected (Munkejord et al. 2016), and thermodynamic equilibrium assumption between the constituent fluid phases is no longer valid. Such non-equilibrium behaviour can significantly affect the decompression characteristics. Cosham et al. (2012) for example experimentally observed that the non-equilibrium behaviour resulted in larger decompression wave speeds as compared to the HEM model predictions.

In light of the above, the Homogeneous Relaxation Mixture (HRM) model was first developed Bilicki & Kestin (1990). In this case, by explicitly modelling of the finite rate of interface mass exchange, thermodynamic non-equilibrium during pipeline decompression can be accounted for. Brown et al. (2013) successfully demonstrated the HRM model capability in predicting the pipeline FBR decompression for CO_2. However, by far, the HRM model is limited to single-component flow, which puts a significant restriction on its practical application in the quantitative failure consequence assessment of high-pressure transportation pipelines, as most of flows encountered in industry are mixtures with multiple impurities. The presence of impurities can largely impact the fluid physicochemical properties (Pershad et al. 2010; Patchigolla & Oakey 2013; Solomon Brown et al. 2014).

Heterogeneous flow is another important phenomenon reported by Brown et al. (2013) based on pipeline decompression tests involving the direct visual observation of the in-pipe flow through a reinforced glass section. The Drift Flux Mixture (DFM) model accounts for such phenomenon through the addition of a slip relation between the constituent fluid phases in the HEM model (Ishii 1977). Munkejord et al. (2010) studied the impact of phase slip on CO_2 pipeline decompression using the DFM model. The authors concluded that phase slip between the vapour and liquid phases resulted in a higher decompression rate as compared to the HEM model predictions where such effect is ignored. However, it should be pointed out that in the application of the DFM model, the velocity of each fluid phase must be strongly coupled, such that a slip relation can be prescribed (Munkejord et al. 2010). As such, the DFM model is only applicable to limited flow regimes during pipeline decompression (e.g. bubbly/slug flow; Hibiki & Ishii 2003), for which the HEM model has already been

proven to be effective. As such the additional mathematical complexity introduced in the DFM model may not be justified.

Although important in the context of pipeline failure consequence assessment, the forgoing flow models are mostly suitable for the most catastrophic but least likely pipeline FBR failures where homogenous flow has been shown to prevail during the most part of the decompression process (Robert M. Woolley et al. 2014). However, in practice, pipeline punctures are found to be far more frequent than FBR (Transportation Research Board 2004). Here, based on direct visual observation of in-pipe flow, significant vapour-liquid phase stratification has been reported during the course of the CO_2QUEST European Commission FP7 project (Solomon Brown et al. 2014). During pipeline puncture decompression, the constituent fluid phases behave independently involving weak interface interactions, which renders the HEM inapplicable.

The Two-Fluid Mixture (TFM) model, mostly employed in the nuclear industry for heterogeneous water/steam flow as part of the quantitative failure consequence assessment, considers the conservation equations separately for each of the constituent fluid phases (Toumi et al. 1999). Although successfully verified against pipeline FBR decompression experiments (S. Brown et al. 2014; Munkejord & Hammer 2015), the model's capability in handling pipeline puncture decompression flows has not been investigated.

Given the above overview of the limitations of the previous pipeline failure decompression models, the main objectives of this thesis are to develop, verify and where applicable validate:

- a HEM pipeline decompression flow model accounting for the formation of solid phase CO_2 in the context of high pressure CO_2 transmission pipelines employed as part of the CCS chain
- a HRM pipeline decompression flow model capable of handling thermodynamic non-equilibrium in multi-phase multi-component mixtures
- a TFM flow model capable of handling pipeline puncture decompression, accounting for heterogeneous flow

The following presents an overview of each of the proceeding chapters:

Chapter 2 commences with a detailed description of the background theory of the most popular pipeline decompression flow models reported in the open literature. It covers the governing conservation equations, constituent relations for fluid/wall and fluid/fluid interface interactions during pipeline decompression, EoS for predicting fluid thermal properties and phase equilibrium data and the mathematical properties of the overall formulations. This is followed by a review of the applications of these flow models for predicting pipeline decompression, including a discussion of their performance in reproducing available experimental data and the limitations worthy of further development.

In Chapter 3, the development of the HEM flow model accounting for the solid CO_2 as a third phase is presented. This includes a description of the conservation equations, the thermodynamic consideration for the solid phase and the numerical solution scheme employed. The developed model is then tested by solving a specified Riemann problem, where the predicted wave structure in a solid-vapour-liquid three-phase flow is presented and discussed. This is followed by validation against available experimental data.

In Chapter 4, the development, testing and validation of the HRM model capable of predicting thermodynamic non-equilibrium in multi-phase multi-component mixtures during pipeline decompression is given. The chapter commences with the mathematical formulation for describing the thermodynamics and fluid dynamics. In particular, the methodology for predicting thermodynamic non-equilibrium in multi-component mixtures is presented in details. For verification and testing purposes, the model is employed to solve a specified Riemann problem, showing the impact of thermodynamic non-equilibrium on the resulting wave structure. Finally, three validation case studies are performed in which the model predictions are compared to available data such as the decompression wave speed measured during pipeline decompression tests for CO_2 rich mixtures.

Chapter 5 presents the development, testing and validation of the TFM model for simulating heterogeneous flow during pipeline puncture decompression. The mass, momentum and energy conservation equations for each of the constituent fluid phases are presented together with the closure relations for specifying fluid/wall (friction and heat transfer) and fluid/fluid interface interactions (mass, momentum and energy

exchange). To predict the outflow through the puncture at the pipeline release end, an additional boundary condition is introduced. For validation purposes, the TFM model developed is employed to simulate two CO_2 pipeline puncture decompression tests, where the predicted pressure, temperature and remaining inventory mass variations as a function of time are compared against the corresponding measurements.

Chapter 6 demonstrates an important example of utilising the predicted outflow data from the pipeline decompression models for simulating the jet expansion, and ultimately, the atmospheric dispersion of the escaping hazardous fluids. The above focuses on the use of the simulated outflow data as the input for predicting the subsequent fully expanded jet conditions based on an especially developed integral jet expansion model accounting for turbulence generation. Using a series of case studies, the integral jet expansion model's performance is in turn verified based on the comparison of its predictions of the fully expanded jet conditions against those from an established rigorous but highly computationally demanding CFD jet expansion model.

Chapter 7 presents a summary of the important conclusions of this work, followed by recommendations for future work.

Chapter 2:
Literature Review

In view of the safety hazards involved in the event of CO_2 pipeline failures, appropriate mathematical models for their quantitative consequence assessment are essential. In this section, the corresponding background theory and examples of their applications in predicting medium/large-scale pipeline decompression are presented.

Given the above, the following literature review has been split into two parts. The first part comprises a detailed description of the key building blocks for pipeline decompression modelling, including the governing equations for describing fluid flow; constituent relations for describing fluid/pipe wall heat transfer and friction; Equations of State (EoS) for predicting real fluid thermal properties and phase equilibrium data. Also included is a discussion regarding the mathematical nature of the resulting overall equation systems. The knowledge of the mathematical natures of the governing equations is required for seeking appropriate numerical solution strategies.

In the second part, relevant studies focusing on the applications of the reviewed mathematical models for predicting CO_2 pipeline decompression behaviour are reported. In each case, the model performances are assessed based on the degree of agreement between the predictions and the measured data for pipeline decompression tests. Moreover, the model limitations at their current stage of their development are summarised.

2.1 Background Theory

2.1.1 General Conservation Equations for Fluid Dynamics

For the description of the fluid dynamics of the k^{th} fluid phase within an arbitrary flow Control Volume (CV), V_{CV}^{k} with a Control Surface (CS), S_{CV}^{k}, the corresponding general time-averaged mass, momentum and energy conservation equations read (see Sections A1.1 to A1.4, Appendix for more details):

$$\frac{\partial \alpha_k \overline{\overline{\rho_k}}}{\partial t} + \nabla \cdot \left(\alpha_k \overline{\overline{\rho_k}} \underline{\underline{\boldsymbol{u}_k}} \right) + I_k = 0 \qquad 2.1$$

$$\frac{\partial \alpha_k \overline{\overline{\rho_k}} \underline{\underline{\boldsymbol{u}_k}}}{\partial t} + \nabla \cdot \left(\alpha_k \overline{\overline{\rho_k}} \underline{\underline{\boldsymbol{u}_k}} \underline{\underline{\boldsymbol{u}_k}} \right) + \nabla \cdot \left(\alpha_k \overline{\overline{p_k}} \boldsymbol{I} \right) - \nabla \cdot \alpha_k \left(\boldsymbol{\tau}_k^t + \overline{\overline{\boldsymbol{\tau}_k}} \right) + I_k^{\boldsymbol{u}_k} - \alpha_k \overline{\overline{\boldsymbol{F}_k}} = 0 \qquad 2.2$$

$$\frac{\partial \alpha_k \overline{\overline{\rho_k}} \underline{\underline{E_k}}}{\partial t} + \nabla \cdot \left(\alpha_k \overline{\overline{\rho_k}} \underline{\underline{\boldsymbol{u}_k}} \underline{\underline{E_k}} \right) + \nabla \cdot \left(\alpha_k \overline{\overline{p_k}} \boldsymbol{I} \cdot \underline{\underline{\boldsymbol{u}_k}} \right) - \nabla \cdot \left(\alpha_k \overline{\overline{\boldsymbol{\tau}_k}} \cdot \underline{\underline{\boldsymbol{u}_k}} \right) + \nabla \cdot \alpha_k \left(\boldsymbol{q}_k^t + \overline{\overline{\boldsymbol{q}_k}} \right) + \overline{\overline{p}} \frac{\partial \alpha_k}{\partial t} + I_k^{E_k *} - \alpha_k \overline{\overline{\boldsymbol{F}_k}} \cdot \underline{\underline{\boldsymbol{u}_k}} = 0 \qquad 2.3$$

Where, the scalar variables, α_k, ρ_k, p_k, h_k, E_k and $\dot{Q}_k$ are respectively the volume fraction, density, pressure, enthalpy, total energy, and added heat per volume of the k^{th} fluid phase; E_k is defined as the sum of the internal energy, e_k and the kinetic energy, $|\boldsymbol{u}_k|^2/2$, that is, $E_k = e_k + |\boldsymbol{u}_k|^2/2$. The interface mass, momentum and energy exchange (interaction) terms are denoted by I_k, $I_k^{\boldsymbol{u}_k}$ and $I_k^{E_k *}$, respectively. The vectors, $\boldsymbol{u}_k$, $\boldsymbol{q}_k$, and $\boldsymbol{F}_k$ respectively represent the velocity, heat flux and body force. $\boldsymbol{\tau}_k$ and $\boldsymbol{I}$ are the stress tensor and the identity matrix, respectively. The subscript, k and the superscripts, t respectively represent the k^{th} fluid phase and the turbulence. The averaging operators, '$\overline{\overline{\ }}$' and '$\underline{\underline{\ }}$' respectively denote phase-weighted time-averaging, and mass-weighted (Farve) time-averaging (see Section A1.1.1, Appendix for their definitions).

2.1.2 Conservation Equations for Pipe Flows

2.1.2.1 General Assumptions and Simplifications

The full conservation equations for mass, momentum and energy derived above are applicable to any type of flows. However, given that they are a set of coupled, non-linear and high-order Partial Differential Equations (PDEs), seeking a complete solution would be difficult and computationally demanding (Ferziger & Peric 2002). For most practical engineering problems, inconsequential terms in equations 2.1 to 2.3

are often neglected. These include viscous term in inviscid flow and the convection term in Stokes flow.

In the case of pipe flow, it is assumed to be one-dimensional, and momentum diffusion, energy diffusion and turbulence are usually neglected (Mahgerefteh et al. 1999; Oke et al. 2003; Cleaver et al. 2003). Accordingly, equations 2.1 to 2.3 are simplified to:

$$\frac{\partial \alpha_k \overline{\overline{\rho_k}}}{\partial t} + \frac{\partial}{\partial x}\left(\alpha_k \overline{\overline{\rho_k}}\,\underline{u_{x,k}}\right) + I_k = 0 \qquad 2.4$$

$$\frac{\partial \alpha_k \overline{\overline{\rho_k}}\,\underline{u_{x,k}}}{\partial t} + \frac{\partial}{\partial x}\left(\alpha_k \overline{\overline{\rho_k}}\,\underline{u_{x,k}}\,\underline{u_{x,k}}\right) + \frac{\partial}{\partial x}\left(\alpha_k \overline{\overline{p_k}}\right) + I_k^{u_{x,k}} - \alpha_k \overline{\overline{F_{x,k}}} = 0 \qquad 2.5$$

$$\frac{\partial \alpha_k \overline{\overline{\rho_k}}\,\underline{E_k}}{\partial t} + \frac{\partial}{\partial x}\left(\alpha_k \overline{\overline{\rho_k}}\,\underline{u_{x,k}}\,\underline{E_k}\right) + \frac{\partial}{\partial x}\left(\alpha_k \underline{u_{x,k}}\,\overline{\overline{p_k}}\right) + \overline{\overline{p_k}}\frac{\partial \alpha_k}{\partial t} + I_k^{E_k *} - \alpha_k\left(\overline{\overline{F_{x,k}}}\,\underline{u_{x,k}} + \overline{\overline{\dot{Q}_k}}\right) = 0 \qquad 2.6$$

Such simplification is based on cross-sectional area averaging over equations 2.1 to 2.3 (Ishii & Hikiki 2006c), and as a result, terms $I_k^{u_{x,k}}$ and $I_k^{E_k *}$ now respectively correspond to fluid/wall friction and heat transfer of which the closure relations will be provided in later sections. For simplicity, the volumetric terms (representing the body force and the added work/heat per volume) and the interface exchange terms are combined. The resulting conservation equations are given by:

$$\frac{\partial \alpha_k \overline{\overline{\rho_k}}}{\partial t} + \frac{\partial}{\partial x}\left(\alpha_k \overline{\overline{\rho_k}}\,\underline{u_{x,k}}\right) = S_{M,k} \qquad 2.7$$

$$\frac{\partial \alpha_k \overline{\overline{\rho_k}}\,\underline{u_{x,k}}}{\partial t} + \frac{\partial}{\partial x}\left(\alpha_k \overline{\overline{\rho_k}}\,\underline{u_{x,k}}\,\underline{u_{x,k}}\right) + \frac{\partial}{\partial x}\left(\alpha_k \overline{\overline{p_k}}\right) = S_{F,k} \qquad 2.8$$

$$\frac{\partial \alpha_k \overline{\overline{\rho_k}}\,\underline{E_k}}{\partial t} + \frac{\partial}{\partial x}\left(\alpha_k \overline{\overline{\rho_k}}\,\underline{u_{x,k}}\,\underline{E_k}\right) + \frac{\partial}{\partial x}\left(\alpha_k \underline{u_{x,k}}\,\overline{\overline{p_k}}\right) + \overline{\overline{p_k}}\frac{\partial \alpha_k}{\partial t} = S_{E,k} \qquad 2.9$$

Finally, by dropping the subscript, x and all the averaging operators in the above equations, the final form of the conservation equations describing pipe flow of the k^{th} fluid phase reads:

$$\frac{\partial}{\partial t}\alpha_k\rho_k + \frac{\partial}{\partial x}\alpha_k\rho_k u_k = S_{M,k} \qquad 2.10$$

$$\frac{\partial}{\partial t}\alpha_k\rho_k u_k + \frac{\partial}{\partial x}\left(\alpha_k\rho_k u_k^2 + \alpha_k p_k\right) = S_{F,k} \qquad 2.11$$

$$\frac{\partial}{\partial t}\alpha_k\rho_k E_k + \frac{\partial}{\partial x}\left(\alpha_k\rho_k u_k E_k + \alpha_k u_k p_k\right) + p_k\frac{\partial \alpha_k}{\partial t} = S_{E,k} \qquad 2.12$$

It should be noted that the solutions of equations 2.10 to 2.12 represent the time-averaged flow (over finite Δt) within the control volume of interest.

2.1.2.2 Multi-Phase Flow Modelling

During pipeline decompression, multi-phase flow occurs mainly as a result of evaporation of the liquid phase, or condensation of the compressed vapour phase. This leads to complex interface interactions. Such interactions may completely change the flow characteristics.

For example, with very rapid rates of interphase mass, momentum and energy exchange, the constituent fluid phases are at thermodynamic and mechanical equilibrium (homogeneous equilibrium), that is, no differences can be observed between the phasic temperatures, pressures or velocities. When interphase momentum exchange rate is not sufficiently high, mechanical equilibrium cannot be retained, and heterogeneous flow (e.g. slug flow, annular flow and stratified flow) occurs. In the case of delayed interface mass and energy exchange, thermodynamic non-equilibrium is respectively manifested in fluid metastable states (e.g. superheated liquid phase) and distinctive phasic temperatures (thermal stratification).

The accurate simulation of the above phenomena has been the focus of many studies, involving different modelling approaches for dealing with the interface interactions.

These models may be generally divided into four groups namely (Pham & Rusli 2016; Munkejord et al. 2016):

- Homogeneous Equilibrium Mixture (HEM) model
- Homogeneous Relaxation Mixture (HRM) model
- The nonhomogeneous equilibrium mixture model (commonly known as the Drift Flux Mixture (DFM) model)
- Two-Fluid Mixture (TFM) model.

Table 2.1 is a list of the above models and their top level features.

Table 2.1: Common flow models for predicting pipeline decompression.

Multi-phase flow Model	**Remarks**
HEM model	The HEM model assumes thermodynamic and mechanical equilibrium between the fluid phases
HRM model	The HRM model accounts for thermodynamic non-equilibrium between the fluid phases as a result of delay in phase transition (interphase mass exchange)
DFM model	The DFM model takes mechanical non-equilibrium into consideration
TFM model	Neither of thermodynamic and mechanical equilibrium is assumed; interface interactions are modelled explicitly

An elaborated review of the various models in Table 2.1 is presented in the following.

2.1.2.2.1 Homogeneous Equilibrium Mixture Model

The HEM model assumes instantaneous mass, momentum and energy exchange between fluid phases. As a result, all fluid phases share the same velocity, temperature and pressure.

Taking vapour-liquid two-phase flow as an example, adding the conservation equations of each fluid phase gives:

$$\frac{\partial\left(\alpha_v\rho_v+\alpha_l\rho_l\right)}{\partial t}+\frac{\partial}{\partial x}\left(\alpha_v\rho_v+\alpha_l\rho_l\right)u=S_{M,v}+S_{M,l}=S_M \tag{2.13}$$

$$\frac{\partial\left(\alpha_v\rho_v+\alpha_l\rho_l\right)u}{\partial t}+\frac{\partial}{\partial x}\left(\left(\alpha_v\rho_v+\alpha_l\rho_l\right)u^2+p\right)=S_{F,v}+S_{F,l}=S_F \tag{2.14}$$

$$\frac{\partial}{\partial t}\left(\alpha_v\rho_vE_v+\alpha_l\rho_lE_l\right)+\frac{\partial}{\partial x}\left(\left(\alpha_v\rho_vE_v+\alpha_l\rho_lE_l\right)u+pu\right)=S_{E,v}+S_{E,l}=S_E \tag{2.15}$$

Note that all the interface exchange terms for each fluid phase sum up to zero.

By defining the bulk mixture properties as:

$$\rho=\alpha_v\rho_v+\alpha_l\rho_l \tag{2.16}$$

$$\rho E=\alpha_v\rho_vE_v+\alpha_l\rho_vE_l \tag{2.17}$$

the resulting governing conservation equations are given by:

$$\frac{\partial\rho}{\partial t}+\frac{\partial}{\partial x}\rho u=S_M \tag{2.18}$$

$$\frac{\partial\rho u}{\partial t}+\frac{\partial}{\partial x}\left(\rho u^2+p\right)=S_F \tag{2.19}$$

$$\frac{\partial\rho E}{\partial t}+\frac{\partial}{\partial x}\left(\rho uE+pu\right)=S_E \tag{2.20}$$

Despite the strong assumptions made, the HEM model is the most frequently applied model in academic research and industry involving multi-phase flow (Mahgerefteh et al. 1997; Adeyemi Oke et al. 2003; Mahgerefteh et al. 2006; Teng et al. 2016) due to its simplicity and its relatively low computational demand.

2.1.2.2.2 Homogeneous Relaxation Mixture Model

The HRM model is developed to account for thermodynamic non-equilibrium caused by delayed phase transition during decompression. For a vapour-liquid two-phase mixture, as the phase fraction can no longer be assumed at thermodynamic equilibrium values, an additional equation describing its evolution with the flow needs to be introduced. Following Bilicki & Kestin (1990), Downar-Zapolski & Bilicki (1996), Brown et al. (2013) and Nouri-Borujerdi & Shafiei Ghazani (2017), such an equation is essentially a scalar transport equation given by:

$$\frac{\partial \alpha}{\partial t} + u\frac{\partial \alpha}{\partial x} = \frac{\Gamma}{\rho} \qquad 2.21$$

where Γ stands for the rate of interface mass exchange per unit volume. Note that the phase index, *k* is dropped as equation 2.21 generally only concerns the vapour phase.

Before equation 2.21 can be solved in conjunction with the mass, momentum and energy conservation equations, Γ needs to be specified. For example, the following relations can be adopted:

$$\Gamma = K_t\left(\varphi - \varphi_{eq}\right) \qquad 2.22$$

Where, ϕ is the thermodynamic variable of choice. It can be the pressure (Woolley et al. 2013; Wen et al. 2016), enthalpy (S. Brown et al. 2014), chemical potential (Lund 2013) and phase composition (Downar-Zapolski & Bilicki 1996; Brown et al. 2013; Nouri-Borujerdi & Shafiei Ghazani 2017). The subscript, *eq* denotes thermodynamic equilibrium, and K_t is the (empirical) relaxation parameter. The physical interpretation of the above is that, at thermodynamic equilibrium, the mass exchange rate is zero, and the thermal properties of the flow must be at their equilibrium values.

For example, for the choice of $\varphi = \phi$ (ϕ is the vapour phase mass fraction) and $K_t = 1/\tau$, equation 2.22 becomes:

$$\Gamma = \frac{1}{\tau}\rho\left(\phi - \phi_{eq}\right) \qquad 2.23$$

where τ is the relaxation time determined empirically.

Substituting equation 2.23 into equation 2.21 gives:

$$\frac{d\alpha}{dt} = \frac{1}{\tau}\left(\phi - \phi_{eq}\right) \qquad 2.24$$

with the total derivative of α defined as:

$$\frac{d\alpha}{dt} = \frac{\partial\alpha}{\partial t} + u\frac{\partial\alpha}{\partial x} \qquad 2.25$$

Analytical integration of equation 2.24 indicates an exponential tendency of the HRM system towards the HEM system (Downar-Zapolski & Bilicki 1996).

The full set of the HRM model conservation equations are summarised in the following:

$$\frac{\partial\alpha}{\partial t} + u\frac{\partial\alpha}{\partial x} = \frac{\Gamma}{\rho} \qquad 2.26$$

$$\frac{\partial\rho}{\partial t} + \frac{\partial}{\partial x}\rho u = 0 \qquad 2.27$$

$$\frac{\partial\rho u}{\partial t} + \frac{\partial}{\partial x}\left(\rho u^2 + p\right) = 0 \qquad 2.28$$

$$\frac{\partial\rho E}{\partial t} + \frac{\partial}{\partial x}\left(\rho u E + p u\right) = 0 \qquad 2.29$$

2.1.2.2.3 Drift Flux Mixture Model

In the case of finite rate of interface momentum exchange, mechanical non-equilibrium may significantly impact the fluid flow and thus needs to be accounted for. Such consideration leads to the development of the DFM model (Munkejord et al. 2010), as summarised in the following for vapour-liquid two-phase flows.

Starting from the previously derived phasic conservation equations 2.10 to 2.12, summation of the vapour and liquid phases gives:

$$\frac{\partial\left(\alpha_v\rho_v+\alpha_l\rho_l\right)}{\partial t}+\frac{\partial}{\partial x}\left(\alpha_v\rho_v u_v+\alpha_l\rho_l u_l\right)=S_M \tag{2.30}$$

$$\frac{\partial\left(\alpha_v\rho_v u_v+\alpha_l\rho_l u_l\right)}{\partial t}+\frac{\partial}{\partial x}\left(\alpha_v\rho_v u_v^2+\alpha_l\rho_l u_l^2+\alpha_v p_v+\alpha_l p_l\right)=S_F \tag{2.31}$$

$$\frac{\partial}{\partial t}\left(\alpha_v\rho_v E_v+\alpha_l\rho_l E_l\right)+\frac{\partial}{\partial x}\left(\alpha_v\rho_v E_v u_v+\alpha_l\rho_l E_l u_l+p_v\alpha_v u_v+p_l\alpha_l u_l\right)=S_E \tag{2.32}$$

In the absence of volumetric terms, the RHS of the above equations are zero, as in the case of the HEM model. However, unlike the HEM model, the phasic velocities, u_v and u_l are different and related via a prescribed relation referred to as the phase slip relation. Such a relation is generally empirical and often in the form of (Munkejord et al. 2010):

$$u_v-u_l=\mathrm{f}_n\left(\alpha_v\rho_v,\ \alpha_l\rho_l,\ u_v\right) \tag{2.33}$$

where the LHS of equation 2.33 is the so-called 'slip velocity'. The exact expression of equation 2.33 varies with the flow regimes, and an example can be found in Section 2.2.3. It is worth noting that the DFM model is limited to flow regimes where the two fluid phases are strongly coupled (e.g. bubbly flow) so that a slip relation can be prescribed (Ishii 1977; Hibiki & Ishii 2003).

The final form of the DFM model is given by (Munkejord et al. 2010):

$$\frac{\partial\left(\alpha_v\rho_v+\alpha_l\rho_l\right)}{\partial t}+\frac{\partial}{\partial x}\left(\alpha_v\rho_v u_v+\alpha_l\rho_l u_l\right)=S_M \tag{2.34}$$

$$\frac{\partial\left(\alpha_v\rho_v u_v+\alpha_l\rho_l u_l\right)}{\partial t}+\frac{\partial}{\partial x}\left(\alpha_v\rho_v u_v^2+\alpha_l\rho_l u_l^2+p\right)=S_M \tag{2.35}$$

$$\frac{\partial}{\partial t}\left(\alpha_v\rho_v E_v+\alpha_l\rho_l E_l\right)+\frac{\partial}{\partial x}\left(\alpha_v\rho_v E_v u_v+\alpha_l\rho_l E_l u_l+p\left(\alpha_v u_v+\alpha_l u_l\right)\right)=S_M \tag{2.36}$$

2.1.2.2.4 Two-Fluid Mixture Model

In the case of the HEM, HRM and DFM models, there exists only one set of conservation equations for all the constituent fluid phases. Such flow models are often referred to as 'single-fluid model', involving several assumptions relating the thermal and mechanical properties of each fluid phase. Examples include the homogeneous equilibrium assumption in the case of the HEM model, the mechanical equilibrium assumption in the case of the HRM model, and the phase slip relation in the case of the DFM model.

In reality, the fluid phases properties may not be closely related. For example, during pipeline puncture decompression, complete fluid phase separation (stratification) may occur as a result of significant density differences between the vapour and liquid phases. Interface interactions may be limited by a much smaller interface area in comparison to e.g. bubbly flow. As such, the interface exchange terms must be explicitly modelled, and the conservation equations of mass, momentum and energy must be solved for each constituent phase as shown below (Paillère et al. 2003; Chang & Liou 2007; Yeom & Chang 2013; S. Brown et al. 2014):

$$\frac{\partial}{\partial t}\alpha_v\rho_v + \frac{\partial}{\partial x}\alpha_v\rho_v u_v = S_{M,v} \tag{2.37}$$

$$\frac{\partial}{\partial t}\alpha_l\rho_l + \frac{\partial}{\partial x}\alpha_l\rho_l u_l = S_{M,l} \tag{2.38}$$

$$\frac{\partial}{\partial t}\alpha_v\rho_v u_v + \frac{\partial}{\partial x}\left(\alpha_v\rho_v u_v^2 + \alpha_v p_v\right) = S_{F,v} \tag{2.39}$$

$$\frac{\partial}{\partial t}\alpha_l\rho_l u_l + \frac{\partial}{\partial x}\left(\alpha_l\rho_l u_l^2 + \alpha_l p_l\right) = S_{F,l} \tag{2.40}$$

$$\frac{\partial}{\partial t}\alpha_v\rho_v E_v + \frac{\partial}{\partial x}\left(\alpha_v\rho_v u_v E_v + \alpha_v u_v p_v\right) + p_v\frac{\partial\alpha_v}{\partial t} = S_{E,v} \tag{2.41}$$

$$\frac{\partial}{\partial t}\alpha_l\rho_l E_l + \frac{\partial}{\partial x}\left(\alpha_l\rho_l u_l E_l + \alpha_l u_l p_l\right) + p_l\frac{\partial\alpha_l}{\partial t} = S_{E,l} \tag{2.42}$$

Here, the phasic pressures are often assumed to be identical:

$$p_v = p_l \tag{2.43}$$

The resulting flow model is referred to as the *'six-equation TFM model'*.

As no prescribed closure relations are required for the TFM model to relate phasic mechanical and thermal properties, in comparison to the single-fluid models, the TFM model is more physically relevant, complete and thus has a wider range of applicability in (but not limited to) pipeline decompression modelling.

2.1.3 Constitutive Relations

In the case of pipe flow, the volumetric terms in the above flow models (as part of the RHS of the conservation equations) represent fluid/wall heat transfer and friction and need to be accounted for.

In this section, examples of the constitutive relations for specifying fluid/wall heat transfer and friction in the open literature are presented.

2.1.3.1 Fluid/wall Heat Transfer

During pipeline decompression, heat transfer to the fluid within the pipe is mainly from warmer pipe wall. Heat loss to the ambient surroundings is ignored if the pipe is thermally insulated.

The constitutive relations for both the single-fluid and TFM models are given in the following.

In the single-fluid models: The heat flux from the pipe wall to the fluid reads:

$$\dot{q} = U\left(T_w - T\right) \qquad 2.44$$

where U is the overall heat transfer coefficient. It is usually calculated using empirical correlations. For forced convection heat transfer, examples include the Dittus-Boelter equation (Knudsen et al. 1997a) adopted by Brown et al. (2014) and the Colburn correlation (Knudsen et al. 1997a) adopted by Munkejord & Hammer (2015). The Dittus-Boelter equation reads:

$$\mathrm{Nu} = 0.023\mathrm{Re}^{0.8}\mathrm{Pr}^{0.4} \qquad 2.45$$

where the bulk flow Nusselt number, Nu, Reynolds number, Re and Prandtl number, Pr are respectively defined as:

$$\mathrm{Nu} = \frac{UD_{w,in}}{k} \qquad 2.46$$

$$\mathrm{Re} = \frac{\rho u D_{w,in}}{\mu} \qquad 2.47$$

$$\mathrm{Pr} = \frac{C_p \mu}{k} \qquad 2.48$$

where k, μ and C_p are respectively the bulk flow thermal conductivity, viscosity and heat capacity. By obtaining $\mathrm{N_u}$ from equation 2.45, U can be readily calculated (from equation 2.46) and hence the corresponding heat flux may be determined (from equation 2.44).

In the case of boiling, the heat transfer is enhanced and the resulting heat transfer flux can be estimated using appropriate correlations. An example (the Rohsenow's correlation (Knudsen et al. 1997b)) is presented below:

$$\dot{q} = \mu_l h_{fg} \left(\frac{g\left(\rho_l - \rho_v\right)}{\sigma} \right) \left(\frac{C_{p,l}\left(T_w - T\right)}{0.013 h_{fg} \mathrm{Pr}_l^1} \right)^3 \qquad 2.49$$

where μ_l, σ, h_{fg} and $C_{p,l}$ are respectively the viscosity, surface tension, latent heat and constant pressure heat capacity of the liquid phase. Pr_l is the liquid phase Prandtl number given by:

$$\mathrm{Pr}_l = \frac{C_{p,l}\mu_l}{k_l} \qquad 2.50$$

where k_l is the liquid phase thermal conductivity.

The wall temperature, T_w can be modelled by first assuming constant pipe wall density and specific heat capacity. Thereafter, further neglecting any temperature gradient across the wall thickness (given that the thermal conductivity of the pipe wall is high (ca. 40 W/m-K (Liiey et al. 2008)), the wall temperature variation as a function of time during decompression following the energy balance is given by:

$$C_{p,w}\rho_w \frac{dT_w}{dt} = \dot{q}\tilde{A} \qquad 2.51$$

where $\tilde{A}$ is the available heat transfer area per unit volume given by:

$$\tilde{A} = \frac{\pi D_{w,in} L_w}{\pi \left(D_{w,out}^2 - D_{w,in}^2\right) L_w / 4} = \frac{4 D_{w,in}}{\left(D_{w,out}^2 - D_{w,in}^2\right)} \qquad 2.52$$

where $D_{w,in}$ and $D_{w,out}$ are respectively the inner and outer pipeline diameters.

Finally, the heat flux, $\dot{q}$ is converted to the volumetric heat source, $\dot{Q}$, following:

$$\dot{Q} = \frac{\dot{q}\pi D_{w,in} L_w}{\pi D_{w,in}^2 L_w / 4} = \frac{4}{D_{w,in}} \dot{q} \qquad 2.53$$

In the TFM model: As the energy conservation equation is solved for each constituent fluid phase, it is possible to consider distinctive heat transfer modes in the vapour and liquid phases.

An excellent example would be stratified flow encountered during puncture-induced pipeline decompression. Here, the vapour and liquid fluid phases are completely separated from each other. Figure 2.1 gives a schematic representation of a cross-section of stratified pipe flow (with an assumed flat interface).

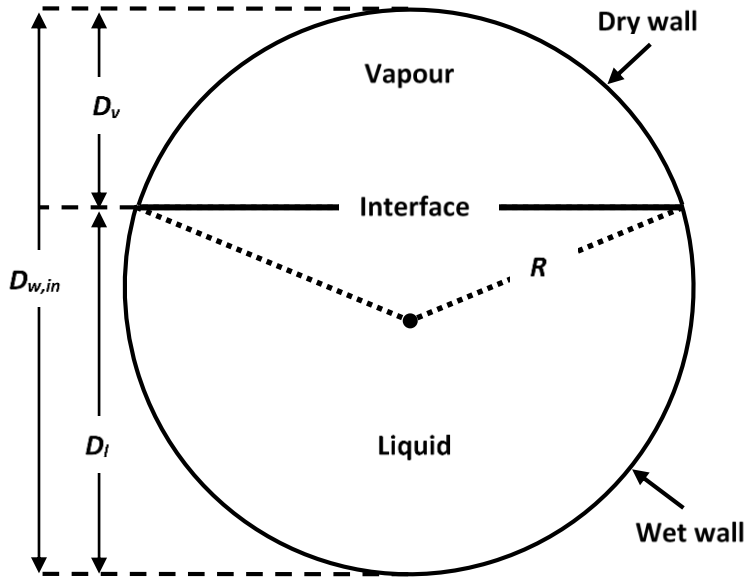

Figure 2.1: Schematic representation of stratified flow in a pipeline during decompression. D_v and D_l are respectively the elevations of the stratified vapour and liquid phases, $D_{w,in}$ is the pipe inner diameter, *R* is the corresponding radius.

Tuning our attention to the heat transfer from the dry wall to the stratified vapour phase first, convection can take place, and the correlation discussed in the single-fluid model above can be applied with all the relevant properties calculated for the vapour phase.

The corresponding heat transfer flux then reads:

$$\dot{q}_v = U_v \left(T_{w,v} - T_v \right) \qquad 2.54$$

With regards to the dry wall temperature, $T_{w,v}$, equation 2.51 is still applicable with the available heat transfer area between the dry wall and the stratified vapour phase per unit volume of the dry wall, $\tilde{A}_v$ given by:

$$\tilde{A}_v = \frac{D_{w,in} \cos^{-1}\left(2D_l / D_{w,in} - 1\right) L_w}{\left(\left(D_{w,out}^2 - D_{w,in}^2 / 4\right)\cos^{-1}\left(2D_l / D_{w,in} - 1\right) - \left(D_{w,in} D_v - D_v^2\right)\right) L_w} \qquad 2.55$$

where the definitions of D_v and D_l are given in the figure 2.1 caption. The corresponding vapour phase volumetric heat source, $\dot{Q}_v$ is then:

$$\dot{Q}_v = \dot{q}_v \frac{D_{w,in}\cos^{-1}\left(2D_l/D_{w,in}-1\right)L_w}{\pi D_{w,in}^2 L_w/4} = \dot{q}_v \frac{4\cos^{-1}\left(2D_l/D_{w,in}-1\right)}{\pi D_{w,in}} \quad 2.56$$

Next, with regards to the stratified liquid phase, the corresponding heat flux, $\dot{q}_l$ and the wet wall temperature, $T_{w,l}$ can be computed respectively following equations 2.49 and 2.51 with the available heat transfer area per unit volume defined as:

$$\tilde{A}_l = \frac{D_{w,in}\left(\pi-\cos^{-1}\left(2D_l/D_{w,in}-1\right)\right)L_w}{\left(\pi D_{w,in}^2/4\right)L_w - \left(\left(D_{w,in}^2/4\right)\cos^{-1}\left(2D_l/D_{w,in}-1\right)-\left(D_{w,in}D_v - D_v^2\right)\right)L_w} \quad 2.57$$

The corresponding liquid phase volumetric heat source, $\dot{Q}_l$ is given by:

$$\dot{Q}_l = \dot{q}_l \frac{4\left(\pi-\cos^{-1}\left(2D_l/D_{w,in}-1\right)\right)}{\pi D_{w,in}} \quad 2.58$$

2.1.3.2 Fluid/wall Friction

For one-dimensional pipeline decompression flow models, fluid/wall friction can be included as a body force in the momentum conservation equation. It is correlated with the friction factor, *f* determined by appropriate empirical relations.

In the single-fluid model: For laminar pipe flow (Re < 2300), the friction factor is given by (Tilton 1997):

$$f = \frac{16}{\mathrm{Re}} \quad 2.59$$

In transitional and turbulent flows ($4000 < \mathrm{Re} < 4\times10^8$), the Chen's correlation (Chen 1979) can be applied (Brown et al. 2013; Martynov et al. 2014; R. M. Woolley et al. 2014). The corresponding friction factor is given by:

$$\frac{1}{\sqrt{f}} = 3.48 - 1.7372 \ln\left(\frac{\varepsilon}{D_{w,in}/2} - \frac{16.2446}{\mathrm{Re}} \ln B \right) \qquad 2.60$$

where:

$$B = \frac{\left(\varepsilon / \left(D_{w,in}/2\right)\right)^{1.0198}}{6.0983} + \left(\frac{7.149}{Re} \right)^{0.8981} \qquad 2.61$$

and ε is the pipe wall roughness.

After obtaining f, the wall friction force per volume is given by:

$$F_w = -(1/2)\,\rho u |u|\, f \left(\frac{\pi D_{w,in} L_w}{\pi D_{w,in}^2 / 4 L_w} \right) = -\frac{2\rho u |u| f}{D_{w,in}} \qquad 2.62$$

In the TFM model: Recalling the phasic momentum conservation equations 2.39 and 2.40 in the two-fluid model, fluid/wall friction force can be specified for the vapour and liquid phases individually.

Again, taking stratified flow as an example (figure 2.1), according to Taitel & Dukler (1976), the friction factor for the stratified vapour phase is given by:

$$f_v = C_v \left(\frac{D_{h,v} u_v}{\mu_v / \rho_v} \right)^{-n} = C_v \left(\mathrm{Re}_v \right)^{-n} \qquad 2.63$$

and that of the stratified liquid phase is:

$$f_l = C_l \left(\frac{D_{h,l} u_l}{\mu_l / \rho_l} \right)^{-m} = C_l \left(\mathrm{Re}_l \right)^{-m} \qquad 2.64$$

where $D_{h,v}$ and $D_{h,l}$ are the hydraulic diameters of the vapour and liquid phases respectively, defined in (Taitel & Dukler 1976). C_v, C_l, n and m are model constants. For laminar flow, $C_v = C_l = 16$, $n = m = 1.0$, and for turbulent flow, $C_v = C_l = 0.046$, $n = m = 0.2$. The resulting friction force per volume each in the vapour and liquid phases is respectively given by:

$$F_{w,v} = -\frac{2\cos^{-1}\left(2D_l/D_{w,in}-1\right)\rho_v u_v |u_v| f_v}{\pi D_{w,in}} \quad 2.65$$

$$F_{w,l} = -\frac{2\left(\pi-\cos^{-1}\left(2D_l/D_{w,in}-1\right)\right)\rho_l u_l |u_l| f_l}{\pi D_{w,in}} \quad 2.66$$

2.1.4 Thermodynamics

2.1.4.1 Equation of State

To determine the fluid flow thermal properties (e.g. pressure and temperature) and phase equilibrium data, an Equation of State (EoS) can be applied.

For pipeline decompression modelling, the most commonly adopted EoS are the cubic EoS which are computationally efficient (Munkejord et al. 2016). Examples include (Mahgerefteh et al. 2008; Teng et al. 2016; Nouri-Borujerdi & Shafiei Ghazani 2017). Among these, the most widely validated for CO_2 is the Peng-Robinson EoS (PR RoS; Peng & Robinson 1976) and its variations (e.g. volume-translated Peng-Robinson EoS (Abudour et al. 2013)). Its general form and key parameters are presented below:

$$p = \frac{RT}{v-\tilde{b}} - \frac{\tilde{a}}{v^2+2\tilde{b}v-\tilde{b}} \quad 2.67$$

where:

$$\tilde{a} = \tilde{a}_c \alpha \quad 2.68$$

$$\tilde{a}_c = 0.45724\frac{R^2T_c^2}{p_c^2} \quad 2.69$$

$$\alpha = \left(1+\kappa\left(\frac{T}{T_c}\right)^{0.5}\right)^2 \quad 2.70$$

$$\kappa = 0.48+1.574\omega-0.175\omega^2 \quad 2.71$$

$$\tilde{b} = 0.07780\frac{RT_c}{p_c} \qquad 2.72$$

In the above equations, p_c, T_c and v are the critical pressure, critical temperature and molar volume, respectively. ω is the accentric factor. For multi-component mixtures, $\tilde{a}$ and $\tilde{b}$ are modified to include the dependence on component molar fractions:

$$\tilde{a} = \sum_i \sum_j z_i z_j \left(\tilde{a}_{c,ij}\alpha_{ij}\right) \qquad 2.73$$

$$\tilde{a}_{c,ij}\alpha_{ij} = \left(1 - k_{ij}\right)\sqrt{\left(\tilde{a}_{c,i}\tilde{a}_i\right)\left(\tilde{a}_{c,j}\tilde{a}_j\right)} \qquad 2.74$$

$$\tilde{b} = \sum_i z_i \tilde{b}_i \qquad 2.75$$

where k_{ij}, and $z_{i,j}$ are respectively the binary interaction parameter and component molar composition.

Recently, more advanced multi-parameter EoS have become popular for pipeline decompression modelling, especially for multi-component mixtures, due to their superior accuracy (see (Elshahomi et al. 2015; Munkejord & Hammer 2015), for example). According to Aursand et al. (2017), multi-parameter EoS are the most accurate EoS for the regions where thermal property experimental data are available. The general structure of such an EoS is given as follows (Lemmon & Tillner-Roth 1999):

$$a\left(\rho, T\right) = a^o\left(\rho, T\right) + a^r\left(\rho, T\right) \qquad 2.76$$

where a is the specific Helmholtz energy. a^o and a^r are respectively the ideal and residual contributions. a^o is defined as:

$$a^o\left(\rho, T\right) = h^o - RT - Ts^o = \qquad 2.77$$
$$\left[\int_{T_0}^{T} Cp^o dT + h_0^o\right] - RT - T\left[\int_{T_0}^{T} \frac{Cp^o - R}{T} dT - R\ln\left(\frac{\rho}{\rho_0^o}\right) + s_0^o\right]$$

where h_0^o , ρ_0^o and s_0^o are respectively the enthalpy, density and entropy at an arbitrary reference state. C_p^o is the ideal gas heat capacity (as a function of T). The residual contribution, a^r is given by:

$$a^r(\rho,T) = RT\sum_{k=1}^{K_{pol}} n_k \left(\frac{\rho}{\rho_c}\right)^{d_k} \left(\frac{T_c}{T}\right)^{t_k} + RT\sum_{k=K_{pok}+1}^{K_{pol}+K_{exp}} n_k \left(\frac{\rho}{\rho_c}\right)^{d_k} \left(\frac{T_c}{T}\right)^{t_k} \exp\left(-\left(\frac{\rho}{\rho_c}\right)^{e_k}\right) \quad 2.78$$

where the first term on the RHS of the above equation represents the sum of K_{pol} polynomial functions in terms of the reduced density, ρ/ρ_c and the inverse reduced temperature, T_c/T . The second term consists of K_{exp} exponential functions. The collection of these two terms is referred to as the bank of terms, of which the coefficients, n_k , d_k , t_k and e_k are determined by multi-property fitting and optimisation methods based on available experimental measurements.

For multi-component mixtures, much like in the case of PR EoS, the dependence on component molar compositions needs to be accounted for. Hence:

$$a(\rho,T,z_i) = a^o(\rho,T,z_i) + a^r(\rho,T,z_i) \quad 2.79$$

where:

$$a^o(\rho,T,z_i) = \sum_{i=1}^{N} z_i\left[a_i^o(\rho,T) + \ln(z_i)\right] \quad 2.80$$

$$a^r(\rho,T,z_i) = \sum_{i=1}^{N} z_i a_i^r(\rho,T) + \Delta a^r(\rho,T,z_i) \quad 2.81$$

$$\Delta a^r(\rho,T,z_i) = \sum_{i=1}^{N-1}\sum_{j=i+1}^{N} z_i z_j k_{ij} a_{ij}^r(\rho,T) \quad 2.82$$

where k_{ij} is again the parameter specific to a binary mixture, and a_{ij}^r is given by:

$$a_{ij}^{r}\left(\rho,T\right)=RT\sum_{k=1}^{K_{pol,ij}}n_{ij,k}\left(\frac{\rho}{\rho_r}\right)^{d_{k,ij}}\left(\frac{T_r}{T}\right)^{t_{k,ij}} \qquad 2.83$$
$$+RT\sum_{k=K_{pok,ij}+1}^{K_{pol,ij}+K_{exp,ij}}n_{k,ij}\left(\frac{\rho}{\rho_r}\right)^{d_{k,ij}}\left(\frac{T_r}{T}\right)^{t_{k,ij}}\exp\left(-\left(\frac{\rho}{\rho_r}\right)^{c_{k,ij}}\right)$$

where ρ_r and T_r are the so-called reducing functions respectively for the mixture density and temperature which impose combining rules for the critical parameters (e.g. critical temperatures) of the pure components.

It is interesting to note that PR EoS (or other cubic EoS) can also be recast in terms of Helmholtz free energy with the residual part defined as:

$$a^{r}\left(\rho,T\right)=RTln\left(\frac{1}{1-\tilde{b}\rho}\right)+\frac{\tilde{a}}{2\sqrt{2}}ln\left(\frac{1+\left(\sqrt{2}+1\right)\tilde{b}\rho}{1-\left(\sqrt{2}+1\right)\tilde{b}\rho}\right) \qquad 2.84$$

Examining equation 2.84 shows that there are only two parameters in contrast to multi-parameter EoS of which a typical number of adjustable parameters is around 500 (Kunz et al. 2007). This has direct impact on the accuracy of PR EoS in its predictions of thermal properties and phase equilibrium data, which will be further discussed later.

2.1.4.2 Predictions of Key Thermal Properties

Following the above, the calculation of the fluid pressure, specific enthalpy and specific entropy based on an EoS is presented (Lemmon & Tillner-Roth 1999):

$$p=\rho RT+\frac{\rho^2}{\rho_r}\left(\frac{\partial a^r}{\partial\left(\rho/\rho_r\right)}\right) \qquad 2.85$$

$$h=RT+RT_r\left(\left(\frac{\partial a^o}{\partial\left(T_r/T\right)}\right)+\left(\frac{\partial a^r}{\partial\left(T_r/T\right)}\right)\right)+\frac{\rho RT}{\rho_r}\left(\frac{\partial a^r}{\partial\left(\rho/\rho_r\right)}\right) \qquad 2.86$$

$$s = \frac{RT_r}{T^2}\left(\left(\frac{\partial a^o}{\partial(T_r/T)}\right)+\left(\frac{\partial a^r}{\partial(T_r/T)}\right)\right)-\frac{R\left(a^o+a^r\right)}{T} \qquad 2.87$$

Note that the above equations are all explicit in Helmholtz free energy and its derivatives.

Alternatively for PR EoS (equation 2.67), the departure equation can be applied as shown in the following. Writing PR EoS in terms of compressibility factor, *Z*:

$$Z = 1+\frac{\tilde{b}\rho}{1-\tilde{b}\rho}-\frac{\tilde{a}}{\tilde{b}RT}\left(\frac{\tilde{b}\rho}{1+2\tilde{b}\rho-\tilde{b}^2\rho^2}\right) \qquad 2.88$$

the fluid specific enthalpy and entropy are respectively given by:

$$h-h^o = RT\left[\int_0^\rho -T\left(\frac{\partial Z}{\partial T}\right)\frac{d\rho}{\rho}+Z-1\right] \qquad 2.89$$

$$s-s^o = R\left[\int_0^\rho\left(-T\left(\frac{\partial Z}{\partial T}\right)-(Z-1)\right)\frac{d\rho}{\rho}+\ln(Z)\right] \qquad 2.90$$

where the value zero in the integration limit represents the ideal gas limit ($Z = 1$). h^o and s^o are respectively the ideal gas specific enthalpy and entropy at a given state (p and T).

Another important thermodynamic variable is the fluid speed of sound defined as:

$$c = \sqrt{\left(\frac{\partial\rho}{\partial p}\right)_s} \qquad 2.91$$

Its significance in pipe flow modelling will be elucidated in Section 2.1.6.

2.1.4.3 Predictions of Equilibrium States

For a non-reacting mixture of *N* components, thermodynamic equilibrium between the coexisting phases (e.g. vapour and liquid phases) implies the following equalities (Kunz et al. 2007):

$$T_v = T_l = T_{eq} \tag{2.92}$$

$$p_v = p_l = p_{eq} \tag{2.93}$$

$$\varphi_{v,i} = \varphi_{l,i} \tag{2.94}$$

$\varphi_{v,i}$ and $\varphi_{l,i}$ are the chemical potentials of each component *i* in the vapour and liquid phases, respectively given by:

$$\varphi_{i,v} = \left(\frac{\partial n_v a}{\partial n_{v,i}} \right)_{T_v, v_v, n_{v,j}} \tag{2.95}$$

$$\varphi_{i,l} = \left(\frac{\partial n_l a}{\partial n_{l,i}} \right)_{T_l, v_l, n_{l,j}} \tag{2.96}$$

where n_v, n_l, $n_{v,i}$ and $n_{l,i}$ are respectively the total number of moles of the mixture and that of component *i* in the vapour and liquid phases. y_i and x_i correspond to vapour and liquid phase molar compositions, respectively. They are linked to the overall molar composition, z_i through the material balance:

$$y_i = \frac{K_i z_i}{1 - \beta + \beta K_i} \tag{2.97}$$

$$x_i = \frac{z_i}{1 - \beta + \beta K_i} \tag{2.98}$$

where:

$$\beta = \frac{n_v}{n} \tag{2.99}$$

$$K_i = \frac{n_{v,i}}{n_{l,i}} = \frac{y_i}{x_i} \qquad 2.100$$

Note:

$$\sum_i y_i = 1 \qquad 2.101$$

$$\sum_i x_i = 1 \qquad 2.102$$

Examining equations 2.92, 2.93, 2.94, 2.97 (or 2.98), 2.99, 2.100, 2.101 and 2.102 reveals that there are in total $2N + 6$ equations with $3N + 7$ variables (including T_v, T_l, p_v, p_l, v_v (ρ_v), v_l (ρ_l), y_i, x_i, z_i, β). It follows that $N + 1$ variables (e.g. T_{eq} and z_i) need to be specified in order to fully define an equilibrium state.

Solving this non-linear algebraic system is equivalent to minimising the overall Gibbs energy at given T, p and z_i as shown below:

$$dg = dg_v + dg_l \qquad 2.103$$

$$dg_v(T, p, y_i) = \left(\frac{\partial g_v}{\partial p}\right)_{T,y_i} dp + \left(\frac{\partial g_v}{\partial T}\right)_{p,y_i} dT + \sum_i \left(\frac{\partial g}{\partial y_i}\right)_{p,T,y_{j\neq i}} dy_i \xrightarrow{T,p} \sum_i \left(\frac{\partial g}{\partial y_i}\right)_{p,T,y_{j\neq i}} dy_i \qquad 2.104$$

$$dg_l(T, p, x_i) = \left(\frac{\partial g_l}{\partial p}\right)_{T,x_i} dp + \left(\frac{\partial g_l}{\partial T}\right)_{p,x_i} dT + \sum_i \left(\frac{\partial g_l}{\partial x_i}\right)_{p,T,x_{j\neq i}} dx_i \xrightarrow{T,p} \sum_i \left(\frac{\partial g_l}{\partial y_i}\right)_{p,T,x_{j\neq i}} dx_i \qquad 2.105$$

The overall Gibbs energy is minimised when $dg = 0$. Hence:

$$dg_v + dg_l = 0 \qquad 2.106$$

which implies:

$$\left(\frac{\partial g_v}{\partial y_i}\right)_{p,T,y_{j\neq i}} = \left(\frac{\partial g_l}{\partial x_i}\right)_{p,T,x_{j\neq i}} \qquad 2.107$$

Following the definition of chemical potential:

$$\varphi_i = \left(\frac{\partial g}{\partial z_i}\right)_{p,T,z_{j\neq i}} \qquad 2.108$$

equation 2.94 is reproduced.

It is noteworthy that the above discussion is general to any EoS as they all can be written in terms of Helmholtz energy (see equation 2.84 for example).

As stated earlier, PR EoS (or other cubic EoS) has much less adjustable terms as compared to a multi-parameter EoS, resulting in a lower accuracy in e.g. predicting phase equilibrium data. This is demonstrated by plotting the predicted bubble and dew curves from PR EoS and GERG 2008 EoS (a typical multi-parameter EoS; (Kunz & Wagner 2012)) for pure CO_2 and CO_2-rich mixtures of CH_4 and N_2. Both EoS are readily available in the off-the-shelf thermodynamic package, REFPROP (Lemmon et al. 2010). The results are shown in figure 2.2.

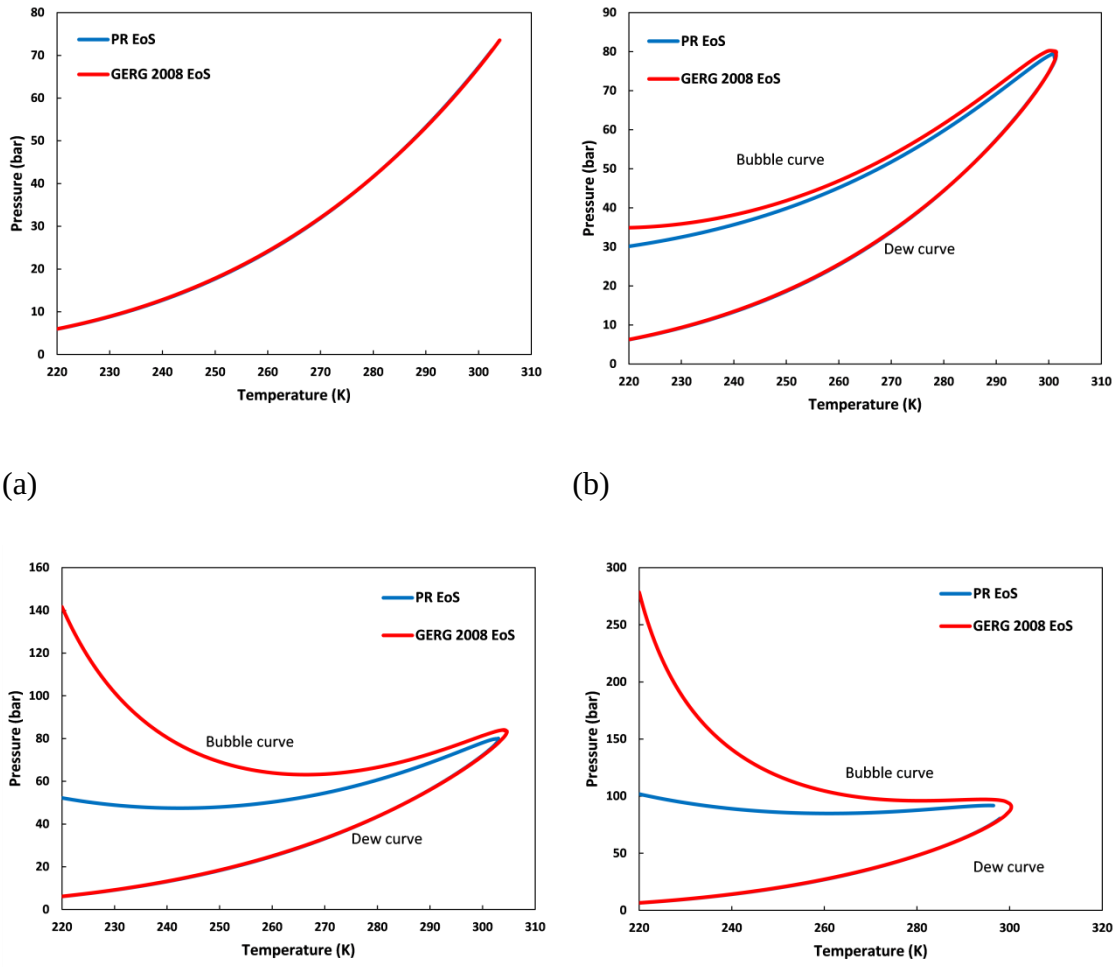

Figure 2.2: Comparisons between the predicted bubble and dew curves of pure CO_2 (a) and CO_2-rich mixtures from PR EoS and GERG 2008 EoS. The included mixtures are: 96% CO_2 + 4% N_2 (b), 97.4% CO_2 + 2.6% N_2 (c) and 92% CO_2 + 4% H_2 +4% N_2 (d).

In figure 2.2, for pure CO_2, both the vapour-liquid phase transition boundary predictions from PR and GERG 2008 EoS are in close agreement. In this case, PR EoS may be preferable due to its higher computational efficiency. However, with regards to multi-component mixtures, significant deviations between the two EoS predictions can be observed especially for the bubble curves. In some cases (see figures 2.2 (c) and (d)), the difference exceeds 100 bar at relatively low temperatures (ca. 230 K). Clearly, (at least) for the tested mixtures, GERG 2008 EoS should be selected over PR EoS.

2.1.4.4 Predictions of Metastable States

During rapid pipeline decompression, delayed phase transition may occur. Such a phenomenon is referred to as relaxation from thermodynamic equilibrium, and in the case of evaporation, the liquid phase will be superheated in its metastable/non-equilibrium state.

The metastable states can also be predicted using an EoS. Taking cubic EoS as an example, its typical predictions for an arbitrary pure fluid are depicted in figure 2.3.

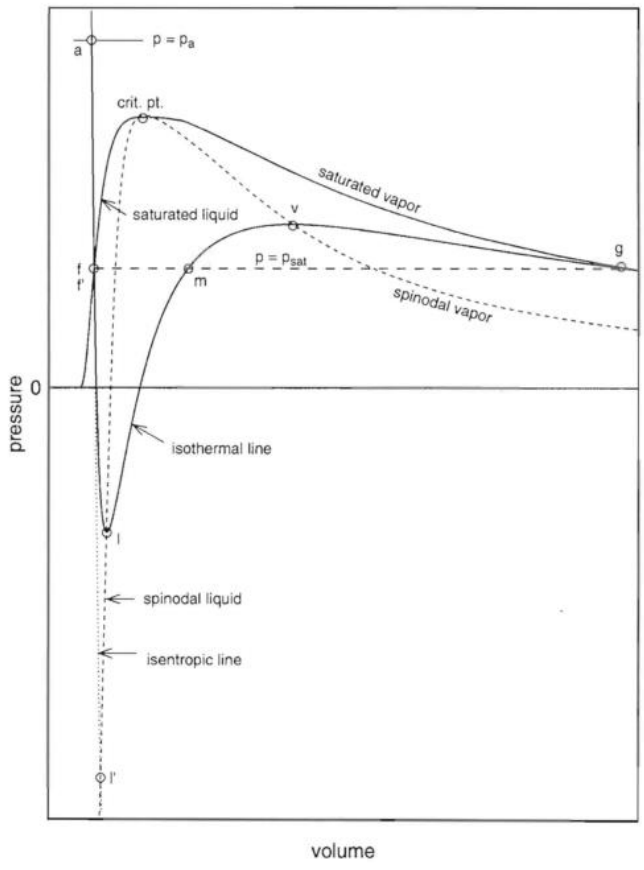

Figure 2.3: Schematic representation of the cubic EoS prediction of a real fluid isotherm (through points a, f, l), isentropes (through points a, f', l') and spinodal lines in *p-v* plane (Shamsundar & Lienhard 1993).

As it may be observed, superheated liquid states lie on the isotherm between points f and l, where the fluid remains as liquid upon crossing the vapour-liquid phase transition boundary (at point f). Point l is referred to as the liquid spinodal limit (superheating limit), beyond which there is no thermodynamically stable state (up to

point v). A collection of these limits (from different isotherms) results in a liquid spinodal curve which ends at the critical point (see the dashed curve on the LHS of the critical point in figure 2.3). It is also noted that the isotherm encompasses a region of negative pressures. However, this has little physical relevance and is often discarded (Shamsundar & Lienhard 1993).

Turing to the isentrope (denoted as 'isentropic line') starting from point a in the liquid phase, it is worth noting that decompression processes (from point a) are bounded by the relevant isentrope and isotherm which respectively represent the isentropic decompression process and the isothermal decompression process (with delayed phase transition beyond point f or f').

There are much less studies in the open literature discussing the accuracy of EoS in predicting non-equilibrium states as compared to those for equilibrium states. One of the major difficulties is obtaining experimental measurements of highly metastable fluids, as minimal disturbances can trigger for example rapid evaporation, and the fluids return to equilibrium states. In a recent publication by Aursand et al. (2016), it states that the uncertainty of an EoS can be characterised by comparing their predictions of liquid spinodal limits to available experimental measurements. In their study, Aursand et al. (2016) used four EoS, including PR EoS (Peng & Robinson 1976), extended corresponding state EoS (Ely 2010), Statistical Associating Fluid Theory (Gross & Sadowski 2001) and GERG 2008 EoS (Kunz & Wagner 2012) to predict such data mainly for hydrocarbons. The performances of PR EoS and GERG 2008 are discussed in the following given their relevance to this work.

Figure 2.4 shows the predicted isotherms for methane at 175 K using various EoS.

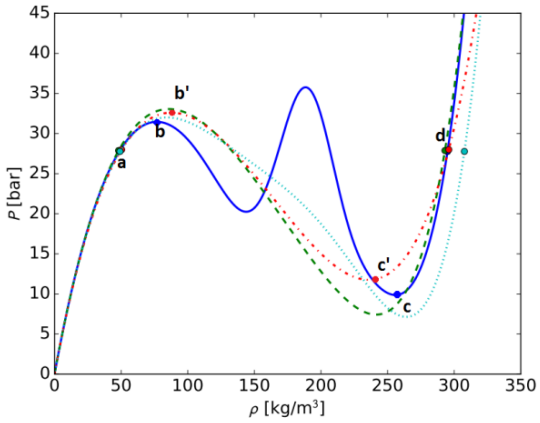

Figure 2.4: Predictions of methane isotherm at 175 K by a variety of EoS. PR EoS and GERG 2008 EoS are marked by red and blue curves, respectively (Aursand et al. 2017). Point a: saturated vapour; points b' and b: vapour spinodal limits respectively predicted by PR EoS and GERG 2008 EoS; points c' and c: liquid spinodal limits (superheating limit) respectively predicted by PR EoS and GERG 2008 EoS; point d: saturated liquid.

From figure 2.4, both PR and GERG 2008 EoS produce similar 'humps' in the metastable vapour and liquid region (portions between points a-b, a-b', c-d and c'-d). Although the predicted isotherm behaviour in the unstable region (b-c and b'-c') differ significantly, they are not thermodynamically admissible and hence pose little importance.

Next, the EoS predictions of liquid superheating limits of various pure fluids and multi-component mixtures are plotted in figure 2.5 together with the measurements (Aursand et al. 2017). Discussion again focuses on the performance of PR EoS and GERG 2008 EoS.

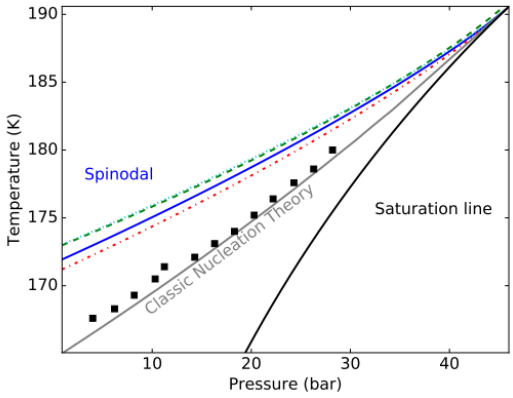

(a)

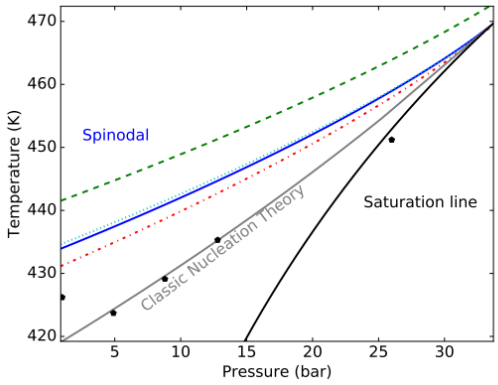

(b)

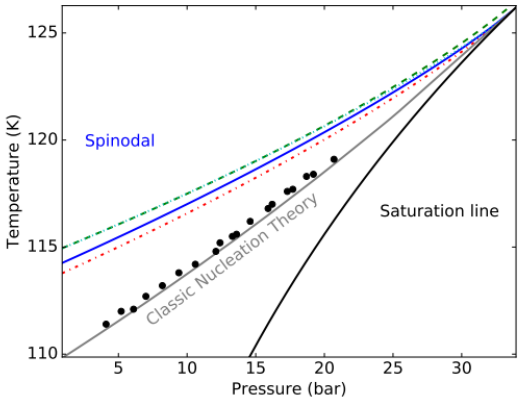

(c)

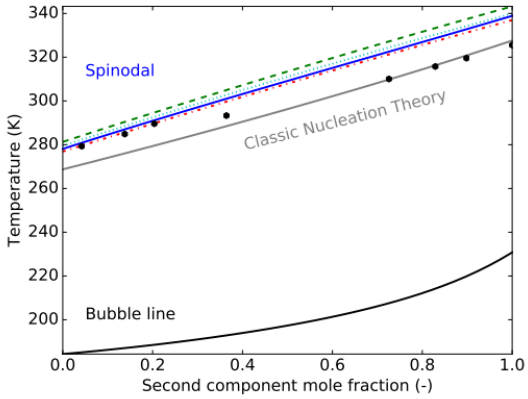

(d)

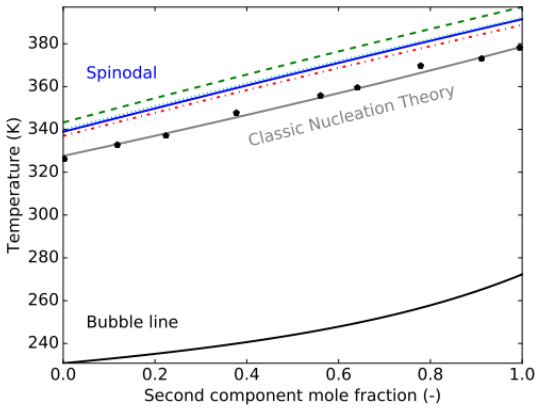

(e)

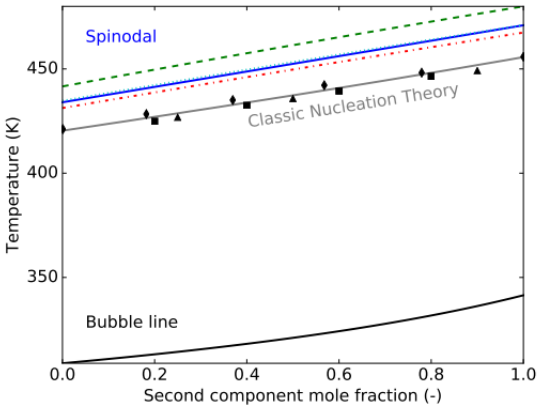

(f)

Figure 2.5: Prediction of the superheating limits by a variety of EoS for methane (a), n-pentane (b), nitrogen (c), ethane + propane mixture (d), propane + n-butane mixture

(e) and n-pentane + n-hexane mixture (f) (Aursand et al. 2017). The PR and GERG 2008 EoS predictions are marked by red and blue curves. The measured data is shown by black markers.

As may be observed in figure 2.5, in contrast to the case of the phase equilibrium predictions, the performances of PR and GERG 2008 EoS in predicting the liquid superheating limits and hence superheated states in general are similar. The overall standard deviations from the measured data are 1.4 and 2.7 K for pure fluids and multi-component mixtures, respectively (Aursand et al. 2017).

2.1.5 Transport Properties

Fluid transport properties, including viscosity, thermal conductivity and surface tension are required in the modelling of fluid/wall heat exchange and friction (see Section 2.1.3).

For individual fluid phases, they are readily calculated using off-the-shelf software such REFPROP (Lemmon et al. 2010). With regards to multi-phase mixtures, the bulk overall transport properties are usually determined by averaging between the constituent fluid phases. As suggested by Daubert & Danner (1989), for a vapour-liquid two-phase mixture, the averaging procedure for viscosity and thermal conductivity reads:

$$\frac{1}{\varphi} = \frac{\beta}{\varphi_v} + \frac{1-\beta}{\varphi_l} \qquad 2.109$$

where $\varphi = \mu$ or k.

2.1.6 Mathematical Nature of the Conservation Equations

The conservation equations for the previously discussed single-fluid and TFM models are systems of PDEs. Their solution methods vary significantly according to the corresponding mathematical natures. They can be elliptic, parabolic and hyperbolic, depending on the eigenvalues of the PDE systems.

2.1.6.1 PDEs for the Single-Fluid Models

2.1.6.1.1 Hyperbolicity

The conservation equations for the single-fluid models are hyperbolic (Toro 2009d). This can be shown by performing a characteristic analysis on the corresponding PDE system. An example based on the HEM model is presented below.

Recall the conservation equations of mass, momentum and energy for the HEM model:

$$\frac{\partial \rho}{\partial t} + \frac{\partial \rho u}{\partial x} = 0 \qquad 2.110$$

$$\frac{\partial \rho u}{\partial t} + \frac{\partial}{\partial x}\left(\rho u u + p\right) = 0 \qquad 2.111$$

$$\frac{\partial \rho E}{\partial t} + \frac{\partial}{\partial x}\left(\left(\rho E + p\right)u\right) = 0 \qquad 2.112$$

This PDE system can be recast in vector form:

$$\frac{\partial}{\partial \mathrm{t}}\boldsymbol{U} + \frac{\partial}{\partial x}\boldsymbol{F}\left(\boldsymbol{U}\right) = \boldsymbol{0} \qquad 2.113$$

Herein, the vector of conservative variables, $\boldsymbol{U}$ and its flux function, $\boldsymbol{F}$ are defined as:

$$\boldsymbol{U} = \begin{pmatrix} \rho \\ \rho u \\ \rho E \end{pmatrix},\ \boldsymbol{F}\left(\boldsymbol{U}\right) = \begin{pmatrix} \rho u \\ \rho u^2 + p \\ \rho u E + p u \end{pmatrix} \qquad 2.114$$

It can be readily seen that equations 2.110 to 2.112 are essentially the Euler equations in conserved form. Expanding the time and space derivatives in equations 2.110 to 2.112, the primitive form of the Euler equations can be derived and is given by:

$$\frac{\partial \rho}{\partial t} + \rho \frac{\partial u}{\partial x} + u \frac{\partial \rho}{\partial x} = 0 \qquad 2.115$$

$$\frac{\partial u}{\partial t} + u\frac{\partial u}{\partial x} + \frac{1}{\rho}\frac{\partial p}{\partial x} = 0 \qquad 2.116$$

$$\frac{\partial e}{\partial t} + u\frac{\partial e}{\partial x} + u\left(\frac{\partial u}{\partial t} + u\frac{\partial u}{\partial x}\right) + \frac{p}{\rho}\frac{\partial u}{\partial x} + \frac{u}{\rho}\frac{\partial p}{\partial x} = 0 \qquad 2.117$$

Note that volumetric source terms (e.g. representing fluid/wall heat transfer and friction) are neglected for this analysis, as they do not alter the mathematical nature of the PDE system (Stadtke 2006). Equations 2.116 and 2.117 can be combined:

$$\frac{\partial e}{\partial t} + u\frac{\partial e}{\partial x} + \frac{p}{\rho}\frac{\partial u}{\partial x} = 0 \qquad 2.118$$

Alternatively, one can introduce the entropy, *s* as a new primitive variable. Appling the fundamental thermodynamic relation for the internal energy, *e*:

$$de = Tds - pdv = Tds + \frac{p}{\rho^2}d\rho \qquad 2.119$$

and substituting the above into equation 2.118:

$$T\frac{\partial s}{\partial t} + \frac{p}{\rho^2}\frac{\partial \rho}{\partial t} + u\left(T\frac{\partial s}{\partial x} + \frac{p}{\rho^2}\frac{\partial \rho}{\partial x}\right) + \frac{p}{\rho}\frac{\partial u}{\partial x} = \qquad 2.120$$

$$T\frac{\partial s}{\partial t} + Tu\frac{\partial s}{\partial x} + \frac{p}{\rho^2}\left(\frac{\partial \rho}{\partial t} + u\frac{\partial \rho}{\partial x} + \rho\frac{\partial u}{\partial x}\right) = 0$$

In view of equation 2.115, equation 2.120 can be further simplified to:

$$\frac{\partial s}{\partial t} + u\frac{\partial s}{\partial x} = 0 \qquad 2.121$$

The resulting entropy conservation equation is easier to work with as compared to the energy conservation equation 2.118 and thus adopted for the rest of the analysis. The resulting conservation equations are summarised here:

$$\frac{\partial \rho}{\partial t} + \rho \frac{\partial u}{\partial x} + u \frac{\partial \rho}{\partial x} = 0 \qquad 2.122$$

$$\frac{\partial u}{\partial t} + u \frac{\partial u}{\partial x} + \frac{1}{\rho} \frac{\partial p}{\partial x} = 0 \qquad 2.123$$

$$\frac{\partial s}{\partial t} + u \frac{\partial s}{\partial x} = 0 \qquad 2.124$$

An EoS is required to close the above PDE system.

Writing an arbitrary EoS:

$$\rho = \rho(p, s) \qquad 2.125$$

or in differential form:

$$d\rho = \left(\frac{\partial \rho}{\partial p} \right)_s dp + \left(\frac{\partial \rho}{\partial s} \right)_p ds \qquad 2.126$$

Recalling the definition of the speed of sound defined by equation 2.91 and recognising that $ds = 0$ (from equation 2.124), equation 2.126 yields:

$$d\rho = \left(\frac{1}{c^2} \right) dp \qquad 2.127$$

Substitution of equation 2.127 to the mass conservation equation 2.122 gives:

$$\frac{\partial p}{\partial t} + u \frac{\partial p}{\partial x} + \rho c^2 \frac{\partial u}{\partial x} = 0 \qquad 2.128$$

Equations 2.128, 2.123 and 2.124 represent a system of quasi-linear PDEs, as shown in vector form:

$$\frac{\partial}{\partial t} \boldsymbol{V} + \boldsymbol{G}(\boldsymbol{V}) \frac{\partial}{\partial x} \boldsymbol{V} = 0 \qquad 2.129$$

where $\boldsymbol{V}$ is the vector of primitive variables:

$$\boldsymbol{V} = \begin{pmatrix} p \\ u \\ s \end{pmatrix} \tag{2.130}$$

and $\boldsymbol{G}$ is the coefficient matrix:

$$\boldsymbol{G} = \begin{pmatrix} u & \rho c^2 & 0 \\ 1/\rho & u & 0 \\ 0 & 0 & u \end{pmatrix} \tag{2.131}$$

As already mentioned at the beginning of this section, the eigenvalues of the PDE system determines its mathematical nature. The eigenvalues are found by solving the relevant characteristic polynomial given by:

$$\left|\boldsymbol{G} - \lambda \boldsymbol{I}\right| = \boldsymbol{0} \tag{2.132}$$

which gives:

$$\lambda_1 = u + c \tag{2.133}$$

$$\lambda_2 = u - c \tag{2.134}$$

$$\lambda_3 = u \tag{2.135}$$

All three eigenvalues are real, and thus the PDEs in the HEM model are hyperbolic. By definition (Toro 2009b), they describe the propagation of a set of waves travelling at finite velocities (in this case, λ_1, λ_2 and λ_3). More discussion about the wave properties will be presented in the next section.

It should be noted that the above characteristic analysis is general to any set of primitive or conservative variables. This can be shown through similarity transformation (Stadtke 2006).

To change the primitive variable set, $\boldsymbol{V} = \left(p, u, s\right)^T$ in equation 2.130 to e.g. $\boldsymbol{V}' = \left(p, u, h\right)^T$, the similarity transformation of equation 2.129 reads:

$$\boldsymbol{J}\left(\frac{\partial \boldsymbol{V}}{\partial t}\right)+\boldsymbol{JG}\left(\frac{\partial \boldsymbol{V}}{\partial x}\right)=\boldsymbol{J}\left(\frac{\partial \boldsymbol{V}}{\partial t}\right)+\left(\boldsymbol{JGJ}^{-1}\right)\boldsymbol{J}\left(\frac{\partial \boldsymbol{V}}{\partial x}\right)=\left(\frac{\partial \boldsymbol{V'}}{\partial t}\right)+\boldsymbol{G'}\left(\frac{\partial \boldsymbol{V'}}{\partial x}\right)=\boldsymbol{0} \qquad 2.136$$

where the new coefficient matrix, $\boldsymbol{G}^{'}$ and the Jacobian matrix, $\boldsymbol{J}$ are respectively:

$$\boldsymbol{G}^{'}=\boldsymbol{JGJ}^{-1}=\begin{pmatrix} u & \rho c^2 & 0 \\ 1/\rho & u & 0 \\ 0 & c^2 & u \end{pmatrix} \qquad 2.137$$

$$\boldsymbol{J}=\frac{\partial \boldsymbol{V}}{\partial \boldsymbol{V}^{'}}=\begin{pmatrix} (\partial p/\partial p)_s & (\partial p/\partial u) & (\partial p/\partial s)_p \\ (\partial u/\partial p)_s & (\partial u/\partial u) & (\partial u/\partial s)_p \\ (\partial h/\partial p)_s & (\partial h/\partial u) & (\partial h/\partial s)_p \end{pmatrix}=\begin{pmatrix} 1 & 0 & 0 \\ 0 & 1 & 0 \\ 1/\rho & 0 & T \end{pmatrix} \qquad 2.138$$

$\boldsymbol{J}^{-1}$ denotes the inverse matrix of $\boldsymbol{J}$.

On a relevant note, similarity transformation can also be applied to convert the conservative form PDEs (e.g. equation 2.113) to primitive form (or vice versa) following:

$$\boldsymbol{J}\left(\frac{\partial \boldsymbol{U}}{\partial t}\right)+\boldsymbol{J}\left(\frac{\partial \boldsymbol{F}}{\partial x}\right)=\boldsymbol{J}\left(\frac{\partial \boldsymbol{U}}{\partial t}\right)+\left(\boldsymbol{JHJ}^{-1}\right)\boldsymbol{J}\left(\frac{\partial \boldsymbol{U}}{\partial x}\right)=\left(\frac{\partial \boldsymbol{V}}{\partial t}\right)+\boldsymbol{G}\left(\frac{\partial \boldsymbol{V}}{\partial x}\right)=\boldsymbol{0} \qquad 2.139$$

with:

$$\boldsymbol{J}=\frac{\partial \boldsymbol{V}}{\partial \boldsymbol{U}} \qquad 2.140$$

$$\boldsymbol{H}=\frac{\partial \boldsymbol{F}}{\partial \boldsymbol{U}} \qquad 2.141$$

2.1.6.1.2 Elementary Wave Solution of a General Initial Value Problem

Following the above discussion, the wave properties of the PDEs in the HEM model may be better demonstrated by examining the solution of a general Initial Value Problem (IVP) defined as:

$$\begin{cases} \dfrac{\partial}{\partial \mathrm{t}}\boldsymbol{U}+\dfrac{\partial}{\partial x}\boldsymbol{F}\left(\boldsymbol{U}\right)=0, \quad -\infty<x<\infty \\ \boldsymbol{U}\left(x,0\right)=\boldsymbol{U}_0\left(x\right) \end{cases} \tag{2.142}$$

or in primitive form:

$$\begin{cases} \dfrac{\partial}{\partial \mathrm{t}}\boldsymbol{V}+\boldsymbol{G}\left(\boldsymbol{V}\right)\dfrac{\partial}{\partial x}\boldsymbol{V}=0, \quad -\infty<x<\infty \\ \boldsymbol{V}\left(x,0\right)=\boldsymbol{V}_0\left(x\right) \end{cases} \tag{2.143}$$

Since equation 2.129 is hyperbolic, it can be diagonalised again via similarity transformation, given by (Stadtke 2006):

$$\boldsymbol{T}^{-1}\left(\frac{\partial \boldsymbol{V}}{\partial t}\right)+\left(\boldsymbol{T}^{-1}\boldsymbol{G}\boldsymbol{T}\right)\boldsymbol{T}^{-1}\left(\frac{\partial \boldsymbol{V}}{\partial x}\right)=\boldsymbol{T}^{-1}\left(\frac{\partial \boldsymbol{V}}{\partial t}\right)+\boldsymbol{\Lambda}\boldsymbol{T}^{-1}\left(\frac{\partial \boldsymbol{V}}{\partial x}\right)=\boldsymbol{0} \tag{2.144}$$

where $\boldsymbol{\Lambda}$ is the diagonal matrix of the eigenvalues of $\boldsymbol{G}$ given by:

$$\boldsymbol{\Lambda}=\boldsymbol{T}^{-1}\boldsymbol{G}\boldsymbol{T}=\begin{pmatrix} \lambda_1 & 0 & 0 \\ 0 & \lambda_2 & 0 \\ 0 & 0 & \lambda_3 \end{pmatrix} \tag{2.145}$$

and $\boldsymbol{T}$ and $\boldsymbol{T}^{-1}$ are the transformation matrix and its inverse matrix respectively given by:

$$\boldsymbol{T}=\begin{pmatrix} 1/2 & 1/2 & 0 \\ 1/(2c\rho) & -1/(2c\rho) & 0 \\ 0 & 0 & 1 \end{pmatrix} \tag{2.146}$$

$$\boldsymbol{T}^{-1}=\begin{pmatrix} 1 & c\rho & 0 \\ 1 & -c\rho & 0 \\ 0 & 0 & 1 \end{pmatrix} \tag{2.147}$$

where the column vectors of $\boldsymbol{T}$ and the row vectors of $\boldsymbol{T}^{-1}$ are respectively the right and left eigenvectors of $\boldsymbol{G}$:

$$\boldsymbol{r}_1 = \begin{pmatrix} 1/2 \\ 1/(2c\rho) \\ 0 \end{pmatrix}, \boldsymbol{r}_2 = \begin{pmatrix} 1/2 \\ -1/(2c\rho) \\ 0 \end{pmatrix}, \boldsymbol{r}_3 = \begin{pmatrix} 0 \\ 0 \\ 1 \end{pmatrix} \quad 2.148$$

$$\boldsymbol{l}_1 = \begin{pmatrix} 1 & c\rho & 0 \end{pmatrix}, \boldsymbol{l}_2 = \begin{pmatrix} 1 & -c\rho & 0 \end{pmatrix}, \boldsymbol{l}_3 = \begin{pmatrix} 0 & 0 & 1 \end{pmatrix} \quad 2.149$$

Note that:

$$\boldsymbol{r}_m \cdot \boldsymbol{l}_m^T = 1 \quad 2.150$$

and:

$$\boldsymbol{r}_m \cdot \boldsymbol{l}_{n,n\neq m}^T = 0 \quad 2.151$$

The m^{th} component of equation 2.144 is thus:

$$\boldsymbol{l}_m \cdot \left(\frac{\partial \boldsymbol{V}}{\partial t} + \lambda_m \frac{\partial \boldsymbol{V}}{\partial x} \right) = 0 \quad 2.152$$

Equation 2.152 is often called the characteristic (or wave) form of equation 2.129. It is clear that the expression inside the parentheses represents the total derivative of $\boldsymbol{V}$ with respect to t, defined as:

$$\frac{d\boldsymbol{V}}{dt} = \frac{\partial \boldsymbol{V}}{\partial t} + \frac{dx}{dt}\frac{\partial \boldsymbol{V}}{\partial x} \quad 2.153$$

with:

$$\frac{dx}{dt} = \lambda_m \quad 2.154$$

Substituting equation 2.153 into equation 2.152, it is readily shown that the original PDEs are converted to m number of Ordinary Differential Equations (ODEs) given by:

$$\boldsymbol{l}_m \cdot d\boldsymbol{V} = 0 \quad 2.155$$

along the paths defined by equation 2.154. These paths are referred to as characteristic curves, wave curves, or simply, waves. In the case of the HEM model ($m=3$), these are the right-running pressure wave propagating at λ_1, the left-running pressure wave propagating at λ_2 and the entropy wave propagating at λ_3. A schematic representation of the three waves is presented in figure 2.6.

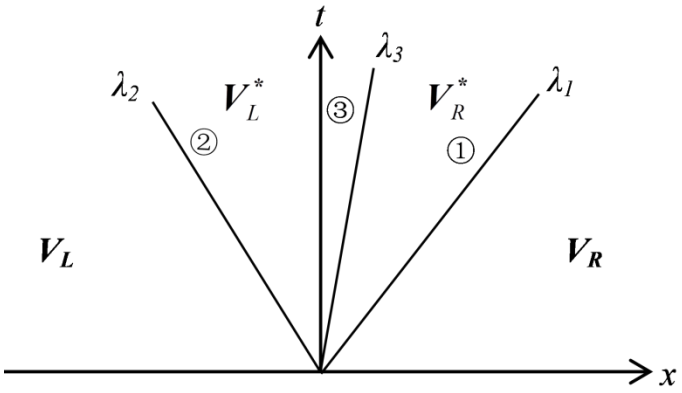

Figure 2.6: Schematic representation of the wave structure of a general IVP solution. The numbers, 1, 2 and 3 respectively denote the right-/left-running pressure waves and the entropy wave. $\boldsymbol{V}_L$ and $\boldsymbol{V}_R$ are the initial data specific to an IVP, whereas $\boldsymbol{V}_L^*$ and $\boldsymbol{V}_R^*$ are the primitive variables in the regions affected by the waves.

Introducing the definition of the linearity factor, ω_m (Fossati & Quartapelle 2014):

$$\omega_m = \boldsymbol{r}_m(\boldsymbol{V}) \cdot \nabla \lambda_m(\boldsymbol{V}) \qquad 2.156$$

The wave is said to be linearly degenerate if $\omega_m = 0$ and genuinely nonlinear otherwise. The corresponding values for waves 1 to 3 in figure 2.6 are given by:

$$\omega_1 = \frac{(\partial c/\partial p)_s}{2} + \frac{c\rho}{2} \qquad 2.157$$

$$\omega_2 = \frac{(\partial c/\partial p)_s}{2} - \frac{c\rho}{2} \qquad 2.158$$

$$\omega_3 = 0 \qquad 2.159$$

It can be readily seen that the pressure waves are genuinely nonlinear, and the entropy wave is linearly degenerate (Toro 2009d). Nonlinear waves can form rarefactions and shocks, whereas linear waves act as contact discontinuities (material interfaces) (Toro 2009b).

2.1.6.1.3 Elementary Wave Solution of the Riemann Problem

In this section, the significance of the wave properties of a hyperbolic PDE system (using the HEM model as an example) in obtaining the solution of a special type of IVPs is discussed. This special IVP, known as the Riemann problem, is defined as:

$$\begin{cases} \dfrac{\partial}{\partial t}\boldsymbol{U}+\dfrac{\partial}{\partial x}\boldsymbol{F}\left(\boldsymbol{U}\right)=\boldsymbol{0}, \quad -\infty<x<\infty \\ \boldsymbol{U}\left(x,0\right)=\boldsymbol{U}_0\left(x\right)=\begin{cases}\boldsymbol{U}_{\mathrm{L}}, x\le 0\\ \boldsymbol{U}_{\mathrm{R}}, x>0\end{cases}\end{cases} \tag{2.160}$$

or:

$$\begin{cases} \dfrac{\partial}{\partial t}\boldsymbol{V}+\boldsymbol{G}\left(\boldsymbol{V}\right)\dfrac{\partial}{\partial x}\boldsymbol{V}=\boldsymbol{0}, \quad -\infty<x<\infty \\ \boldsymbol{V}\left(x,0\right)=\boldsymbol{V}_0\left(x\right)=\begin{cases}\boldsymbol{V}_{\mathrm{L}}, x\le 0\\ \boldsymbol{V}_{\mathrm{R}}, x>0\end{cases}\end{cases} \tag{2.161}$$

From the above definition, there is an initial discontinuity in $\boldsymbol{V}$ at $x = 0$ (note that the location of the discontinuity is entirely arbitrary). Referring to figure 2.6, naturally, the solution to the left of wave 2 is simply the initial data, $\boldsymbol{V}_L$ and to the right of wave 1 is $\boldsymbol{V}_R$. The remaining task is to find $\boldsymbol{V}$ in the region bounded by each wave. These regions are often called the 'star regions', and the corresponding $\boldsymbol{V}$ is denoted by $\boldsymbol{V}_L^*$ or $\boldsymbol{V}_R^*$, separated by wave 3 in figure 2.6.

Riemann invariants: In seeking the solution of $\boldsymbol{V}_{L,R}^*$, the shock-free case is first discussed. Introduce a new scalar function across the m^{th} wave ($m = 1,2, \ldots, M$):

$$I^{\lambda_m} = I^{\lambda_m}(\boldsymbol{V}) \tag{2.162}$$

such that:

$$\nabla I^{\lambda_m} \cdot d\boldsymbol{V} = 0 \tag{2.163}$$

Comparing equations 2.163 and 2.155, it is immediately recognised that ∇I^{λ_m} and the left eigenvector of the PDE system, $\boldsymbol{l}_m$ are parallel. As a result, with equation 2.151, there is:

$$\nabla I^{\lambda_m} \cdot \boldsymbol{r}_{n,n\neq m} = 0 \tag{2.164}$$

Equation 2.164 implies that, given an $M \times M$ system, $M-1$ scalar functions (which relate $\boldsymbol{V}_L$ and $\boldsymbol{V}_L^*$, $\boldsymbol{V}_L^*$ and $\boldsymbol{V}_R^*$, $\boldsymbol{V}_R^*$ and $\boldsymbol{V}_R$ in figure 2.6) can be identified across the m^{th} wave. For example, in the case of the HEM model (M = 3), there exist 2 scalar functions across each of the three waves. These functions are referred to as the Riemann invariants.

Following the above, the subscript, w is added to the notation of the scalar functions (i.e. $I_w^{\lambda_m}$); w represents the w^{th} scalar function across each wave.

According to Toro (2009b), solving equation 2.164 is equivalent to solving $M-1$ ODEs given by:

$$\frac{dV_1}{r_m^{(1)}} = \frac{dV_2}{r_m^{(2)}} = \frac{dV_3}{r_m^{(3)}} = \ldots = \frac{dV_M}{r_m^{(M)}} \tag{2.165}$$

across the m^{th} wave, where the superscript in the parentheses denotes each element in $\boldsymbol{r}_m$. In the case of the HEM model, the corresponding Riemann Invariants are:

$$\frac{dp}{1/2} = \frac{du}{(1/2)\rho c} \rightarrow I_1^{\lambda_1} = p + \int \rho c\, du \tag{2.166}$$

$$\frac{ds}{0} = \frac{du}{(1/2)\rho c} \rightarrow I_2^{\lambda_1} = s \tag{2.167}$$

across the right-running pressure wave (wave 1 in figure 2.6);

$$\frac{dp}{1/2} = \frac{du}{(-1/2)\rho c} \rightarrow I_1^{\lambda_2} = p - \int \rho c du \qquad 2.168$$

$$\frac{ds}{0} = \frac{du}{(-1/2)\rho c} \rightarrow I_2^{\lambda_2} = s \qquad 2.169$$

across the left-running pressure wave (wave 2 in figure 2.6);

$$\frac{dp}{0} = \frac{ds}{1} \rightarrow I_1^{\lambda_3} = p \qquad 2.170$$

$$\frac{du}{0} = \frac{ds}{1} \rightarrow I_2^{\lambda_3} = u \qquad 2.171$$

across the entropy (contact) wave (wave 3 in figure 2.6). By observing the above Riemann Invariants, it is summarised that pressure and velocity changes continuously across a shock-free pressure wave and are otherwise conserved across a contact wave. Entropy (and other related thermodynamic variables, e.g. ρ and T) changes discontinuously across a contact wave.

Rankine-Hugoniot conditions: In the case of shock formation as a result of nonlinear wave steepening, there is a discontinuity in $\boldsymbol{V}$ across the emerging shock wave (Toro 2009b). Taking the right-running pressure wave (wave 1 in figure 2.6) as an example, the corresponding Riemann invariants (equations 2.166 and 2.167) are no longer valid, and instead, $\boldsymbol{V}_R^*$ and $\boldsymbol{V}_R$ across the shock wave can be related through jump conditions. This is known as the Rankine-Hugoniot conditions given by (Toro 2009d):

$$\Delta \boldsymbol{F} = c_{shock} \Delta \boldsymbol{U} \qquad 2.172$$

or with reference to figure 2.6:

$$\boldsymbol{F}(\boldsymbol{U}_R) - \boldsymbol{F}(\boldsymbol{U}_R^*) = c_{shock}(\boldsymbol{U}_R - \boldsymbol{U}_R^*) \qquad 2.173$$

where c_{shock} is the shock wave speed. Note the Rankine-Hugoniot conditions are prescribed based on the conserved form of the PDEs which is interchangeable with the primitive form via similarity transformation (equation 2.139).

To this point, $\boldsymbol{V}_L^*$ and $\boldsymbol{V}_R^*$ in the star region (in figure 2.6) are fully defined (as demonstrated in Section A2, Appendix).

2.1.6.2 PDEs in the TFM Model

2.1.6.2.1 Hyperbolicity

Much the same as in the case of the HEM model, a characteristic analysis can be performed for the PDEs in the TFM model. According to Dinh et al. (2003), the PDEs in the six-equation TFM model (equations 2.37 to 2.42) do not have a complete set of real eigenvalues. As a result, the PDE system is not hyperbolic and does not represent a 'well-posed' initial-boundary value problem, which in turn leads to severe numerical instability and unphysical oscillations (known as 'spurious oscillations').

To address the above, mathematical regularisation can be applied to stabilise the numerical solution towards the six-equation TFM model. One of such approaches is 'hyperbolisation'. In its literal sense, modifications to equations 2.37 to 2.42 are introduced to recover the hyperbolicity, and three examples are given in the following.

Addition of the virtual mass force terms: The virtual mass force terms, first introduced by Drew & Lahey Jr (1987), can be added to the RHS of the phasic momentum conservation equations 2.39 and 2.40. Its general form is given by:

$$F_{vm,v} = -F_{vm,l} = C_{vm}\alpha_v\alpha_l\rho\left(\frac{du_v}{dt} - \frac{du_l}{dt}\right) \qquad 2.174$$

where C_{vm} is the virtual mass coefficient, and with appropriate choices of C_{vm}, the hyperbolicity of the TFM model can be recovered. However, it is noted that the new PDE system does not have analytical expressions of the eigenvalues and eigenvectors.

Addition of the pressure correction terms: The pressure correction terms (more commonly known as the interface pressure terms) can be added to the RHS of both

the phasic momentum and energy conservation equations 2.39 to 2.42. The added terms are denoted by $F_{p^{int}}$ and $W_{p^{int}}$, respectively:

$$F_{p^{\text{int}},v} = -F_{p^{\text{int}},l} = \left(p - \Delta p^{\text{int}}\right)\frac{\partial \alpha_v}{\partial x} \qquad 2.175$$

$$W_{p^{\text{int}},v} = -W_{p^{\text{int}},l} = -\Delta p^{\text{int}}\frac{\partial \alpha_v}{\partial x}u^{\text{int}} \qquad 2.176$$

where Δp^{int} and u^{int} are respectively the interface pressure jump and velocity defined as:

$$\Delta p^{\text{int}} = \delta\frac{\alpha_v\rho_v\alpha_l\rho_l}{\alpha_v\rho_v + \alpha_l\rho_l}\left(u_v - u_l\right)^2 \qquad 2.177$$

$$u^{\text{int}} = \frac{\alpha_v\rho_v u_v + \alpha_l\rho_l u_l}{\alpha_v\rho_v + \alpha_l\rho_l} \qquad 2.178$$

By setting the model constant, $\delta \geq 1$, the hyperbolicity of the TFM model is recovered. The most commonly adopted value is 1.2 according to these authors (Paillère et al. 2003; Munkejord 2010; Yeom & Chang 2013; S. Brown et al. 2014). Note that the added pressure correction terms in the phasic momentum conservation is small in comparison to the pressure force (but sufficient to recover the hyperbolicity of the PDE system in the TFM model) (Dinh et al. 2003).

The TFM model with interface pressure terms still does not have analytical expressions for the eigenvalues and eigenvectors.

Addition of the pressure relaxation equation (the seven-equation TFM model): The last hyperbolisation approach discussed in this section is the inclusion of pressure relaxation, and the constituent fluid phases are no longer assumed to be at the same pressure. The mathematical formulation of the pressure relaxation equation is shown below:

$$\frac{\partial \alpha_v}{\partial t} + u^{int}\frac{\partial \alpha_v}{\partial x} = K_p\left(p_v - p_l\right) \qquad 2.179$$

where K_p is the pressure relaxation parameter. Its modelling is often empirical. For example, Hérard & Hurisse (2012) used the following expression for K_p

$$K_p = \frac{1}{\tau_p}\frac{\alpha_1\alpha_2}{p_v + p_l} \tag{2.180}$$

where τ_p is the pressure relaxation time.

The resulting seven-equation system is given by:

$$\frac{\partial \alpha_v}{\partial t} + u_i \frac{\partial \alpha_v}{\partial x} = K_p\left(p_v - p_l\right) \tag{2.181}$$

$$\frac{\partial \alpha_v \rho_v}{\partial t} + \frac{\partial \alpha_v \rho_v u_v}{\partial x} = S_{M,v} \tag{2.182}$$

$$\frac{\partial \alpha_l \rho_l}{\partial t} + \frac{\partial \alpha_l \rho_l u_l}{\partial x} = S_{M,l} \tag{2.183}$$

$$\frac{\partial \alpha_v \rho_v u_v}{\partial t} + \frac{\partial\left(\alpha_v \rho_v u_v^2 + \alpha_v p_v\right)}{\partial x} = S_{F,v} \tag{2.184}$$

$$\frac{\partial \alpha_l \rho_l u_l}{\partial t} + \frac{\partial\left(\alpha_l \rho_l u_l^2 + \alpha_l p_l\right)}{\partial x} = S_{F,l} \tag{2.185}$$

$$\frac{\partial \alpha_v \rho_v E_v}{\partial t} + \frac{\partial\left(\alpha_v \rho_v u_v E_v + \alpha_v p_v\right)u_v}{\partial x} + p_v \frac{\partial \alpha_v}{\partial t} = S_{E,v} \tag{2.186}$$

$$\frac{\partial \alpha_l \rho_l E_l}{\partial t} + \frac{\partial\left(\alpha_l \rho_l u_l E_l + \alpha_l p_l\right)u_l}{\partial x} + p_l \frac{\partial \alpha_l}{\partial t} = S_{E,l} \tag{2.187}$$

Following Baer & Nunziato (1986) and Embid & Baer (1992), the resulting seven-equation PDE system has a set of seven real eigenvalues of which the analytical expressions are given by:

$$\lambda_1 = u_l + c_l \tag{2.188}$$

$$\lambda_2 = u_v + c_v \tag{2.189}$$

$$\lambda_3 = u_l - c_l \tag{2.190}$$

$$\lambda_4 = u_v - c_v \tag{2.191}$$

$$\lambda_5 = u_l \tag{2.192}$$

$$\lambda_6 = u_l \tag{2.193}$$

$$\lambda_7 = u_v \tag{2.194}$$

The recovered hyperbolicity by introducing the additional pressure relaxation equation is hence apparent.

2.1.6.2.2 Elementary Wave Solution of a General IVP

Following the same procedure adopted in the case of the HEM model, equations 2.181 to 2.187 can also be written in wave form (see equation 2.152) (Embid & Baer 1992).

Analogous to the elementary wave solution in the case of the HEM model, there exist a total number of 7 waves: 4 pressure waves propagating at λ_1, λ_2, λ_3 and λ_4; 2 entropy waves propagating at λ_5 and λ_7; a void wave travelling at λ_6 (corresponding to the inclusion of the pressure relaxation equation 2.181).

Figure 2.7 depicts the corresponding wave structure of the IVP solution.

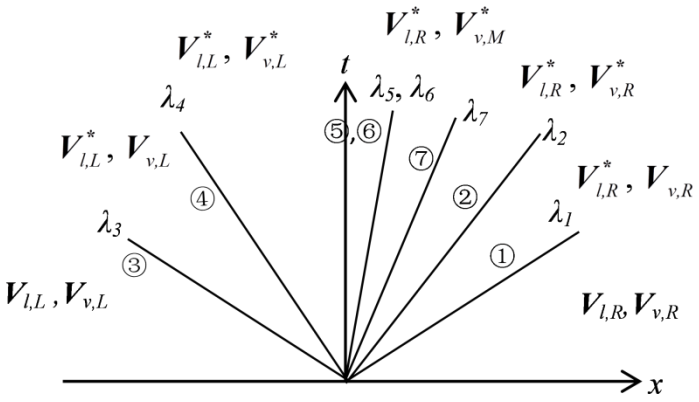

Figure 2.7: Schematic representation of the wave structure of a general IVP solution. Wave 1: the right-running pressure wave in the liquid phase; wave 2: the right-running pressure wave in the vapour phase; wave 3: the left-running pressure wave in the liquid phase; wave 4: the left-running pressure wave in the vapour phase; wave 5: the entropy wave in the liquid phase; wave 6: the void wave; wave 7: the entropy wave in the vapour phase.

Note that waves 1 to 4 (the pressure waves) are genuinely nonlinear, which gives rise to rarefaction waves or shocks, whereas waves 5 to 7 (the entropy waves and void wave) are linearly degenerate, which corresponds to contact discontinuities (Embid & Baer 1992).

2.1.6.2.3 Elementary Wave Solution of the Riemann Problem

For the seven-equation TFM model, the Riemann problem defined by equation 2.160 (2.161) can also be approached via the application of the Riemann invariants and the Rankine-Hugoniot conditions introduced earlier.

Riemann invariants: The Riemann Invariants corresponding to the seven-equation TFM model are summarised in the following (Embid & Baer 1992):

$$I_1^{\lambda_1 or \lambda_3} = p_l \pm \int \rho_l c_l du_l \qquad 2.195$$

$$I_2^{\lambda_1 or \lambda_3} = s_l \qquad 2.196$$

$$I_3^{\lambda_1 or \lambda_3} = \alpha_l \quad 2.197$$

$$I_4^{\lambda_1 or \lambda_3} = u_v \quad 2.198$$

$$I_5^{\lambda_1 or \lambda_3} = p_v \quad 2.199$$

$$I_6^{\lambda_1 or \lambda_3} = s_v \quad 2.200$$

across the pressure waves 1 or 3 in figure 2.7;

$$I_1^{\lambda_2 or \lambda_4} = p_v \pm \int \rho_v c_v du_v \quad 2.201$$

$$I_2^{\lambda_2 or \lambda_4} = s_v \quad 2.202$$

$$I_3^{\lambda_2 or \lambda_4} = \alpha_v \quad 2.203$$

$$I_4^{\lambda_2 or \lambda_4} = u_l \quad 2.204$$

$$I_5^{\lambda_2 or \lambda_4} = p_l \quad 2.205$$

$$I_6^{\lambda_2 or \lambda_4} = s_l \quad 2.206$$

across the pressure waves 2 or 4 in figure 2.7;

$$I_1^{\lambda_7} = p_v \quad 2.207$$

$$I_2^{\lambda_7} = u_v \quad 2.208$$

$$I_3^{\lambda_7} = \alpha_v \quad 2.209$$

$$I_4^{\lambda_7} = u_l \quad 2.210$$

$$I_5^{\lambda_7} = p_l \quad 2.211$$

$$I_6^{\lambda_7} = s_l \quad 2.212$$

across the entropy wave 7 in figure 2.7;

$$I_1^{\lambda_5} = I_1^{\lambda_6} = u_l \tag{2.213}$$

$$I_2^{\lambda_5} = I_2^{\lambda_6} = s_v \tag{2.214}$$

$$I_3^{\lambda_5} = I_3^{\lambda_6} = \alpha_v \rho_v \left(u_l - u_v\right) \tag{2.215}$$

$$I_4^{\lambda_5} = I_4^{\lambda_6} = \alpha_v p_v + \alpha_l p_l + \alpha_l \rho_v \left(u_l - u_v\right)^2 \tag{2.216}$$

$$I_5^{\lambda_5} = I_5^{\lambda_6} = \left(E_v - u_v^2/2 + p_v/\rho_v\right) + \left(u_l - u_v\right)^2/2 \tag{2.217}$$

across the entropy wave 5 and the void wave 6 in figure 2.7. It is worth mentioning that $I_3^{\lambda_5}$ to $I_5^{\lambda_5}$ also indicate a jump in the phasic volume fraction.

Rankine-Hugonoit conditions: For shock waves, the Rankine-Hugoniot conditions (equation 2.172) remain valid in each fluid phase (Embid & Baer 1992). In the case where waves 1 and 2 (figure 2.7) are both shock waves, they are:

$$\boldsymbol{F}\left(\boldsymbol{U}_{l,R}\right) - \boldsymbol{F}\left(\boldsymbol{U}_{l,R}^*\right) = c_{l,shock}\left(\boldsymbol{U}_{l,R} - \boldsymbol{U}_{l,R}^*\right) \tag{2.218}$$

across wave 1;

$$\boldsymbol{F}\left(\boldsymbol{U}_{v,R}\right) - \boldsymbol{F}\left(\boldsymbol{U}_{v,R}^*\right) = c_{v,shock}\left(\boldsymbol{U}_{v,R} - \boldsymbol{U}_{v,R}^*\right) \tag{2.219}$$

across wave 2.

2.2 Applications of the Reviewed Flow Models in Pipeline Decompression Modelling

In the preceeding section, the main features of the most popular fluid dynamic models for pipeline decompression modelling are presented together with the closure models for other relevant physical processes including interphase mass, momentum and energy exchange, fluid/wall heat transfer and friction. This is followed by the discussion regarding the accuracy of PR (Peng & Robinson 1976) and GERG 2008 (Kunz & Wagner 2012) EoS in predicting fluid thermal properties and phase equilibrium data. The mathematical nature of the governing conservation equations is also discussed given its significance in seeking an appropriate solution scheme.

In the following, examples for the applications of the introduced flow models as reported in the open literature are presented with a particular focus on their performance in predicting medium- to large-scale pipeline decompression tests.

The selected relevant studies are grouped into different sections with reference to the employed flow models (including the HEM, HRM, DFM and TFM models). Each section is comprised of a short description of the model development, an assessment of the model performance (based on comparisons against relevant experimental data) and a summary of their limitations meriting further research.

2.2.1 Applications of the HEM Model

2.2.1.1 Mahgerefteh et al. (1999)

The pipeline decompression model developed by Mahgerefteh et al. (1999) is one of the most validated among its kind reported in the open literature. The model was originally developed for the quantitative failure consequence assessment in the event of high-pressure hydrocarbon and CO_2 pipeline Full Bore Rupture (FBR) failures (Mahgerefteh et al. 1999; Mahgerefteh et al. 2007; Mahgerefteh et al. 2008) and later extended to puncture failures (Oke et al. 2003). Other important features were reported in their subsequent studies, including the simulations of emergency dynamic valve responses (Mahgerefteh et al. 2000), ductile fracture propagation of the pipe

wall (Mahgerefteh et al. 2011; Mahgerefteh et al. 2012) and decompression of pipeline networks (Mahgerefteh et al. 2006).

Following their methodology, the HEM model (equations 2.18 to 2.20) is used to describe the fluid flow dynamics. Fluid/wall heat transfer and friction are modelled using standard correlations (following Steiner & Taborek (1992) and Techo et al. (1965), respectively). Real fluid behaviour is also accounted for using PR EoS (Peng & Robinson 1976).

In solving the resulting PDE system, the conservation equations in the HEM model are firstly converted into wave form (equation 2.152). A set of three ODEs are identified along the relevant waves (Section 2.1.6.1.2), given by:

$$dp + \rho c du = \left(cS_F - c^2 \left(\frac{\partial \rho}{\partial s} \right)_p \frac{S_E}{T} \right) dt \qquad 2.220$$

$$dp - \rho c du = \left(-cS_F - c^2 \left(\frac{\partial \rho}{\partial s} \right)_p \frac{S_E}{T} \right) dt \qquad 2.221$$

$$ds = \frac{S_E}{T} dt \qquad 2.222$$

where the wall/fluid friction and volumetric heat source terms, S_F and S_E are given by (see also Section 2.1.3):

$$S_F = \frac{2 f \rho |u| u}{D_{w,in}} \qquad 2.223$$

$$S_E = \frac{4 \dot{q}_w}{D_{w,in}} = \frac{4U \left(T_w - T \right)}{D_{w,in}} \qquad 2.224$$

The Method of Characteristics (MoC) (Zucrow & Hoffman 1976) is then applied to obtain numerical solutions of equations 2.220 to 2.222.

The flow model has been validated against multiple large-scale high-pressure pipeline decompression experiments for both hydrocarbons and CO_2. A selection of these tests

is reviewed in the following including the set-ups, relevant measurements taken and model validation results.

Isle of Grain LPG pipeline depressurisation test P40 (Richardson & Saville 1996): The Isle of Grain test P40 consisted of a 100 m length, 154 mm i.d. carbon steel pipeline filled with commercial LPG (95 mol% propane, 5 mol% n-butane) at 21.6 bar and 20 °C. The ambient temperature was also 20 °C. FBR was initiated at one end of the test pipe, and the pressure and temperature were monitored by multiple pressure transducers and thermocouples placed along the length of the pipe during decompression. In addition, the inventory mass during decompression was measured using load cells. More details about the test can be found in (Richardson & Saville 1996).

Figures 2.8 to 2.9 present the simulated and measured pressure and temperature variations as a function of time at both the pipe open and intact ends during decompression. This is followed by a comparison between the predicted and measured inventory mass, as plotted in figure 2.10.

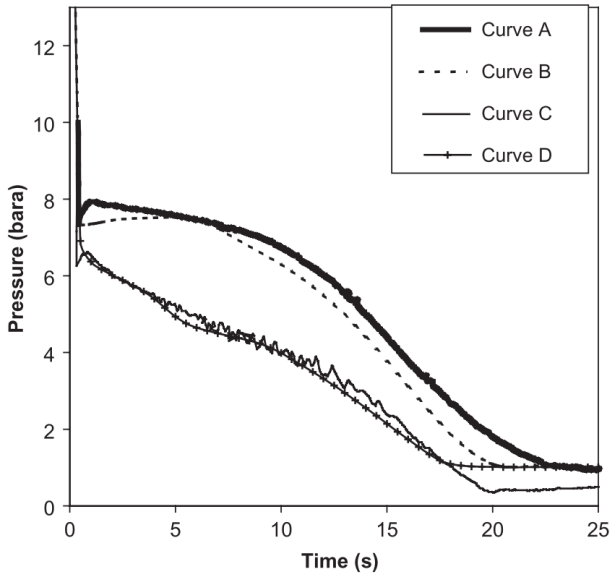

Figure 2.8: Pressure variations with time at the pipe closed and open ends for test P40. Curve A: measured data (closed end); Curve B: model prediction (closed end); Curve C: measured data (open end); Curve D: model prediction (open end) (Oke et al. 2003).

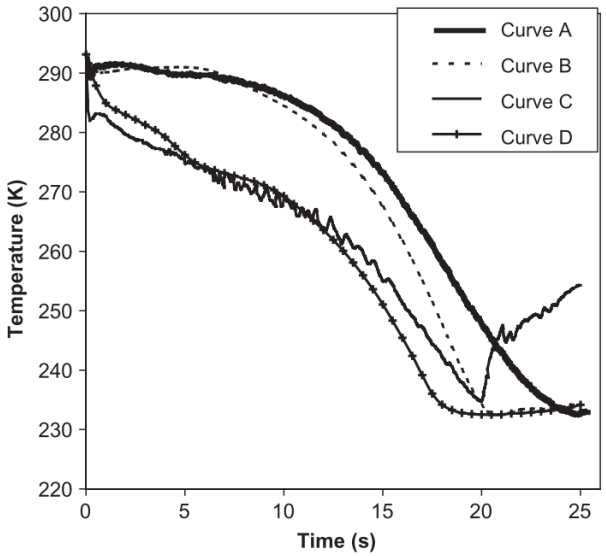

Figure 2.9: Temperature variations with time at the pipe closed and open ends for test P40. Curve A: measured data (closed end); Curve B: model prediction (closed end); Curve C: measured data (open end); Curve D: model prediction (open end) (Oke et al. 2003).

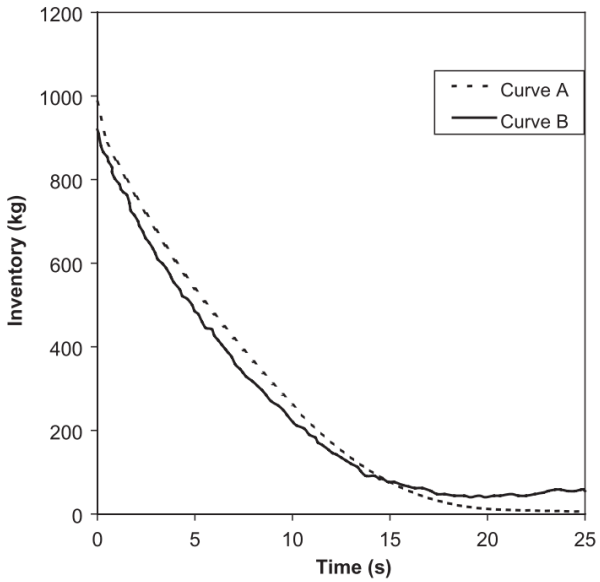

Figure 2.10: Remainig inventory mass with time during decompression for test P40. Curve A: measured data; Curve B: model prediction (Oke et al. 2003).

Referring to the pressure-time profiles in figure 2.8, the measurements show an initial rapid drop in pressure to ca. 6.5 and 7 bar respectively at the open and intact ends of the pipe, followed by a much slower rate of depressurisation. This trend corresponds to the phase transition at the vapour-liquid phase boundary of LPG, where the speed of sound reduces dramatically (Stadtke 2006). A similar observation can be made in the corresponding temperature-time profiles (figure 2.9). It is interesting to note that at the open end, dry-out (complete evaporation of the in-pipe liquid) is experimentally observed, marked by a recovery in temperature at 20 s. With regards to the measured inventory mass as a function of time during decompression (figure 2.10), as expected, the amount decreases monotonically.

In terms of model performance, for all quantities monitored during the test, there is a relatively good agreement between the measured data and model predictions. However, the experimentally observed dry-out is not predicted.

National Grid COOLTRANS CO_2 pipeline decompression tests 6 and 7 (Cosham et al. 2012): As part of the COOTRANS project undertaken by National Grid U.K., a number of shock tube tests (pipeline FBR decompression tests) were carried out for CO_2 and CO_2-rich mixtures in order to understand the decompression wave behaviour in single- and two-phase flows. Among these, tests 6 and 7 consisted of a 144 m length, 150 mm i.d., 11 mm pipe wall thickness heavily insulated ASTM A333 Grade 6 low carbon steel seamless pipe filled with gaseous mixtures of CO_2, N_2 and SO_2. The pertinent test conditions are summarised in table 2.2.

Table 2.2: Relevant initial conditions for test 6 and 7.

Test	Feed compositions	Feed temperature (°C)	Feed pressure (bar)	Ambient temperature (°C)
6	95.97 mol% CO_2 + 4.03 mol% N_2	5.3	37.9	20.4
7	99.14 mol% CO_2 + 0.86 mol% SO_2	9.9	38.0	13.9

The test pipe was instrumented with multiple pressure and temperature transducers along its entire length to monitor transient pressure and temperature variations. In addition, by comparing the recoded pressure-time profiles from adjacent pressure transducers (with known distance apart), decompression wave speed was also reported in the form of a fan diagram (pressure versus decompression wave speed plot).

In validating the flow model, the predicted decompression wave speed was compared to the corresponding measurement. The results are presented in figures 2.11 and 2.12.

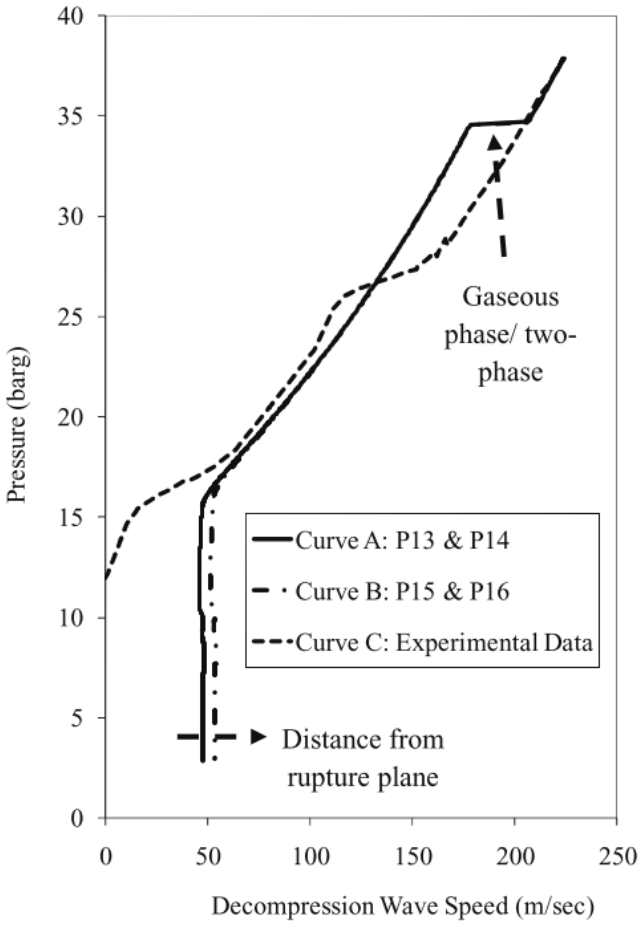

Figure 2.11: fan diagram at pressure transducers P13 to P16 following FBR for test 6. Curves A and B: model predictions; Curve C: measured data (Mahgerefteh et al. 2012).

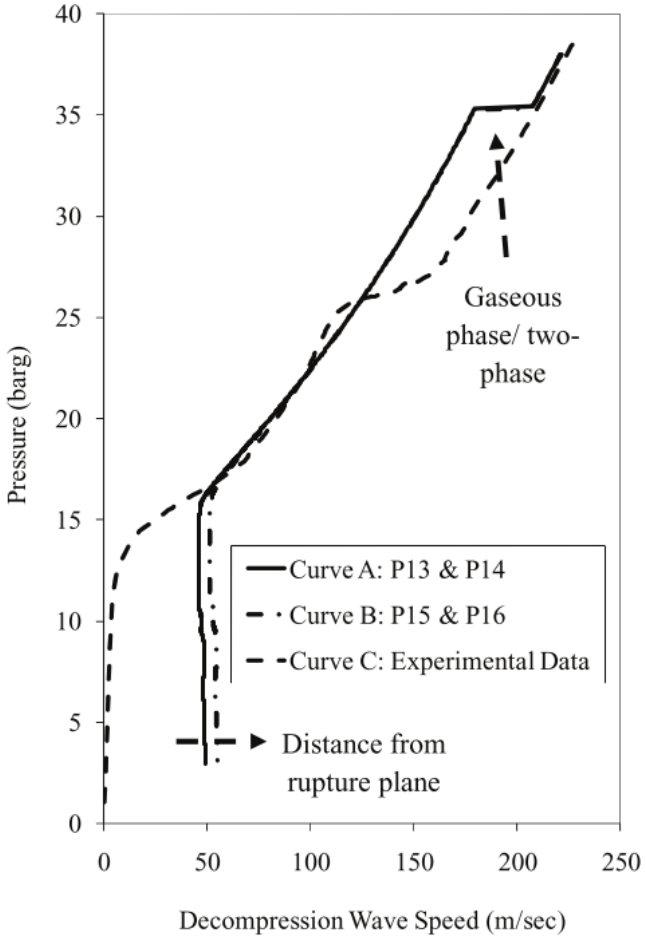

Figure 2.12: fan diagram at pressure transducers P13 to P16 following FBR for test 7. Curves A and B: model predictions; Curve C: measured data (Mahgerefteh et al. 2012).

Focussing on the measured data in both above figures, a pressure plateau can be observed (each at 34 bar for test 6 in figure 2.11 and at 36 bar for test 7 in figure 2.12). Such a pressure plateau corresponds to condensation of vapour, where the speed of sound and hence the decompression wave speed significantly decrease (by ca. 50 m/s in both cases). The wave speed eventually reaches zero when the local flow (between transducer P13 to P16) becomes sonic (choked).

With regards to the model predictions in both cases, despite demonstrating a general agreement with the data, over-predictions can be observed for the pressure plateaux at the vapour-liquid phase transition boundaries and the decompression wave speeds at the later stages of the decompression process. According to the authors, the former is

due to thermodynamic non-equilibrium between the vapour and liquid phases, which is not accounted for in their model. With regards to the over-prediction for the decompression wave speed, this is attributed to the friction correlation adopted (Mahgerefteh et al. 2012).

2.2.1.2 Teng et al. (2016)

Teng et al. (2016) studied the decompression of a CO_2 pipeline using both experimental and mathematical techniques. The experimental set-up consisted of a 70 m length, 25 mm i.d. stainless steel (type 304) pipe. The pipeline was enveloped with an electric heating jackets to enable various starting CO_2 fluid conditions. FBR was initiated at one end of the test pipe, and the variations of pressure and temperature as a function of time were monitored using pressure and temperature sensors. Three different starting flow conditions each at 35 bar, 15 °C (vapour), 55 bar, 5 °C (liquid) and 75 bar, 40 °C (supercritical) were tested.

The measured pressure variations as a function of time at both open and close ends of the test pipe for all three tests with varying starting flow conditions are presented in figure 2.13. Also included are the model predictions for comparison. The mathematical model was also based on the HEM assumption. PR EoS (Peng & Robinson 1976) was adopted for predicting the fluid thermal properties and equilibrium data, and the overall system was solved applying the MoC (Zucrow & Hoffman 1976), same as that employed by Mahgerefteh et al. (1999).

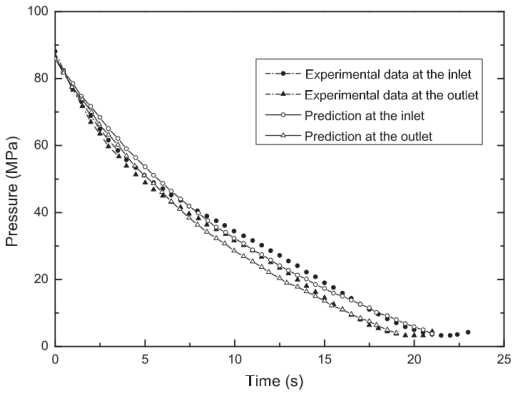

(a)

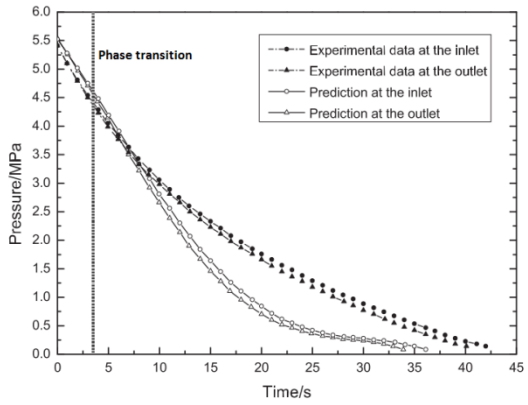

(b)

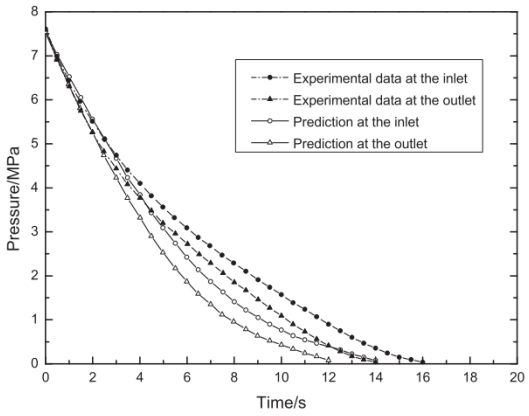

(c)

Figure 2.13: Predicted and measured pressure variations as a function of time at both the closed and open ends of the test pipe for all three decompression tests with the different starting flow conditions at 35 bar, 15 °C in vapour phase (a), 55 bar, 5 °C in liquid phase (b) and 75 bar, 40 °C in supercritical phase (c) (Teng et al. 2016).

From figure 2.13, for all tests, there is good agreement between the model predictions and the measured data during the early stages of the release. As the decompression proceeds, in figures 2.13 (b) and (c) for the tests respectively starting from the CO_2 liquid and supercritical phases, a significant over-prediction of the rate of decompression is observed.

Focusing on figure 2.13 (b) with the decompression test starting in the CO_2 liquid phase, the expected discontinuity in the rate of decompression upon phase transition (indicated by the vertical dashed lines) as previously reported by Oke et al. (2003)

(see Section 2.2.1.1) is not observed. No explanation is provided by the authors regarding the above.

2.2.1.3 Martynov et al. (2014)

Martynov et al. (2014) performed a numerical study on the formation of solid CO_2 (dry ice) at the pipeline release point (e.g. the rupture plane) during decompression, given the potential risk of blockage of the pipeline or more likely, the blockage of emergency pressure relief valves.

The HEM model was used to describe the in-pipe flow fluid mechanics. Friction was assumed to be the only fluid/wall interaction modelled using Chen's correlation (Chen 1979). To account for solid CO_2, the extended PR EoS (Martynov et al. 2013) previously developed by the authors was employed to determine the solid-vapour and solid-vapour-liquid phase equilibrium data. MoC (Zucrow & Hoffman 1976) was applied as the numerical solution technique.

A case study was performed to simulate hypothetical FBR decompression scenarios (up to the triple point) of CO_2 pipelines of various lengths. The results are presented in figure 2.14 in terms of the decompression time to reach the triple point pressure (at the rupture plane) as a function of the test pipeline length and the corresponding mass fraction of the initial inventory released.

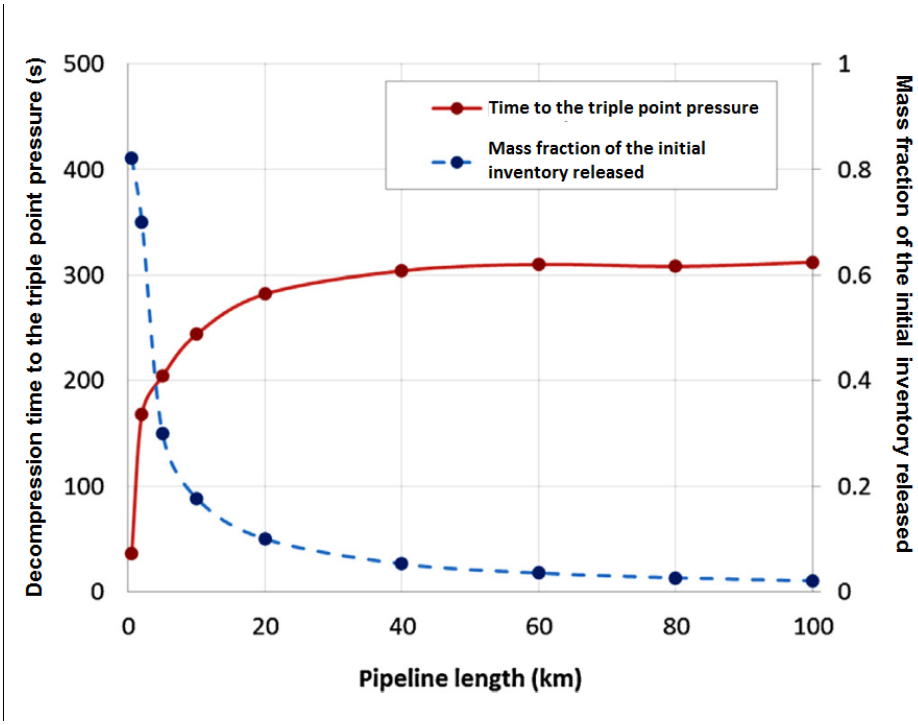

Figure 2.14: Predicted decompression time to the triple point pressure (red curve) and the corresponding mass fraction of the initial inventory released (blue curve) as a function of the pipeline length tested in the case study (Martynov et al. 2014).

From figure 2.14, it can be observed that the decompression time to the triple point rapidly increases with pipeline length at first, stabilising at ca. 300 s when the pipeline length reaches ca. 40 km. At this point, approximately 90% of the initial inventory still remains in the pipeline. The above finding highlights the risk of significant amounts of solid CO_2 formation upon further depressurisation below the triple point and hence the importance of the development of the corresponding models.

2.2.1.4 Hammer et al. (2013)

The computational CO_2 pipeline decompression study performed by Hammer et al. (2013) focuses on solid CO_2 formation within the pipeline when surpassing the triple point.

In comparison to (Martynov et al. 2014), the key difference between the two studies is the adopted numerical solution method. The MoC (Zucrow & Hoffman 1976) adopted by Martynov et al. (2014) requires the conversion of the PDE conservation equations

to a set of ODEs along relevant waves, whereas the Finite Volume Method (FVM) (LeVeque 2002) applied in Hammer et al. (2013) study directly integrates and thus solves the PDE conservation equations.

To test their numerical solution scheme, the developed model was used to obtain the wave solutions of a specified Riemann problem. The initial conditions of the Riemann problem consisted of a step change in pressure (from 30 bar to 1 bar) and a constant temperature profile (at 250 K) along a 100 m long horizontal computational domain. At the start of the simulation, waves were allowed to propagate within the domain. The resulting pressure and temperature profiles along the computational domain at 0.06 s from the start of the simulation are presented in figure 2.15 for visualisation of the wave structure. (The following discussion only concerns the simulated results marked by green curves in figure 2.15).

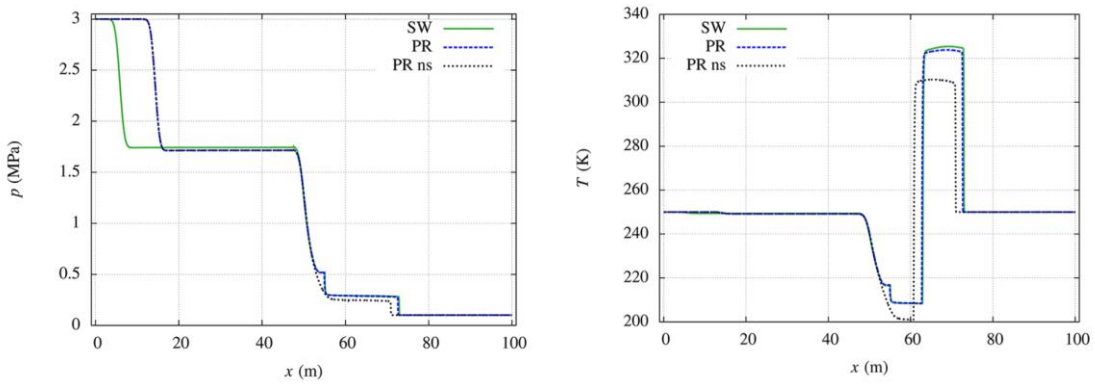

(a) (b)

Figure 2.15: Numerical solution of the specified Riemann problem in terms of the pressure (a) and temperature (b) profiles along the length of the computational domain (denoted by *x*) at 0.06 s from the start of the simulation (Hammer et al. 2013). SW, PR, PR ns EOS are the different EOS tested by the authors.

From figure 2.15 (a), the decompression and shock waves can be easily identified occurring at x = 5 m and 75 m, respectively. The contact wave is at x = 62 m, where there is a jump in temperature (figure 2.15 (b)) while the pressure is conserved (figure 2.15 (a)). These three waves make up the classical wave solution of the Riemann problem (see also Section 2.1.6.1.3). Furthermore, two additional waves are observed

at x = 50 and 55 m in figure 2.15 (a). They are separated from the rarefaction wave (at x = 5 m) by two pressure plateaux each at the CO_2 saturated pressure of 17 bar and triple point pressure of 5.18 bar. According to the authors, the anomalous waves are related to fluid phase transitions (Hammer et al. 2013). However, no further discussion was provided to support their argument.

In the next part of their numerical investigation, a case study was performed for the decompression of a hypothetical CO_2 pipeline across the triple point. The 100 m long pipe was assumed to be initially filled with pure CO_2 at 100 bar and 300 K (in liquid phase), with FBR initiated at one end. The simulated pressure-time profiles along the pipe length at different decompression times in the range of 0.05 to 5.5 s are presented in figure 2.16.

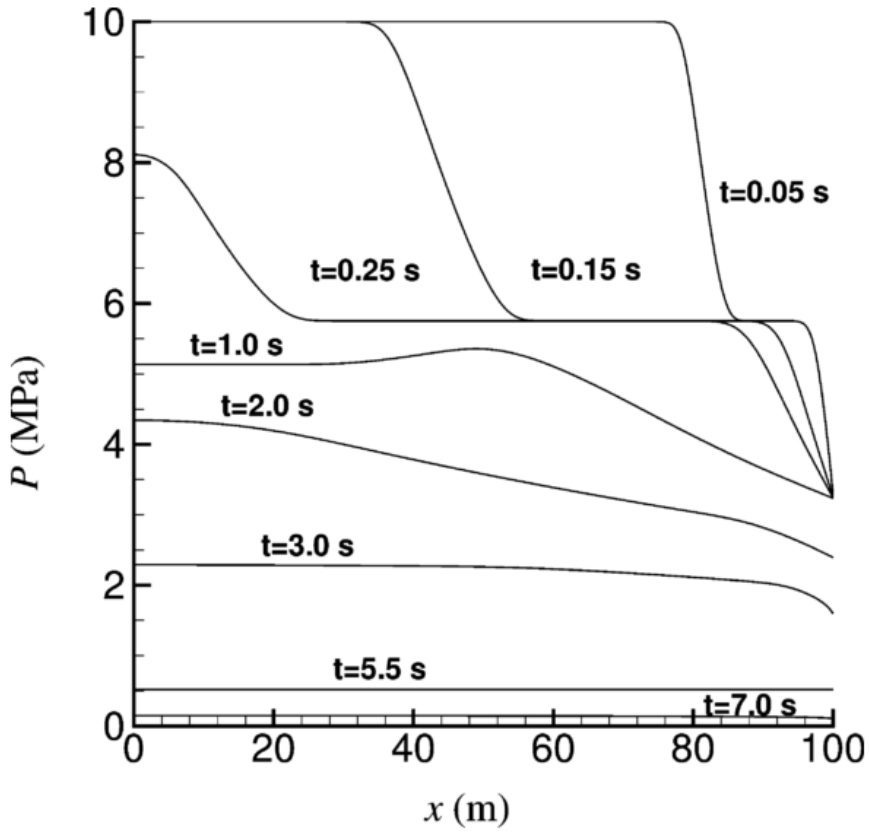

Figure 2.16: Predicted pressure profiles along the entire length of the assumed pipeline at different decompression times (Hammer et al. 2013).

In figure 2.16, the pressure plateau (at ca. 58 bar) each observed at 0.05 s, 0.15 s and 1.0 s following the start of the simulation corresponds to vapour-liquid phase

transition. As the decompression proceeds, all the remaining CO_2 is in vapour-liquid two-phase, and the pressure plateau is no longer observed. Before reaching the ambient pressure (at 7.0 s), a temporal pressure stabilisation at the triple point (at 5.5 s) appears as a result of solid CO_2 formation.

It should be pointed out here that the above model predictions were not validated against experimental data. Moreover, at the triple point, the homogeneous mixture speed of sound turns to zero (with reference to equation 2.91). Consequently, the HEM assumption adopted in their flow model produces a singularity in the corresponding PDEs, which cannot be dealt with using conventional numerical methods based on hyperbolicity. There is no mention of how such a mathematical difficulty was overcome in their study.

2.2.1.5 Concluding Remarks

In reviewing the recent developments of the HEM model for pipeline decompression modelling, it is clear that significant progress has been made in terms of its predictive capabilities. Despite its relatively simple form, notwithstanding the limited number of investigations, its effectiveness in successfully simulating pipeline FBR decompression has been clearly demonstrated.

More specifically, the following is a summary of the key findings in the context of scope and range of applicability:

- A variety of physical phenomena relevant to pipeline decompression such as fluid/wall friction and heat transfer, multicomponent mixtures, phase transitions (including solid phase) are accounted for;
- Good performance in predicting pipeline FBR decompression is achieved;
- For CO_2 pipelines, its accuracy is however limited to decompression before reaching the triple point. Upon surpassing the triple point, the HEM model is yet to be validated against experimental data;
- Heterogeneous flow cannot be accounted for;
- Thermodynamic non-equilibrium due to delayed phase transition cannot be accounted for.

2.2.2 Applications of the HRM Model

2.2.2.1 Angielczyk et al. (2010)

Angielczyk et al. (2010) applied the HRM model (see Section 2.1.2.2.2) for the investigation of non-equilibrium CO_2 flashing flows through a converging-diverging nozzle. The original HRM model was extended to account for smooth change in the flow area. The finite interphase mass transfer rate was modelled following equation 2.23, and a correlation for the relaxation time, τ was proposed:

$$\tau = 2.14\times10^{-7}\left(\phi\frac{\rho}{\rho_{eq}}\right)^{-0.54}\left(\frac{p_{eq}-p}{p_c-p_{eq}}\right)^{-1.76} \qquad 2.225$$

Herein, ϕ is the vapour phase molar fraction. For predicting CO_2 thermodynamic non-equilibrium (metastable) states, PR EoS (Peng & Robinson 1976) was used. Fluid/wall friction and heat transfer were not considered.

Assuming steady state flow, the authors neglected the transient contributions in PDEs. The solutions are thus obtained analytically.

As part of validation, the developed model was used to simulate a CO_2 nozzle flow experiment by Nakagawa et al. (2009). The rectangular test nozzle consisted of a 27.35 mm length converging section and a 56.15 mm length diverging section with adjustable divergence angles. The throat area was 0.24 mm × 3 mm. CO_2 at 91 bar and 36.5 °C was released through the nozzle and steady state pressure profiles were recorded along its length. The measurements together with the corresponding model predictions are given in figures 2.17 to 2.19.

In addition, the simulated vapour quality (vapour phase molar fraction) profiles along the nozzle length from both the HRM model developed and a HEM model are also presented. The inclusion of the HEM model predictions is to showcase the impact of thermodynamic non-equilibrium.

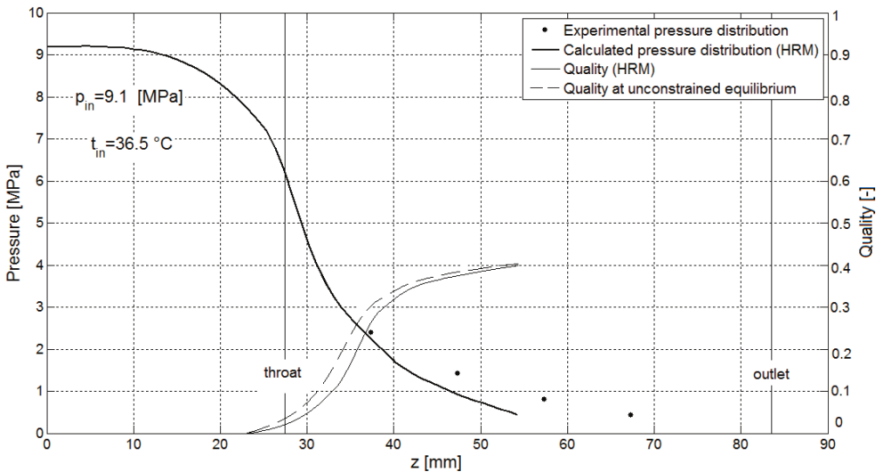

Figure 2.17: Predicted and measured steady state pressure profiles along the nozzle length at a divergence angle of 0.612 °. Also included are the predicted vapour quality profile along the nozzle length both from the HRM model and the HEM model (labelled as 'unconstrained equilibrium' in the figure legend) (Angielczyk et al. 2010).

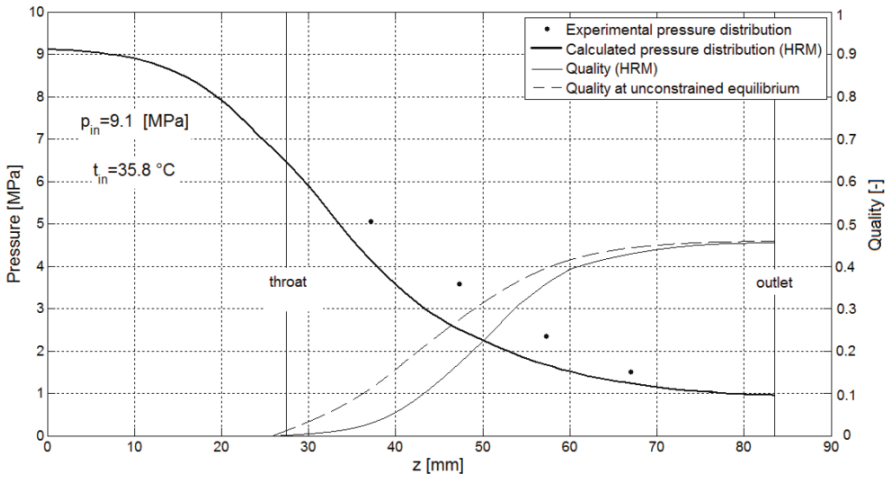

Figure 2.18: Predicted and measured steady state pressure profiles along the nozzle length at a divergence angle of 0.306 °. Also included are the the predicted vapour quality profile along the nozzle length both by the HRM model and the standard HEM model (labelled as 'unconstrained equilibrium' in the figure legend) (Angielczyk et al.

2010).

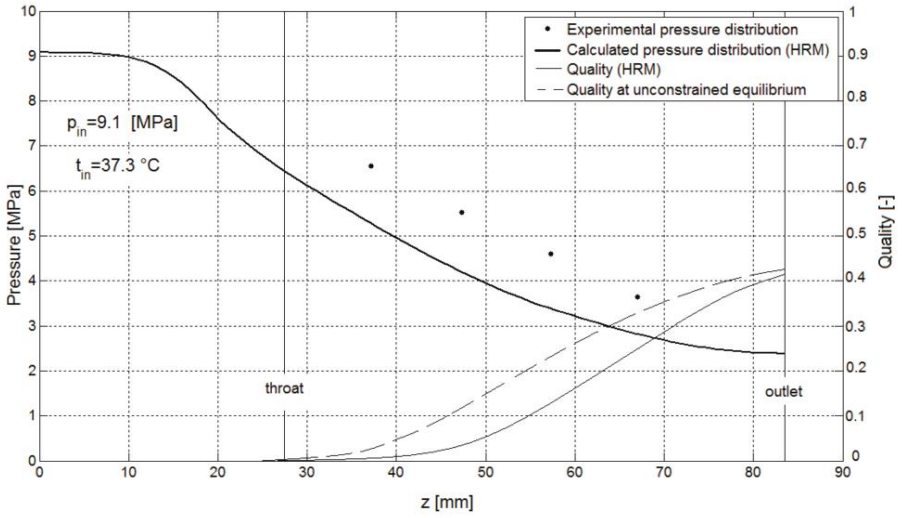

Figure 2.19: Predicted and measured steady state pressure profiles along the nozzle length at a divergence angle of 0.153 °. Also included are the predicted vapour quality profile along the nozzle length both by the HRM model and the HEM model (labelled as 'unconstrained equilibrium' in the figure legend) (Angielczyk et al. 2010).

From figures 2.17 to 2.19, in all cases, pressure decreases as the flow expands through the diverging section. There is a relatively good agreement between the theory and measurements. With regards to the predicted steady state vapour quality profiles, although no experimental data is available, comparison between the HRM and HEM model predictions shows that the HEM model consistently predicts higher vapour qualities.

2.2.2.2 Haida et al. (2016)

In another study on CO_2 nozzle flow in a vapour ejector by Haida et al. (2016), the model developed by Angielczyk et al. (2010) was extended to 2-D with additional consideration of turbulence. By simulating several CO_2 vapour ejection experiments, the model's performance was assessed based on its relative accuracy in predicting the mass flowrate in two different sections of the test ejector (i.e. the motive and suction

sections). The results are shown in figures 2.20 and 2.21. Also included are the results from the HRM model based on constant relaxation times (instead of equation 2.225) in the range of from 1×10^{-6} to 1×10^{-3} s as well as the HEM model for comparison.

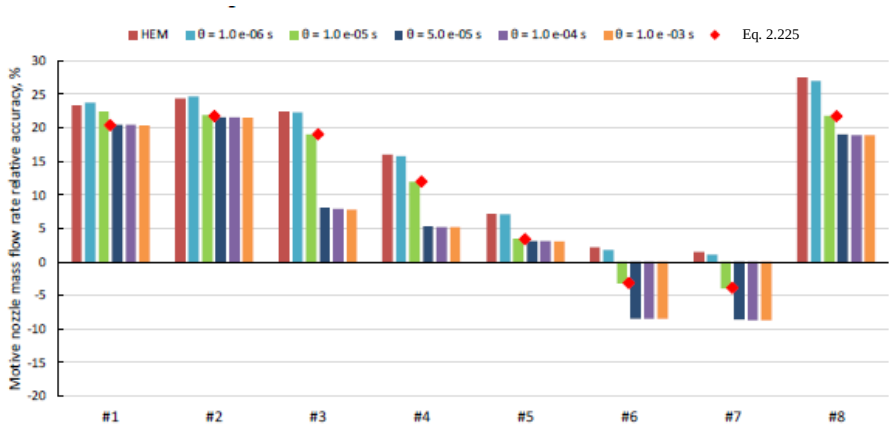

Figure 2.20: Relative accuracy of the mass flowrate predictions (in the motive section of the ejector) from the HEM model and the HRM model based on varying relaxation times (denoted as θ by the authors in the figure legend) either specified by equation 2.225 or of constant values (Haida et al. 2016).

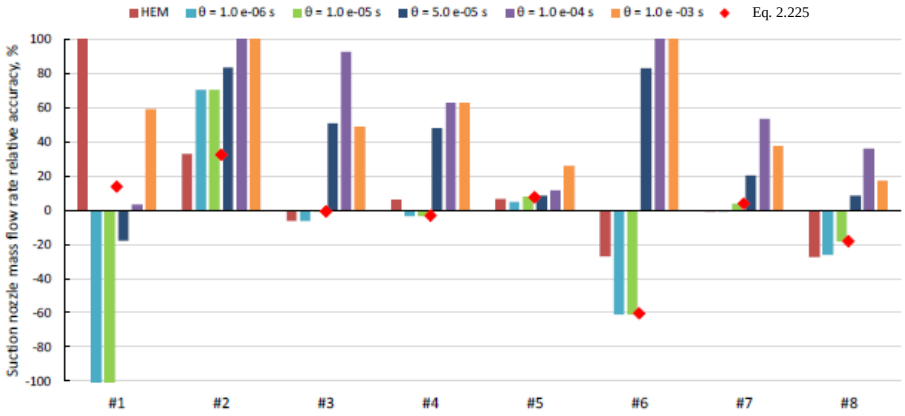

Figure 2.21: Relative accuracy of mass flowrate predictions (in the suction section of the ejector) from the HEM model and the HRM model based on varying relaxation times (denoted as θ by the authors in the figure legend) either specified by equation 2.225 or of constant values (Haida et al. 2016).

As it may be observed in figures 2.20 and 2.21, in general, the HRM model with the relaxation time computed by equation 2.225 is shown to produce an improved relative accuracy (about 20 % for most cases) over the HEM model.

Interestingly, the HRM model predictions based on constant relaxation times occasionally yield better relative accuracy as compared to those based on equation 2.225. However, the results are very sensitive to the specified values of the relaxation time. Within the tested range of between 1×10^{-6} and 1×10^{-3} s, the difference can be as much as 160% (see #1 in figure 2.21).

2.2.2.3 Brown et al. (2013)

Angielczyk et al. (2010) and Haida et al. (2016) have showed that in the case of thermodynamic non-equilibrium flow, the HRM model provided noticeable improvements over the widely used HEM model. However, their work is limited to steady state flows.

In a recent study by Brown et al. (2013), the HRM model was applied to investigate the transient decompression of a high-pressure CO_2 pipeline. The neglected time-dependent terms in the previous studies were accounted for. Fluid/wall friction was computed using Chen's correlation (Chen 1979), and fluid/wall heat transfer was argued to be insignificant given the very short decompression duration.

The resulting PDE system was solved numerically using the FVM (LeVeque 2002) in conjunction with the Harten-Lax-Van Leer (HLL) scheme (Toro 2009e).

The model developed was first verified by solving a specified Riemann problem on a computational domain of 1 m length filled with vapour-liquid two-phase CO_2. The initial conditions for the Riemann problem were given by a step function each in pressure (15 bar to 1 bar) and vapour quality (0.15 to 0.5). Both constant relaxation times (ranging from 0.01 to 1 ms) and those computed using the correlation defined in equation 2.225 were tested. The results in terms of pressure and density profiles along the length of the computational domain are plotted in figure 2.22.

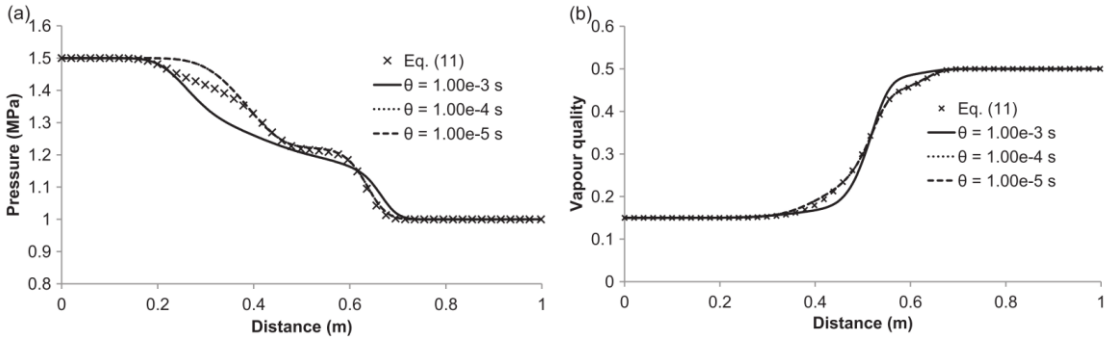

(a) (b)

Figure 2.22: Predicted pressure (a) and vapour quality (b) profiles along the computational domain based on the computed relaxation time (denoted as Eq. (11) in the figure legend) and different constant relaxation times (denoted as θ) at 2 ms from the start of the simulation (Brown et al. 2013).

From figure 2.22 (a), it is clear that a larger relaxation time is observed to produce a faster decompression wave front. The slowest and the fastest fronts are 0.1 m apart, which gives a wave speed difference of ca. 50 m/s. This is attributed to the corresponding increased delay in vapour-liquid phase transition (see figure 2.22 (b)). The relaxation time computed by equation 2.225 is between 0.1 and 1 ms.

The authors went on to simulate a large-scale CO_2 pipeline FBR decompression test performed during the course of the National Grid UK COOLTRANS project (Cosham et al. 2012). The test rig was the same as that presented in Section 2.2.1.1. The pipe was initially filled with pure CO_2 at 153.35 bar and 278.35 K, and FBR was initiated at one end using an explosive charge. Pressure and temperature were measured at multiple points along the pipe length during decompression.

Figure 2.23 presents the predictions from the HRM and HEM models for the variations of pressure as a function of time at both pipe intact and release ends. Also included in figure 2.23 (a) are the measurements at the pipe intact end for comparison.

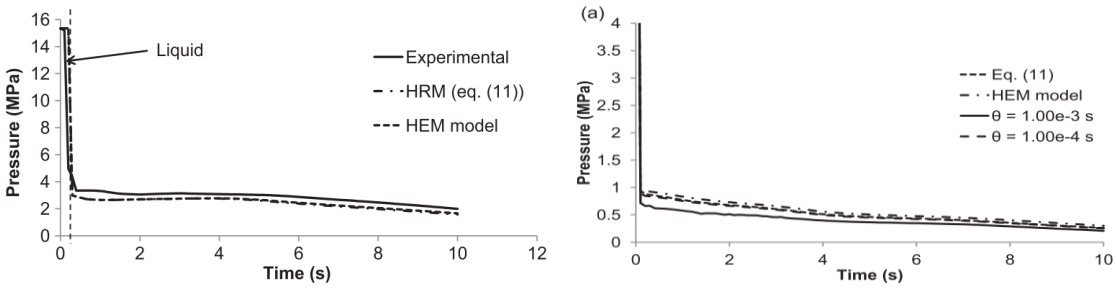

(a) (b)

Figure 2.23: Predicted pressure-time profiles from the HRM and HEM models at the pipe intact end (a) and the release end (b) during decompression. The measurement at the pipe intact end is included in (a) (Brown et al. 2013).

Referring to figure 2.23 (a), there is a marginal difference between the HRM and HEM model predictions; they are both in good agreement with the measured data, showing a rapid drop in the decompression rate at vapour-liquid phase transition boundary (marked by the vertical dashed line in figure 2.23 (a)). Turning to figure 2.23 (b), at the pipe release end, the HRM model predicts a faster decompression rate prior to phase transition. This corresponds to the faster decompression waves as a result of delayed phase transition. Unfortunately, no experimental data is available at the release end, and thus there is no conclusive evidence to support the validity of the simulated results.

2.2.2.4 Concluding Remarks

From the above review of the HRM model applications, where thermodynamic non-equilibrium is relevant, the model has shown to produce a noticeable improvement over the HEM model. However, as compared to the HEM model, the HRM model validation against appropriate experimental data is lacking. Moreover, most previous studies using the HRM are limited to single-component flow, thus significantly reducing its scope in practical applications.

The following is a summary of the key findings:

- Where thermodynamic non-equilibrium is relevant, the HRM model is shown to produce improved accuracy compared to the HEM model;

- The HRM model predictions are sensitive to the relaxation time specified;
- For pipeline decompression, a higher decompression rate (prior to phase transition) is predicted by the HRM model as compared to the HEM model. However, this needs to be verified against experimental data;
- The HRM model development has been confined to single-component flows.

2.2.3 Applications of the DFM Model

2.2.3.1 Munkejord et al. (2010)

To investigate the impact of heterogeneous flow on pipeline decompression, a computational study was carried out by Munkejord et al. (2010) using the DFM model (Section 2.1.2.2.3).

As pointed out in Section 2.1.2.2.3, the DFM model requires an empirical constitutive relation to closely relate the velocities of two fluid phases. In their study, a slip relation proposed by Zuber & Findlay (1965) was used:

$$u_v - u_l = \frac{(K_u - 1)u_v + S_u}{K_u u_l} \qquad 2.226$$

where K_u and S_u are flow regime-dependent parameters.

Fluid/wall friction was modelled using Friedel's correlation (Friedel 1979), and the heat transfer flux was computed assuming a constant heat transfer coefficient throughout the decompression process. The Soave-Redlich-Kwong (SRK) EoS (Soave 1972) was employed for predicting the fluid thermal properties and phase equilibria data.

The DFM model was employed to simulate the FBR decompression of an assumed 100 m length pipe filled with a mixture of CO_2 and CH_4 (at 99 wt% and 1 wt%, respectively) initially at 60 bar and 290.5 K (in liquid phase). The ambient pressure was set to 30 bar. Figures 2.24 and 2.25 respectively display the predicted velocity and pressure profiles along the entire length of the assumed pipe at 1 s following the rupture. Also included is the HEM model predictions (denoted by 'no slip' in the

figure legend) to demonstrate the impact of heterogeneous flow on pipeline decompression.

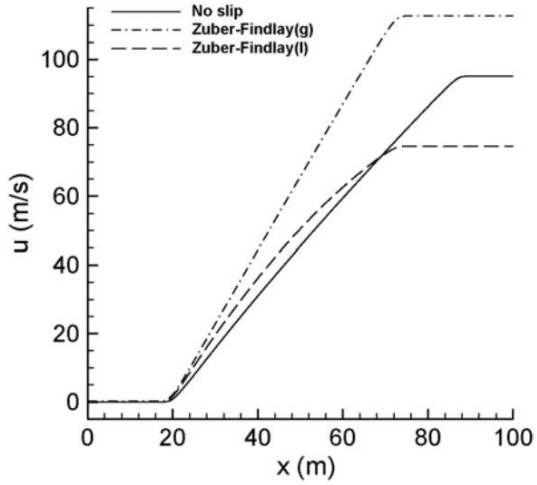

Figure 2.24: Predicted vapour (denoted as *g*) and liquid phase (denoted as *l*) velocity profiles along the pipe length at 1 s following the rupture (Munkejord et al. 2010).

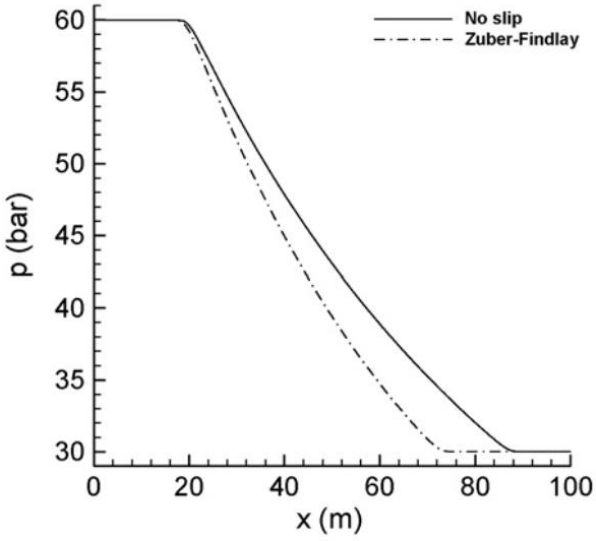

Figure 2.25: Predicted pressure profiles along the pipe length at 1 s following the rupture (Munkejord et al. 2010).

According to figure 2.24, significantly different phasic velocities can be observed for the DFM model (denoted as 'Zuber and Findlay'), which is referred to as 'phase slip' as a result of heterogeneous flow. The phase slip increases to as much as 40 m/s close the pipe release end. For the HEM model, as expected, only a single velocity is predicted for both fluid phases.

Turning to the pressure predictions in figure 2.25, beyond the observed initial plateau marking the finite speed of decompression wave propagation, at any given time, a faster decompression rate is predicted by the DFM model as compared to the HEM model. In practice, this may be significant as the decompression rate is directly related to the fracture propagation length (Cosham & Eiber 2008; Aursand et al. 2016; Martynov et al. 2017) in the event of such type of failure. Unfortunately, no validation against appropriate experimental data was provided by the authors to support their model predictions.

2.2.3.2 Concluding Remarks

For pipeline decompression modelling, based on the reviewed literature, the DFM has attracted less attention in comparison to the HEM and HRM models. This is partially due to the fact that for the DFM model to be credible, the fluid phasic velocities must be strongly coupled (corresponding to slug and bubbly flow regimes (Hibiki & Ishii 2003) that may occur during the decompression process). Given the success of the relatively simple HEM model in simulating the flow behaviour during pipeline FBR decompression encompassing such flow regimes, the mathematical complexity of the DFM model makes it unattractive.

In conclusion, based on the above:

- Phase slip is theoretically shown to have a profound impact on pipeline decompression rate. However, this is yet to be supported by experimental data;
- For pipeline decompression modelling, the DFM model is limited to the flow regimes where the HEM model is known to offer acceptable accuracy. The extra mathematical complexity thus renders it unfavourable especially for

quantitative failure consequence assessment of transportation pipeline networks with hundreds of kilometres in length.

2.2.4 Applications of the TFM model

2.2.4.1 Brown et al. (2014)

As discussed in Section 2.1.2.2.4, the single-fluid models (i.e. the HEM, HRM and DFM models) require additional assumptions or closure relations to relate the constituent fluid phase thermal or mechanical properties. On the other hand, by solving the mass, momentum and energy conservation equations for each fluid phase separately along with explicit modelling of interface interactions, such a limitation can be removed in the TFM model.

Brown et al. (2014) applied the six-equation TFM model for CO_2 pipeline FBR decompression modelling, where both thermal and mechanical non-equilibrium were considered. This was achieved by appropriate modelling of the interface mass, momentum and energy exchange via the source terms in the corresponding conservation equations 2.37 to 2.42. The net interface mass exchange rate per unit volume is given by (S. Brown et al. 2014):

$$\Gamma = \Gamma_v = -\Gamma_l = -\frac{\left(q_v^{\text{int}} + q_l^{\text{int}}\right)}{h_{sat,v} - h_{sat,l}} \qquad 2.227$$

where the subscript, *sat* denotes the saturated vapour or liquid state. q^{int} in each fluid phase is given by (S. Brown et al. 2014):

$$\forall k = v, l; \qquad \dot{q}_k^{\text{int}} = \frac{1}{\tau}\alpha_k\left(1-\alpha_k\right)\left(h_k^{sat} - h_k\right) \qquad 2.228$$

where τ is the relaxation time set as constant values by the authors.

Moving on to the interface momentum interaction, in addition to the included interphase pressure force terms for hyperbolisation (Section 2.1.6.2.1), only the drag force was accounted for. The drag force is given by (S. Brown et al. 2014):

$$F^d = F_v^d = -F_l^d = C_d \alpha_v \alpha_l \left(k_l \rho_l + k_v \rho_v\right)\left(u_v - u_l\right)\left|u_v - u_l\right| \quad 2.229$$

where C_d, k_v and k_l are model constants.

Fluid/wall interactions are modelled by the authors specific to each fluid phase (see Sections 2.1.3,1). The vapour and liquid phase thermal properties and phase equilibrium data were calculated using PR EoS (Peng & Robinson 1976). Finally, the resulting PDEs are presented for completeness (all symbols are defined in Section 2.1.2 and 2.1.3):

$$\frac{\partial \alpha_v \rho_v}{\partial t} + \frac{\partial \alpha_v \rho_v u_v}{\partial x} = \Gamma \quad 2.230$$

$$\frac{\partial \alpha_l \rho_l}{\partial t} + \frac{\partial \alpha_l \rho_l u_l}{\partial x} = -\Gamma \quad 2.231$$

$$\frac{\partial \alpha_v \rho_v u_v}{\partial t} + \frac{\partial \left(\alpha_v \rho_v u_v^2 + \alpha_v p\right)}{\partial x} = \left(p - \Delta p^{\text{int}}\right)\frac{\partial \alpha_v}{\partial x} + u^{\text{int}}\Gamma + F_d + F_{w,v} \quad 2.232$$

$$\frac{\partial \alpha_l \rho_l u_l}{\partial t} + \frac{\partial \left(\alpha_l \rho_l u_l^2 + \alpha_l p\right)}{\partial x} = \left(p - \Delta p^{\text{int}}\right)\frac{\partial \alpha_l}{\partial x} - u^{\text{int}}\Gamma - F_d + F_{w,l} \quad 2.233$$

$$\frac{\partial \alpha_v \rho_v E_v}{\partial t} + \frac{\partial \left(\alpha_v \rho_v u_v E_v + \alpha_v p u_v\right)}{\partial x} = - \quad 2.234$$
$$p\frac{\partial \alpha_v}{\partial t} - \Delta p^{\text{int}} u^{\text{int}} \frac{\partial \alpha_v}{\partial x} + u^{\text{int}} F_d + u_v F_{w,v} + H_{v,l}\Gamma + \frac{4\dot{q}_{w,v}}{D_{w,in}}$$

$$\frac{\partial \alpha_l \rho_l E_l}{\partial t} + \frac{\partial \left(\alpha_l \rho_l u_l E_l + \alpha_l p u_l\right)}{\partial x} = - \quad 2.235$$
$$p\frac{\partial \alpha_l}{\partial t} - \Delta p^{\text{int}} u^{\text{int}} \frac{\partial \alpha_l}{\partial x} - u^{\text{int}} F_d + u_l F_{w,l} - H_{v,l}\Gamma + \frac{4\dot{q}_{w,l}}{D_{w,in}}$$

In numerically solving the above PDE system, the conservative part (LHS of equations 2.230 to 2.235) were integrated applying the FVM (LeVeque 2002) in conjunction with the AUSM+ scheme (Paillère et al. 2003). The remaining non-conservative spatial ($\partial/\partial x$) and temporal ($\partial/\partial t$) derivative terms were approximated

using the central difference scheme and the forward Euler method, respectively (Paillère et al. 2003; S. Brown et al. 2014).

For validation, the model was employed to simulate a CO_2 pipeline FBR decompression test performed by DUT, China during the course of the CO_2PipeHaz project (Robert M. Woolley et al. 2014). The test rig consisted of a 256 m length, 233 mm i.d. and 20 mm thickness 16Mn carbon steel pipe filled with two-phase CO_2 ($\alpha_v = 0.5$) at saturated pressure of 36 bar. Following the rupture, pressure and temperature variations are monitored at multiple points along the pipe length. Figure 2.26 presents the predicted pressure variations as a function of time both at the pipe release (figure 2.26 (a)) and intact (figure 2.26 (b)) ends, together with the corresponding measurements. Different constant values of τ, including 5×10^{-6}, 5×10^{-5} and 5×10^{-4} s in equation 2.228 were tested using the model. Also included are the predictions from the HEM model for comparison.

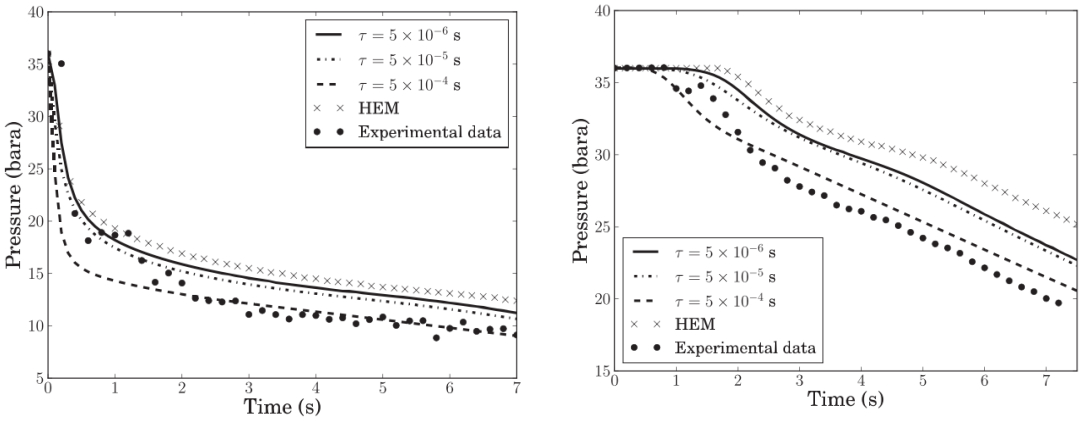

(a) (b)

Figure 2.26: Predicted (from the HEM model and the TFM model based on various values of τ) and measured pressure variations as a function of time at the pipe release end (a) and intact end (b).

From figure 2.26, in agreement with the observation made for the HRM model (Section 2.2.2.3), a faster decompression wave and hence a higher decompression rate can be observed with a larger relaxation time. In terms of the degree of agreement with the measured data, the TFM model outperforms the HEM model. The best accuracy is obtained by setting τ to 5×10^{-4} s. The HEM model on the other hand

consistently over-predicts the fluid pressure by as much as 10 bar (at the pipe intact end; see figure 2.26 (b)).

Next, the vapour and liquid phase temperature predictions as a function of time both at the pipe release and intact ends were compared against the corresponding measurements. The results are shown in figures 2.27 and 2.28.

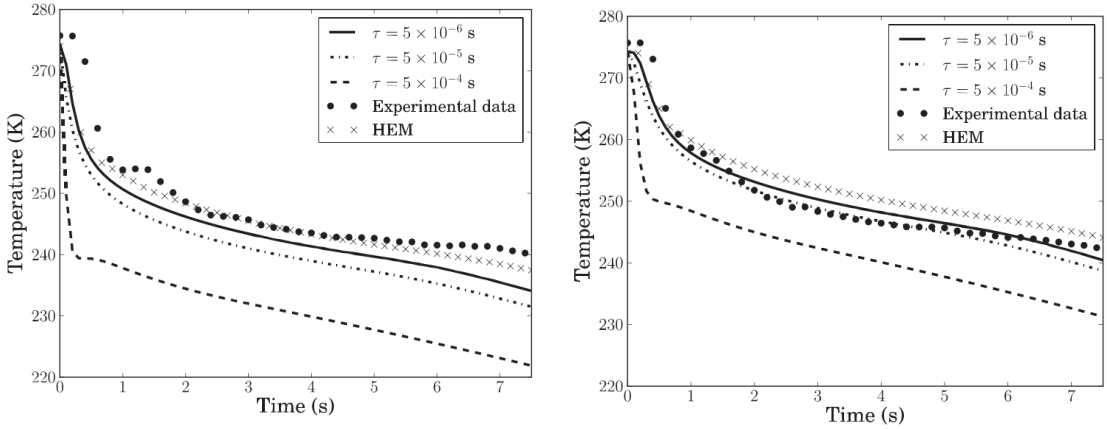

(a) (b)

Figure 2.27: Predicted (from the HEM model and the TFM model based on various values of τ) vapour phase temperature variation as a function of time and the measurement (for the bulk vapour-liqiud mixture) at both the pipe release end (a) and intact end (b).

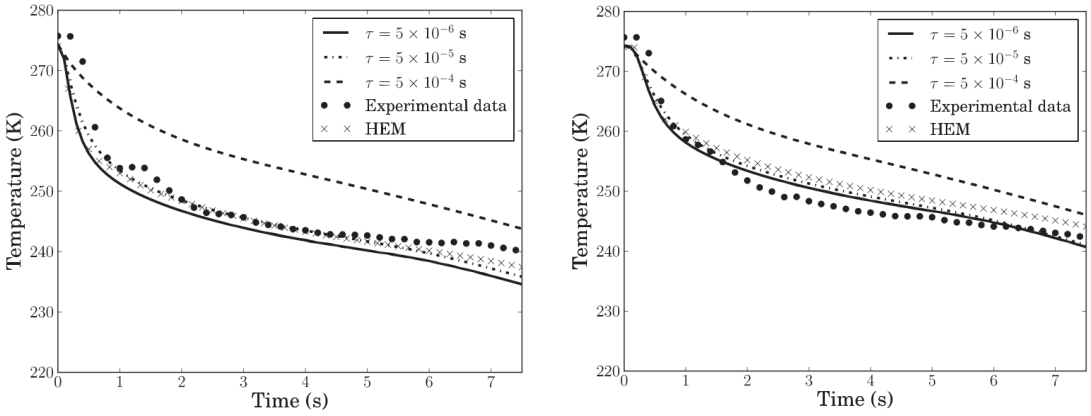

(a) (b)

Figure 2.28: Predicted (from the HEM model and the TFM model based on various values of τ) liquid phase temperature variation as a function of time and the measurement (for the bulk vapour-liqiud mixture) at both the pipe release end (a) and intact end (b).

From figures 2.27 and 2.28, the performances of both HEM and TFM models in terms of the degree of agreement with the experimental data are comparable, except for the case where $\tau = 5\times10^{-4}$ s in the TFM model. In this case, the large relaxation time leads to significant superheating of the liquid phase. In figure 2.29, the corresponding decompression trajectory is plotted in *p-T* thermodynamic plane, together with the HEM model predictions, the measurements and the CO_2 saturation line for reference.

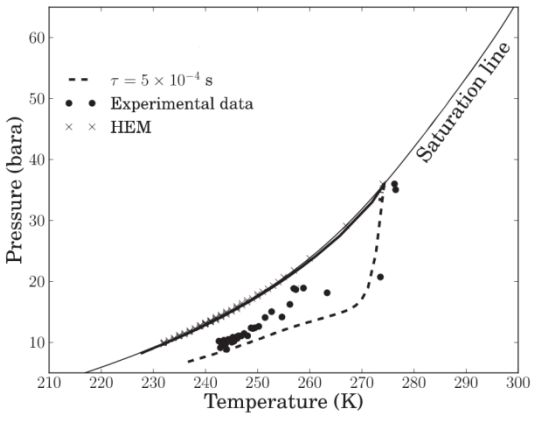

Figure 2.29: Predicted (from the HEM model and the TFM model based on $\tau = 5\times10^{-4}$ s) and measured decomperssion trajectories in the *p-T* plane.

From the above figure, a significant departure from the saturation line is observed for the TFM model prediction with $\tau = 5\times10^{-4}$ s, whereas the HEM prediction exactly follows the saturation line.

In the next part of their study, Brown et al. (2014) investigated the impact of mechanical non-equilibrium on pipeline decompression. This was achieved by manually fixing the interface drag coefficient, C_d in equation 2.229 to different constant values of 0.1, 1 and 10. A higher C_d means a higher rate of interface momentum exchange (and hence being closer to mechanical equilibrium). The simulation was repeated, and the results (in terms of pressure variations at both pipe release and intact ends) are presented in figure 2.30.

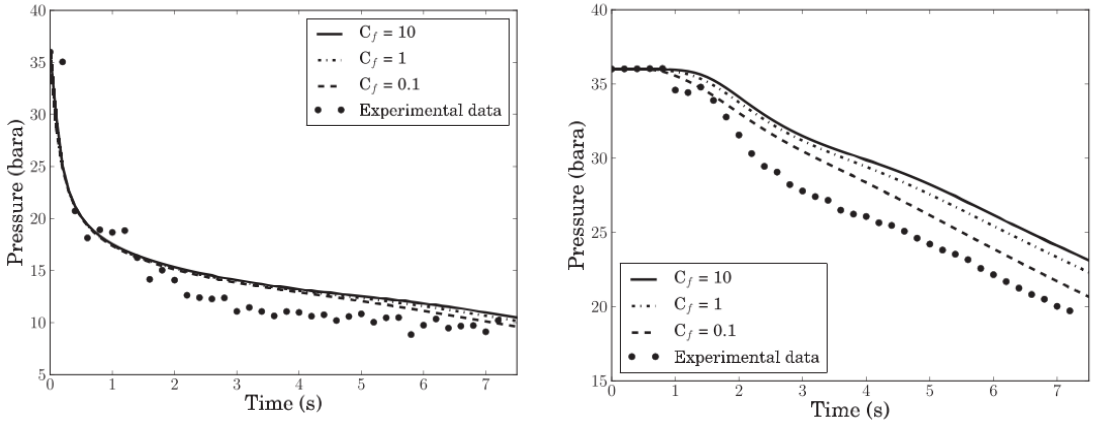

(a) (b)

Figure 2.30: Predicted (from the TFM model based on various drag coeffcients) and measured pressure variations as a function of time at both the release end (a) and intact end (b).

From figure 2.30 (a), it is clear that increasing C_d from 0.1 to 10 results in only a marginal change in the simulated release end pressure data, all producing a reasonably good agreement with measurements. This is in contrast to the simulated intact end pressure data where the predictions are more affected by the specified C_d. The degree of disagreement with the experimental data increases as C_d increases.

2.2.4.2 Munkejord & Hammer (2015)

Another example for the application of the TFM is the study by Munkejord & Hammer (2015) on the decompression of CO_2-rich mixtures. The adopted flow conservation equations were similar to equations 2.230 to 2.235. However, due to the extra consideration of stream impurities, species transport equations were solved for each component in parallel. The species transport equations for both fluid phases are given by (Munkejord & Hammer 2015):

$$\frac{\partial \alpha_v \rho_v y_i}{\partial t} + \frac{\partial \alpha_v \rho_v u_v y_i}{\partial x} = \Gamma_i \qquad 2.236$$

$$\frac{\partial \alpha_l \rho_l x_i}{\partial t} + \frac{\partial \alpha_l \rho_l u_l x_i}{\partial x} = -\Gamma_i \qquad 2.237$$

Moreover, thermal equilibrium between the two constituent fluid phases was assumed, which effectively reduces the two phasic energy conservation equations 2.234 and 2.235 to one mixture energy conservation equation given by:

$$\frac{\partial}{\partial t}\left(\alpha_v \rho_v E_v + \alpha_l \rho_l E_l\right) + \frac{\partial}{\partial x}\left(\alpha_v \rho_v E_v u_v + \alpha_l \rho_l E_l u_l + p\alpha_v u_v + p\alpha_l u_l\right) = S_E \qquad 2.238$$

In equation 2.238, fluid/wall heat exchange is accounted for through the source term, S_E. The Colburn correlation (see (Knudsen et al. 1997a)) and the Gungor and Winterton correlation (Gungor & Winterton 1987) were applied respectively for computing the forced convection and boiling heat fluxes, respectively.

Reynolds number-based correlations were used to compute the fluid/wall friction in each fluid phase and interface drag force.

For validation, the model was employed to simulate several large-scale pipeline FBR decompression tests for CO_2-rich mixtures. Examples are presented in the following, including the details of the experimental set-up and the validation results.

The pipeline for the selected example consisted of a 140 length, 10 mm i.d. horizontal stainless steel pipe initially filled with CO_2-N_2 mixtures at different molar compositions (10% N_2 + 90% CO_2, 20% N_2 + 80% CO_2 and 30% N_2 + 70% CO_2) (Drescher et al. 2014). The mixtures prior to decompression was in its supercritical

state at 120 bar and 20 °C. FBR was initiated at one end of the test pipe, while the other end remained closed during decompression. Pressure and temperature transducers were strategically installed at various locations along the pipe length.

For all three releases, the model predictions were compared against the measurements from the transducer located 50 m away from the pipe close end, and the results are shown in figures 2.31 to 2.33. Also included are the HEM model predictions for comparison.

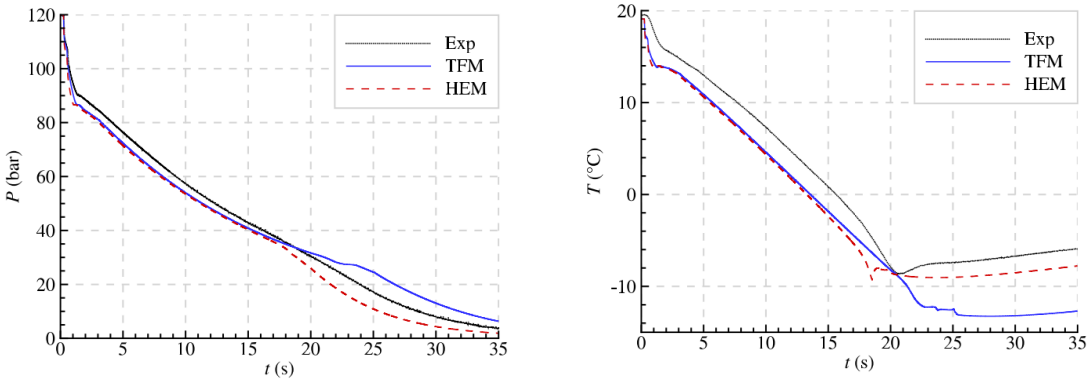

(a) (b)

Figure 2.31: HEM and TFM model predictions and the measured data (denoted as Exp) for the pressure (a) and temperature (b) variations as a function of time 50 m away from the pipe intact end for test 1 (10 % N2 impurity).

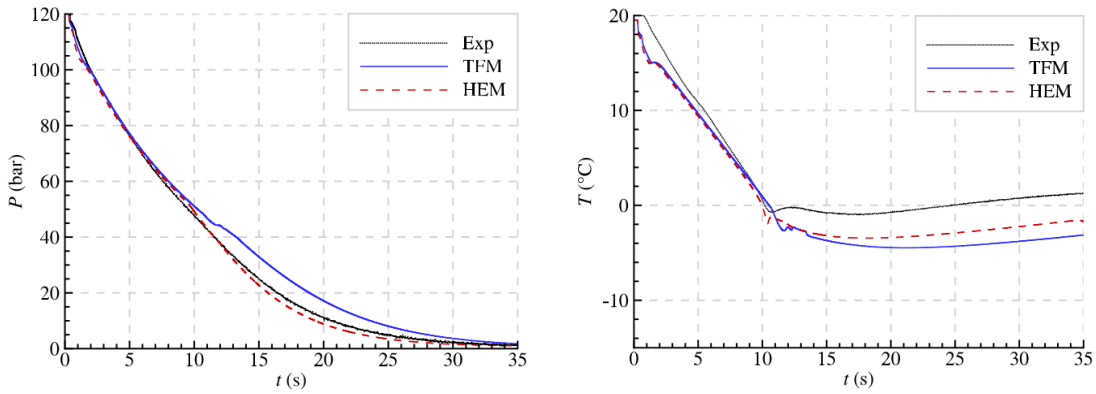

(a) (b)

Figure 2.32: HEM and TFM predictions and the measured data (denoted as Exp) for the pressure (a) and temperature (b) variations as a function of time 50 m away from the pipe intact end for test 2 (20 % N2 impurity).

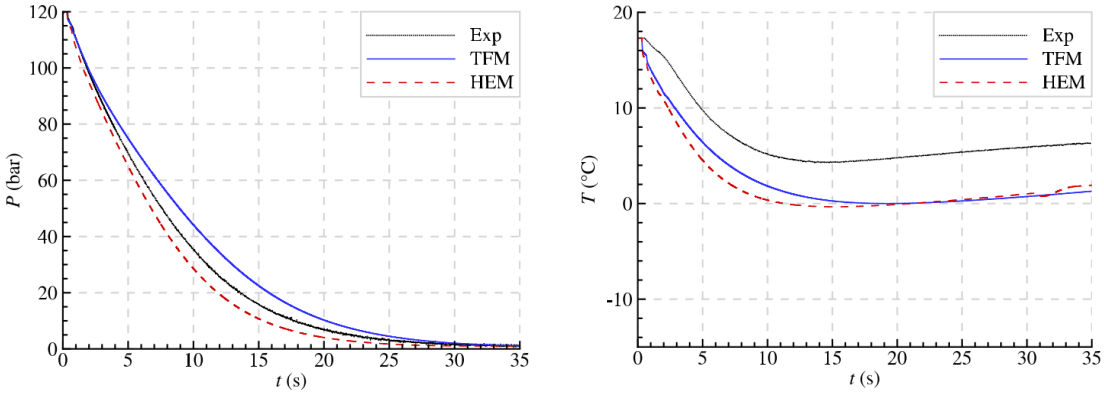

(a) (b)

Figure 2.33: HEM and TFM predictions and the measured data (denoted as Exp) for the pressure (a) and temperature (b) variations as a function of time 50 m away from the pipe intact end for test 3 (30 % N2 impurity).

Comparing figures 2.31 (a), 2.32 (a) and 2.33 (a), the increase in the amount of N_2 in CO_2 can be observed to result in a higher overall rate of decompression; the test pipe is depressurised to the ambient pressure in 35 s for test 1; 30 s for test 2; 27 s for test 3. With regards to the corresponding temperature measurements (figure 2.31 (b) to 2.33 (b)), a higher N_2 molar composition leads to a reduction in the magnitude of the temperature drop. It is interesting to note that dry-out (marked by a temperature

recovery in each temperature-time profiles) takes place as a result of fluid/wall heat transfer.

For the model performance, the HEM and TFM models show no noticeable difference between the model predictions. They both produce good agreement compared to the pressure measurements. This is in contrast to the temperature data where a relatively significant degree of departure between theory and experiment is obtained especially at the later stages of the depressurisation process.

Interestingly in two cases (tests 1 and 2), the HEM model performs better than the TFM model.

2.2.4.3 Concluding Remarks

According to the above investigations, overall, both the HEM and the TFM models perform equally well as compared to measured data for CO_2 pipeline FBR decompression. This suggests that non-equilibrium effects (mechanical non-equilibrium in particular) are largely insignificant during FBR decompression; probably due to the very large fluid velocities resulting in the mixing and entrainment of the constituent fluid phases.

As such, given the mathematical complexity of TFM and its heavy reliance on empirically obtained data (for interface exchange modelling), its use for CO_2 pipeline FBR simulation is not justified.

On the other hand, recently obtained direct experimental evidence involving the visual observation of in-pipe flow during CO_2 pipeline puncture decompression have indicated heterogeneous flow marked by the complete separation of the vapour and liquid phases (Brown et al. 2013). Given the much higher failure rate of pipeline puncture failure compared to pipeline FBR failure (Lydell 2000), the knowledge of the impact of such strong flow heterogeneity on pipeline decompression behaviour is therefore of crucial importance for the quantitative consequence assessment of such failure. Given the above, there is significant scope in the further development, testing and validation of the TFM model for pipeline puncture decompression.

Chapter 3:

Modelling of CO_2 Decompression across the Triple Point

3.1 Introduction

From Chapter 1, the formation of significant quantities of solid CO_2 as a result of surpassing its triple point during rapid decompression of CO_2 pipelines employed as part of the CCS chain can present serious operational and safety challenges. For example, the resulting blockage of depressurising pipeline, or more likely, the blockage of the pressure relief valves can lead to pipeline over-pressurisation and possible rupture.

As part of the risk assessment of solid CO_2 formation in depressurising pipelines, flow models mainly based on the Homogeneous Equilibrium Mixture (HEM) assumption are being developed. However, as pointed out in the review of relevant studies (Sections 2.2.1.3 and 2.2.1.4, Chapter 2), although some interesting flow features associated with solid CO_2 formation such as pressure stabilisation at the triple point have been predicted by the developed models, their accuracy in predicting real pipeline decompression is not tested. The lack of necessary validation against experimental data may introduce uncertainties in quantifying the risk associated with solid CO_2 in pipes.

In this chapter, the development, verification and validation of a CO_2 pipeline decompression model for predicting CO_2 solid formation at any time and distance along the depressurising pipeline is presented. This chapter is organised as follows. Section 3.2 details the flow model formulation, including the conservation equations and the closure models for fluid/wall heat transfer and friction. In addition, a general discussion of the wave properties of the conservation equations is provided to aid the later analysis of the simulated results. Also, the boundary conditions and the pertinent fluid thermal property prediction methods such as for the speed of sound of two-phase and three-phase (vapour-liquid-solid) CO_2 mixtures are presented. The numerical technique for solving the conservation equations is given next in Section 3.3. It is noted that, in contrast to the centred scheme adopted in the study by Hammer et al. (2013) concerning solid CO_2 formation during pipeline decompression, an upwind scheme is implemented in this study. Upwind schemes are known to be less diffusive

than centred schemes and hence provide better accuracy especially at discontinuities or large gradients within the flow. The numerical difficulties associated with the speed of sound turning to zero at the triple point are also discussed and addressed.

In Section 3.4, verification of the flow model consisting of a Riemann problem test is carried out to test the model capability of predicting the wave propagation in a vapour-liquid-solid CO_2 flow. The resulting wave structure is discussed in detail with a particular focus on the impact of solid CO_2 formation. This is followed by model validation against experimental data obtained from a large-scale CO_2 pipeline depressurisation test. Conclusions are drawn in Section 3.5.

3.2 Theory

3.2.1 Flow Model

In order to describe the depressurisation of CO_2 in a pipeline upon failure, the following set of conservation equations is applied based on the HEM model (Section 2.1.2.2.1, Chapter 2):

$$\frac{\partial}{\partial \mathrm{t}}\boldsymbol{U}+\frac{\partial}{\partial x}\boldsymbol{F}(\boldsymbol{U})=\boldsymbol{\Psi} \tag{3.1}$$

where $\boldsymbol{U}$ is the vector of the conservative variables, $\boldsymbol{F}$ is the vector of the corresponding flux functions, and $\boldsymbol{\Psi}$ is vector of volumetric terms (for fluid/wall friction and heat transfer), respectively defined as:

$$\boldsymbol{U}=\begin{pmatrix}\rho\\ \rho u\\ \rho E\end{pmatrix},\boldsymbol{F}=\begin{pmatrix}\rho u\\ \rho u^2+p\\ \rho uE+pu\end{pmatrix},\boldsymbol{\Psi}=\begin{pmatrix}0\\ -2f\rho u^2/D_{w,in}\\ \left(-2f\rho u^3+4\dot{q}\right)/D_{w,in}\end{pmatrix} \tag{3.2}$$

All symbols have been defined previously in Sections 2.1.2.2.1 and 2.1.3, Chapter 2. The friction factor, f is computed following the Chen's correlation (Chen 1979) given in equation 2.60, Chapter 2, and the fluid/wall heat transfer flux, $\dot{q}$ is calculated following Rohsenow's correlation (Knudsen et al. 1997b) introduced in equation 2.49, assuming boiling is the major heat transfer mode between the fluid and the wall.

3.2.2 Hyperbolicity and the Elementary Wave Structure

As discussed in Section 2.1.6.1.1, Chapter 2, equation 3.1 is hyperbolic and has three eigenvalues, $\lambda_1 = u - c$, $\lambda_2 = u$, $\lambda_3 = u + c$, where c is the sound speed in the fluid. (Note the ordering of the eigenvalues differs from that in Section 2.1.6.1.) In view of equation 3.1, the classical wave structure from solving an Initial Value Problem (IVP) relevant to practical engineering flows is schematically shown in figure 3.1.

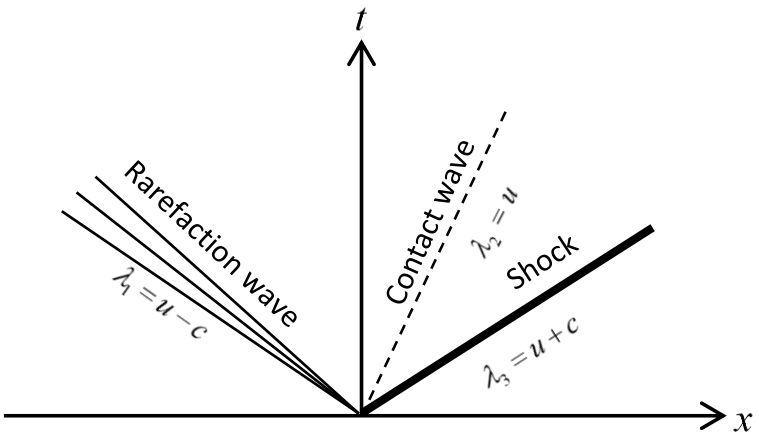

Figure 3.1: Schematic representation of the classical wave structure from solving equation 3.1 for an IVP.

As may be observed in figure 3.1, a left-running expansion wave and a right-running shock are separated by a contact wave. It should be noted that this classical wave structure in figure 3.1 applies only to the case where isentropes in the pressure-specific volume (p-v) thermodynamic plane, $(\partial p/\partial v)_s$ remain convex and smooth (Menikoff & Plohr 1989). Since isentropes are directly related to speed of sound, as shown below:

$$c = \sqrt{\left(\frac{\partial p}{\partial \rho}\right)_s} = \sqrt{\left(\frac{\partial p}{\partial v}\frac{\partial v}{\partial \rho}\right)_s} = v\sqrt{-\left(\frac{\partial p}{\partial v}\right)_s} \qquad 3.3$$

the speed of sound as a result must be continuous.

As shown by Menikoff & Plohr (1989), isentropes are smooth and convex if and only if the fundamental derivative, defined below remains positive everywhere:

$$\varsigma = -\frac{1}{2} v \frac{\left(\partial^2 p/\partial v^2\right)_s}{\left(\partial p/\partial v\right)_s} \qquad 3.4$$

On the other hand, non-classical wave structures, also known as anomalous wave structures, arise when ς becomes zero or undefined (often referred to as 'vanished'). This typically happens at phase transition boundaries where isentropes (in *p*-*v* plane) exhibit a discontinuous change in the slopes (and hence the speed of sound).

For example, Menikoff and Plohr (Menikoff & Plohr 1989) showed that in a real fluid, evaporation induced by decompression would produce a pair of rarefaction waves splitting at the corresponding saturated pressure.

3.2.3 Boundary Conditions

In order to close equation 3.1 to enable their numerical solutions, appropriate boundary conditions for describing the flow at both the pipe closed and rupture ends need to be specified.

At the closed end, the velocity is set to zero, whilst for scalar variables, zero-gradient extrapolation is applied.

Turning to the rupture end, where the flow is expected to be choked (sonic) during the most part of the decompression process, the boundary condition is determined from the analysis of local waves corresponding to the governing equations. Following Munkejord & Hammer (2015), the Riemann invariant across the right-running pressure wave reads (see also Section 2.1.6.1.3, Chapter 2):

$$u_{bc} = u_{mx} - \int_{p_{mx}}^{p_{bc}} \frac{dp}{\rho c} \qquad 3.5$$

where the subscripts, *bc* and *mx* represent the boundary numerical cell at the pipe release end and the cell adjacent to it, respectively. By assuming isentropic flow condition (i.e. $s_{bc} = s_{mx}$), ρ and c can be computed at a given pressure from flash

calculations. Knowing that the outflow is sonic (i.e. $u_{bc} = c_{bc}$), equation 3.5 can be solved for p_{bc}.

3.2.4 Physical Properties

In order to predict the thermal properties of CO_2 required for the HEM flow model, both GERG 2008 Equation of State (EoS) (Kunz & Wagner 2012) and ePR ('e' stands for 'extended') EoS (Martynov et al. 2013) are employed. The former is applied for the predictions of CO_2 above its triple point. Below the triple point, ePR EoS is employed which has been shown to produce good accuracy in handling solid phase CO_2 (Martynov et al. 2013).

The general HEM speed of sound is defined in equation 3.3. In the case of a vapour-liquid mixture, the HEM speed of sound is numerically approximated, given by (Mahgerefteh et al. 1999):

$$c = \left(\frac{\Delta p}{\rho(p,s) - \rho(p - \Delta p, s)} \right)^{0.5} \qquad 3.6$$

where Δp is the infinitesimal change in pressure ($\Delta p = 1 \times 10^{-6}$ bar; Mahgerefteh et al. 1999).

With regards to the vapour-liquid-solid mixture at the triple point, following the definition (equation 3.3), the speed of sound is zero. This implies that waves cannot propagate upstream of the triple-point region of the flow and hence, leading to unrealistic scenario of permanent pressure stabilisation at the triple point pressure (5.18 bar for CO_2).

To address the above, a suitable non-zero estimate for the speed of sound at the triple point is required. Accordingly, in this study, the speed of sound is calculated as:

$$\forall k = v, l, s; \quad \frac{1}{c^2} = \sum_k \frac{\alpha_k}{c_k^2} \tag{3.7}$$

Such an expression has been used to provide estimates for two-phase mixture speed of sound (Brown et al. 2013; Nouri-Borujerdi & Shafiei Ghazani 2017; De Lorenzo et al. 2017) and is often referred to as the 'Homogeneous Frozen Mixture (HFM)' speed of sound.

Equation 3.7 effectively removes the singularity at the triple point introduced by equation 3.3. The corresponding impacts on the predictions of the wave structure and furthermore, on the depressurisation of high-pressure CO_2 pipelines are presented and discussed in Section 3.4.

3.3 Numerical Method

Knowing the hyperbolicity of the conservation equation 3.1, the finite volume Godunov's method is adopted (LeVeque 2002). In this method, equation 3.1 is integrated over a control volume $\left[x_{i-1/2}, x_{i+1/2}\right] \times \left[t_n, t_{n+1}\right]$ as depicted in figure 3.2:

$$\int_{x_{i-1/2}}^{x_{i+1/2}} \boldsymbol{U}(x, t_{n+1}) dx = \int_{x_{i-1/2}}^{x_{i+1/2}} \boldsymbol{U}(x, t_n) dx + \int_{t_n}^{t_{n+1}} \boldsymbol{F}(\boldsymbol{U}(x_{i-1/2}, t) dt - \int_{t_n}^{t_{n+1}} \boldsymbol{F}(\boldsymbol{U}(x_{i+1/2}, t)) dt \tag{3.8}$$

where $x_{i-1/2}$ and $x_{i+1/2}$ are the coordinates of two adjacent cell interfaces i-1/2 and i+1/2, respectively.

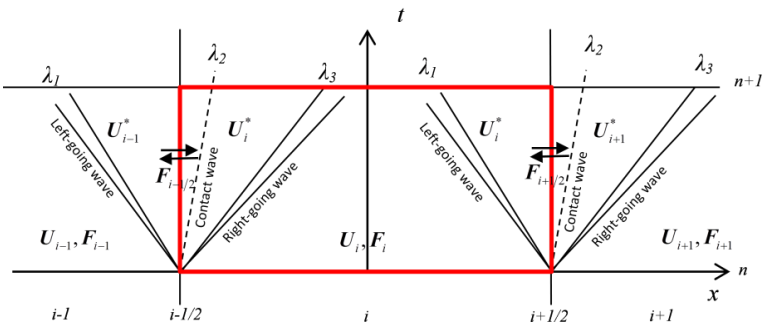

Figure 3.2: Schematic representation of the wave configuration emerging at cell

interfaces $i\pm1/2$ of the discretised computational cell $\left[x_{i-1/2}, x_{i+1/2}\right]$ over the time interval $\left[t_n, t_{n+1}\right]$. The superscript, * corresponds to the 'star regions' bounded by the left- and right-running waves.

Equation 3.8 can be rewritten as (see Section A3, Appendix):

$$\boldsymbol{U}_i^{n+1} = \boldsymbol{U}_i^n + \frac{\Delta t}{\Delta x}\left[\boldsymbol{F}_{i-1/2} - \boldsymbol{F}_{i+1/2}\right] \tag{3.9}$$

where $\boldsymbol{U}_i$ is the vector of averaged conservative variables in $\left[x_{i-1/2}, x_{i+1/2}\right]$, $\boldsymbol{F}_{i\pm1/2}$ is the so-called Godunov's fluxes evaluated at the cell interfaces (see figure 3.2), the timestep, Δt satisfies the CFL condition defined as:

$$CFL = \frac{\Delta t\left(\left(\left|u \pm c\right|\right)_{\max}\right)}{\Delta x} \leq 1 \tag{3.10}$$

In the current work, the Harten-Lax-van Leer-Contact (HLLC) approximate Riemann solver (Toro 2009e) is used to compute the required Godunov's fluxes. Its derivation can be found in Section A3, Appendix. The corresponding expression for $\boldsymbol{F}_{i-1/2}$ at interface $i-1/2$ is given by:

$$\boldsymbol{F}_{i-1/2} = \begin{cases} \boldsymbol{F}_{i-1}, & \text{if} \quad 0 \leq \lambda_1 \\ \boldsymbol{F}_{i-1} + \lambda_1\left(\boldsymbol{U}_{i-1}^* - \boldsymbol{U}_{i-1}\right), & \text{if} \quad \lambda_1 < 0 < \lambda_2 \\ \boldsymbol{F}_i + \lambda_3\left(\boldsymbol{U}_i^* - \boldsymbol{U}_i\right), & \text{if} \quad \lambda_2 \leq 0 < \lambda_3 \\ \boldsymbol{F}_i, & \text{if} \quad 0 \geq \lambda_3 \end{cases} \tag{3.11}$$

where:

$$\boldsymbol{U}_{i-1}^* = \rho_{i-1}\left(\frac{\lambda_1 - u_{i-1}}{\lambda_1 - \lambda_2}\right)\begin{bmatrix} 1 \\ \lambda_2 \\ \dfrac{E_{i-1}}{\rho_{i-1}} + \left(\lambda_2 - u_{i-1}\right)\left[\lambda_2 + \dfrac{p_{i-1}}{\rho_{i-1}\left(\lambda_1 - u_{i-1}\right)}\right] \end{bmatrix} \tag{3.12}$$

$$\boldsymbol{U}_i^* = \rho_i \left(\frac{\lambda_3 - u_i}{\lambda_3 - \lambda_2} \right) \begin{bmatrix} 1 \\ \lambda_2 \\ \dfrac{E_i}{\rho_i} + (\lambda_2 - u_i)\left[\lambda_2 + \dfrac{p_i}{\rho_i (\lambda_3 - u_i)} \right] \end{bmatrix} \quad 3.13$$

$$\lambda_2 = \frac{p_i - p_{i-1} + \rho_{i-1} u_{i-1} (\lambda_1 - u_{i-1}) - \rho_i u_i (\lambda_3 - u_i)}{\rho_{i-1} (\lambda_1 - u_{i-1}) - \rho_i (\lambda_3 - u_i)} \quad 3.14$$

Finally, the source term vector, $\boldsymbol{\Psi}$ in equation 3.1 is accounted for using the fractional splitting technique (LeVeque 2002).

3.4 Results and Discussion

3.4.1 Riemann Problem Tests

In order to verify the flow model developed above, a Riemann problem test is performed, where equation 3.1 is solved to obtain the flow profiles, numerically approximating the wave structure of the solution.

The simulation is performed for a 100 m long horizontal flow domain, initially filled with CO_2. The left half of the domain is at 250 K and 30 bar (in liquid phase), whilst the right half is at 250 K and 1 bar (in vapour phase) for the prevailing conditions, as summarised in table 3.1.

The flow domain is discretised uniformly into 2000 cells found to be sufficient to guarantee convergence (see figure A5.1, Appendix for the the grid convergence study results). The CFL number is set to be 0.5.

Table 3.1: Initial conditions of CO_2 in left and right part of the computational domain for the Riemann problem test.

Fluid property	**Left state (x<50 m)**	**Right state (x>50m)**
Pressure (bar)	30	1
Temperature (K)	250	250
Fluid phase	Liquid	Vapour

Figure 3.3 depicts the flow pressure and temperature profiles along the computational domain at 0.06 s following the start of the simulation. The predictions based on both equations 3.3 and 3.7 for calculating the fluid speed of sound at the triple point are presented. Also included in figure 3.3 (a) is a magnified plot for the boxed region of the pressure profile.

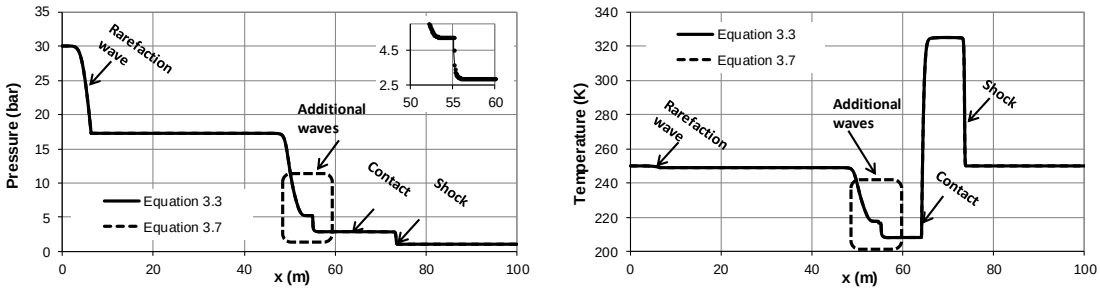

(a) (b)

Figure 3.3: Variations of pressure (a) and temperature (b) along the flow domain at 0.06 s following the start of the simulation for the Riemann problem test. The predictions based on equations 3.3 and 3.7 are overlapped.

Referring to figure 3.3, as it may be expected according to the classical wave structure (see figure 3.1), three waves emerge, including a rarefaction wave at ca. x = 5 m, a contact wave at ca. x = 65 m and a shock at x = ca. 75 m. The main features of these three classical waves are predicted consistently with those identified in Section 2.1.6.1.3, Chapter 2. In particular, across the rarefaction wave, all the flow properties change continuously and smoothly; across the contact wave, there is a discontinuous change in the temperature (and other related thermal properties such as density and entropy) while the pressure and velocity remain constant; across the shock wave, all the flow properties change discontinuously.

Interestingly, apart from these three waves, two additional waves respectively at ca. x = 50 m and x = 55 m can be observed in the left part of the domain (as marked by dashed-line box). They are separated from the most left rarefaction wave by two pressure plateaux, respectively at ca. 17 bar (saturated liquid) and 5.18 bar (the triple point) pressures (figure 3.3 (a)).

In order to verify the above finding, the model prediction is then compared to the wave structure obtained from an analytical analysis of the isentrope (at the entropy

value corresponding to the initial flow conditions at the left part of the simulated domain) in *p*-*v* plane following Menikoff & Plohr (1989).

Figure 3.4 shows *p*-*v* phase diagram for CO_2 with several isentropes crossing the two-phase equilibrium region and the triple point.

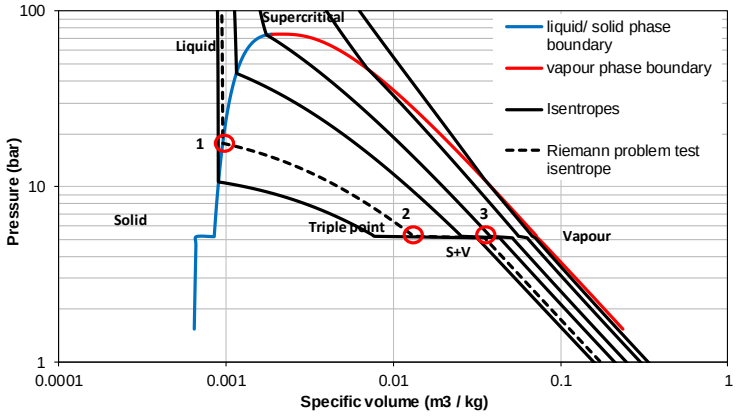

Figure 3.4: CO_2 *p*-*v* phase diagram, showing the phase boundaries and isentropes crossing the phase equilibrium regions; following the isentrope corresponding to the Riemann problem test (the dashed curve), points 1, 2 and 3 mark the vapour-liquid, triple point and solid-vapour phase transition boundaries, respectively.

Focusing on the isentrope presented by the dashed curve in figure 3.4, three points exist at which its slope changes discontinuously. In the order of appearance these include at the phase transition boundaries of vapour-liquid (point 1), the triple point (point 2), and solid-vapour (point 3).

Figure 3.5 shows the calculated fundamental derivative, ς along this isentrope. It can be seen that ς vanishes at points 1, 2 and 3, indicating the formation of anomalous waves.

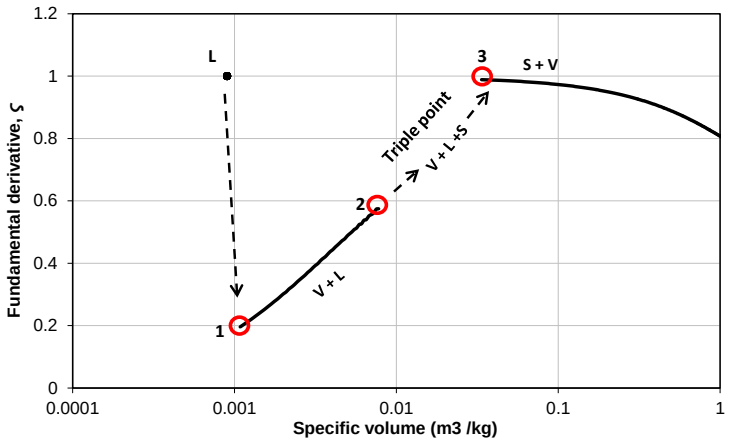

Figure 3.5: Fundamental derivative, ς (defined by equation 3.4) along the isentrope marked by dashed curve in figure 3.4; phase transition boundaries are marked and circled in red.

To determine the type of the anomalous waves emerging at these three points, the convexity of the isentrope across these points is examined. Referring to figure 3.5, on both sides of point 1 (representing pure liquid phase and vapour-liquid mixture), ς remains positive, and the convexity of the isentrope is preserved. As such, following Menikoff & Plohr (1989), at this phase transition boundary, the emerging wave is identified as a split rarefaction wave from the rarefaction wave at ca. x = 5 m (see figure 3.3).

As it also can be seen in figure 3.5, in contrast to point 1, ς vanishes both at and between points 2 and 3 where the fluid remains at the triple point. As such, the analysis applied above to identify the anomalous wave at point 1 cannot be directly extended to that for points 2 and 3. Alternatively, the nature of these waves may be partly determined by looking at the predicted decompression wave propagation speed profile near the triple point.

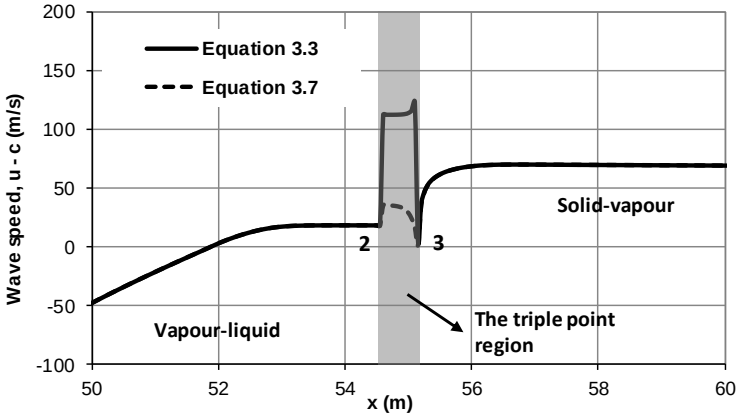

Figure 3.6: Predicted decompression wave speed profiles (corresponding to figure 3.3) in the proximity of the triple point based on both equations 3.3 and 3.7 for calculating the fluid speed of sound at the triple point.

Figure 3.6 shows the decompression wave speed profiles corresponding to figure 3.3 in the proximity of the triple point. As it can be seen in figure 3.6 for both speed of sound models, the predicted wave speeds only differ within the triple point region. The predicted wave speed beyond phase transition boundary at point 3 (in the solid-vapour mixture) increases rapidly and becomes significantly larger than that at point 2. This gives rise to a second split rarefaction wave, as can be observed in figure 3.3 (at ca. x = 55 m). Returning to figure 3.6, given that at the triple point the pressure remains constant, pure convection at flow velocity, u occurs, and the different wave speeds predicted by equations 3.3 and 3.7 have no impact on the solution of the Riemann problem. This is supported by a comparison between the two predicted profiles presented in figure 3.3, showing overlapped results.

The wave structure from the above analysis is shown in figure 3.7.

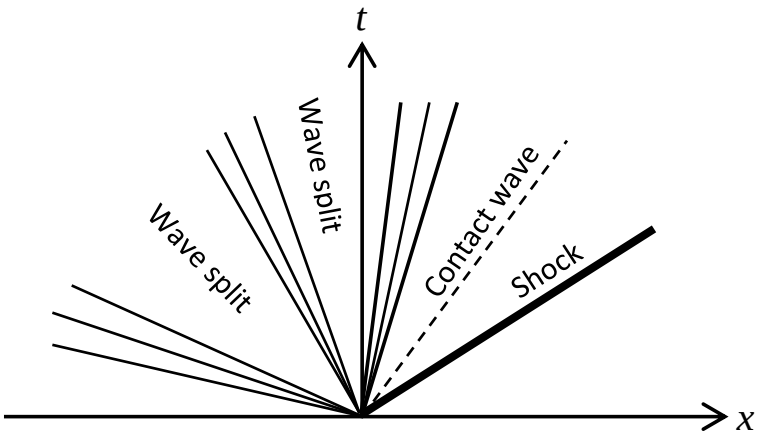

Figure 3.7: Schematic representation of the wave structure from solving equation 3.1 for the Riemann problem test defined in table 3.1.

It is also worth noting that the isentropes originating either in the liquid or supercritical phases all exhibit discontinuous changes at the previously discussed phase transition boundaries (see figure 3.4). Given that CO_2 is normally transported in the liquid or supercritical phases due to economic considerations, the numerically discovered anomalous waves are thus expected during the complete decompression of CO_2 transmission pipelines.

3.4.2 Model Validation

In the following, the flow model presented above is validated against measurements taken from a large-scale pipeline decompression experiment performed as part of the COOLTRANS UK National Grid project (Brown et al. 2015). The test involved the Full Bore Rupture (FBR) of a thermally insulated 144 m long, 150 mm i.d. and 11 mm wall thickness steel pipe containing liquid phase CO_2 initially at 5.25 ^{o}C (278.38 K) and 153.3 bar. The pipe was instrumented with fast response pressure and temperature transducers strategically placed along its length. The full details of the test set-up can be found in (Cosham et al. 2012).

Simulations are performed based on a computational domain of 500 discretised cells (further grid refinement produces little variance in the results; see figure A5.2, Appendix) and using a CFL number of 0.5.

Figure 3.8 shows the predicted and measured variations of pressure with time at the intact end of the test pipe during its decompression following FBR.

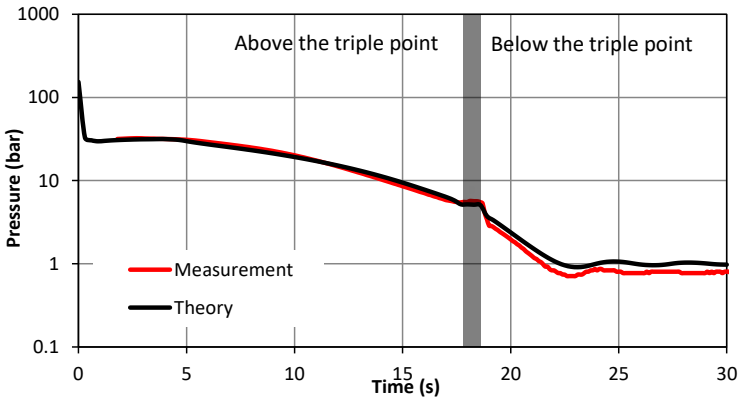

Figure 3.8: The variation of CO_2 intact end pressure with time during decompression. The shaded area shows the triple point location.

As it may be observed, theory and experiment are in excellent agreement. The initial rapid drop in pressure from 153.3 to 30 bar synonymous with FBR is followed by temporary pressure stabilisation at ca. 30 bar lasting for ca. 4.5 s. The latter corresponds to the split rarefaction wave at the vapour-liquid phase transition boundary (see Section 3.4.1).

Following this temporary stabilisation, the pressure gradually decreases until 18 s, where a second pressure plateau is observed at the CO_2 triple point (5.18 bar). This is attributed to the additional split rarefaction wave at the triple point phase transition boundary. As can be further observed from figure 3.8, after ca. 18 s, the depressurisation of two-phase solid−vapor mixture proceeds until reaching the ambient pressure.

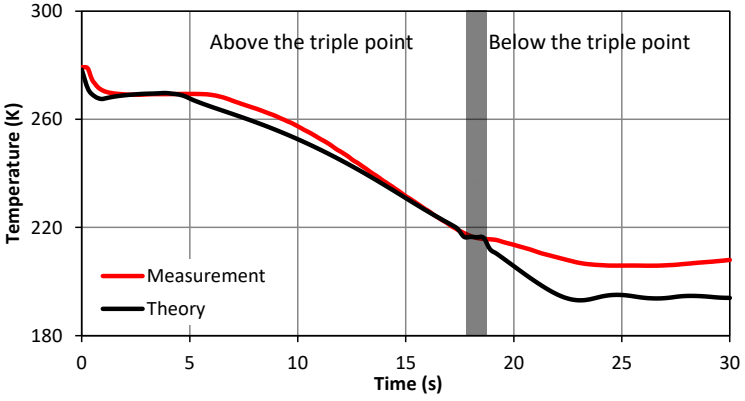

Figure 3.9: The variation of CO_2 intact end temperature with time during decompression. The shaded area shows the triple point location.

Figure 3.9 shows the corresponding variations of intact end temperature with time during decompression based on the measurements and model predictions. As it may be observed, the temperature profiles follow very similar trends as with the pressure profiles presented and discussed in figure 3.8. However, although theory and experiment are in good accord up to the triple point, the degree of agreement decreases beyond this point where the flow model under-predicts the CO_2 temperature by as much as ca. 12 K.

We postulate that the observed discrepancy is mainly a consequence of the extent of the validity of the HEM assumption embedded in the flow governing equation 3.1 in which the constituent fluid phases are assumed to be at thermal and mechanical equilibrium. Prior to surpassing the CO_2 triple point, the observed reasonably good agreement between theory and experiment indicates that such an assumption holds in this region. This is most likely due to the relatively high momentum and thus good mixing of the liquid and vapour phases such that inhomogeneity would be expected to be insignificant, that is, the flow is fully dispersed.

However, the passing of the triple point marks the formation of much denser solid CO_2 which separates and settles out of the solid-vapour mixture due to the gravitation. Thereafter, the fluid/wall heat transfer to the vapour phase may result in its superheated states (instead of saturated vapour predicted by the present model). Given that in the current study the fluid phase separation is not accounted for, this leads to the discrepancy observed between the present model temperature predictions and the measured data.

Figures 3.10 shows the variation of solid mass fraction along the pipe at different decompression times of 15.6, 17.4 and 19.2 s following FBR. The data indicates that by 15.6 s following rupture, approximately 35% of the total mass of the remaining CO_2 at the release end is in solid phase with the rest of the content upstream remaining in vapour phase. By 17.4 s following rupture (2.4 s later), the ‘solid front’ has propagated by approximately 30 m, reaching the pipe intact end at 19.2 s, where the percentage solid along the entire pipe length is approximately 30%.

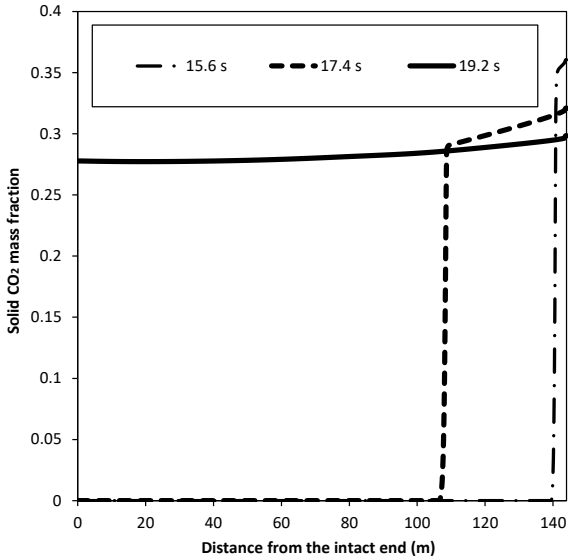

Figure 3.10: Variation of predicted solid phase CO_2 mass fraction along the pipeline at different decompression times following FBR.

As mentioned earlier, the solid-vapour phase separation is not accounted for in the current HEM flow model, and thus the predicted distributions of the solid CO_2 along the length of the pipe may be inaccurate. However, we may expect the HEM approximation to be applicable at the point of phase transition from vapour-liquid to vapour-liquid-solid at the triple point (i.e. at the solid front), providing valid estimates for the solid front propagation and the amount of solid CO_2 formed behind. Such information is vitally important as it directly governs the likelihood of pipeline or emergency pressure relief valve blockage.

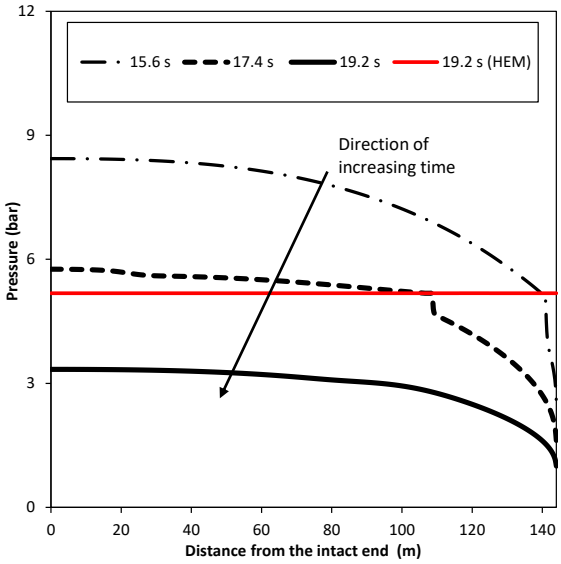

Figure 3.11: Variation of predicted pressure along the pipeline at different decompression times following FBR.

Figure 3.11 shows the corresponding pressure profiles along the pipeline at the same times following FBR as those in figure 3.10. The data based on the speed of sound calculated using equation 3.3 (as opposed to equation 3.7) at 19.2 s following FBR is also included indicating an unrealistic constant pressure throughout the entire pipeline length at the triple point pressure (5.18 bar). In contrast, the proposed model produces a continuous drop in pressure below the triple point. The discontinuities in pressure profiles at 15.6 and 17.4 s following FBR in figure 3.11 correspond to the phase transition from the triple point to solid-vapour mixture.

3.5 Concluding Remarks

Based on the results and analysis presented in this chapter, the following key conclusions may be made:

- A HEM flow model accounting for solid CO_2 formation as pipeline decompression across the triple point is developed;
- Model verification involving a Riemann problem test revealed emerging anomalous wave structure consisting of split rarefaction waves as a result of

phase transition. This is in agreement with the results obtained from the thermodynamic analysis performed as part of the study;

- Comparisons of the model predictions and the corresponding measurements for the variations of pressure and temperature as a function of time during decompression showed a good agreement. In particular, the experimentally observed temporal pressure stabilisation at the triple point pressure was successfully captured;
- The error in the temperature prediction was observed to grow systematically at the later stages of the decompression process (below the triple point), as heterogeneous flow may occur;
- As heterogeneous flow is currently not accounted for, for accurately predicting the solid CO_2 distributions along the length of the pipe, further study is required.

Chapter 4:
Modelling of Thermodynamic Non-Equilibrium during Decompression of CO_2-Rich Mixtures

4.1 Introduction

In Chapter 1, it was shown that delayed phase transition between the constituent fluid phases during rapid pipeline decompression leads to thermodynamic non-equilibrium. In the case of a non-equilibrium vapour-liquid mixture with superheated liquid phase, a faster decompression wave front and hence a higher decompression rate are expected (as compared to the corresponding Homogenous Equilibrium Mixture (HEM) system) before the constituent fluid phases return to equilibrium. Moreover, upon approaching the superheating limit (Section 2.1.4.4, Chapter 2), violent boiling in the liquid phase may lead to a catastrophic Boiling Liquid Expanding Vapour Explosion (BLEVE). As such, for the quantitative consequence assessment of pipeline decompression involving thermodynamic non-equilibrium, the HEM model is not applicable.

To address the above, the Homogeneous Relaxation Mixture (HRM) model is developed (see Section 2.1.2.2.2, Chapter 2). However, as pointed out in the review of the HRM model applications (Section 2.2.2, Chapter 2), although studies have shown to produce improved accuracy over the widely used HEM model in predicting multiphase flow where thermodynamic non-equilibrium becomes relevant, its application has been limited to single-component flows. Given that most pipe flows encountered in practice are multi-component mixtures (in the case of CCS mostly CO_2 containing N_2, O_2, H_2O), and the fact that even a small amount of impurities can change the fluid properties drastically (Mahgerefteh et al. 2012), such a limitation significantly restricts the practical applications of the HRM model.

In this chapter, the HRM model is extended to account for multi-component mixtures, which removes the previous limitation on its application in modelling thermodynamic non-equilibrium during rapid decompression. Given the focus of the present work being on CCS, CO_2-rich mixtures are chosen as the working fluid.

The chapter is organised as follows: Section 4.2 provides a description of the mathematical development of the model. In particular, the method for determining

superheated liquid states for a multi-component mixture is presented. The numerical method for solving the overall PDE system is given in Section 4.3. In Section 4.4, the developed model is validated against the measurements from three high-pressure pipeline decompression tests for CO_2-rich mixtures conducted by the UK National Grid during the course of the COOLTRANS project (Cosham et al. 2012). Conclusions are drawn in Section 4.5.

4.2 Theory

4.2.1 Homogeneous Relaxation Mixture (HRM) Model

Recalling Section 2.1.2.2.2, the basic form of the HRM model is once again presented:

$$\frac{\partial \rho}{\partial t} + \frac{\partial \rho u}{\partial x} = 0 \tag{4.1}$$

$$\frac{\partial \rho u}{\partial t} + \frac{\partial \left(\rho u^2/2 + p\right)}{\partial x} = -\frac{2 f \rho u^2}{D_{w,in}} \tag{4.2}$$

$$\frac{\partial \rho E}{\partial t} + \frac{\partial \left(\rho u E + p u\right)}{\partial x} = -\frac{2 f \rho u^3}{D_{w,in}} + \frac{4\dot{q}}{D_{w,in}} \tag{4.3}$$

$$\frac{\partial \rho \alpha}{\partial t} + \frac{\partial \rho u \alpha}{\partial x} = \rho \frac{\phi_{eq} - \phi}{\tau} \tag{4.4}$$

where ϕ is the vapour phase mass fraction. All other symbols have been defined previously (see Section 2.1.2.2.2, Chapter 2).

In the case of two-phase flow, the bulk mixture properties are defined as follows:

$$u = u_v = u_l \tag{4.5}$$

$$p = p_v = p_l \tag{4.6}$$

$$\rho = \alpha \rho_v + \left(1 - \alpha\right) \rho_l \tag{4.7}$$

$$e = \phi e_v + \left(1 - \phi\right) e_l \tag{4.8}$$

where the subscripts, *v* and *l* respectively denote the vapour and liquid fluid phases. Note that in equations 4.7 and 4.8:

$$\alpha \neq \alpha_{eq},\ \phi \neq \phi_{eq} \qquad 4.9$$

where the subscript, *eq* stands for thermodynamic equilibrium states.

Returning to the conservation equations 4.1 to 4.3, the friction factor, *f* is computed following the Chen's correlation given in Section 2.1.3.2, Chapter 2, and the fluid/wall heat transfer flux $\dot{q}$ is assumed negligible following Brown et al. (2013).

The transport equation 4.4 describes the evolution of α with the flow where the relaxation time, τ is given by (Angielczyk et al. 2010):

$$\tau = 2.15\times10^{-7}\left(\phi\frac{\rho}{\rho_v}\right)^{-0.54}\left(\frac{p_0-p}{p_c-p_0}\right)^{-1.76} \qquad 4.10$$

where p_c is the critical pressure of the mixture, and p_0 refers to as the saturated pressure at the (pipe) initial temperature. It is noted that, although this correlation has been successfully applied in predicting pure CO_2 pipe flow (Brown et al. 2013), its accuracy for CO_2-rich mixtures remains uncertain.

It is noteworthy that as already mentioned in Section 2.1.2.2.2, Chapter 2, equation 4.4 indicates an exponential tendency of the HRM system towards the HEM system as the flow develops at a rate governed by τ.

Finally, accounting for multi-component mixture flows, species transport can be modelled using the following equations:

$$\forall j = 1,2,3...J;\qquad \frac{\partial\rho\tilde{z}_j}{\partial t}+\frac{\partial\rho\tilde{z}_j u}{\partial x}=0 \qquad 4.11$$

where $\tilde{z}_j$ is the component *j* mass composition in the bulk mixture. Note that:

$$\forall j = 1,2,3...J;\qquad \tilde{z}_j = z_j\frac{M_j}{M} \qquad 4.12$$

where z_j is the corresponding molar composition. M and M_j are the molecular weight of the bulk mixture and component j, respectively.

The complete expression of the HRM model is given below in vector form for numerical purposes:

$$\frac{\partial}{\partial t}\boldsymbol{U}+\frac{\partial}{\partial x}\boldsymbol{F}\left(\boldsymbol{U}\right)=\boldsymbol{\Psi} \qquad 4.13$$

where, $\boldsymbol{U}$, $\boldsymbol{F}$ and $\boldsymbol{\Psi}$ are respectively the vectors of the conservative variables, the flux functions and the source terms given by:

$$\forall j=1,2,3...J\ ; \qquad 4.14$$

$$\boldsymbol{U}=\begin{pmatrix}\rho\\ \rho u\\ \rho E\\ \rho\alpha\\ \rho\tilde{z}_j\end{pmatrix},\ \boldsymbol{F}=\begin{pmatrix}\rho u\\ \rho u^2/2+p\\ \rho uE+pu\\ \rho\alpha u\\ \rho\tilde{z}_j u\end{pmatrix},\ \boldsymbol{\Psi}=\begin{pmatrix}0\\ -2f\rho u^2/D_{w,in}\\ \left(-2f\rho u^3+4\dot{q}\right)/D_{w,in}\\ \rho\left(\phi_{eq}-\phi/\tau\right)\\ 0\end{pmatrix}$$

4.2.2 Physical Properties

Referring to equation 4.13, its solution consists of ρ, u, e, α and $\tilde{z}_j$ (or z_j). Other flow properties of interest such as the temperature, pressure and speed of sound need to be computed through flash calculations. Their accurate predictions largely rely on the EoS employed.

In this study, GERG-2008 EoS (Kunz & Wagner 2012) as implemented in the commercialised thermodynamic package, REFPROP (Lemmon et al. 2010), is employed given its superior accuracy in predicting fluid phase equilibrium as compared to cubic EoS (figure 2.2, Chapter 2). In the case of the HEM model, standard density-energy (ρ-e) flash calculation (available in REFPROP) is performed to obtain the corresponding fluid thermal properties and phase equilibrium data. On the other hand for the HRM model, given the need of accounting for fluid non-equilibrium states, the flash calculation is re-formulated as presented in the following.

4.2.2.1 Multi-component Non-Equilibrium Flash Calculation

With known ρ, e and α from solving equation 4.13, the standard ρ-e flash calculation is first performed to determine the equilibrium state of the flow, including α_{eq} (ϕ_{eq}) and the corresponding component molar compositions in the vapour and liquid phases (denoted by $x_{j,sat}$ and $y_{j,sat}$, respectively).

Next, assuming that the vapour phase remains saturated at the prevailing pressure during decompression (whilst the liquid phase is superheated) (De Lorenzo et al. 2017; Nouri-Borujerdi & Shafiei Ghazani 2017), its density and internal energy can be expressed as a function of p and y_j:

$$e_v = e_{v,sat}\left(p, y_j\right) \tag{4.15}$$

$$\rho_v = \rho_{v,sat}\left(p, y_j\right) \tag{4.16}$$

Here, y_j is set to be equal to $y_{j,sat}$.

Turning to the liquid phase, with known ρ_v, e_v and α, solving equations 4.7 and 4.8 gives ρ_l and e_l. The liquid phase molar composition, x_j can be obtained from the material balance:

$$\forall j = 1,2,3...J; \qquad x_j = \frac{z_j - \beta y_j}{1-\beta} \tag{4.17}$$

where β is the vapour phase molar fraction ($\beta = \phi M / M_v$).

With the help of the selected EoS, the liquid phase density and internal energy can also be respectively expressed as:

$$\rho_l = \rho_{l,sh}\left(p, T_l, x_j\right) \tag{4.18}$$

and:

$$e_l = e_{l,sh}\left(p, T_l, x_j\right) \tag{4.19}$$

where the subscript, *sh* represents the superheated liquid state. It is noted that the temperature of the liquid phase, T_l differs from that of the vapour phase, T_v. The pressures of the vapour and liquid phases are however equal as mechanical equilibrium is assumed to be retained.

To this end, there exist 6 + *J* equations (4.7, 4.8, 4.15 to 4.19) and 6 + *J* unknowns (e_v, ρ_v, e_l, ρ_l, p, T_l and x_j). The non-linear algebraic system is closed, and both the saturated vapour and superheated liquid states are fully defined. The above non-linear system is solved with the numerical solver, DNSQE (Powell 1970) adopted in this study.

4.2.2.2 Two-Phase Mixture Speed of Sound

The speed of sound, *c* is one of the most important thermodynamic variables in determining the accuracy of a decompression flow model. As such, its predictive method for vapour-liquid two-phase mixtures is discussed separately in this section.

For the HEM model, the vapour-liquid mixture speed of sound is given by equation 3.6, Chapter 3.

In the case of the HRM model, according to Brown et al. (2013), the vapour-liquid mixture speed of sound is instead defined as:

$$\frac{1}{c^2} = \frac{\alpha}{c_v^2} + \frac{(1-\alpha)}{c_l^2} \qquad 4.20$$

4.3 Numerical Method

In this section, the solution strategy for the multi-component HRM model is presented. It can be shown that the corresponding PDEs are hyperbolic and hence exhibit wave behaviour (Bilicki & Kestin 1990). The general wave structure emerging at cell interface *i*-1/2 is displayed in figure 4.1.

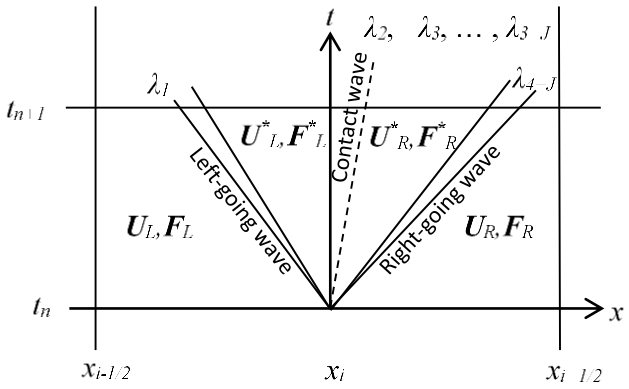

Figure 4.1: Schematic representation of the wave configuration emerging at cell interface *i*-1/2 between the discretised computational cells *i*-1 and *i* over the time interval $[t_n, t_{n+1}]$. The superscript, * corresponds to the 'star regions' bounded by the left- and right-running waves. λ denotes the wave speed of each wave listed.

From figure 4.1, it is evident that compared to the HEM model (see figure 2.6, Chapter 2), additional J+1 waves arise with the inclusion of the transport equations for α and $\tilde{z}_j$. As these quantities are passively advected by the bulk flow, the corresponding waves propagate at the same speed u (i.e. $\lambda_2 = \lambda_3 = \ldots = \lambda_{3+J}$), overlapping with the contact wave shown in figure 4.1 (LeVeque 1992).

With hyperbolicity, the PDEs are solved numerically using the Godunov's method in conjunction with the HLLC Riemann solver (Toro 2009; see also Section A3, Appendix). However, due to the emerging additional waves, modifications are introduced to the intermediate states, $\boldsymbol{U}^*$. Using $\boldsymbol{U}^*_{i-1}$ as an example, the corresponding intermediate state reads:

$$\boldsymbol{U}^*_{i-1} = \rho_{i-1}\left(\frac{\lambda_1 - u_{i-1}}{\lambda_1 - \lambda_2}\right)\begin{bmatrix} 1 \\ \lambda_2 \\ \dfrac{E_{i-1}}{\rho_{i-1}} + (\lambda_2 - u_{i-1})\left[\lambda_2 + \dfrac{p_{i-1}}{\rho_{i-1}(S_{i-1} - u_{i-1})}\right] \\ \alpha_{i-1} \\ \tilde{z}_{j=1,2,3\ldots,n} \end{bmatrix} \qquad 4.21$$

Thereafter, the cell interface flux, $\boldsymbol{F}_{i-1/2}$ (figure 4.1) can be calculated exactly following equation A3.16, Appendix.

4.4 Results and Discussion

In the following, the HRM model developed for predicting thermodynamic non-equilibrium during rapid pipeline decompression of multi-component mixtures is first tested by solving a specified Riemann problem (see equations 2.160 and 2.161, Chapter 2 for the definition of the Riemann problem).

Thereafter, the model is validated against three large-scale pipeline decompression tests for binary and ternary CO_2-rich mixtures carried out by National grid during the COOLTRANS project (Cosham et al. 2012). The predicted decompression wave curves and pressure/temperature variations as a function of time are compared to the corresponding measurements.

The above tests are repeated for the HEM model and the HRM model based on constant relaxation times (in replacement of equation 4.10) to demonstrate the significance of the relaxation time on the extent of thermodynamic non-equilibrium during pipeline decompression.

4.4.1 Riemann Problem Test

The Riemann problem test consists of vapour and liquid phase CO_2-N_2 binary mixture (4 mol% CH_4 + 96 mol% CO_2) initially separated by a diaphragm at the middle of an assumed 1 m length horizontal domain. The initial flow conditions left and right to the diaphragm are respectively set at 60 bar, 260 K (in liquid phase) and 10 bar, 260 K (in vapour phase). The diaphragm is removed at the start of the simulations to allow the initial discontinuity to evolve.

For simplicity, the fluid/wall friction terms are switched off. The computational domain is discretised into 500 equally-spaced cells (see figure A5.3, Appendix for the grid convergence test results), and the CFL number is fixed at 0.1.

To demonstrate the impact of the relaxation time on the Riemann problem solution, the above test is repeated for the HRM model based on constant relaxation times of 0.05, 0.1 and 0.2 ms as well as the HEM model (representing an infinitely small relaxation time).

The results are shown in figure 4.2 in terms of pressure, vapour molar fraction, density and velocity profiles along the domain length at 1 ms following the start of the simulation.

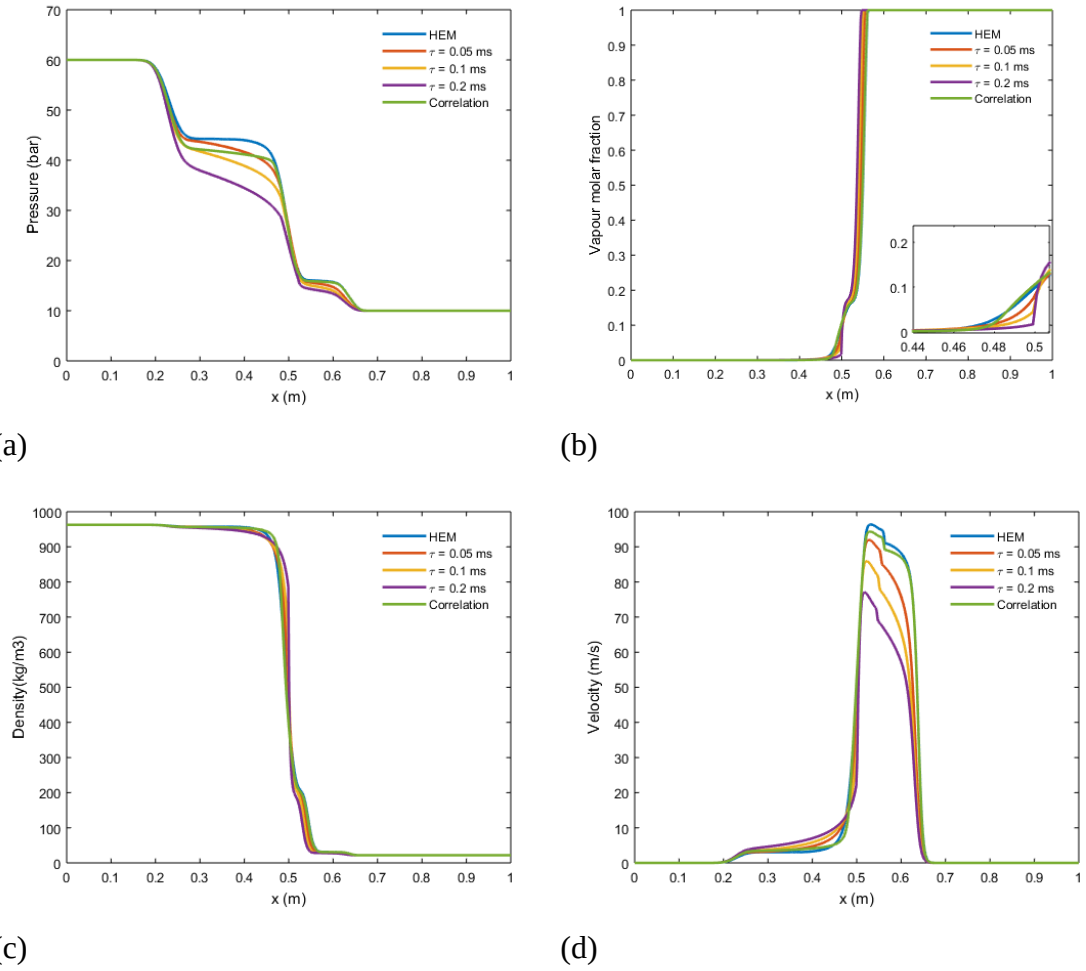

Figure 4.2: Predicted pressure (a), vapour mole fraction (b), density (c) and velocity (d) profiles along the domain length at 1 ms following the start of the simulation for the defined Riemann problem. The predictions from the HEM model and the HRM model based on τ of constant values as well as computed following equation 4.10 (the correlation) are all included.

In figure 4.2 (a), focusing on the decompression waves in the vapour-liquid two-phase flow between x = 0.2 to 0.5 m, a faster decompression wave can be observed as the relaxation time increases. This is attributed to the increased delay in phase transition (in this case, evaporation). Such delay can be clearly observed from the vapour molar fraction profile magnified between x = 0.4 to 0.5 m as shown in figure 4.2 (b). This is consistent with the observation made by Brown et al. (2013) for pure CO_2 flow. The predicted results using the correlation (equation 4.10) lies somewhere between the HEM model predictions and the HRM model predictions based on τ of 0.1 ms.

4.4.2 Model Validation

In the following section, the multi-component HRM model developed is employed to simulate three large-scale pipeline Full Bore Rupture (FBR) decompression tests for CO_2-rich mixtures performed by National grid during the COOLTRANS project (Cosham et al. 2012). These three tests involved an insulated 144 m length, 146.36 mm i.d. and 10.97 mm wall thickness carbon steel seamless pipe. The average roughness was 0.005 mm (see also Section 2.2.1.1). The details of the initial conditions for each test are presented in table 4.1.

Table 4.1: Initial conditions of the pipeline FBR decompression tests.

Test	Fluid pressure (bar)	Fluid temperature (K)	Impurity compositions	Fluid phase	Ambient pressure (bar)	Ambient temperature (K)
26	140.4	293.0	4.04 mol% N_2	Liquid	1.0	273.6
27	141.0	293.2	2.62 mol% H_2			273.6
28	140.6	293.1	4 mol% N_2 + 4.29 mol% H_2			274.3

FBR was initiated at one end of the test pipe whilst the other end remained intact during the decompression process. The pipe was instrumented with a total number of 35 pressure and 14 temperature transducers strategically distributed at various locations along its length. For the selected tests, the published measured data include the decompression wave curves at the interval of 3.64 to 6.04 m from the pipe release end, and the pressure and temperature evolutions at 143.78 m from the pipe release

end. For reference purposes, from here on, these two locations are respectively referred to as the open and close ends, respectively.

The model validation is performed in two parts. This involves comparing the predicted decompression wave curves at the open end, and the pressure and temperature evolutions at the closed end with the corresponding measurements.

All the simulations are performed based on a uniformly-spaced computational grid of 200 cells (see Section A5.4, Appendix for the grid convergence test results). The CFL factor is set to be constant at 0.1.

4.4.2.1 Decompression Wave Curves

In figure 4.3, the predicted open end pressure is plotted against the corresponding decompression wave speed during the simulated decompression period from the HEM model and the HRM models with various relaxation times. The resulting curve is referred to as the decompression wave curve often used for the construction of the Batelle two-curve for pipeline fracture propagation analysis (see (Aursand et al. 2016; Martynov et al. 2017) for examples). Also included are the corresponding measurements for comparison.

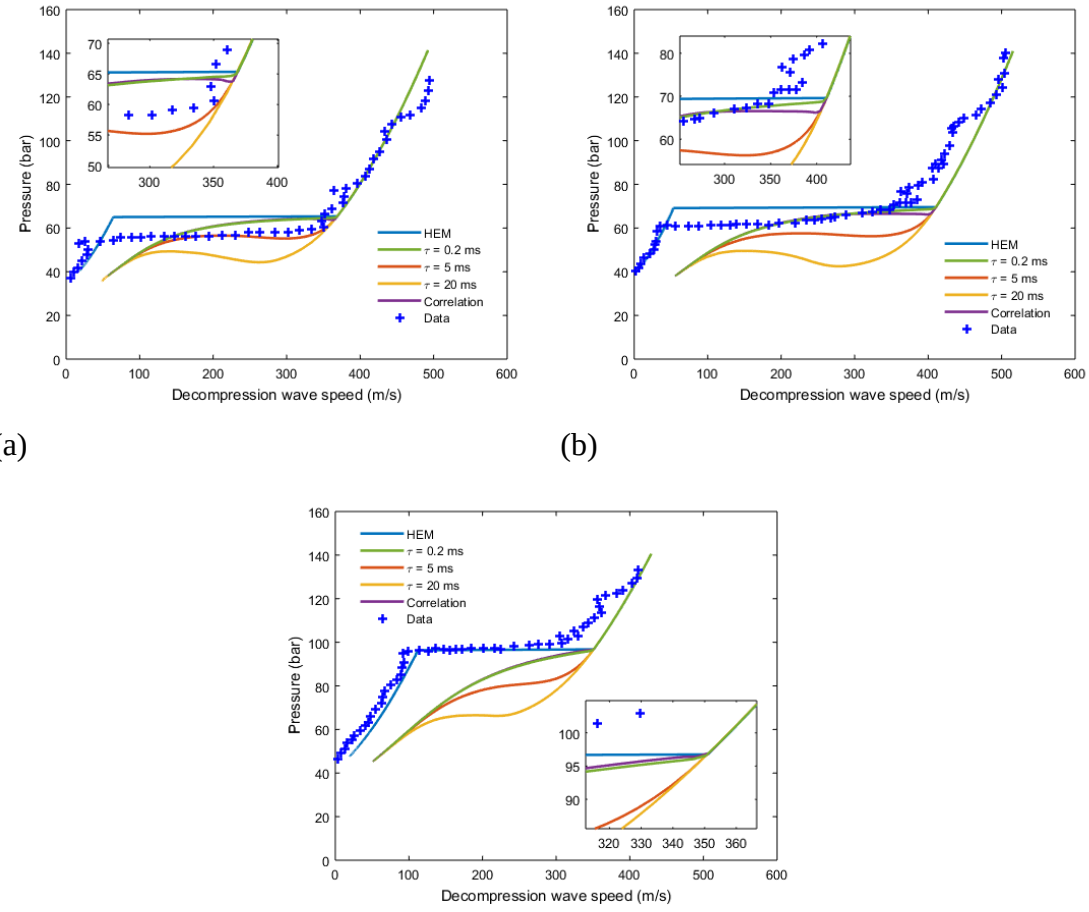

(a) (b)

(c)

Figure 4.3: Predicted (from the HEM model and the HRM model based on τ of constant values as well as computed following equation 4.10 (the correlation)) and measured decompression wave curves for tests 26 (a), 27 (b) and 28 (c) following FBR. Also included are the zoom-in views at the phase transition point.

Referring to the measured data, the decompression wave speed remains high (above 300 m/s) in liquid phase for all the multi-component mixtures tested. Upon phase transition, pressure plateaux are observed (respectively at ca. 54, 60 and 97 bar in figures 4.3 (a) to (c) for tests 26 to 28), while the decompression wave speed drops discontinuously. The observed trend is associated with the formation of the vapour phase which significantly reduces the mixture sound speed. In all cases, the decompression wave speed eventually approaches zero, which corresponds to the sonic flow conditions at the pipe open end.

Turning to the model predictions, prior to phase transition, both the HEM model and the HRM model based on different relaxation times produce a relatively good agreement with the measurements. This is to be expected as thermodynamic non-equilibrium plays no part at this stage of the decompression process.

However, at the onset of evaporation, the impact of non-equilibrium becomes apparent. In all cases, as the relaxation time, τ increases, a lower pressure plateau is predicted by the HRM model. The difference obtained as compared to the HEM model predictions reaches more than 30 bar (test 28, figure 4.3 (c)). In comparison to the measured data, for tests 26 and 27, the best fit with the measured data is observed for the HRM model based on τ = 5 ms. On the other hand, the HEM model over-predicts the pressure plateaux by more than 10 bar.

In addition, the HEM model under-predicts the decompression wave speed as compared to the HRM model (at any given pressures), which is further elucidated by plotting the pressure profiles along the entire pipe length at different decompression times for test 26, as shown in figure 4.4.

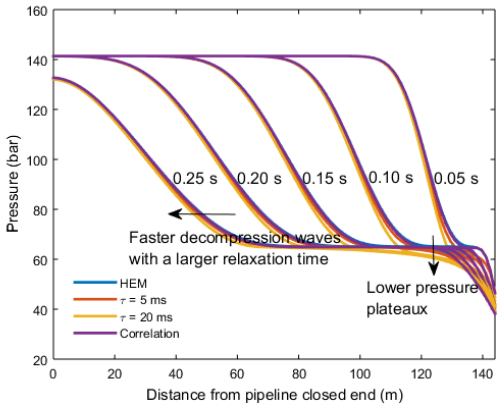

Figure 4.4: Predicted (from the HEM model and the HRM model based on τ of constant values as well as computed following equation 4.10 (the correlation)) pressure profiles along the pipe length at different decompression times for test 26 following FBR. Arrows point towards the direction of increasing relaxation time.

The under-prediction of the decompression wave speed from the HEM model can be significant e.g. for pipeline fracture propagation analysis, where this can lead to an over-estimation of the fracture length (Brown et al. 2013).

As decompression proceeds, it is interesting to note that the experimentally measured wave speeds are in close agreement with the HEM model predictions, and consistent over-predictions are observed for the HRM model. This indicates that, with significant phase transition, equation 4.20 for computing the speed of sound in the HRM model may become inaccurate, and equation 3.6, Chapter 3 may be used instead. In light of the above, the calculation of the speed of sound in the HRM model is modified, and the above simulations are repeated. The modification consists of changing the calculation of the speed of sound from equation 4.20 to equation 3.6 at $\phi \geq 0.01$ (which is determined to produce the best agreement between the theoretical predictions and the measured data in all cases tested). The corresponding simulated results are plotted in figure 4.5.

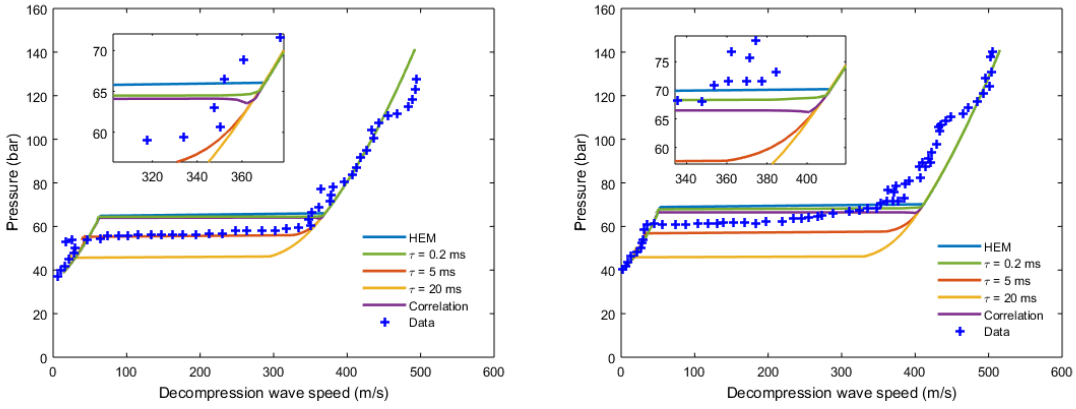

(a) (b)

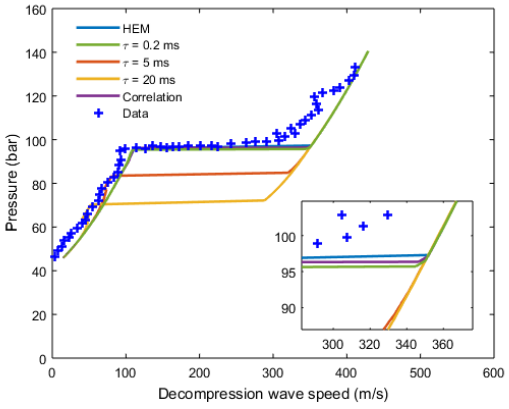

(c)

Figure 4.5: Predicted (from the HEM model and the HRM model based on τ of constant values as well as computed following equation 4.10 (the correlation)) and measured decompression wave curves for tests 26 (a), 27 (b) and 28 (c) following

FBR. The speed of sound calculation in the HRM model has been changed from equation 4.20 to equation 3.6, Chapter 3 at $\phi \geq 0.01$.

As it may be observed from figure 4.5, the accuracy of the wave speed predictions from the HRM model during the later stages of the decompression process is significantly improved, in agreement with the experimental data.

Returning to figure 4.3, it is noted that for all tests, τ computed following equation 4.10 is in the proximity of 0.2 ms. In the case of tests 26 and 27, with equation 4.10, the HRM model over-predicts the pressure plateaux (as compared to the measured data), whereas in the case of test 28, a relatively good agreement is obtained. This reveals the limitation of the direct application of equation 4.10 (based on pure CO_2) to CO_2-rich mixture flows. To address the above, equation 4.10 may be re-adjusted based on available experimental data as suggested by Angielczyk et al. (2010).

4.4.2.2 Variations of Pressure and Temperature against Time

The second part of validation includes comparisons between the predicted and the measured pressure and temperature variations as a function of time at the pipe close end during decompression. The results for tests 26 and 28 are presented in figures 4.6 and 4.8, respectively. Unfortunately, the measured transient pressure data during the first 2 s following FBR is not available.

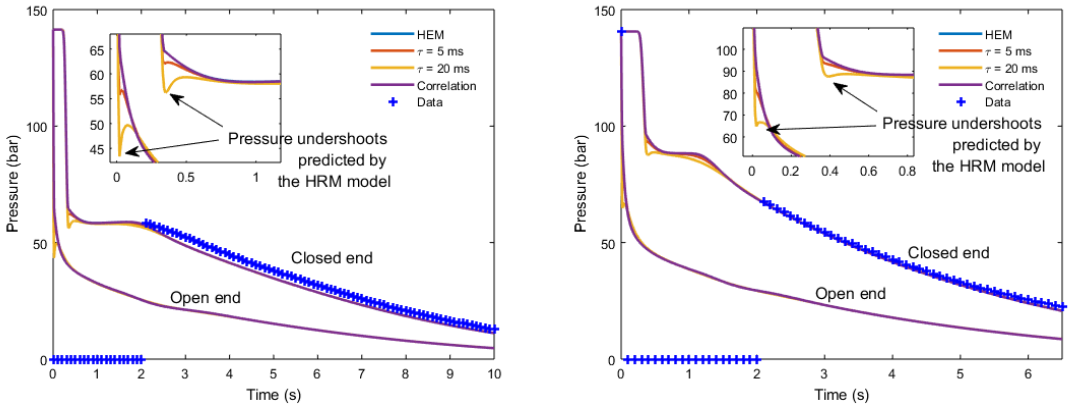

(a) (b)

Figure 4.6: Predicted (from the HEM model and the HRM model based on τ of constant values as well as computed following equation 4.10 (the correlation)) pressure variations as a function of time at the pipe open and closed ends and the measured data at the closed end for test 26 (a) and test 28 (b). Also included in the figures are the zoom-in views for the first 1 s following FBR.

As it can be seen in figure 4.6, the vapour-liquid phase transition boundary is marked by the sudden changes in the decompression rates both at the open and close ends of the pipe. Interestingly, in contrast to the HEM model, pressure undershoots are predicted by the HRM model, the magnitude of which increases with τ during the early stages of the depressurisation (ca. t = 0 to 0.5 s). This trend is explained by plotting the corresponding decompression trajectories on the pressure-temperature (p-T) phase diagrams as shown in figure 4.7.

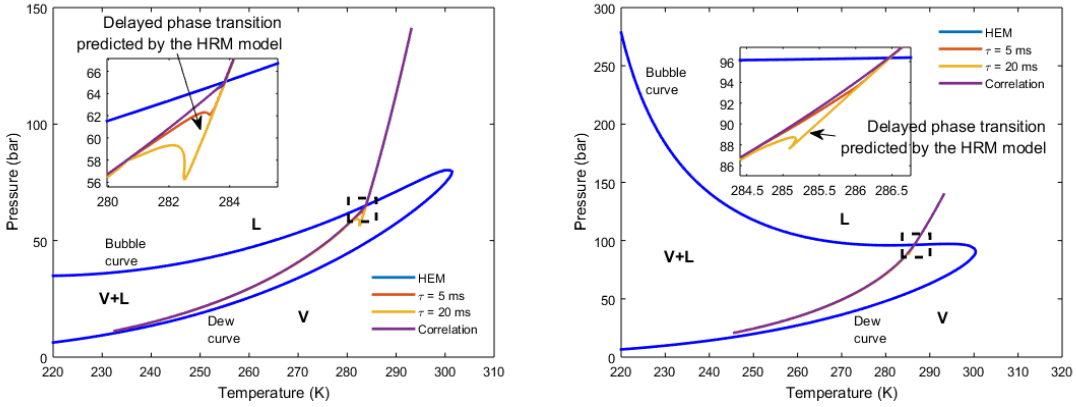

(a) (b)

Figure 4.7: Predicted decompression trajectories at the pipe close end for tests 26 (a) and 28 (b) in relation to the *p*-*T* phase diagrams. Also included in (a) and (b) are the zoom-in views near the phase transition boundaries (marked by the boxes).

From figure 4.7, as it may be observed for both cases, delayed phase transition results in the depressurising fluid to temporarily remain in liquid-like phase instead of forming an equilibrium vapour-liquid mixture (cf. the HEM and the HRM model predictions). As a result, pressure undershoots below the corresponding equilibrium (saturated) values (65 bar for test 26 and 95 bar for test 28) are observed in the HRM model predictions. As the decompression process continues, rapid phase transition occurs, coinciding with a pressure rebound towards the equilibrium values.

Returning to figure 4.6, after the HRM system approaches equilibrium, both model predictions are in-line with each other and in good agreement with the measurements.

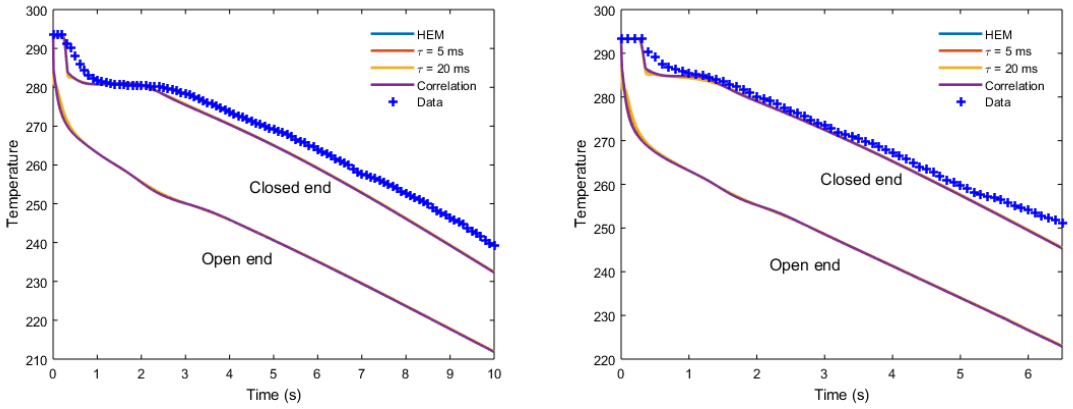

(a) (b)

Figure 4.8: Temperature variation with time for test 26 (a) and test 28 (b). The model predictions at both the open and close end and the measurements at the close end at different relaxation times are presented.

Moving on to the in-pipe temperature evolutions in figure 4.8, as it may be observed, throughout the entire duration of the decompression process considered, good agreement with the measurements is obtained by both the HEM and HRM models. The maximum error is +5 K.

4.4.2.3 Degree of Superheat

Another important safety concern arising due to thermodynamic non-equilibrium occurring during rapid pipeline decompression is the risk of a BLEVE. It is directly related to the degree of superheat in the liquid phase (computed as $T_l - T_v$) (Casal & Salla 2006). Such data predicted as a function of time at both the pipe open and close ends from the HRM model based on different relaxation times are presented in figure 4.9 for test 26, as an example.

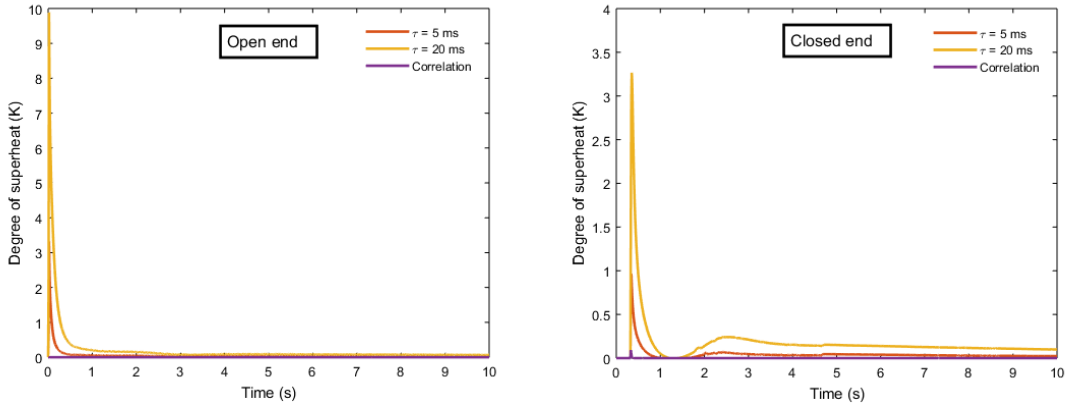

(a) (b)

Figure 4.9: predicted degree of superheat as a function of time at both the open (a) and close ends (b) during decompression for test 26.

From figure 4.9, as it may be observed, in accordance to the HRM model, superheating of the liquid phase is predicted at both the open and close ends for both tests. The degree of superheat increases with the extent of delayed phase transition (denoted by a larger relaxation time), and a maximum of 10 K is observed at the pipe open end (for τ = 20 ms). Minimal degree of superheat is predicted by the HRM model with τ computed following equation 4.10.

The data in figure 4.9 in conjunction with an appropriate explosion model can form the basis for quantifying the failure consequences in the event of a BLEVE occurring during rapid pipeline decompression, such as the explosion overpressure.

4.5 Concluding Remarks

Based on the results and analysis presented in this chapter and the ranges of the parameters investigated, the following key conclusions may be made:

- The HRM model has been successfully extended to simulate multi-component mixture flows occurring during rapid pipeline decompression;
- By performing the Riemann problem test, the wave structure in a multi-component mixture flow with thermodynamic non-equilibrium was revealed. The results indicated that delayed phase transition resulted in faster decompression waves and hence higher rates of decompression as compared to

the HEM model predictions. This observation agrees with the previous studies for single-component flow;

- The HRM model developed was validated against pipeline FBR decompression experiments for CO_2-rich mixtures. By comparing its predictions against the measurements for the decompression wave curves as well as the recorded variations of pressure and temperature as a function of time, overall, it was shown that improved accuracy could be obtained as compared to the HEM model;
- Superheating in the liquid phase was captured by the HRM model at both the pipe open and closed ends during decompression. Its magnitude increased with an increase in delayed phase transition (marked by an increase in the relaxation time). The results indicated the risk of a BLEVE occurring;
- The study also revealed the limitation of the HRM model due to the lack of suitable closure relations for computing the relaxation times for multi-component mixtures.

Chapter 5:

Modelling of Heterogeneous Flow during CO_2 Pipeline Puncture Decompression

5.1 Introduction

So far, the main focus of the work presented has been on studying pipeline Full Bore Rupture (FBR) failures. Another possible failure mode encountered in practice is pipeline puncture. Although in comparison to pipeline FBR failure, pipeline puncture failure is much less catastrophic (given that the release flowrate of hazardous materials is much less), its significantly higher failure rate requires equal attention when performing quantitative failure consequence assessment for high-pressure transmission pipelines.

As explained in Chapter 1, during pipeline puncture decompression, vapour-liquid phase separation (stratification) occurs (see figure 5.1). Such heterogeneous flow behaviour was observed to result in significant temperature difference between the two phases (referred to as thermal stratification) during the course of the CO_2QUEST project.

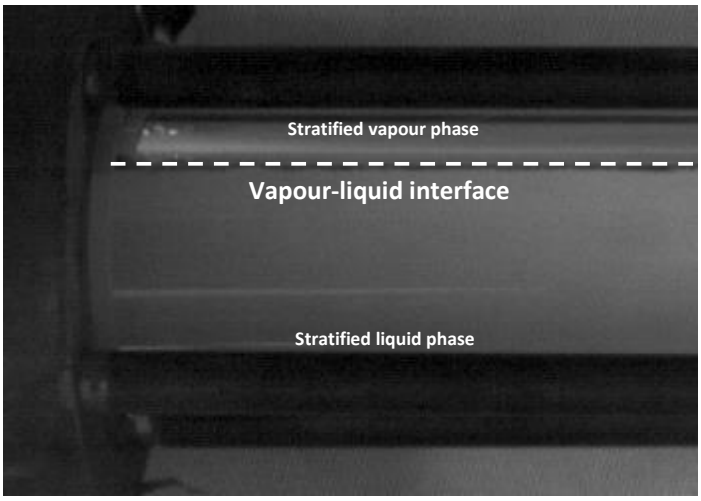

Figure 5.1: Photograph of vapour-liquid phase separation taken during a CO_2 pipeline puncture decompression test as part of the CO_2QUEST project (Solomon Brown et al. 2014).

Such flow behaviour invalidates the Homogenous Equilibrium Mixture (HEM) assumption.

Given the above, heterogeneous flow during pipeline puncture decompression must be considered when developing appropriate flow models for the safety assessment. With reference to the literature review (Section 2.1.2.2.4, Chapter 2), such a phenomenon may be accounted for by applying the Two-Fluid Mixture (TFM) model, which involves solving the mass, momentum and energy conservation equations separately for each fluid phase. However, as pointed out in the review of the TFM model applications in pipeline decompression studies (Section 2.2.4.3, Chapter 2), its current development is limited to pipeline FBR decompression, and thus its applicability in predicting pipeline puncture decompression remains uncertain.

In this chapter, the TFM model is extended to enable the modelling of puncture-induced depressurising pipe flow. Such extension is made via the construction of a puncture outflow boundary condition. In addition, a numerical scheme is developed aiming at improving the stability and accuracy of the existing scheme for solving the TFM model at locations within the two-phase flow where fluid phase volume fractions change rapidly.

The study is organised as follows: Section 5.2 presents the basic mathematical formulation of the flow model and the closure relations for modelling the fluid-fluid interface mass, momentum and energy exchange. The development of the puncture outflow boundary condition for the TFM model is also presented in the same section. Section 5.3 commences with a detailed discussion on a widely used numerical scheme for the solution of the TFM model. This is followed by a description of the modifications introduced in the present study. In Section 5.4, the modified scheme is tested by performing a series of standard numerical experiments. Thereafter, the model developed is validated by comparing the predicted temperature and pressure variations as a function of time for two CO_2 pipeline puncture decompression tests against the measured data. In addition, the impact of fluid phase separation on decompression characteristics (e.g. pressure and temperature) is shown by comparing the TFM model predictions to those from a HEM model. Conclusions are drawn in the last section.

5.2 Theory

5.2.1 Two-Fluid Mixture (TFM) Flow Model

In developing the pipeline puncture decompression model, both the stratified vapour and liquid phases are assumed to be compressible, and the depressurising flow is assumed to be one-dimensional. Furthermore, pressure relaxation is neglected (which leads to equal phasic pressures). The resulting six-equation Two-Fluid Mixture (TFM) model hence reads (see also Section 2.1.2.2.4, Chapter 2):

$$\frac{\partial \alpha_v \rho_v}{\partial t} + \frac{\partial \alpha_v \rho_v u_v}{\partial x} = \Gamma \tag{5.1}$$

$$\frac{\partial \alpha_l \rho_l}{\partial t} + \frac{\partial \alpha_l \rho_l u_l}{\partial x} = -\Gamma \tag{5.2}$$

$$\frac{\partial \alpha_v \rho_v u_v}{\partial t} + \frac{\partial \left(\alpha_v \rho_v u_v^2 + \alpha_v p \right)}{\partial x} = F^{\text{int}} + u^{\text{int}} \Gamma + F_{w,v} \tag{5.3}$$

$$\frac{\partial \alpha_l \rho_l u_l}{\partial t} + \frac{\partial \left(\alpha_l \rho_l u_l^2 + \alpha_l p \right)}{\partial x} = -F^{\text{int}} - u^{\text{int}} \Gamma + F_{w,l} \tag{5.4}$$

$$\frac{\partial \alpha_v \rho_v E_v}{\partial t} + \frac{\partial \left(\alpha_v \rho_v u_v E_v + \alpha_v p u_v \right)}{\partial x} + p \frac{\partial \alpha_v}{\partial t} = \Gamma H_{v,l} + F^{\text{int}} u^{\text{int}} + \dot{Q}_v \tag{5.5}$$

$$\frac{\partial \alpha_l \rho_l E_l}{\partial t} + \frac{\partial \left(\alpha_l \rho_l u_l E_l + \alpha_l p u_l \right)}{\partial x} + p \frac{\partial \alpha_l}{\partial t} = -\Gamma H_{v,l} - F^{\text{int}} u^{\text{int}} + \dot{Q}_l \tag{5.6}$$

where $H_{v,l}$ is the total enthalpy ($H_{v,l} = h_{v,l} + u_{v,l}^2 / 2$) of each fluid phase. The subscripts, *v* and *l* denote vapour and liquid phases, respectively. The phasic volume fractions additionally fulfil:

$$\alpha_l + \alpha_v = 1 \tag{5.7}$$

In the mass conservation equations 5.1 and 5.2, the net rate of interface mass exchange per volume, Γ is determined by:

$$\Gamma = \Gamma_l + \Gamma_v \tag{5.8}$$

where Γ_l denotes the mass transfer from the liquid phase to the vapour phase (positive), while Γ_v represents the mass transfer from the vapour phase to the liquid phase (negative). Following Wen et al. (2016):

$$\Gamma_l = \frac{\alpha_l \rho_l}{\tau} \frac{p_{l,sat} - p}{p_{l,sat}} \tag{5.9}$$

$$\Gamma_v = \frac{\alpha_v \rho_v}{\tau} \frac{p_{v,sat} - p}{p_{v,sat}} \tag{5.10}$$

In the above equations, the subscript, *sat* represents the saturated states for the simulated vapour and liquid phases. τ is the relaxation time. Thermodynamic non-equilibrium is not considered in this study.

Turning to the momentum conservation equations 5.3 and 5.4, the first term on the RHS, F^{int} represents the interface momentum exchange due to the interface pressure force, $F_{p^{\text{int}}}$ and drag force, F_d. The interface pressure force is given by equation 2.175, Chapter 2. For the interface drag force, F_d is expressed as (Taitel & Dukler 1976):

$$F_d = \tilde{A}^{\text{int}} \frac{C_d \rho_v \left(u_v - u_l\right) \left|u_v - u_l\right|}{2} \tag{5.11}$$

where $\tilde{A}^{\text{int}}$ and C_d are respectively the interface area per unit volume and the drag coefficient. For stratified flow with an assumed flat interface (Taitel & Dukler 1976):

$$\tilde{A}^{\text{int}} = \frac{4\sqrt{1-\left(2D_l/D_{w,in}-1\right)^2}}{\pi D_{w,in}} \tag{5.12}$$

where D_l and $D_{w,in}$ are respectively the liquid phase elevation and the pipe inner diameter (see figure 2.1, Chapter 2). Returning to equation 5.11, the drag coefficient for stratified flow is given by Taitel & Dukler (1976):

$$C_d = 0.046\,\text{Re}_v^{-0.2} \tag{5.13}$$

where Re_v is the vapour phase Reynolds number.

The second term on the RHS of equations 5.3 and 5.4 accounts for the momentum exchange due to mass exchange, where the interface velocity, u^{int} is given by equation 2.178, Chapter 2. The last term corresponds to the fluid/wall friction force in each fluid phases, given by equations 2.65 and 2.66, Chapter 2.

Moving on to the RHS of the energy conservation equations 5.5 and 5.6, the first term describes energy exchange associated with mass exchange. The second term corresponds to the work done by the interface forces (including the interphase pressure force and drag force). The last term accounts for fluid/wall heat transfer in each fluid phase. The corresponding volumetric heat sources, $\dot{Q}_v$ and $\dot{Q}_l$ are computed by assuming forced convection and nucleate boiling as the dominating heat transfer modes respectively in the vapour and liquid phases, following equations 2.56 and 2.58, Chapter 2.

5.2.2 Boundary Conditions

In order to close the conservation equations 5.1 to 5.6, suitable boundary conditions must be specified. In this study, the boundary conditions are implemented by introducing 'ghost cells' at both ends of the computational domain, representing the pipe closed and release ends.

At the closed end, the velocity in the added ghost cell is set to be zero, whilst the scalar variables are equated to the corresponding values at the adjacent cell centre within the computational domain.

At the release end, figure 5.2 is a schematic representation of the flow through the puncture.

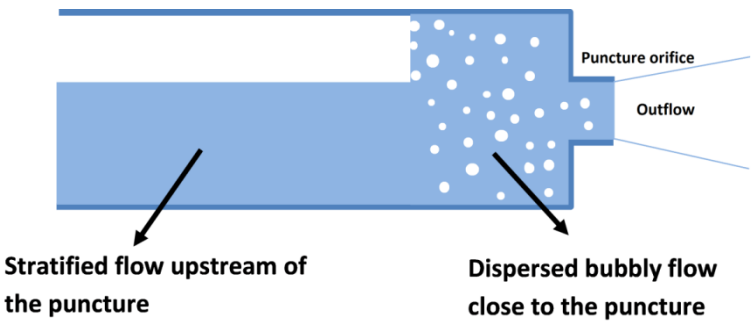

Figure 5.2: Schematic representation of the flow through the puncture.

From figure 5.2, it can be seen that the flow area changes significantly from the pipeline to the puncture orifice. The flow accelerates until becoming sonic (choked) at the puncture orifice. The development of the required boundary condition for simulating the above is detailed below.

According to Brown et al. (2013), during pipeline puncture decompression, in the proximity of the puncture, the vapour and liquid phases are dispersed due to relatively high velocity (as illustrated in figure 5.2). Given the above, the HEM assumption is applied in the ghost cell at the release end. The corresponding HEM model conservation equations are presented in Section 2.1.2.2.1, Chapter 2.

Next, the flow at the puncture orifice is further assumed to be adiabatic and frictionless (Richardson et al. 2006). As a result, the energy conservation equation can be neglected, and the remaining mass and momentum conservation equations are rewritten as (Thompson 1987; Thompson 1990):

$$\frac{\partial \rho}{\partial t} + \left(\frac{\zeta_1 + \zeta_2}{2} \right) = 0 \qquad 5.14$$

$$\frac{\partial u}{\partial t} + \frac{c}{\rho} \left(\frac{\zeta_2 - \zeta_1}{2} \right) = 0 \qquad 5.15$$

Herein, ζ is referred to as the wave amplitude, for which the generic expressions are given by:

$$\zeta_1 = (u - c) \left(\frac{\partial \rho}{\partial x} - \frac{\rho}{c} \frac{\partial u}{\partial x} \right) \qquad 5.16$$

$$\zeta_2 = (u + c) \left(\frac{\partial \rho}{\partial x} + \frac{\rho}{c} \frac{\partial u}{\partial x} \right) \qquad 5.17$$

Following Thompson (1987), modifications to equations 5.16 and 5.17 may be required at the flow boundaries. In our case, ζ_1 needs to be specified in accordance with the flow acceleration through the variable flow areas (from the pipeline to the puncture orifice).

Multiplying equation 5.14 by *u* and equation 5.15 by ρ gives:

$$u\frac{\partial \rho}{\partial t}+u\left(\frac{\zeta_1+\zeta_2}{2}\right)=0 \qquad 5.18$$

$$\rho\frac{\partial u}{\partial t}+c\left(\frac{\zeta_2-\zeta_1}{2}\right)=0 \qquad 5.19$$

By adding equations 5.18 and 5.19, the following equation is derived:

$$\zeta_1=\frac{1}{u-c}\left[-2\frac{\partial \dot{m}}{\partial t}-(u+c)\zeta_2\right] \qquad 5.20$$

Where, $\dot{m}=\rho u$. In equation 5.20, ζ_2 is a known quantity from equation 5.17, and the derivative of the mass flux with respect to time is approximated by:

$$\frac{\partial \dot{m}}{\partial t}\cong\frac{1}{\Delta t}\left[\dot{m}\big|_n-\dot{m}\big|_{n-1}\right] \qquad 5.21$$

where the subscripts, *n*-1 and *n* respectively denote the previous and current timesteps. $\dot{m}\big|_n$ is given by:

$$\dot{m}\big|_n=\frac{(\rho uA)_{up}\big|_n}{A_{up}}\cong\frac{(\rho uA)_{orifice}\big|_n}{A_{up}}=\frac{A_{orifice}}{A_{up}}(\rho u)_{orifice}\big|_n \qquad 5.22$$

where the subscripts, *orifice* and *up* respectively represent the flow at the puncture orifice and its upstream. $(\rho u)_{orifice}$ is computed following Section 3.2.3, Chapter 3.

Finally, equations 5.14 and 5.15 can now be readily solved for a complete description of the flow conditions in the ghost cell at the pipe release end. It is noted here that the developed boundary condition is also directly applicable to the HEM model.

5.2.3 Thermodynamics

In this study, the fluid thermal properties and phase equilibrium data are computed using Peng-Robinson (PR) Equation of State (EoS) (Peng & Robinson 1976). PR EoS has been extensively applied and validated in pipeline decompression studies especially for CO_2 (Mahgerefteh et al. 2012; Brown et al. 2013; S. Brown et al. 2014).

5.3 Numerical Method

5.3.1 AUSM+-up Flux Splitting Scheme

In this section, the AUSM flux splitting scheme first proposed by Paillère et al. (2003) for solving hyperbolic conservation equations 5.1 to 5.6 is summarised.

As a first step, equations 5.1 to 5.6 are written in vector form:

$$\frac{\partial \boldsymbol{U}}{\partial t}+\frac{\partial \boldsymbol{F}}{\partial x}=\boldsymbol{C}^{nv}+\boldsymbol{S} \tag{5.23}$$

where:

$$\boldsymbol{U}=\begin{pmatrix}\alpha_v\rho_v\\ \alpha_l\rho_l\\ \alpha_v\rho_v u_v\\ \alpha_l\rho_l u_l\\ \alpha_v\rho_v E_v\\ \alpha_l\rho_l E_l\end{pmatrix},\ \boldsymbol{F}=\begin{pmatrix}\alpha_v\rho_v u_v\\ \alpha_l\rho_l u_l\\ \alpha_v\rho_v u_v^2+\alpha_v p\\ \alpha_l\rho_l u_l^2+\alpha_l p\\ \alpha_v\rho_v u_v H_v\\ \alpha_l\rho_l u_l H_l\end{pmatrix}, \tag{5.24}$$

$$\boldsymbol{C}^{nv}=\begin{pmatrix}0\\ 0\\ (p-\Delta p)\dfrac{\partial \alpha_v}{\partial x}\\ (p-\Delta p)\dfrac{\partial \alpha_l}{\partial x}\\ -p\dfrac{\partial \alpha_v}{\partial t}-u^{\text{int}}\Delta p\dfrac{\partial \alpha_v}{\partial x}\\ -p\dfrac{\partial \alpha_l}{\partial t}-u^{\text{int}}\Delta p\dfrac{\partial \alpha_l}{\partial x}\end{pmatrix},\ \boldsymbol{S}=\begin{pmatrix}0\\ 0\\ u^{\text{int}}\Gamma+F^d+F_v^{wall}\\ -H_l\Gamma-F^d+F_l^{wall}\\ H_{v,l}\Gamma+u^{\text{int}}F^d+\tilde{A}^{\text{int}}q^{\text{int}}+\tilde{A}^v q_v^{wall}\\ -H_{v,l}\Gamma-u^{\text{int}}F^d-\tilde{A}^{\text{int}}q^{\text{int}}+\tilde{A}^v q_l^{wall}\end{pmatrix}$$

Following Paillère et al. (2003), the discretised form is given by:

$$\boldsymbol{U}_i^{n+1} = \boldsymbol{U}_i^n + \frac{\Delta t}{\Delta x}\left(\boldsymbol{F}_{i-1/2} - \boldsymbol{F}_{i+1/2}\right) + \Delta t\left(\boldsymbol{C}_i^{nv}\right) + \Delta t\left(\boldsymbol{S}_i\right) \quad 5.25$$

where n and i respectively represent the n^{th} timestep and i^{th} numerical cell in the computational domain. $i\pm1/2$ denotes the left/right cell interface.

The next task at hand is to compute the interface flux, $\boldsymbol{F}_{i\pm1/2}$. The interface flux for k^{th} fluid phase can be split into the advection flux, $\left(\boldsymbol{A}_k\right)_{i+1/2}$ and the pressure flux, $\left(\boldsymbol{P}_k\right)_{i+1/2}$, such that:

$$\left(\boldsymbol{F}_k\right)_{i+1/2} = \begin{pmatrix} \alpha_k\rho_k u_k \\ \alpha_k\rho_k u_k^2 + \alpha_k p \\ \alpha_k\rho_k u_k H_k \end{pmatrix}_{i+1/2} = \left(\boldsymbol{A}_k\right)_{i+1/2} + \left(\boldsymbol{P}_k\right)_{i+1/2} = \quad 5.26$$

$$\left(\dot{m}_k\right)_{i+1/2}\begin{pmatrix} 1 \\ u_k \\ H_k \end{pmatrix}_{i+1/2} + \begin{pmatrix} 0 \\ \alpha_k p \\ 0 \end{pmatrix}_{i+1/2}$$

Here, $\left(\dot{m}_k\right)_{i+1/2}$ is the cell interface mass flux, given by:

$$\left(\dot{m}_k\right)_{i+1/2} = \quad 5.27$$

$$\left(a_k\right)_{i+1/2}\left(\left(\alpha_k\rho_k\right)_i \frac{\left(M_k\right)_{i+1/2} + \left|\left(M_k\right)_{i+1/2}\right|}{2} + \left(\alpha_k\rho_k\right)_{i+1}\frac{\left(M_k\right)_{i+1/2} - \left|\left(M_k\right)_{i+1/2}\right|}{2}\right)$$

where:

$$\left(a_k\right)_{i+1/2} = \sqrt{\left(a_k\right)_i\left(a_k\right)_{i+1}} \quad 5.28$$

$$\left(M_k\right)_i = \frac{\left(u_k\right)_i}{\left(a_k\right)_{i+1/2}} \quad 5.29$$

$$\left(M_k\right)_{i+1/2} = \mathscr{M}^+\left(\left(M_k\right)_i\right) + \mathscr{M}^-\left(\left(M_k\right)_{i+1}\right) \quad 5.30$$

with the polynomials, $\mathscr{M}^{\pm}$ given by:

$$\mathscr{M}_1^{\pm} = \frac{1}{2}\left(M_k + \left|M_k\right|\right) \quad 5.31$$

$$\mathscr{M}_2^{\pm} = \begin{cases} \mathscr{M}_1^{\pm} & \text{if } |M_k| \geq 1 \\ \pm\frac{1}{4}\left(M_k \pm |M_k|\right)^2 & \text{else} \end{cases} \quad 5.32$$

$$\mathscr{M}^{\pm} = \begin{cases} \mathscr{M}_1^{\pm} & \text{if } |M_k| \geq 1 \\ \pm\mathscr{M}_2^{\pm}\left(1 \mp 16\times(1/8)\,\mathscr{M}_2^{\mp}\right) & \text{else} \end{cases} \quad 5.33$$

The advection flux is then readily computed as:

$$\left(\boldsymbol{A}_k\right)_{i+1/2} = \begin{cases} \left(\dot{m}_k\right)_{i+1/2} \begin{pmatrix} 1 \\ u_k \\ H_k \end{pmatrix}_i & \text{if } \left(\dot{m}_k\right)_{i+1/2} > 0 \\ \left(\dot{m}_k\right)_{i+1/2} \begin{pmatrix} 1 \\ u_k \\ H_k \end{pmatrix}_{i+1} & \text{else} \end{cases} \quad 5.34$$

and the pressure flux is given by:

$$\left(\boldsymbol{P}_k\right)_{i+1/2} = \left(\boldsymbol{P}_k\right)_{i+1/2}^{AUSM} = \mathscr{P}^{+}\left(\left(M_k\right)_i\right)\left(\alpha_k p\right)_i + \mathscr{P}^{-}\left(\left(M_k\right)_{i+1}\right)\left(\alpha_k p\right)_{i+1} \quad 5.35$$

with the polynomials, $\mathscr{P}^{\pm}$ defined as:

$$\mathscr{P}^{\pm} = \begin{cases} \mathscr{M}_1^{\pm}/M_k & \text{if } |M_k| \geq 1 \\ \pm\mathscr{M}_2^{\pm}\left(2 \mp M_k - 16\times(3/8)\,M_k\mathscr{P}_2^{\mp}\right)^2 & \text{else} \end{cases} \quad 5.36$$

On an additional note, for low Mach number flows, numerical diffusion can be added to both the advection and pressure fluxes to improve the stability of the scheme, which leads to:

$$\left(M_k\right)_{i+1/2} = \left(M_k\right)_{i+1/2} - K_p \max\left(1-\sigma\left(\overline{M_k}\right)^2, 0\right)\frac{\left(\alpha_k p\right)_{i+1} - \left(\alpha_k p\right)_i}{\overline{\alpha_k \rho_k}\left(a_k\right)_{i+1/2}} \quad 5.37$$

$$\left(\mathrm{P}_k\right)_{i+1/2}^{AUSM} = \left(\mathrm{P}_k\right)_{i+1/2}^{AUSM} - K_u \mathscr{P}^{+}\left(\left(M_k\right)_i\right)\mathscr{P}^{-}\left(\left(M_k\right)_{i+1}\right)\left(\left(\alpha_k\rho_k\right)_i + \left(\alpha_k\rho_k\right)_{i+1}\right)\left(a_k\right)_{i+1/2}\left(\left(u_k\right)_{i+1} - \left(u_k\right)_i\right) \quad 5.38$$

where:

$$K_u = K_p = 0.1 \tag{5.39}$$

$$\overline{M_k} = 1/2\left(\left(M_k\right)_i + \left(M_k\right)_{i+1}\right) \tag{5.40}$$

$$\overline{\alpha_k \rho_k} = 1/2\left(\left(\alpha_k \rho_k\right)_i + \left(\alpha_k \rho_k\right)_{i+1}\right) \tag{5.41}$$

Thereafter, following equation 5.26, addition of the advection flux and the pressure flux gives the sought interface flux.

Turning to the non-conservative terms in equation 5.25, its discretisation in vector form reads:

$$\boldsymbol{C}_i^{nv} = \begin{pmatrix} 0 \\ 0 \\ \Delta t\left(\left(p-\Delta p\right)_i \dfrac{\left(\alpha_v\right)_{i+1} - \left(\alpha_v\right)_{i-1}}{\Delta x}\right) \\ \Delta t\left(\left(p-\Delta p\right)_i \dfrac{\left(\alpha_l\right)_{i+1} - \left(\alpha_l\right)_{i-1}}{\Delta x}\right) \\ -\Delta t\left(p_i \dfrac{\left(\alpha_v\right)_i^n - \left(\alpha_v\right)_i^{n-1}}{\Delta t}\right) + \Delta t\left(\left(-u_{\text{int}}\Delta p\right)_i \dfrac{\left(\alpha_v\right)_{i+1} - \left(\alpha_v\right)_{i-1}}{\Delta x}\right) \\ -\Delta t\left(p_i \dfrac{\left(\alpha_l\right)_i^n - \left(\alpha_l\right)_i^{n-1}}{\Delta t}\right) + \Delta t\left(\left(-u_{\text{int}}\Delta p\right)_i \dfrac{\left(\alpha_l\right)_{i+1} - \left(\alpha_l\right)_{i-1}}{\Delta x}\right) \end{pmatrix} \tag{5.42}$$

following Paillère et al. (2003) and S. Brown et al. (2014).

Lastly, the volumetric source terms are accounted for explicitly using fractional step approach (LeVeque 1992).

5.3.2 Modifications towards the AUSM Scheme

Focusing on the $\partial\left(\alpha_k p\right)/\partial x$ and $p\partial\alpha_k/\partial x$ terms in equation 5.24 (respectively in the momentum flux and the non-conservative terms), according to Chang & Liou (2007), their discretisation must be compatible in order to avoid numerical instability at the locations where α_k varies rapidly. In the presented scheme above, $\partial\left(\alpha_k p\right)/\partial x$ is discretised following equation 5.35, and $p\partial\alpha_k/\partial x$ on the other hand is discretised

following the centred difference scheme (equation 5.42). It is clear that the compatibility requirement is unlikely to be fulfilled.

To address such an issue, in what follows, modifications towards the AUSM scheme are introduced.

5.3.2.1 Modified Discretisation

According to Munkejord et al. (2009), the non-conservative term in equation 5.23, $\boldsymbol{C}^{nv}$ can be recast into its mathematically equivalent form given by:

$$\boldsymbol{C}^{nv} = -\boldsymbol{B}\frac{\partial \boldsymbol{W}}{\partial x} \qquad 5.43$$

where:

$$\boldsymbol{B} = \begin{pmatrix} 0 & 0 & 0 & 0 & 0 \\ 0 & p-\Delta p & 0 & 0 & 0 \\ -\eta\alpha_v\alpha_l\left(u_v-u_l\right) & -u^{\text{int}}\Delta p & -\eta\rho_v\alpha_l a_v^2 & \eta\rho_l\alpha_v a_l^2 & 0 \\ 0 & 0 & 0 & 0 & 0 \\ 0 & \Delta p-p & 0 & 0 & 0 \\ \eta\alpha_v\alpha_l\left(u_v-u_l\right) & u^{\text{int}}\Delta p & \eta\rho_v\alpha_l a_v^2 & -\eta\rho_l\alpha_v a_l^2 & 0 \end{pmatrix} \qquad 5.44$$

$$\boldsymbol{W} = \begin{pmatrix} p \\ \alpha_l \\ \alpha_v u_v \\ \alpha_l u_l \\ \Delta p \end{pmatrix}$$

$$\eta = \frac{p}{\alpha_v\rho_l a_l^2 + \alpha_l\rho_v a_v^2}$$

Note that $\partial\alpha_v = -\partial\alpha_l$ (from equation 5.7), and $\boldsymbol{W}$ is a function of $\boldsymbol{U}$. Substitution of equation 5.44 into 5.23 gives:

$$\frac{\partial \boldsymbol{U}}{\partial t} + \frac{\partial \boldsymbol{F}}{\partial x} + \boldsymbol{B}\frac{\partial \boldsymbol{W}}{\partial x} = \boldsymbol{0} \qquad 5.45$$

Here, the source term, $\boldsymbol{S}$ is dropped temporarily for simplicity. Following Tokareva & Toro (2016), equation 5.45 can be split into two systems:

$$\frac{\partial \boldsymbol{U}}{\partial t}+\frac{\partial \boldsymbol{A}}{\partial x}=\boldsymbol{0} \tag{5.46}$$

$$\frac{\partial \boldsymbol{U}}{\partial t}+\frac{\partial \boldsymbol{P}}{\partial x}+\boldsymbol{B}\frac{\partial \boldsymbol{W}}{\partial x}=\boldsymbol{0} \tag{5.47}$$

where $\boldsymbol{A}$ and $\boldsymbol{P}$ are defined in Section 5.3.1. The overall numerical fluxes at cell interfaces corresponding to equation 5.45 are then computed as the sum of the numerical fluxes corresponding to equations 5.46 and 5.47 (denoted as $\boldsymbol{A}_{i\pm1/2}$ and $\boldsymbol{D}_{i\pm1/2}$ respectively). From the above, the updating formula for $\boldsymbol{U}_i$ reads:

$$\boldsymbol{U}_i^{n+1}=\boldsymbol{U}_i^{n}+\frac{\Delta t}{\Delta x}\left(\boldsymbol{A}_{i-1/2}-\boldsymbol{A}_{i+1/2}\right)+\frac{\Delta t}{\Delta x}\left(\boldsymbol{D}_{i-1/2}-\boldsymbol{D}_{i+1/2}\right) \tag{5.48}$$

In equation 5.48, $\boldsymbol{D}_{i\pm1/2}$ is computed following the PRImitive CEntred scheme of the First ORder CEntred type (PRICE-FORCE) analogous to the implementation by Munkejord et al. (2009) (see also Section A4.3, Appendix), which gives:

$$\boldsymbol{D}_{i+1/2}=\boldsymbol{D}_{i+1/2}^{PRICE-FORCE}=\frac{1}{2}\left(\boldsymbol{D}_{i+1/2}^{PRICE-LF}+\boldsymbol{D}_{i+1/2}^{PRICE-LW}\right) \tag{5.49}$$

where $\boldsymbol{D}_{i+1/2}^{PRICE-LF}$ is computed following the *PRICE-Lax-Friedrichs* scheme given by (Toro & Siviglia 2003):

$$\boldsymbol{D}_{i+1/2}^{PRICE-LF}=\frac{1}{2}\left(\boldsymbol{P}_i+\boldsymbol{P}_{i+1}\right)+\frac{1}{2}\frac{\Delta x}{\Delta t}\left(\boldsymbol{U}_i-\boldsymbol{U}_{i+1}\right)+\frac{1}{2}\boldsymbol{B}_i\left(\boldsymbol{W}_i+\boldsymbol{W}_{i+1}\right) \tag{5.50}$$

and $\boldsymbol{D}_{i+1/2}^{PRICE-LW}$ is given by the *PRICE-Lax-Wendroff* scheme (Toro & Siviglia 2003):

$$\boldsymbol{D}_{i+1/2}^{PRICE-LW}=\boldsymbol{P}\left(\boldsymbol{U}_{i+1/2}^{*}\right)+\boldsymbol{B}_i\left(\boldsymbol{W}\left(\boldsymbol{U}_{i+1/2}^{*}\right)\right) \tag{5.51}$$

where:

$$\boldsymbol{U}_{i+1/2}^{*}=\frac{1}{2}\left(\boldsymbol{U}_i+\boldsymbol{U}_{i+1}\right)+\frac{\Delta t}{2\Delta x}\left(\boldsymbol{P}_i-\boldsymbol{P}_{i+1}\right)+\frac{\Delta t}{2\Delta x}\boldsymbol{B}_{i+1/2}\left(\boldsymbol{W}_i-\boldsymbol{W}_{i+1}\right) \tag{5.52}$$

with:

$$\boldsymbol{B}_{i+1/2} = \boldsymbol{B}\left(\frac{\boldsymbol{W}_i + \boldsymbol{W}_{i+1}}{2}\right) \qquad 5.53$$

From the above, in contrast to the implementation in the original AUSM scheme, $\partial(\alpha_k p)/\partial x$ and $p\partial\alpha_k/\partial x$ are discretised following the same numerical scheme.

5.3.2.2 MUSTA Scheme

It is known that centred schemes are more diffusive as compared to upwind schemes (Toro 2006), which leads to loss of accuracy in capturing discontinuities (e.g. shocks) and large gradients in flows. As a remedy, the MUltiStage Approach (MUSTA) first introduced by Toro (2006) is adopted here.

The central idea of the MUSTA scheme is to subdivide each numerical cell on the global grid into 2*N* sub-cells (*N* = 1, 2, 3…), resulting in the so-called MUSTA grid. The solutions of the relevant equation system is then advanced on the MUSTA grid for *M* successive stages with a local timestep, Δt_{total}. Δt_{total} is determined by the CFL condition (with a specified constant local CFL factor). With *M* increasing from 1 to ∞, the accuracy of the centred scheme approaches the most accurate upwind scheme (Toro 2006).

However, this is achieved at the expense of computational efficiency. For example, Munkejord et al. (2009) found that at least 200 stages with 200 sub-cells (i.e. *N* = 100, *M* = 200) was necessary to obtain a comparable performance to the tested upwind scheme.

The implementation of the MUSTA scheme is discussed in the following. Equation 5.47 is first solved on the MUSTA gird of 2*N* sub-cells with a local timestep of Δt_{total}. Thereafter, all the variables at each sub-cell centre are updated, and $\boldsymbol{D}_{i\pm1/2}$ are re-computed. The updated cell centre values are adopted as the initial conditions for the next stage, and the above procedure is repeated until the required number of stages, *M* is reached. On an important note, to avoid undesired numerical oscillations, it is recommended to set $M \leq 2N$ (Toro 2006). Finally, $\boldsymbol{D}_{i\pm1/2}$ obtained at the end of the

final stage are substituted into the updating formula equation 5.48 to advance the solution in time and space on the global grid.

The resulting scheme is simply referred to as the MUSTA scheme.

5.3.2.3 AUSM-MUSTA Scheme

As mentioned above, the MUSTA scheme can be computationally demanding to achieve an accuracy comparable to upwind schemes. To address such an issue, the following is proposed.

The idea stems from the fact that the AUSM scheme only loses accuracy at the locations where α_k changes rapidly. At each timestep, the difference in α_v between two adjacent cells is evaluated and checked against the set-point value, $\Delta\alpha_v^{set}$ ($\Delta\alpha_v^{set} = 1\times10^{-5}$). The modifications introduced in this study will be activated only if $\Delta\alpha_v > \Delta\alpha_v^{set}$.

For the sake of clarity, the final scheme is referred to as the AUSM-MUSTA scheme.

5.3.2.4 Second-Order Extension of the AUSM-MUSTA Scheme

The AUSM-MUSTA scheme proposed in the present study is of first-order accuracy both in time and space. To obtain its second-order extension, the Monotone Upwind-centred Scheme of Conservation Laws (MUSCL) (Toro 2009f) is adopted. The central component of the MUSCL scheme is the reconstruction of the flow variables based on interpolation techniques. Herein, a set of primitive flow variables, $\boldsymbol{V} = \left(\alpha_v, p, u_v, u_l, T_v, T_l\right)$ (in replacement of $\boldsymbol{U}$) is selected following the recommendation by Munkejord et al. (2009). Applying piecewise linear interpolation, the corresponding interpolated values on the left/right surface of the cell interface, i+1/2 respectively read:

$$\boldsymbol{V}_{i+1/2}^{R} = \boldsymbol{V}_i + \frac{\Delta x}{2}\Delta_i \qquad 5.54$$

$$\boldsymbol{V}_{i+1/2}^{L} = \boldsymbol{V}_{i+1} - \frac{\Delta x}{2}\Delta_{i+1} \qquad 5.55$$

$$\Delta_i = \theta(\boldsymbol{V}_{i+1} - \boldsymbol{V}_i),\ \Delta_{i+1} = \theta(\boldsymbol{V}_{i+2} - \boldsymbol{V}_{i+1}) \qquad 5.56$$

where θ is the standard van Leer slope limiter function (see (Toro 2009a) and (Toro & Billett 2000) for details) to supress numerical oscillations introduced by high-order schemes.

After data reconstruction, the primitive variable set, $\left(\boldsymbol{V}_{i+1/2}^{R}, \boldsymbol{V}_{i+1/2}^{L}\right)$ are converted to the corresponding conservative variable set, $\left(\boldsymbol{U}_{i+1/2}^{R}, \boldsymbol{U}_{i+1/2}^{L}\right)$ for the computation of the interface fluxes exactly following the procedure introduced earlier in this section, in replacement of $\left(\boldsymbol{U}_{\mathrm{i}}, \boldsymbol{U}_{\mathrm{i+1}}\right)$.

5.4 Results and Discussion

5.4.1 Model Verification

For the verification of the proposed AUSM-MUSTA scheme for solving the TFM model equations 5.1 to 5.6, three numerical experiments that are most commonly seen in the literature (Tokareva & Toro 2010; Paillère et al. 2003; Munkejord et al. 2009; Munkejord 2010) are performed. They are the moving discontinuity test, the water faucet problem test and the Toumi's shocktube problem test.

During all three numerical experiments, the ideal gas and stiffened gas EoS (see (FlÅtten et al. 2011) for details) are respectively applied to the vapour and liquid fluid phases. For the stiffened gas EoS, one needs to specify three parameters, κ, p^{∞} and $C_{p.}$ Their constant values are given in table 5.1. In addition, the terms representing interface and fluid/wall interactions are omitted in equations 5.1 to 5.6.

Table 5.1: Ideal gas and stiffened gas EoS constant parameters employed in this study.

	κ	$\boldsymbol{p^{\infty}}$ **(pa)**	$\boldsymbol{C_p}$ **(J/kg-K)**
Vapour	1.4	0.0	1008.7
liquid	2.8	8.5×10^{8}	4186.0

5.4.1.1 Moving Discontinuity Test

The moving discontinuity test concerns the propagation of the initial vapour-liquid interface with the flow of uniform pressure and velocity. With reference to equations 5.1 to 5.6, in such case, no variations in pressure and velocity should be introduced by a numerical scheme as the discontinuity propagates. This is sometimes called the 'pressure non-distribution' condition (Munkejord et al. 2009). The details of the test initial conditions are given in table 5.2.

Table 5.2: Initial conditions for the moving discontinuity test.

Quantity	Left (x = 0 ~ 6 m)	Right (x = 6 ~ 12 m)
Fluid pressure (bar)	1	1
Fluid temperature (K)	315.9	315.9
Vapour phase volume fraction	0.9999 (~1.0)	0.0001 (~0.0)
Vapour phase velocity (m/s)	100	100
Liquid phase velocity (m/s)	100	100

The numerical test is simulated using the AUSM scheme, the AUSM-MUSTA (M = 4) scheme and the MUSTA (M = 4) scheme on a computational domain of 400 equal-spaced cells with a CFL number of 0.5. The results are presented in figure 5.3. Also included are the corresponding exact solution for comparison.

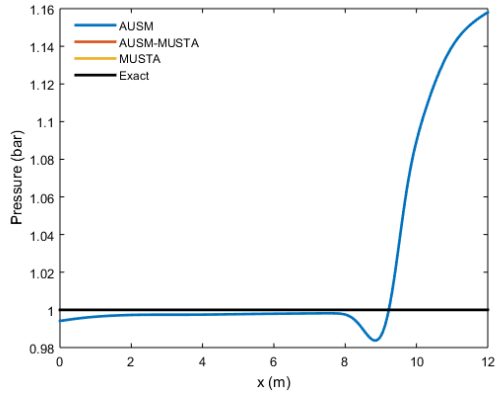

(a)

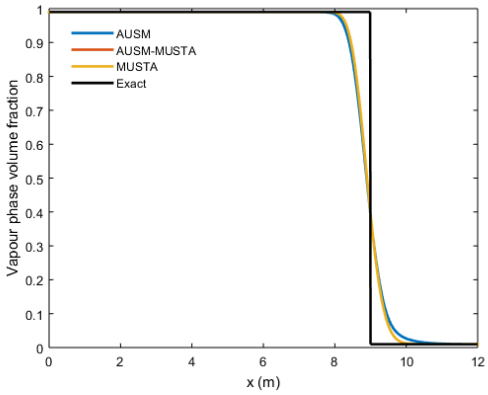

(b)

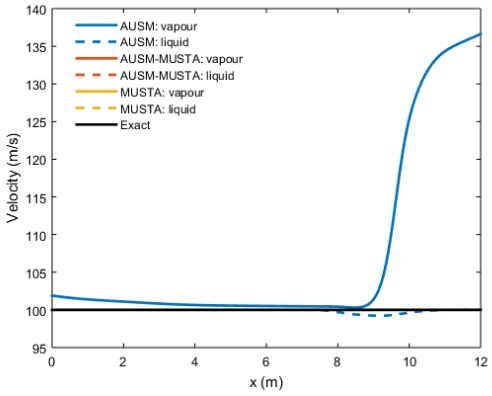

(c)

Figure 5.3: Predicted and exact pressure (a), vapour phase volume fraction (b) and velocity (c) profiles along the length of the computational domain at 0.03 s following the sart of the simulation for the moving discontinuity test. In (a) and (b), the red and yellow curves (respectively representing the AUSM-MUSTA and MUSTA schemes predictions) conicide with the exact solution (marked by the black curve).

From figure 5.3, although all three schemes are capable of predicting the propagation of the vapour-liquid interface, in reasonably good agreement with the exact solution (see figure 5.3 (b)), it is clear that the AUSM scheme does not fulfil the pressure non-distribution condition. As it can be seen in figures 5.3 (a) and (c), disturbances are introduced to both pressure and velocity profiles along the computational domain. This is attributed to the incompatibility between the discretisation of the $\partial(\alpha_k p)/\partial x$ and $p\partial\alpha_k/\partial x$ terms respectively in the momentum and non-conservative terms in the AUSM scheme.

With regards to the MUSTA and AUSM-MUSTA schemes, in both cases, the pressure non-distribution condition is met.

5.4.1.2 Water Faucet Problem Test

The water faucet problem was firstly introduced by Ransom (1987) and later studied by a number of researchers (Tokareva & Toro 2016; Paillère et al. 2003; Munkejord et al. 2009; Munkejord 2010) mainly to test the accuracy of the numerical schemes for solving the TFM model in one-dimension. The test consists of a water column of 12 m length initially moving at 10 m/s, which is surrounded by air at the same velocity. Other relevant initial conditions are given in table 5.3.

Table 5.3: Initial conditions for the water faucet problem.

Quantity	x = 0 ~ 12 m
Fluid pressure (bar)	1
Fluid temperature (K)	300
Vapour phase volume fraction	0.2
Vapour phase velocity (m/s)	10
Liquid phase velocity (m/s)	10

The gravity force is applied to the flow field, causing the water column to accelerate and become narrower along its length due to mass conservation. There exists an analytical solution for the corresponding vapour phase volume fraction profile along the flow domain at any given time.

In what follows, the predicted pressure, temperature, vapour volume fraction and velocity profiles along the length of the computational domain at 0.5 s following the start of the simulation using all three schemes described above are presented. In particular, the vapour volume fraction profile predictions are compared to the analytical solution. The results are displayed in figure 5.4. All the simulations are performed on a uniform computational grid of 2000 cells with a CFL number of 0.5. (The grid convergence test results can be found in figure A5.5, Appendix).

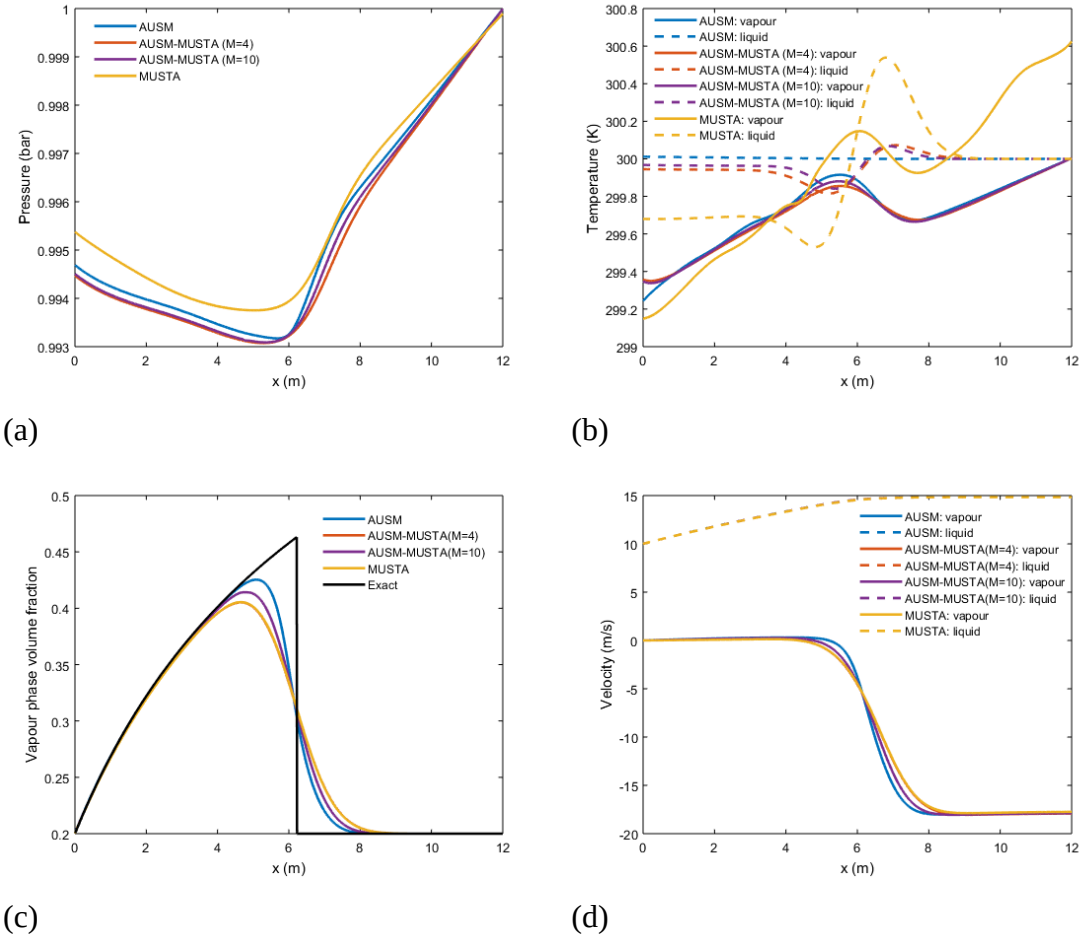

Figure 5.4: The predicted pressure (a), temperature (b), vapour volume fraction (c) and velocity (d) profiles along the length of the computational domain at 0.5 s following the sart of the simulation for the water faucet problem test. The analytical solution of the vapour volume fraction profile is also included in (c).

From figure 5.4, it can be seen that all three schemes predict similar profiles. However, by comparing the predicted vapour phase volume fraction profiles to the analytical solution (figure 5.4 (c)), the AUSM-MUSTA and MUSTA schemes with 4 stages ($M = 4$) are more diffusive than the AUSM scheme.

Such an undesired property of the AUSM-MUSTA and MUSTA schemes can be mitigated by increasing the number of the stages, M. $M = 10$ is tested in this study. The corresponding predictions from the AUSM-MUSTA scheme are included in figure 5.4. As may be observed, a noticeable improvement in the accuracy is obtained. However, as pointed out in Section 5.3.2.2, such an improvement is at the expense of much increased computational workload. Figure 5.5 depicts the runtime for all

schemes tested for the water faucet problem, and that for M = 10 is more than 250 % higher than that for M = 4.

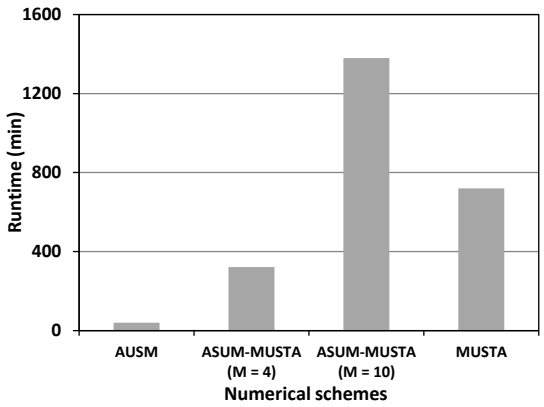

Figure 5.5: Computaional runtimes of each tested numerical schemes in the water faucet problem test using a Intel ® Core ™ i5 4590 CPU at 3.30 GHz

Return to figure 5.4, no numerical instability is observed in the AUSM scheme predictions in this particular test case.

5.4.1.3 Toumi's Shocktube Problem Test

The Toumi's shocktube problem, first introduced by Toumi et al. (1999), is another classic test for examining the accuracy of the numerical schemes for the TFM model. The problem consists of a horizontal tube filled with two fluids of different initial states separated by a diaphragm in the middle. To commence the simulation, the diaphragm is removed, and the flow field starts to evolve. The relevant initial conditions are given in table 5.4.

Table 5.4: Initial conditions for the Toumi's shocktube problem test. All symbols are defined previously.

Quantity	Left (x = 0 – 5 m)	Right (x = 5– 10 m)
Fluid pressure (bar)	200	100
Fluid temperature (K)	308.15	308.15
Vapour phase volume fraction	0.25	0.1
Vapour phase velocity (m/s)	0	0
Liquid phase velocity (m/s)	0	0

The tests are performed using all three schemes on a uniform computational grid of 2000 cells with a CFL number of 0.5 (The grid convergence test results are shown in figure A5.6, Appendix). The results are presented in figure 5.6.

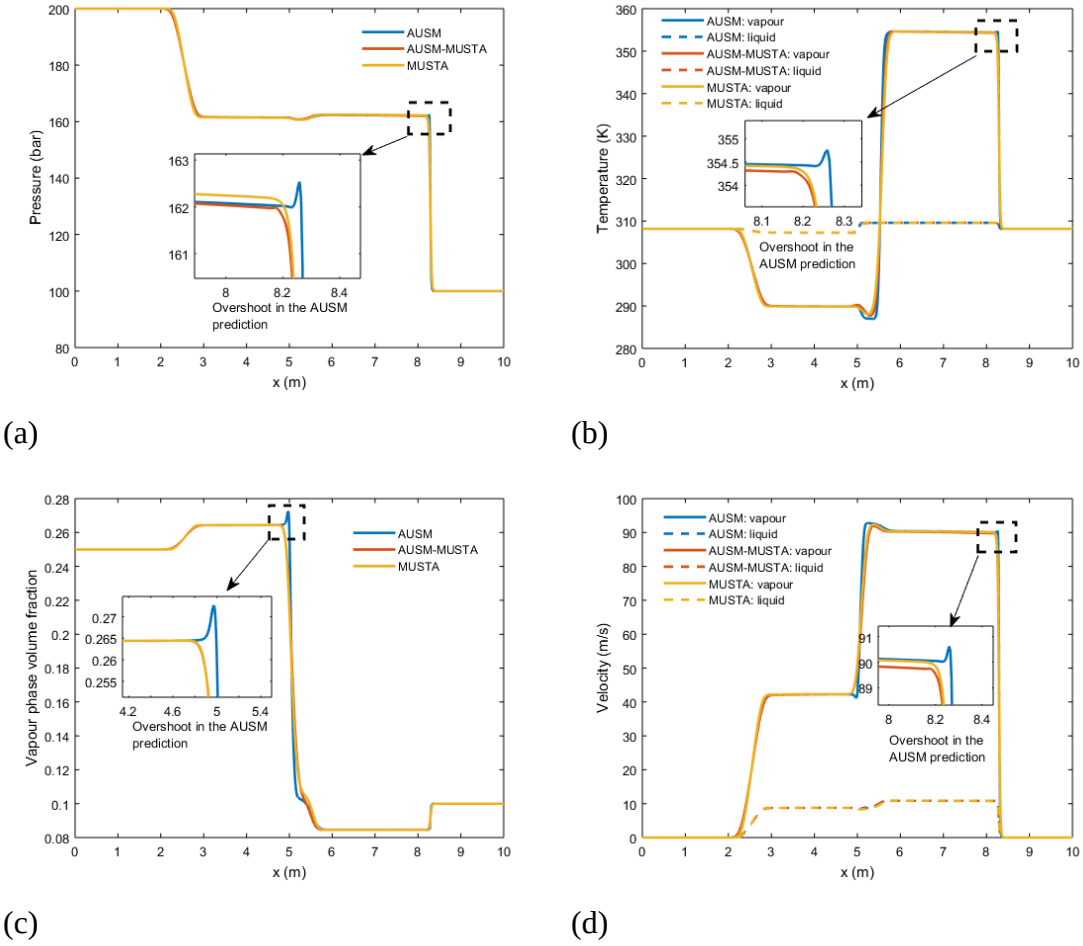

Figure 5.6: The predicted pressure (a), temperature (b), vapour volume fraction (c) and velocity (d) profiles along the length of the computational domain at 0.06 s following the start of the simulation for the Toumi's shocktube problem test.

From figure 5.6, some general observations can be made first: all three schemes are capable of predicting the propagation of the initial discontinuities; the AUSM scheme is again the least diffusive at locations with large gradients (at ca. 5 m in the vapour volume fraction profile and the vapour velocity profile).

Turning to the included magnified plots for the boxed regions in the predicted flow profiles in figures 5.6 (a) to (d), overshoots can be observed in all AUSM scheme predictions. Such a numerical instability and hence the loss of accuracy is again caused by the AUSM scheme being unable to meet the compatibility requirement (see Section 5.3.2.1). On the other hand, both the proposed AUSM-MUSTA and MUSTA schemes give satisfactory results.

In terms of computational efficiency, from figure 5.7 showing the runtimes of all three schemes, the AUSM scheme again comes first, followed by the AUSM-MUSTA scheme which is more than 250 % faster than the MUSTA scheme, indicating the effectiveness of the AUSM-MUSTA scheme in improving the computational efficiency while maintaining its accuracy.

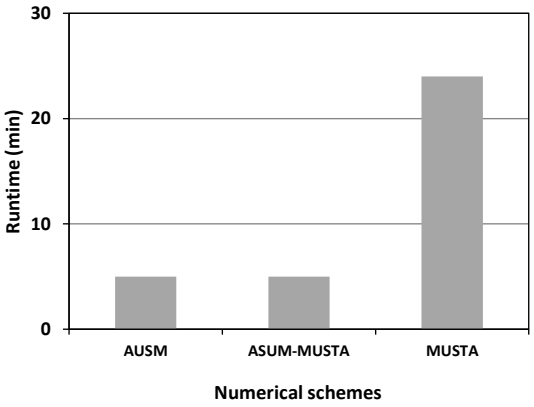

Figure 5.7: Computaional runtimes of each tested numerical schemes in the Toumi's shocktube problem test using a Intel ® Core ™ i5 4590 CPU at 3.30 GHz.

5.4.1.4 Effect of Second-Order Extension on the AUSM-MUSTA Scheme

As presented in Section 5.3.2.4, the proposed ASUM-MUSTA scheme is readily extended to second-order accuracy via the MUSCL scheme. The resulting second-order scheme is tested by repeating the water faucet problem and Toumi's shocktube problem tests. The results (in terms of vapour phase volume fraction as an example) are presented in figure 5.8, together with the predictions from the first-order ASUM-MUSTA scheme for reference. The number of numerical cells (2000 cells) and the CFL number (0.5) remain unchanged.

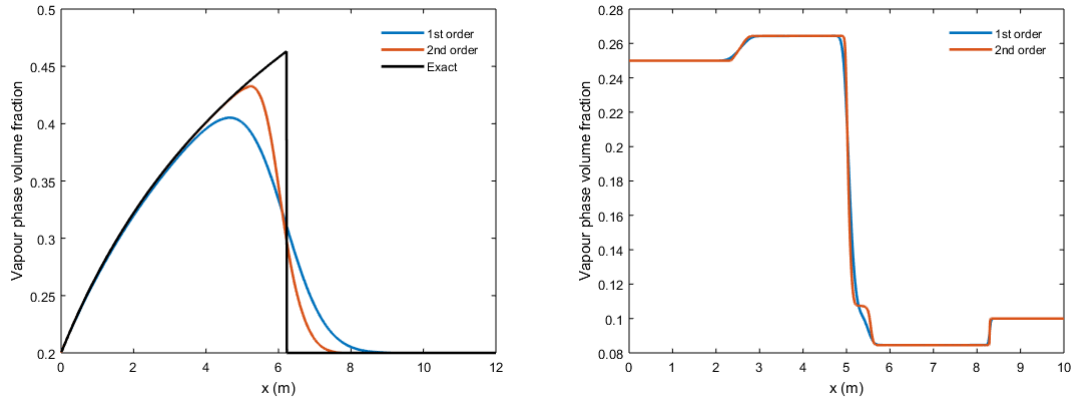

(a) (b)

Figure 5.8: Comparisons of the predictions of vapour phase volume fraction profiles along the computational domain from the fisrt- and second-order ASUM-MUSTA schemes for the water faucet problem test (a) and the Toumi's shocktube prblem test (b). The profiles are recored at 0.5 s and 0.06 s respectively for the two tests.

As can be seen in figure 5.8, in both cases, a significant improvement in accuracy especially for the predictions at the locations with large gradients is obtained.

5.4.2 Model Validation

In the following section, the TFM model with the AUSM-MUSTA scheme is used to simulate two CO_2 pipeline puncture decompression tests conducted during the course of the collaborative CO_2QUEST FP7 project (Solomon Brown et al. 2014). The model predictions are compared to available experimental measurements for validation purpose. In addition, the HEM model (Section 2.1.2.2.1, Chapter 2) is applied to repeat the simulations, and the results are included in the comparisons.

5.4.2.1 INERIS Medium-Scale Pipeline Puncture Decompression Test

In this experiment, the test rig involved a thermally insulated horizontal pipe of 37 m length and 50.8 mm i.d. A 6 mm i.d. orifice release nozzle was attached to one end of the test pipe while the other end remained closed, mimicking a puncture failure-induced pipeline decompression. The pipeline was initially filled with saturated

vapour-liquid two-phase CO_2. The full details of the initial conditions are given in table 5.5.

Table 5.5: INERIS CO_2 pipeline puncture decompression test conditions.

Quantity	x = 0 ~ 37 m
Fluid pressure (bar)	55
Fluid temperature (K)	292
Ambient pressure (bar)	1
Ambient temperature (K)	293
Inventory (kg)	41
Fluid phase	Two-phase (with 30 vol% vapour)

Upon decompression, the CO_2 temperatures and pressures were monitored at four different locations of 0.5, 12.5, 25 and 36.5 m from the closed end along the pipe length, using K-type thermocouples (1 mm sleeve Inconel, ± 1.0 ^oC error) and piezoresistive gauge pressure sensors (Kistler 4622A, 0 – 300 bar, ± 0.05% accuracy). At each location, there were three thermocouples installed at top, middle and bottom of the pipe cross-section; the top and bottom thermocouples respectively recorded the temperature of the stratified vapour and liquid phases. The remaining inventory mass in the pipe was measured using load cells (Tedea-Huntleigh 1250, ± 0.02 %accuracy).

The simulations are performed on a uniform grid of 100 discretised computation cells with a CFL number of 0.3. Further grid refinement results in little difference in the simulated results (see figure A5.7, Appendix)

Figure 5.9 shows the TFM and HEM model simulated variations of CO_2 pressure with release time 12.5 m from the closed end of the pipe together with the corresponding measured data.

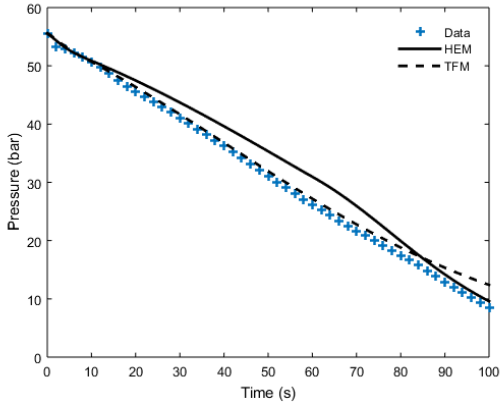

Figure 5.9: Predicted (from both the HEM and TFM models) and measured CO_2 pressure variations as a function of time during decompression for the INERIS pipeline puncture decompression test.

As can be seen in figure 5.9, the pressure variations with time follow an approximately linear trend which is expected for two-phase mixture flows (Martynov et al. 2014). Turning to the model predictions, the TFM model is in close agreement with the measurement, with a maximum difference of 3 bar occurring at the later stages of the depressurisation process. With regards to the HEM model, in spite of producing a generally agreement with the measured data, it predicts a slower rate of decompression compared to the TFM prediction and measurement between 0 and 60 s following the release. The predicted decompression rate increases to the end of the simulated decompression period.

Figure 5.10 shows the corresponding variations of CO_2 temperature as a function of time following release. It is particularly noted that the measured data reported are those recorded from the top (stratified vapour phase) and bottom (stratified liquid phase) sections of the pipe.

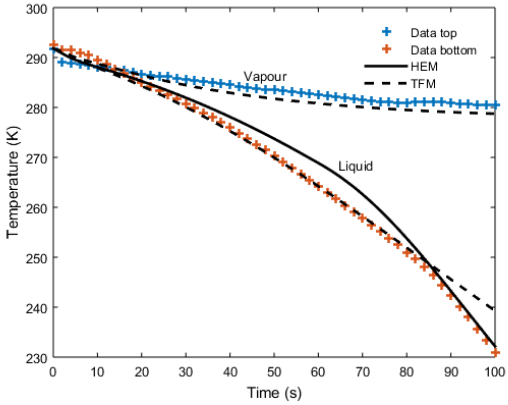

Figure 5.10: Predicted (from both the HEM and TFM models) and measured CO_2 temperature variations with time during decompression for the INERIS pipeline puncture decompression test.

As it may be observed, the measured data indicate a significantly larger drop in the liquid phase temperature (ca. 60 K) as compared to that of the vapour phase (ca. 10 K). Such heterogeneous flow phenomenon is often referred to as thermal stratification. During puncture decompression in a two-phase mixture, the convection heat flux from the dry wall to the stratified vapour phase significantly reduces the cooling effect brought by its expansion. On the other hand, the nucleate boiling heat flux from the wet wall to the liquid phase supplies the latent heat of vaporisation, and the liquid phase temperature continues to drop following the saturation line.

As the energy conservation equation is solved for vapour and liquid phases separately in TFM model, the different heat transfer modes in the separated two fluid phases can be accounted for as demonstrated in the model formulation (equations 5.1 to 5.6; see also Section 2.1.3.1, Chapter 2). As it may be observed from the data in figure 5.10, the TFM model produces good predictions of the measured liquid and vapour phase temperatures during the most part (up to 90s) of the decompression process. In the case of the liquid phase, the TFM over predicts the temperature by as much as 8 K in the remaining 10s (90 – 100s) of the simulated depressurisation period.

The HEM model does not distinguish between the vapour and liquid phases given the implicit homogeneous flow assumption, and hence only one fluid temperature may be simulated. In this case, the computed convection and boiling heat fluxes only facilitate vaporisation in the liquid phase, and both vapour and liquid phases follow the

saturation temperature corresponding to the prevailing pressure in the pipe (figure 5.9). As it may be observed from figure 5.10, the HEM follows the recorded liquid space temperature producing a reasonably good agreement with the measured data with the maximum discrepancy being +5 K.

In practice, the observed relatively large temperature difference between the stratified vapour and liquid phases (ca. 50 K in the present case) will result in a thermal stress gradient across the pipe wall. The above coupled with the prevailing pressure stress may therefore in extreme circumstances poses the risk of pipeline rupture especially if the pipe wall temperature falls below its ductile-brittle transition temperature. For such failure scenarios, the advantages of the TFM model as a predictive tool is clear.

Figure 5.11 shows the impact of the two modelling approaches on the corresponding simulated CO_2 vapour molar fraction during depressurisation.

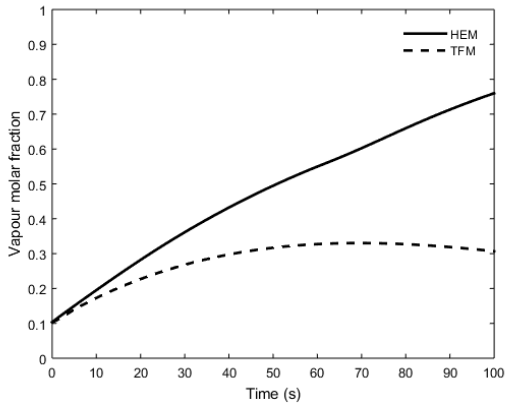

Figure 5.11: Predicted (from both the HEM and TFM models) CO_2 vapour molar fraction variation as a function of time during decompression for the INERIS pipeline puncture decompression test.

As compared to the TFM model, it is clear that the HEM model consistently over-predicts the vapour molar fractions throughout the release. Further discussion regarding the above will be carried out in Section 5.4.3.

Figure 5.12 shows the corresponding measured and simulated (from both the HEM and TFM models) variations of the remaining CO_2 inventory in the pipe as a function of time during decompression.

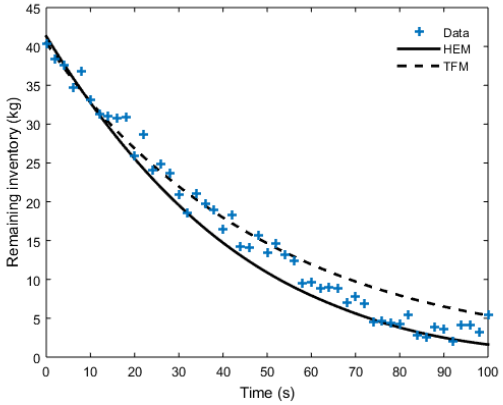

Figure 5.12: Predicted (from both the HEM and TFM models) and measured remaining CO_2 mass during the decompression for the INERIS pipeline puncture decompression test.

From figure 5.12, compared to the TFM model, the HEM model under-predicts the remaining mass (by ca. 60 % at most). However, both model predictions are within the range of the measured data with the TFM producing a slightly better performance.

5.4.2.2 DUT Large-Scale Pipeline Puncture Decompression Test

The DUT pipeline puncture decompression test conducted as part of the CO_2QUEST FP7 project (Solomon Brown et al. 2014) consisted of a 256 m length, 223 mm i.d. insulated horizontal pipe filled with pure CO_2. A 50 mm i.d. orifice release nozzle was attached to one end of the test pipe. The test conditions are summarised in table 5.6.

Table 5.6: DUT large-scale pipeline puncture decompression test conditions.

Quantity	x = 0 ~ 256 m
Fluid pressure (bar)	55
Fluid temperature (K)	291
Ambient pressure (bar)	1
Ambient temperature (K)	295
Inventory (kg)	2800
Fluid phase	Two-phase (with 80 vol% vapour)

At the onset of decompression, pressures and temperatures were monitored at various locations along the testing pipe, using low-temperature fast-response pressure transducers and K-type thermocouples. At each location, two thermocouples were placed respectively at the top and bottom sections of the pipe. The mass of the remaining inventory was however not measured. The validation of the TFM models is performed by comparing the predictions of the pressure and temperature vs. time profiles 150 m from the pipe closed end to the corresponding measurements.

Simulations are performed on a uniform grid of 300 discretised computation cells with a CFL number of 0.3. Further grid refinement shows little difference in the predictions (see figure A5.8, Appendix). The pressure variation as a function of time obtained from the TFM and HEM models is presented in figure 5.13. Also included are the corresponding measurements for comparison.

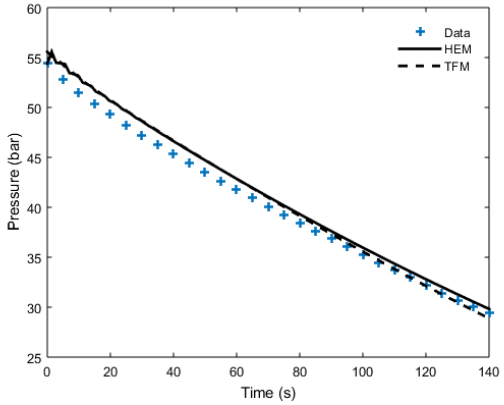

Figure 5.13: Predicted (from the HEM and TFM models) and measured pressure variations as a function of time 150 m from the pipe closed end for the DUT puncture decompression test.

From figure 5.13, similar to the INERIS test, the pressure trajectory follows an almost linear decline with time in both cases. Additionally, both model predictions are very close, producing a relatively good agreement (ca. ± 1 bar) with the measured data.

The corresponding predicted temperature variations as a function of time are displayed in figure 5.14.

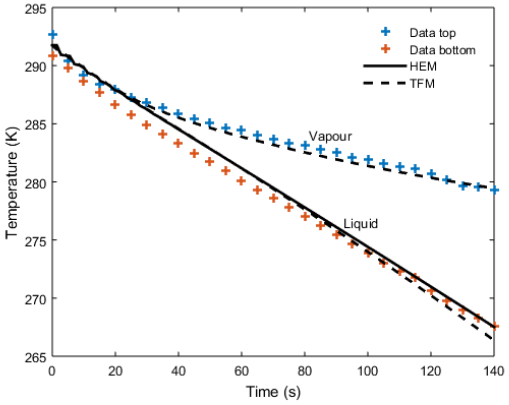

Figure 5.14: Predicted (from the HEM and TFM models) and measured temperature variations as a function of time 150 m from the closed end for the DUT puncture decompression test.

Much the same as in the case of the INERIS test, thermal stratification is observed in the measurements with a maximum temperature difference of ca. 15 K between the

liquid and vapour phases, which is predicted correctly by the TFM model. On the other hand, the HEM model prediction closely follows the measured liquid phase temperature but completely misses the vapour phase.

Moving on to the predictions of the evolution of the vapour molar fraction 150 m from the pipe closed end during decompression, as plotted in figure 5.15. As it may be observed, in comparison to the TFM model, once again, the HEM model predicted a higher vapour phase molar fraction throughout the simulated decompression process.

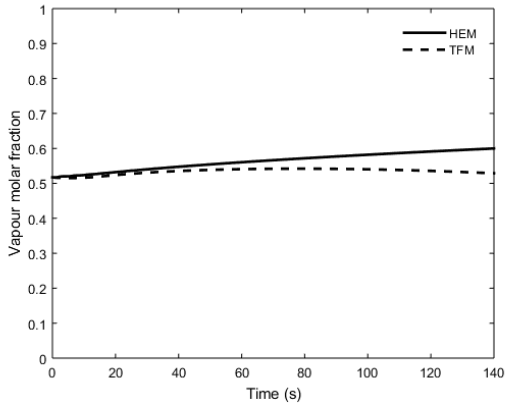

Figure 5.15: HEM and TFM model predictions of the vapour phase mole fraction variation as a function of time 150 m from the closed end for the DUT puncture decompression test.

Finally, the predictions of the remaining mass from both HEM and TFM models are compared in figure 5.16.

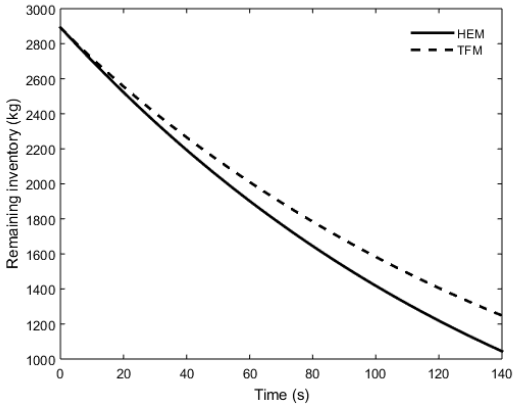

Figure 5.16: Predicted (from the HEM and TFM models) remaining fluid mass as a

function of time for the DUT puncture decompression test.

From the above plot, the HEM model again under-predicts the remaining inventory during decompression.

5.4.3 Effect of Finite Interface Momentum Exchange

In the case of stratified flow, finite interface momentum exchange may result in different phasic velocities (often referred to as 'phase slip'). The TFM model simulated CO_2 liquid and vapour phase velocities along the entire length of the pipe at 5 and 50 s following decompression for both the INERIS (table 5.5) and DUT (table 5.6) tests are plotted in figure 5.17.

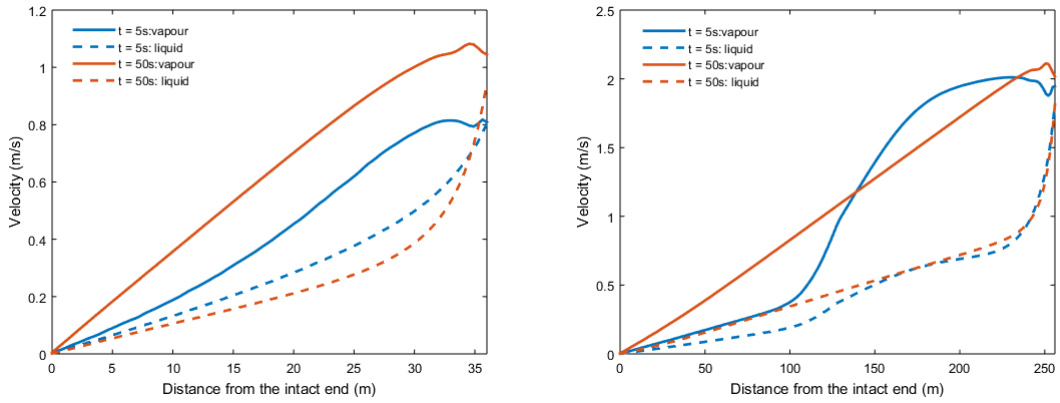

(a) (b)

Figure 5.17: Predicted vapour and liquid phase velocities along the length of the pipe at two decompression times (of 5 and 50 s) for both the INERIS (a) and DUT (b) tests.

As it may be observed from the data, in both cases, at any given time during depressurisation, the stratified vapour phase is at a higher velocity than the stratified liquid phase. The difference, or phase slip becomes more significant on approaching the release end of the pipe. Close to the release end (ca. 30 m and 230 m from the release ends for the INERIS and DUT tests, respectively), phase slip decreases rapidly due to the HEM assumption imposed in the puncture outflow boundary condition in the formulation of the TFM.

In order to isolate and hence demonstrate the impact of phase slip on the transient flow behaviour during pipeline puncture decompression, fluid/wall heat transfer and friction terms in both the HEM and TFM models are disabled. Figures 5.18 (a) to (d) show the corresponding simulated and measured pressure, temperature vapour molar fraction and remining CO_2 inventory in pipe data for the DUT test (table 5.6).

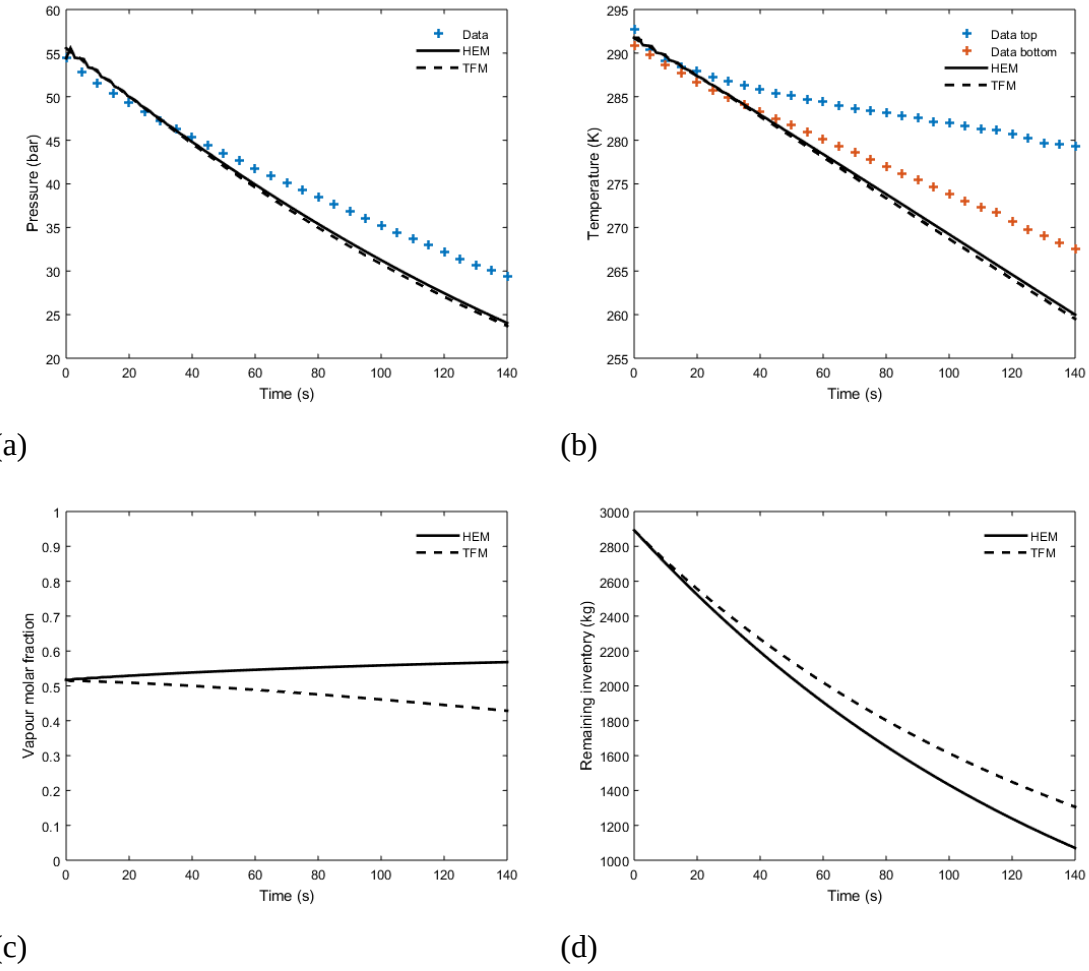

Figure 5.18: Predicted variations of pressure (a), temperature (b), vapour molar fraction (c) and remianing mass (d) from the HEM and TFM models as a function of time 150 m from the closed end for the DUT puncture decompression test. Also included in (a) and (b) are the corresponding experimental measurements.

As it may be observed from the pressure data in figure 5.18 (a), both model predictions closely agree with each other, producing a faster rate of depressurisation as compared to the measured data. This is in turn reflected in the faster rate of fluid temperature drop as compared to the measure data (figure 5.18 (b)), as expected. The

close agreement between two model predictions for the pressure data (figure 5.18 (a)) indicates that phase slip has minimal effect on the rate of depressurisation. However, this is only true given that the phasic velocities during pipeline puncture decompression are very small (< 2 m/s, figure 5.17); the flow upstream of the puncture is approximately stagnant.

In figure 5.18 (c), a comparison of the HEM and TFM model predictions of the vapour molar fraction shows that at any given time during the simulated depressurisation process, the TFM model consistently predicts a lower vapour fraction, as compared to the HEM based prediction, with the difference increasing with the passage of time. This is due to that, in the case of the TFM model, the vapour phase is at a higher velocity as compared to the liquid phase (figure 5.17), while in the case of the HEM model, both phases are at the same velocity (mechanical equilibrium).

Finally, from figure 5.18 (d), a lower release flowrate is predicted by the TFM model as compared to the HEM model. The same observations are made in model validation (figures 5.12 and 5.16). This is again attributed to phase slip.

5.5 Concluding Remarks

- The TFM model capability presented in Section 2.2.4, Chapter 2 has been extended to predict heterogeneous flows during pipeline puncture decompression by incorporating a puncture outflow boundary condition;
- A numerical scheme, AUSM-MUSTA for solving the TFM model equations was proposed. Standard numerical tests showed that the proposed scheme was both accurate and numerically efficient, combining both features of the previously established AUSM and MUSTA schemes;
- The developed model was successfully validated against the experimental data recorded during medium- and large-scale pipeline puncture decompression tests. The experimentally observed thermal stratification between the vapour and liquid phases due to heterogeneous flow was accurately captured;
- The HEM model on the other hand was shown to be incapable of correctly predicting the vapour phase temperature. As a result, the experimentally observed fluid phase thermal stratification cannot be simulated by the HEM

model. In practice, thermal stratification will result in a thermal stress gradient across the pipe wall. The above coupled with the prevailing pressure stress may therefore in extreme circumstances poses the risk of pipeline rupture especially if the pipe wall temperature falls below its ductile-brittle transition temperature;

- Phase slip during pipeline puncture decompression was observed in the TFM model predictions; the vapour phase was found to travel at a higher velocity as compared to the liquid phase except close to the release end (where the two-phase flow is assumed to be at homogeneous equilibrium);
- The comparisons between the HEM and TFM model predictions showed that phase slip resulted in lower vapour phase molar fractions and release flowrates during most of the decompression process.

Chapter 6:
Modelling of the Jet Expansion of Outflows Released from Pressurised Containments

6.1 Introduction

In foregoing chapters, we mainly focused on the decompression modelling in the event of containment failure, or during scheduled maintenances, and one of the key predictions is the discharge outflow. Such data is used in determining the dispersion of the toxic vapour cloud, the possibility of jet fire as well as vapour cloud explosions in the case of hydrocarbon, and hence the minimum safety distance from populated areas (Oke et al. 2003; Cleaver et al. 2003; Cumber 2007; Mahgerefteh et al. 2007).

In performing a dispersion analysis, two additional models, the jet expansion model and the dispersion model, are required. With simulated outflow data as the input, the former determines the corresponding fully expanded jet conditions, and the latter in turn utilises such conditions to determine the dispersion behaviour of the emerging toxic cloud (e.g., CO_2 cloud).

Dispersion modelling is a mature subject having received considerable attention in the past decades (Cleaver & Edwards 1990; Cleaver et al. 1995; Witlox et al. 2009; Gant et al. 2014; Wen et al. 2016). For CO_2, recent publications include (Woolley et al. 2013; Gant et al. 2014; Wen et al. 2016), all showing good agreement with available experimental measurements, such as the CO_2 concentrations as a function of distance from the release point.

On the other hand, the modelling of jet expansion to the ambient pressure is often based on the solution of the integral form of the mass, momentum and energy conservation equations, assuming frictionless, adiabatic and laminar flow conditions without air entrainment (Bricard & Friedel 1998; Witlox et al. 2007). Neglecting interactions between the jet and the surroundings (in the form of mass, momentum and energy exchange) may be justified provided that the length scale of jet expansion is short enough (Bricard & Friedel 1998). However, as the high-speed jet penetrates the stagnant surrounding air, turbulences generation at the jet boundary is expected (due to the large velocity gradient at the jet boundary). The kinetic energy of these

turbulent motions, also known as the turbulent kinetic energy, is acquired directly from the mean flow of the expanding jet (see Section A1.5.2, Appendix). This leads to the loss of the jet mean flow kinetic energy, which may be significant and should thus be considered.

This chapter presents the development and testing of an integral multi-phase jet expansion model accounting for turbulence generation during its expansion. Section 6.2 presents the model formulation. Also included is a description of a CFD turbulent jet model which is later used to verify the predictions from the developed integral model. In Section 6.3, using the puncture release of CO_2 from a high-pressure vessel as a working example, the integral model's performance is evaluated by comparing its predictions against the rigorous but computationally demanding CFD model. Furthermore, the importance of accounting for turbulence generation is also demonstrated by comparing the predictions from the present model to the previous integral model where such effect is ignored. Conclusions are drawn in Section 6.4.

6.2 Theory

6.2.1 Integral Jet Expansion Model

Following Bricard & Friedel (1998), during jet expansion, the emerging fluid phases are assumed to be at thermodynamic and mechanical equilibrium (i.e. the Homogeneous Equilibrium Mixture (HEM) assumption). Furthermore, air entrainment, turbulence, friction and heat transfer between the jet and its surroundings are also neglected. The resulting integral form of the conservation equations of mass, momentum and energy of the expanding jet can be written as follows (Bakkum & Duijm 2005):

$$\tilde{\rho}_1 \tilde{u}_1 A_1 = \tilde{\rho}_2 \tilde{u}_2 A_2 \qquad 6.1$$

$$-\tilde{\rho}_1 \tilde{u}_1 A_1 \tilde{u}_1 + \tilde{\rho}_2 \tilde{u}_2 A_2 \tilde{u}_2 = A_1 \left(\tilde{p}_1 - \tilde{p}_2\right) \qquad 6.2$$

$$\tilde{h}_1 + \tilde{u}_1^2/2 = \tilde{h}_2 + \tilde{u}_2^2/2 \qquad 6.3$$

where $\tilde{u}_{1,2}$, $\tilde{p}_{1,2}$, $\tilde{\rho}_{1,2}$ and $\tilde{h}_{1,2}$ are respectively the averaged velocity, pressure, density and enthalpy over the jet cross-section area, *A*. The subscripts, 1 and 2 stand for the

locations at the release point and at full expansion, respectively. Solving the above algebraic system together with an Equation of State (EoS), the jet flow conditions such as its density, enthalpy, velocity and area at full expansion are obtained.

However, as stated in Section 6.1, turbulence generation may lead to the loss of the jet mean kinetic energy. To account for such effect, an additional term, k_t representing the turbulent kinetic energy following expansion to ambient pressure is added to equation 6.3. The modified energy conservation is given by:

$$\tilde{h}_1 + \tilde{u}_1^2/2 = \tilde{h}_2 + \tilde{u}_2^2/2 + k_t \qquad 6.4$$

Adequate modelling is required for k_t; according to Richards & Norris (2011), by assuming constant pressure and shear stress in the direction transverse to the flow and applying k-ε turbulence models, k_t can be approximated by the following for flows away from solid boundaries:

$$k_t = \frac{u_\tau^2}{\sqrt{C_\mu}} \qquad 6.5$$

where C_μ is a constant of 0.09, and u_τ is the friction velocity. For calculating u_τ, the velocity profile along the jet radius is first approximated by a logarithmic velocity profile given by:

$$u(r) = \frac{u_\tau}{\kappa} \ln\left(\frac{z + z_0}{z_0}\right) \qquad 6.6$$

where z denotes the distance from jet boundary, κ is the Von Karman constant of 0.41, z_0 is the aerodynamic surface roughness length of 0.004 (Jacobson 2005). Averaging equation 6.6 (with function translations) across the jet cross-section area gives an expression relating $\tilde{u}_2$ to u_τ:

$$\tilde{u}_2 = \frac{u_\tau}{\kappa \pi R_2^2} \int_0^{R_2} \left[\ln\left(\frac{(-r + R_2) + z_0}{z_0}\right) 2\pi r \right] dr \qquad 6.7$$

where r is the distance from the jet centre, and R_2 is the jet radius corresponding to A_2.

To this point, the sought solution for k_t is complete.

It should be noted that, as both previous and present integral models neglect dissipation (energy conversion between thermal and mechanical energy), the predictions of the jet average enthalpy at full expansion, $\tilde{h}_2$ and hence other thermal properties from the two models, are equal. As a result, the additional consideration of the turbulence effect by the present model is reflected on the predictions of $\tilde{u}_2$ and A_2. They are obtained by solving equations 6.1, 6.4, 6.5 and 6.7 numerically using Matlab.

For simplicity, in later sections, the previous integral jet expansion model and the present model in this study are respectively referred to as IJEM and IJEM-T (where 'T' stands for turbulence).

6.2.2 CFD Turbulent Jet Expansion Model

In order to test the performance of IJEM and IJEM-T, their model predictions are compared to a rigorous CFD jet expansion model.

The following describes the corresponding conservation equations and the turbulence model used in this study.

6.2.2.1 Governing Conservation Equations

The Reynolds-Average Navier-Stokes multiphase mixture model is used to describe the flow during jet expansion. Following Section A1.5.2, Appendix, the resulting mass, momentum and energy conservation equations of a HEM are respectively given by:

$$\frac{\partial}{\partial t}\bar{\rho} + \nabla \cdot \bar{\rho}\bar{\boldsymbol{u}} = 0 \qquad 6.8$$

$$\frac{\partial}{\partial t}\bar{\rho}\bar{\boldsymbol{u}} + \nabla \cdot \left(\bar{\rho}\bar{\boldsymbol{u}}\bar{\boldsymbol{u}} + \bar{p}\boldsymbol{I}\right) - \nabla \cdot \left(\bar{\boldsymbol{\tau}} + \bar{\rho}\overline{\boldsymbol{u}'\boldsymbol{u}'}\right) = 0 \qquad 6.9$$

$$\frac{\partial}{\partial t}\bar{\rho}\bar{E} + \nabla \cdot \left(\bar{\rho}\bar{\boldsymbol{u}}\bar{E} + \bar{p}\boldsymbol{I} \cdot \bar{\boldsymbol{u}}\right) - \nabla \cdot \left(\bar{\rho}\overline{\boldsymbol{u}'h} + \bar{\boldsymbol{u}} \cdot \bar{\rho}\left(\overline{\boldsymbol{u}'\boldsymbol{u}'}\right) - \bar{\boldsymbol{\tau}} \cdot \bar{\boldsymbol{u}}\right) = 0 \qquad 6.10$$

where $\bar{\rho}$, $\bar{p}$, $\bar{T}$ and $\bar{E}$ are the time-averaged mean flow density, pressure, temperature and total energy ($\bar{E} = \bar{e} + \bar{\boldsymbol{u}}^2/2$), respectively. $\boldsymbol{\tau}$ and $\bar{\rho}\overline{(\boldsymbol{u}'\boldsymbol{u}')}$ are respectively the viscous and Reynolds stress tensors. The closure relation for $\boldsymbol{\tau}$ is given in equation A1.52, Appendix, and $\bar{\rho}\overline{(\boldsymbol{u}'\boldsymbol{u}')}$ is modelled using turbulent-viscosity model which is discussed in the following (see also Section A1.5.2, Appendix).

6.2.2.2 Turbulence Modelling.

According to the turbulent-viscosity assumption, the Reynolds stress tensor is related to the mean strain rate tensor (see also equations A1.58 to A1.60, Appendix):

$$\bar{\rho}\overline{\boldsymbol{u}'\boldsymbol{u}'} = \bar{\rho}\frac{2}{3}k\boldsymbol{I} + \bar{\rho}2\mu_t\boldsymbol{s} \tag{6.11}$$

where μ_t is the turbulent viscosity, k is the turbulent kinetic energy, $\boldsymbol{s}$ is the mean strain rate tensor given by:

$$\boldsymbol{s} = \frac{\nabla\bar{\boldsymbol{u}}}{2} + \frac{\left(\nabla\bar{\boldsymbol{u}}\right)^T}{2} \tag{6.12}$$

For computing μ_t, as a first approximation, the k-ω Shear Stress Transport (SST) model (Menter et al. 2003) is employed, given by:

$$\frac{\partial\left(\bar{\rho}k\right)}{\partial t} + \cdot\nabla\left(\bar{\rho}\bar{\boldsymbol{u}}k\right) = \nabla\cdot\left(\left(\mu + \frac{\mu_t}{\sigma_k}\right)\nabla k\right) + P_k - \beta^*\bar{\rho}k\omega \tag{6.13}$$

$$\frac{\partial\left(\bar{\rho}\omega\right)}{\partial t} + \nabla\cdot\bar{\rho}\bar{\boldsymbol{u}}\omega = -\nabla\cdot\left(\left(\mu + \frac{\mu_t}{\sigma_\omega}\right)\nabla\omega\right) + P_\omega - \beta\bar{\rho}\omega^2 + 2\bar{\rho}\left(1 - F_1\right)\frac{\mu_t}{\sigma_{\omega,2}k}\nabla\omega\cdot\nabla k \tag{6.14}$$

where P_k and P_ω are the effective production rates of the turbulent kinetic energy and its specific dissipation, respectively. σ_k, σ_ω, $\sigma_{\omega,2}$ β and β^* are model coefficients (see (Rocha et al. 2014)). F_1 is the blending function. The k-ω SST model reduces to the k-

ε model (equations A1.62 and A1.66, Section A1.5.2, Appendix) with F_1 = 1 and to the k-ω model with F_1 = 0 (equations A1.62 and A1.69, Appendix).

According to Menter et al. (2003), the incorporation of the blending function enables the k-ω SST formulation to yield the best behaviour of both the standard k-ε and k-ω models; it outperforms the k-ε model in predicting the turbulence close to the wall, while retains its accuracy in the non-turbulent free-stream away from the wall (unlike the standard k-ω model).

In addition, modifications of the turbulent kinetic energy transport equation 6.13 are required to take the compressibility effect into account. Following Sarkar et al. (1991), a dilation dissipation term given by $S_k = -\overline{\rho} M_t^2 \varepsilon$ is introduced to the RHS of equation 6.13, where M_t is the turbulent Mach number defined as $M_t = \sqrt{2k} / c$.

Finally, the turbulent viscosity is calculated following $\mu_t = C_\mu \overline{\rho} k^2 / \left(1 + M_t^2\right) \varepsilon$.

The resulting overall system is solved in ANSYS Fluent 14.0 using a pressure-based implicit scheme (the PISO scheme) (ANSYS 2013a).

6.2.2.3 Boundary Conditions

Figure 6.1 (a) shows the axisymmetric computation flow domain adopted for simulating the expanding CO_2 jet downstream of a 6 mm diameter, 9 mm long release nozzle. The computational flow domain dimensions are set as 200 mm across and 1000 mm long to fully envelop the expanding jet observed in the experiment (figure 6.1 (b)).

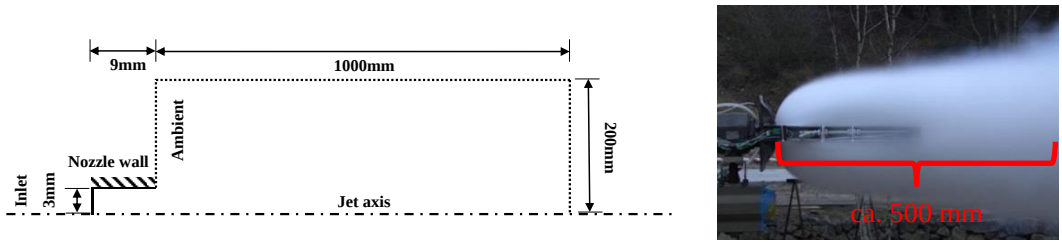

(A) (B)

Figure 6.1: Computational domain (a) and a photograph (b) for the expanding jet.

To close the conservation equations 6.8 to 6.10 and the transport equations 6.13 and 6.14, the boundary conditions adopted for the flow are specified at the edges of the simulated flow domain (see figure 6.1 (a)):

(i) Inlet: Specified mass flowrate, pressure and temperature; for k and ω, they are usually small at the inlet and are estimated in terms of the turbulence intensity, I and length scale, l given by (ANSYS 2013c):

$$I = 0.16\,\mathrm{Re}^{-1/8} \qquad 6.15$$

$$l = 0.07 D_{w,in} \qquad 6.16$$

where Re is the Reynolds number and $D_{w,in}$ is the orifice diameter. k and ω are then estimated by:

$$k = \frac{3}{2}(uI)^2 \qquad 6.17$$

$$\omega = \frac{k^{1/2}}{0.09^{1/4} l} \qquad 6.18$$

(ii) Wall: Standard wall functions (ANSYS 2013b);

(iii) Outlet (ambient): Constant pressure; zero-gradient boundary condition for other relevant variables;

(iv) Jet axis: Symmetry plane.

The entire flow domain is initialised with stagnant air at the ambient conditions corresponding to each test (see table 6.1).

The discretised flow domain with 0.3 million cells was adopted for the simulations (see figure A5.9, Appendix for grid convergence test results). The timestep size is 5×10^{-7} s.

6.2.3 Thermodynamics

In this study, thermal properties of each fluid phase and phase equilibrium data are computed using extended PR EoS (Martynov et al. 2013) capable of handling the solid phase.

On an important note, unlike in Chapter 3, solid-vapour-liquid three-phase coexistence at the triple point is neglected; all liquid is assumed to transform into solid phase at the triple point, and a smoothing function is used to connect the thermal properties of the saturated liquid and solid phases. Following Woolley et al.(Woolley et al. 2013), the smoothing function reads:

$$\phi(T) = \left(1 - S(T)\right)\phi_l(T) + S(T)\phi_s(T) \tag{6.19}$$

where:

$$S(T) = 0.5 + 0.5\tanh\left(\frac{T - 216.7}{b}\right) \tag{6.20}$$

where b is the smoothing interval of 4 K.

6.3 Results and Discussion

Six case studies of assumed high-pressure vessel release scenario, applying IJEM, IJEM-T and the CFD model (as base case) are carried out to simulate the jet expansion.

6.3.1 About the Case Studies

For the purpose of this study, the relevant initial conditions for the high pressure vessel CO_2 release tests conducted by Hébrard et al. (2016) are adopted for our simulations. In these tests, a 2 m^3 heavily insulated spherical CO_2 tank was connected to a 6 m length, 50.8 mm i.d. very smooth steel pipe incorporating a 9 mm length and 6 mm i.d. orifice nozzle at its end. The other end of the pipe terminated at a height of ca. 150 cm above the vessel's base. The vessel was initially partly filled with saturated CO_2.

The adopted upstream and ambient conditions are given in table 6.1 for each of the six case studies. The upstream conditions are assumed constant. Case studies 1a – 3a are for saturated vapour phase upstream whereas case studies 1b – 3b are for saturated liquid phase upstream. Table 6.1 also shows the corresponding calculated outflow conditions based on isentropic expansion approximation (Moody 1965).

Table 6.1: Relevant flow conditions for all case studies. The subscripts, 0, *amb* and 1 represent the upstream, ambient and outflow, respectively. All symbols are defined previously.

	Case study no.	T_0 (K)	p_0 (bar)	T_{amb} (K)	p_{amb} (bar)
Vapour upstream	1a	264.3	27	272.1	1
	2a	280.1	44	281.6	
	3a	278.1	39	278.1	
Liquid upstream	1b	264.3	27	272.1	
	2b	280.1	44	281.6	
	3b	278.1	39	278.1	

(Table 6.1 continued)

	Case study no.	$\tilde{T}_1$ (K)	$\tilde{p}_1$ (bar)	$\tilde{\rho}_1$ (kg/m^3)	$\tilde{e}_1$ (×10^5 J/kg)	$\tilde{u}_1$ (m/s)	$\tilde{\rho}_1\tilde{u}_1A_1$ (kg/s)	Liquid phase mass fraction
Vapour upstream	1a	246.0	16	43.7	6.73	198.0	0.24	0.07
	2a	260.7	25	72.8	6.68	188.4	0.38	0.11
	3a	258.5	23	67.2	6.83	190.6	0.36	0.10
Liquid upstream	1b	256.3	22	501.4	4.92	42.3	0.60	0.94
	2b	271.2	33	523.0	5.23	55.4	0.81	0.91
	3b	267.2	30	458.7	5.19	57.1	0.74	0.90

6.3.2 CFD Model Results

Figures 6.2 to 6.5 respectively represent the CFD simulation results for the pressure, temperature, liquid/solid phase mass fraction, and velocity profiles along the jet axis from the release point at 1.0 s following the start of the simulation. Also included are the corresponding contour plots.

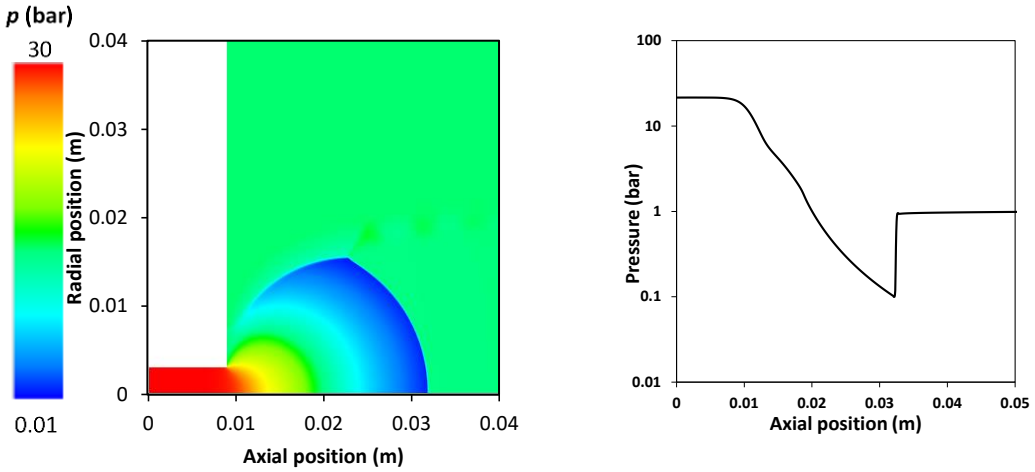

(a) (b)

Figure 6.2: Pressure contour plot across the expanding CO_2 jet (a) and the pressure profile along the jet axis (b) at 1.0 s for case study 1b.

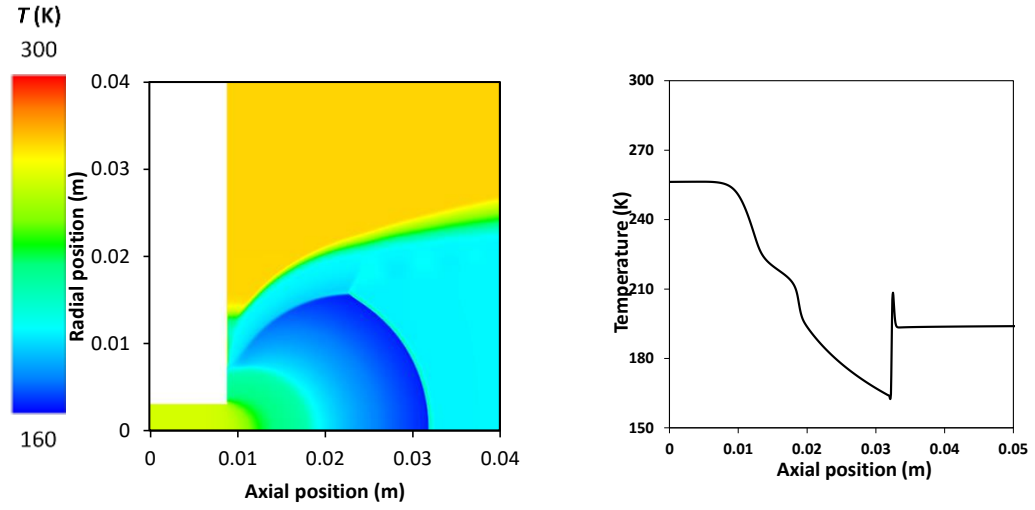

(a) (b)

Figure 6.3: Temperature contour plot across the expanding jet (a) and the temperature profile along the jet axis (b) at 1.0 s for case study 1b.

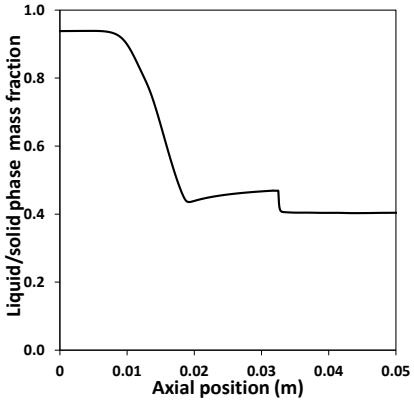

Figure 6.4: Liquid/solid phase mass fraction profile along the jet axis (b) at 1 s for case study 1b.

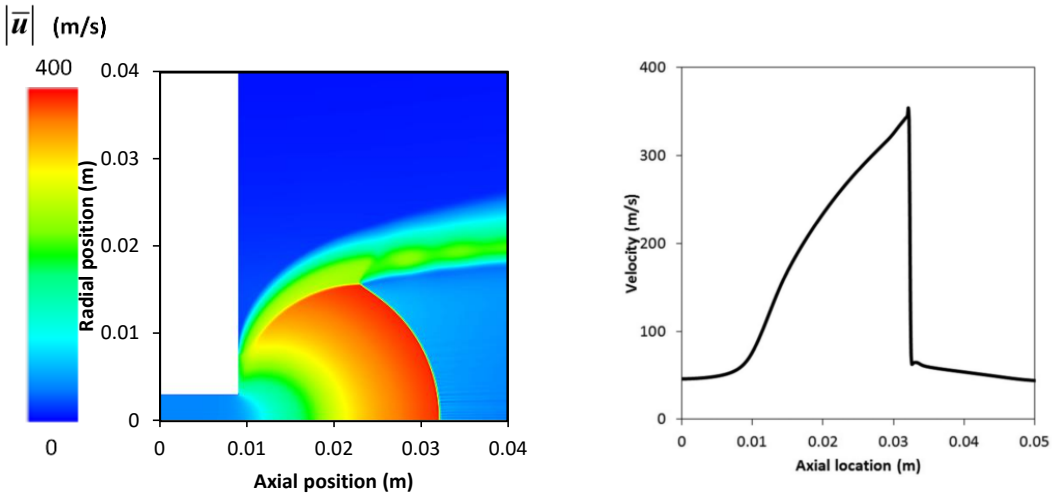

(a) (b)

Figure 6.5: Velocity contour plot of the expanding jet (a) and the velocity profile along the jet axis (b) at 1 s for Case study 1b.

From these figures, three common trends may be observed. In the order of appearance these are: (i) An initial plateau representing the almost constant flow conditions along the 9 mm long nozzle; (ii) A Discontinuity corresponding to the location of the Mach shock (ca. 0.03 m from the release point). (iii) A second plateau corresponding to flow pressure stabilisation at the ambient pressure (1.0 bar; see figure 6.2 (b)). At this point, the jet remains at its sublimation temperature of 194.3 K (see figure 6.3) and solid phase CO_2 is present (at mass fraction of ca. 0.40; figure 6.4).

Figure 6.6 is the corresponding CFD contour plot for CO_2 mass fraction. As it may be observed, air entrainment only occurs at the jet boundary as most of the jet core is pure CO_2. This supports the validity of negligible air entrainment assumption employed in the development of the integral jet expansion models (both the previous and present models).

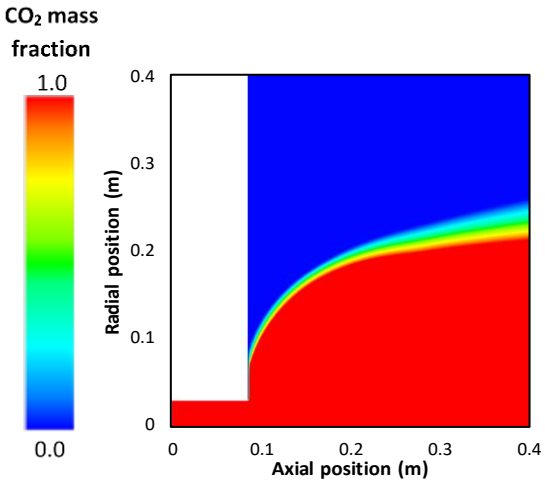

Figure 6.6: CO_2 mass fraction (including all fluid phases) contour plot of the expanding jet at 1s for case study 1b.

Figures 6.7 to 6.9 respectively represent the corresponding CFD model predictions (solid lines) for the momentum flux, temperature and density profiles along the jet radius at full expansion (ca. 0.03 m from the release point). The origin of each plot represents the jet centre. Additionally, in order to enable comparisons between the CFD and the integral model predictions (presented in the next section), the corresponding average values over the jet cross-section area are given by the dotted lines. The cut off points (dotted vertical lines) represent the locations of the jet/air boundaries; they are obtained by conserving the discharge mass flowrate (table 6.1).

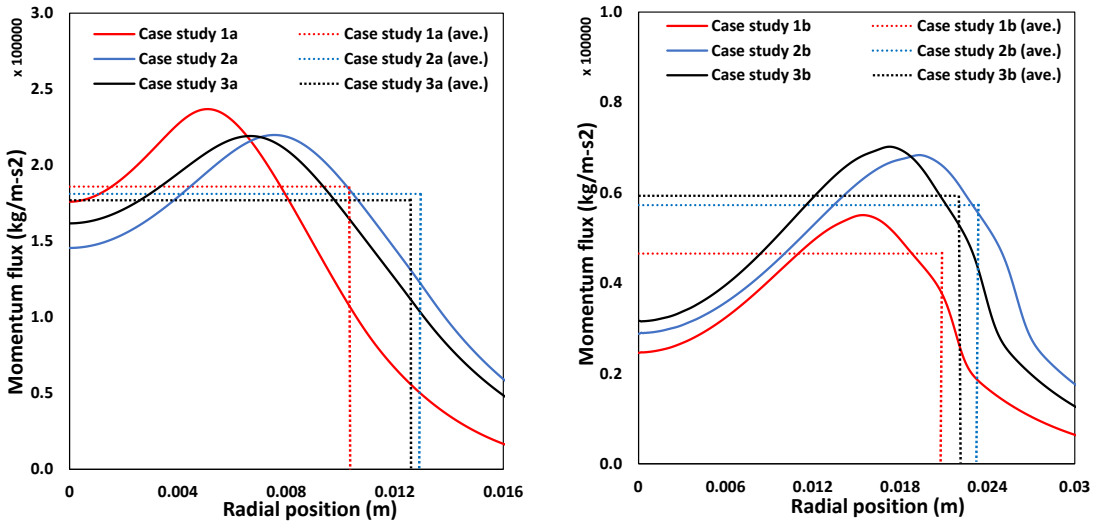

(a) (b)

Figure 6.7: Fully expanded jet momentum flux profiles along the jet radius for the various case studies (see table 6.1); (a): Case studies 1a – 3a (saturated vapour upstream); (b): Case studies 1b – 3b (saturated liquid upstream). Solid lines: CFD simulation; Dotted lines: average values over the jet cross-section area at full expansion.

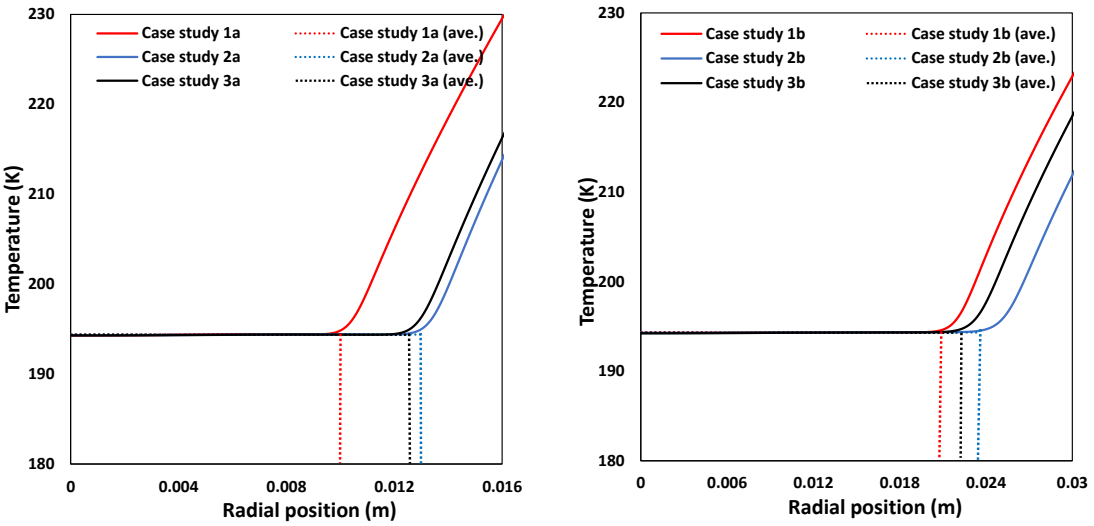

(a) (b)

Figure 6.8: Fully expanded jet temperature profiles along the jet radius for the various tests (see table 6.1); (a): Case studies 1a – 3a (saturated vapour upstream);

(b): Case studies 1b – 3b (saturated liquid upstream). Solid lines: CFD simulation; Dotted lines: average values over the jet cross-section area at full expansion.

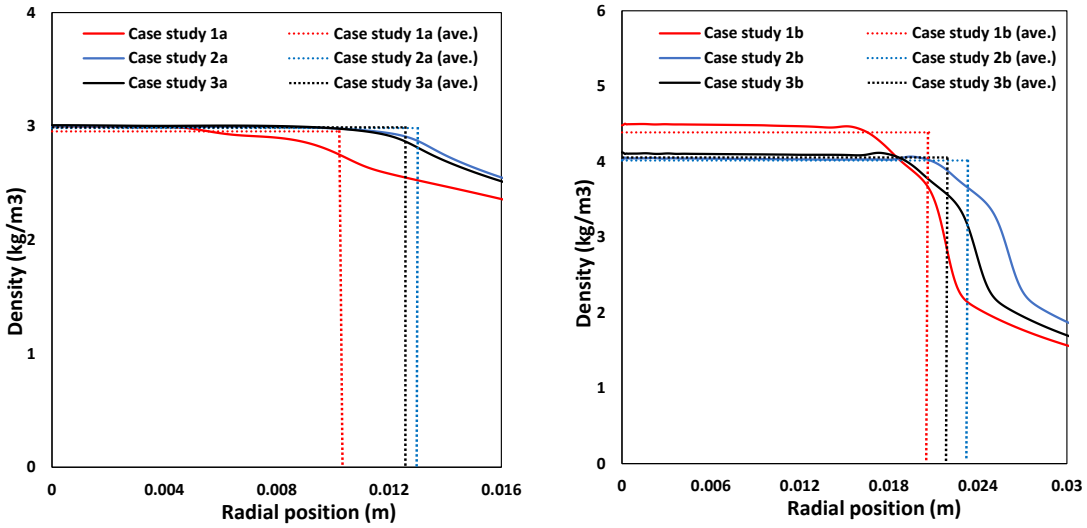

(a) (b)

Figure 6.9: Fully expanded jet density profiles along the jet radius for the various tests (see table 6.1); (a): Case studies 1a – 3a (saturated vapour upstream); (b): Case studies 1b – 3b (saturated liquid upstream). Solid lines: CFD simulation; Dotted lines: average values over the jet cross-section area at full expansion.

From the figures, a larger jet radius is obtained in the case of the liquid CO_2 upstream (1b – 3b) as compared to the vapour upstream (1a – 3a). Also, the jet radius increases with an increase in the upstream pressure (table 6.1).

Referring to the temperature plots (figure 6.8) as it may be observed, in all cases the jet temperature remains constant at the CO_2 sublimation temperature (194.3 K). The jet boundary is marked by a rapid rise in temperature due to the mixing with surrounding warmer air.

Turning to figure 6.9 (b), as expected in the case of the liquid upstream, a rapid drop in the density is observed on crossing the jet boundary due to the mixing with less dense surrounding air. This trend is less pronounced in the case of the vapour upstream (figure 6.9 (a)).

All relevant CFD simulated average values are also summarised in table 6.2.

Table 6.2: CFD model simulated fully expanded jet conditions. The subscript, *CFD* denotes the CFD turbulent jet expansion model.

	Case study no.	$\tilde{T}_{2,CFD}$ (K)	$\tilde{p}_{2,CFD}$ (bar)	$\tilde{\rho}_{2,CFD}$ (kg/m^3)	$\tilde{e}_{2,CFD}$ (×10^5 J/kg)	Solid phase mass fraction	$R_{2,CFD}$ (m)	$(\tilde{\rho}\tilde{u}\tilde{u})_{2,CFD}$ (×10^5 kg/m-s^2)
Vapour upstream	1a	194.3	1	2.95	6.44	0.05	0.0010	1.86
	2a			2.98	6.39	0.06	0.0129	1.81
	3a			2.99	6.37	0.07	0.0125	1.77
Liquid upstream	1b			4.39	4.65	0.40	0.017	0.46
	2b			4.02	4.99	0.34	0.019	0.57
	3b			4.06	4.93	0.35	0.018	0.59

6.3.3 Integral Model Results

Table 6.3 represents the fully expanded jet conditions (including temperature, pressure, density, internal energy, CO_2 solid phase mass fraction, jet radius and momentum flux) for all the test scenarios as predicted by IJEM-T. Also included are the jet radius and momentum flux predictions from IJEM without accounting for turbulence generation, for comparison. Given that dissipation is assumed negligible, the predicted thermal property data (e.g. the internal energy and solid phase mass fraction) are the same for both integral models (see Section 6.2.1).

Table 6.3: The fully expanded jet conditions from IJEM and IJEM-T.

	Case study no.	$\tilde{T}_2$ (K)	$\tilde{p}_2$ (bar)	$\tilde{\rho}_2$ (kg/m^3)	$\tilde{e}_2$ (×10^5 J/kg)	Solid phase mass fraction
Vapour upstream	1a	194.3	1	3.06	6.29	0.08
	2a			3.1	6.23	0.10
	3a			3.09	6.25	0.09
Liquid upstream	1b			4.68	4.66	0.40
	2b			4.29	4.94	0.35
	3b			4.34	4.90	0.36

(Table 6.3 continued)

	Case study no.	R_2 by IJEM (m)	R_2 by IJEM-T (m)	$(\tilde{\rho}\tilde{u}\tilde{u})_2$ by IJEM (×10^5 kg/m-s^2)	$(\tilde{\rho}\tilde{u}\tilde{u})_2$ by IJEM-T (×10^5 kg/m-s^2)
Vapour upstream	1a	0.0084	0.0097	4.13	1.99
	2a	0.011	0.013	4.04	2.12
	3a	0.010	0.012	4.08	2.11
Liquid upstream	1b	0.017	0.019	0.91	0.51
	2b	0.019	0.022	1.19	0.70
	3b	0.018	0.021	1.21	0.69

In what follows, a discussion of the model comparison results is provided.

6.3.4 Comparison of the Different Model Results

In this section, comparisons of the IJEM and IJEM-T predictions against the averaged CFD simulation data for the fully expanded jet conditions, including the density, internal energy and momentum flux are presented. (As the fully expanded jet is at solid/vapour equilibrium, the pressure and temperature data are excluded from the comparisons.) The results are displayed in figures 6.10 to 6.12 with a 45 degree line

drawn in each figure to provide a direct measure of the degree of agreement between the integral and the CFD model predictions.

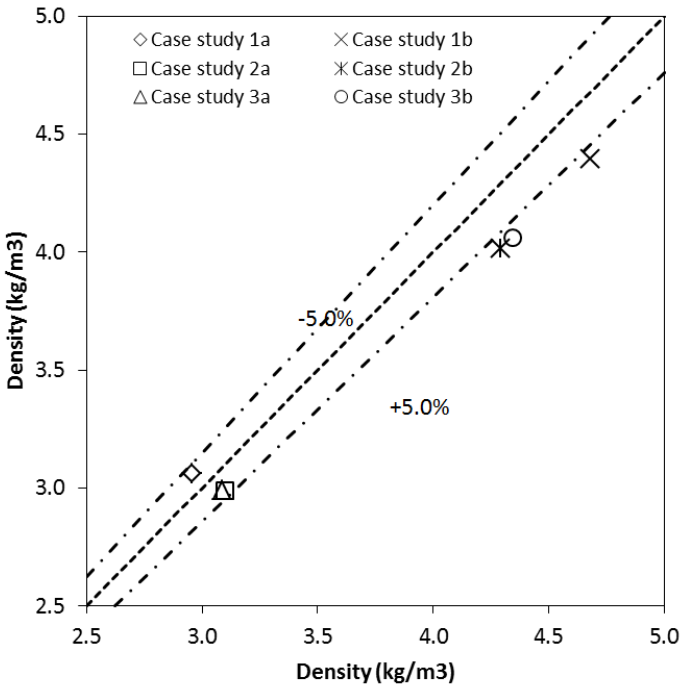

Figure 6.10: Comparison of the predicted jet density at full expansion; the dash-dot lines show the percentage difference (5%) of the integral model predictions from the CFD model predictions.

Figure 6.10 is the comparison of the density predictions. Since thermal property predictions (i.e. the density and internal energy) are the same for both integral models, only one set of data is presented. As may be observed, the maximum percentage difference between the integral models and the CFD model is ± 5%.

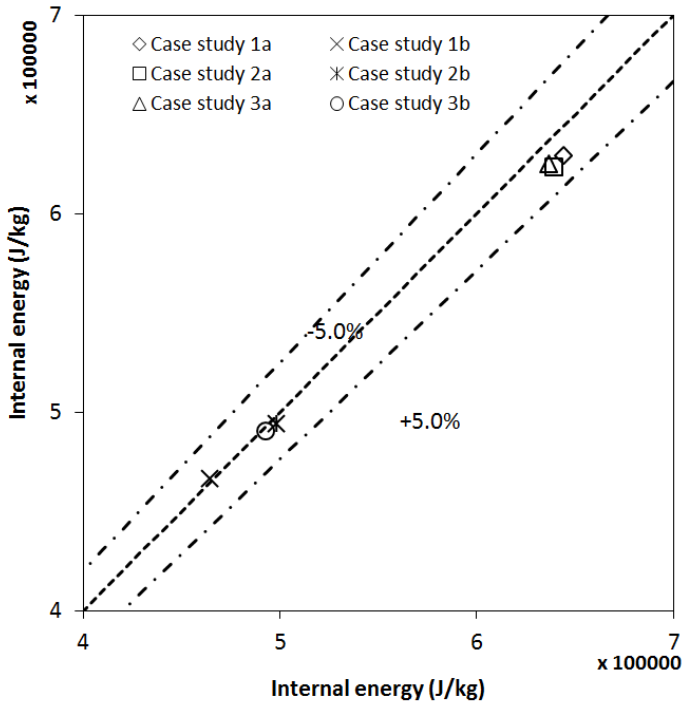

Figure 6.11: Comparison of the predicted jet internal energy at full expansion; the dash-dot lines show the percentage difference (5%) of the integral model predictions from the CFD model predictions.

Turning to figure 6.11 showing the comparison of the internal energy predictions, the reasonably good agreement (± 5 %) between the integral and CFD models is indicative of the validity of negligible energy dissipation assumption (see Section 6.2.1) made in the integral models.

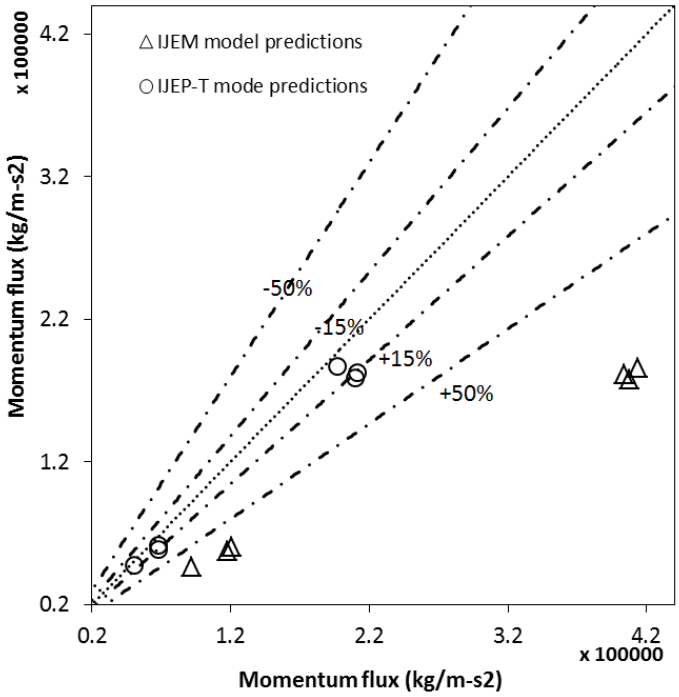

Figure 6.12: Comparison of the predictions of the averaged momentum flux, $(\tilde{\rho}\tilde{u}\tilde{u})_2$ from IJEM, IJEM-T and the CFD model; the dash-dot lines show the percentage difference (5%) of the integral model predictions from the CFD model predictions.

Moving on to figure 6.12 for the comparison of the momentum flux predictions from the three models, IJEM grossly over predicts the momentum flux by more than 50%. In the case of IJEM-T, which accounts for the mean flow kinetic energy loss due to turbulence generation, this disagreement is significantly reduced, producing a maximum overestimate of ca. 15%. This finding is significant given that the jet momentum largely determines the subsequent 'spread' of the dispersing cloud.

6.4 Concluding Remarks

- An integral jet expansion model was developed accounting for the mean flow kinetic energy loss due to turbulence generation;
- Releases from a pressurised CO_2 storage vessel were selected as test cases for model verification. The corresponding predictions of the fully expanded jet

conditions from both the integral models, IJEM and IJEM-T were compared against a rigorous but computationally demanding CFD model;

- For the thermal property predictions such as density and internal energy, all the three models were in good agreement with a maximum difference of ca. ±5%
- With regards to momentum predictions, IJEM without accounting for turbulence was observed to over predict the fully expanded jet momentum flux by as much as 50%. The developed IJEM-T on the other hand significantly reduced the percentage error to about 15%;
- Given that the subsequent dispersion of the toxic cloud is largely dependent on the jet momentum, the improved accuracy of the developed model can be significant in the relevant quantitative consequence analysis (e.g. predicting the safety distance from populated areas);
- It is noted that the model predictions are yet to be validated against experimental data. To this end, as part of the CO_2QUEST project, significant effort was devoted in developing techniques for recording the jet expansion zone pressure and temperature immediately downstream of the release point. Unfortunately, these attempts failed due to the extremely high momentum of the expanding jet which resulted in the damage and in some cases, the dislodging of the in-line recording instrumentations.

Chapter 7:
Conclusions and Future Work

7.1 Conclusions

Recent appreciation of the impact of greenhouse gas emissions on global warming has resulted in the development of a number of decarbonisation strategies aiming to reduce the amount of CO_2 emissions into the atmosphere from coal fired power plants and other CO_2 intensive industries. Central to this strategy is Carbon Capture and Sequestration (CCS) technology which involves capturing CO_2 and storing it in geological formations.

In the near future, large quantities of CO_2 will be transported over hundreds of kilometres from the capture sites to on-shore and off-shore underground storage sites. High-pressure transmission pipelines is widely recognised represent as the most practical and economic transportation mode for the captured CO_2. Given the hazardous nature of CO_2, the significant amounts transported, and the inevitable likelihood of such pipelines passing near or through populated areas, their safe operation is of paramount importance.

In light of the above, this thesis describes the further development, testing and validation of four flow models for the quantitative failure consequence assessment of high-pressure CO_2 transmission pipelines. These include:

- the extension of the HEM flow model to account for vapour-liquid-solid three-phase flow occurring during rapid decompression of high-pressure CO_2 transmission pipelines
- the extension of the HRM model to predict the experimentally observed thermodynamic non-equilibrium phenomenon of depressurising multi-component mixtures
- the extension of the TFM model to simulate heterogeneous flows during pipeline puncture decompression, including:
    I. developing a puncture outflow boundary condition for the TFM model

II. proposing, testing and verifying a discretisation scheme, AUSM-MUSTA, which combines the computational efficiency of the AUSM scheme and the accuracy of the MUSTA scheme

- the extension of the existing integral jet expansion model to take into account the mean flow kinetic energy loss due to turbulence generation during jet expansion

The following is a summary of the main findings in each chapter:

In Chapter 2, a detailed description of the mathematical formulations of four popular multi-phase flow models, including the HEM, HRM, DFM and TFM models, were presented. These included the governing conservation equations for fluid mechanics, the constituent relations for fluid/pipe wall and fluid/fluid interface interactions and the Equation of State (EOS) for predicting the fluid thermal properties and equilibrium data.

This was followed by a review of relevant studies focusing on the applications of the flow models for predicting CO_2 pipeline decompression behaviour. It was found that:

- the HEM model was limited to vapour-liquid two-phase flow;
- the HRM model was only capable of predicting rapid depressurisation-induced thermodynamic non-equilibrium of single-component fluids;
- the TFM model application was limited to simulating pipeline FBR failure.

Chapter 3 presented the development, testing and validation of a rigorous decompression flow model for predicting the amount of solid CO_2 formed as a function of time and distance along high-pressure pipelines during decompression. In practice, such predictive capability is important for a number of safety and operational reasons. These include pressure relief valve sizing, appropriate pipeline design in order to avoid blockage and minimising the risk of exposure of personnel to high doses of undiscovered accumulated sublimating solid CO_2 following pipeline depressurisation for maintenance purposes.

The flow model developed was based on the solution of the mass, momentum and energy conservation equations, accounting for the fluid/wall heat transfer and frictional effects. The pertinent thermodynamic and phase equilibrium data for CO_2

above and below its triple point were computed using GERG 2008 and ePR EoS, respectively. The Homogenous Frozen Mixture (HFM) model was employed for predicting the speed of sound of multi-phase CO_2 at the triple point.

For model verification, a Riemann problem test was performed, showing the wave structure in a vapour-liquid-solid flow. Anomalous waves (as compared to in the case of single-phase flow) were predicted by the flow model, consisting of two split rarefaction waves separating at the vapour-liquid and triple point phase transition boundaries.

The flow model was next validated against the pressure and temperature measurements obtained from a large-scale CO_2 pipeline FBR decompression test. Typical data generated using the model included the variations of pressure, temperature and solid mass fraction as a function of time and space (along the pipe) during decompression.

Indicating generally good agreement with the measured data, the model successfully reproduced the experimentally observed temporal pressure stabilisation at the triple point. In addition, the amount of solids was predicted to increase with distance towards the rupture plane, peaking at a maximum value of 35 wt% for the condition tested.

In Chapter 4, the HRM model was successfully extended for predicting thermodynamic non-equilibrium during the depressurisation of CO_2-rich mixtures. This is an important development, since in CCS, depending on the capture technology employed, the CO_2 streams will contain a range of different types and concentrations of impurities such as Ar, N_2, H_2, CH_4, and SO_2.

GERG 2008 EoS was employed to predict the thermal properties of both equilibrium and non-equilibrium fluid phases. The two-phase mixture speed of sound was calculated based on the HFM model, following previous studies.

Verification of the developed model was carried out by a Riemann problem test, numerically approximating the wave structure in a non-equilibrium two-phase mixture. It was found that thermodynamic non-equilibrium resulted in faster decompression waves and hence higher decompression rates compared to that for equilibrium mixtures.

For validation, the model predictions were compared against the experimental measurements of the decompression wave speed, pressure and temperature as a function of time at both the test pipe open and close ends during several pipeline FBR decompression tests. The HEM model was also applied to simulate the same tests. Overall, it was found that based on comparisons with measured data, the HRM model performed better than the HEM model. In addition, the degree of superheat in the liquid phase at the test pipe open and close ends was determined as a function of time during pipeline decompression. A higher degree of superheat was observed at the open end as compared to the closed end given the less rapid expansion in the case of the latter.

Chapter 5 presented the development of a TFM model for modelling heterogeneous flow during pipeline puncture decompression. Such work is particularly important for the quantitative failure consequence assessment of high-pressure transportation pipelines, given that puncture failures are far more frequent than FBR. Any flow heterogeneity may significantly impact the pipeline decompression behaviour and hence the outflow.

The flow modelling involved solving the conservation equations of mass, momentum and energy individually for each fluid phase. Heterogeneous interface interactions were accounted for using appropriate constitutive relations. The fluid thermal properties and phase equilibrium data were predicted using the PR EoS.

For the numerical solutions of the TFM model conservation equations, the mathematical development of a pipeline puncture outflow boundary condition was presented. This was followed by a description of a new discretisation scheme. The proposed scheme is both computationally efficient and accurate, combining the features of two popular existing schemes, AUSM and MUSTA schemes.

For validation, the model developed was used to simulate two pipeline puncture decompression tests conducted during the course of the CO_2QUEST project. In the meanwhile, the HEM model was also used to repeat the simulations for comparison. The predicted pressure, temperature and remaining inventory mass as a function of time were compared to the corresponding measurements, showing good agreement in all cases. In particular, the experimentally observed fluid thermal stratification as a

result of heterogeneous flow was accurately captured, in contrast to the HEM model where a single temperature was predicted for both fluid phases.

In addition, the comparison of the TFM model and HEM model predictions for the remaining inventory mass revealed that phase slip encountered during heterogeneous flow resulted in a reduced discharge flowrate. Both predictions from the TFM and HEM models were however found to be in relatively close agreement with the measured data.

In Chapter 6, the development and testing of an integral jet expansion model aimed at predicting the fully expanded jet conditions was presented. Typical output data included the jet radius, temperature, density, fluid phase mass fraction and momentum flux. The availability of such data is important given it serves as the input for modelling the subsequent atmospheric dispersion behaviour of the escaping hazardous fluid and hence determining the minimum safe distances to populated areas. In contrast to the previous formulations reported in the open literature, the jet expansion model accounted for the important and inevitable loss of the mean flow kinetic energy of the expanding jet due to turbulence generation.

Model verification was based on the comparison of the integral jet expansion model's predictions to those obtained from a rigorous but far more computationally demanding CFD based jet expansion model.

The verification test cases involved a series of realistic release scenarios for high-pressure gas and liquid phase CO_2 from a pressurised containment. Extended PR EoS was employed to provide the pertinent phase equilibrium data including accounting for CO_2 solid formation as a result of significant temperature drop associated with the jet expansion process.

Based on the predicted profiles of e.g. the jet temperature, density, momentum flux across the jet cross-section area from the CFD model, the corresponding average values were obtained. In order to demonstrate the impact of ignoring turbulence generation, the results were in turn compared against those from the existing integral jet expansion model.

It was observed that in all cases, similar values for the jet thermal properties such as internal energy were obtained by the integral models as compared to those from the CFD model, indicating negligible energy dissipation during jet expansion.

However, the jet momentum flux was the parameter whose predicted magnitude was by far the most affected by the simulation technique employed. Here it was shown that ignoring turbulence generation during jet expansion resulted in as much as 50% overestimate of the jet momentum flux as compared to the CFD prediction. This overestimate was substantially reduced to about 15% when the mean kinetic energy loss associated with turbulence generation was incorporated in the developed integral model.

This finding has significant implications given that the jet momentum is one of the key factors in determining the dispersion behaviour of the escaping vapour cloud, impacting the minimum safety distances to populated areas.

In conclusion, the work presented in this study provides the mathematical and computational basis for the accurate assessment of the consequences associated with the rupture of high-pressure CO_2 pipelines. It goes beyond the current state of the art by allowing the analysis of complex physical phenomena (including dry ice formation, thermodynamic non-equilibrium, heterogeneous flow and turbulence during pipeline decompression) and addressing some of the critical drawbacks of the established theory. The models developed are also directly applicable to systems of hydrocarbons.

Since the predicted data from the flow models act as the input in determining the likelihood of pipeline or pressure relief valve blockage due to CO_2 solid formation, the fracture propagation length along the pipe wall and where relevant, the subsequent dispersion, fire and explosion characteristics, the developments in this work will help to quantify the corresponding hazard profiles with improved certainty. This in turn yields cost benefits in view of the design and implementation of relevant protection and mitigation systems. Thus, the fundamental nature of this work will benefit process safety in, but not limited to, CCS by protecting life, property and the environment.

7.2 Suggestions for Future Work

7.2.1 Heterogeneous Modelling of the Accumulation of Solid Phase CO_2

In Chapter 3, a HEM flow model capable of predicting the amount of solid CO_2 formed in pipelines as a result of decompression below the CO_2 triple point was developed. However, to be able to quantify the risk of pipeline or pressure relief valve blockage due to the accumulation of solids, the spatial variation (in 3-D) of the formed solids must be known.

In addition, given the significant density difference between the vapour and solid phases, disengagement and eventual settling of the solid CO_2 during the pipeline decompression process can occur, as clearly demonstrated in practice. This largely invalidates the HEM assumption adopted in the presented flow model.

In light of the above, future work should involve the extension of the present model to 3-D (for the flow through the pressure relief valves and other restrictions) and account for heterogeneous flow.

7.2.2 Development of Dedicated Correlations for Specifying the Relaxation Time in the HRM Model for CO_2-Rich Mixtures

In Chapter 4, the HRM model was successfully extended to account for multi-component mixtures. Model validation against experimental data performed as part of the study showed that, with certain constant relaxation times, improved agreement was obtained as compared to the HEM model. However, the performance of the HRM model using the relaxation time predicted from the correlation developed for pure CO_2 was not as good.

Clearly, to extend the applicability of the HRM model to CO_2-rich mixture flows in practice, the development of dedicated correlations for determining the relaxation times for CO_2 with a variety of impurities is necessary.

7.2.3 Development, Testing and Validation of the TFM Model for All Heterogeneous Flow Regimes

In the development of the TFM model for predicting pipeline puncture decompression (Chapter 5), the heterogeneous vapour and liquid phases were assumed to be stratified with a perfectly flat fluid/fluid interface in between. The interface drag force, the interface area and the heat transfer area between the pipe wall and the fluid were then calculated accordingly.

In reality, as the pipeline puncture diameter increases, the separated two fluid phases may become more disturbed following decompression, and hence the heterogeneous flow regime may transform to different flow regimes such as stratified-wavy flow, plug/slug flow, annular flow. As a result, the assumption of flat interface becomes invalid, and so do the calculations for interface and heat transfer areas. Furthermore, the correlation adopted for specifying interface drag force needs to be adjusted accordant to the specific flow regimes.

To address the above, the further extension of the TFM model accounting for various flow regimes encountered during pipeline puncture decompression would be useful. This will involve the implementation of appropriate methodology for determining the prevailing flow regimes during the decompression process (e.g. based on individual fluid phase Reynolds number) and hence the use of the appropriate constitutive relations for computing the corresponding heat transfer area, interface area as well as interface drag force.

7.2.4 Validation of the Jet Expansion Model

In Chapter 6, the integral jet expansion model developed was verified against a rigorous CFD model for the predictions of the fully expanded jet conditions. This was achieved by performing a number of case studies based on assumed realistic release conditions.

However, where practical, validations against experimentally data would be extremely useful. To this end as part of the CO2QUEST project, significant effort was devoted to developing techniques for recording the pressure and temperature within the jet expansion zone immediately downstream of the release point. Unfortunately,

these attempts failed due to the extremely high momentum of the expanding jet which resulted in the damage and in some cases the dislodging of the inline recording pressure and temperature transducers.

Alternatively, one can use the predicted fully expanded jet conditions from the model developed and use the data as the input to a fully validated dispersion model. The resulting predictions for the dispersion behaviour of the escaping CO_2 cloud (e.g. CO_2 concentration as a function of space downstream of the release point) may then be compared against available experimental measurements for validation.

References

Abudour, A.M. et al., 2013. Volume-translated Peng-Robinson equation of state for liquid densities of diverse binary mixtures. *Fluid Phase Equilibria*, 349, pp.37–55. Available at: http://dx.doi.org/10.1016/j.fluid.2013.04.002.

Angielczyk, W. et al., 2010. 1-D Modeling of supersonic carbon dioxide two-phase flow through ejector motive nozzle. In *International Refrigeration and Air Conditioning Conference*. Purdue, pp. 1–8.

ANSYS, 2013a. Pressure-velocity coupling. In *ANSYS Fluent 15.0 user's guide*. Canonsburg, PA: ANSYS Inc., pp. 649–653.

ANSYS, 2013b. Standard wall functions. In *ANSYS Fluent theory guide*. Canonsburg, PA: ANSYS Inc., pp. 67, 115–119.

ANSYS, 2013c. Using flow boundary conditions. In *ANSYS Fluent 15.0 user's guide*. Canonsburg, PA: ANSYS Inc., pp. 257–261.

Aursand, E. et al., 2016. Fracture propagation control in CO_2 pipelines: Validation of a coupled fluid-structure model. *Engineering Structures*, 123, pp.192–212. Available at: http://dx.doi.org/10.1016/j.engstruct.2016.05.012.

Aursand, P. et al., 2017. The spinodal of single- and multi-component fluids and its role in the development of modern equations of state. *Fluid Phase Equilibria*, 436, pp.98–112. Available at: http://linkinghub.elsevier.com/retrieve/pii/S0378381216306227.

Baer, M.R. & Nunziato, J.W., 1986. A two-phase mixture theory for the deflagration-to-detonation transition (DDT) in reactive granular materials. *International Journal of Multiphase Flow*, 12(6), pp.861–889.

Bakkum, E.A. & Duijm, D.J., 2005. Vapour cloud dispersion. In C. J. H. van den Bosch & R. A. P. M. Weterings, eds. *Methods for the Calculation of Physical Effects*. Committee for the prevention of disasters.

Bilicki, Z. & Kestin, J., 1990. Physical aspects of the relaxation model in two-phase flow. In *Proceedings of the Royal Society A: Mathematical, Physical and*

Engineering Sciences. The Royal Society, pp. 379–397. Available at: http://rspa.royalsocietypublishing.org/cgi/doi/10.1098/rspa.1990.0040.

Bricard, P. & Friedel, L., 1998. Two-phase jet dispersion. *Journal of Hazardous Materials*, 59(2), pp.287–310. Available at: http://linkinghub.elsevier.com/retrieve/pii/S0304389497001593.

Brown, S. et al., 2013. A homogeneous relaxation flow model for the full bore rupture of dense phase CO_2 pipelines. *International Journal of Greenhouse Gas Control*, 17, pp.349–356. Available at: http://linkinghub.elsevier.com/retrieve/pii/S1750583613002363 [Accessed October 31, 2014].

Brown, S. et al., 2014. CO_2QUEST: Techno-economic assessment of CO_2 quality effect on its storage and transport. *Energy Procedia*, 63, pp.2622–2629. Available at: http://dx.doi.org/10.1016/j.egypro.2014.11.284.

Brown, S. et al., 2014. Modelling the non-equilibrium two-phase flow during depressurisation of CO_2 pipelines. *International Journal of Greenhouse Gas Control*, 30, pp.9–18. Available at: http://dx.doi.org/10.1016/j.ijggc.2014.08.013.

Brown, S., Martynov, S. & Mahgerefteh, H., 2015. A coupled two-phase flow model for predicting the flashing of liquid CO_2 during pipeline decompression. In K. Hanjalic et al., eds. *Turbulence, Heat and Mass Transfer 8*. Sarajevo, Bosnia and Herzegovina: Begell House, Inc, pp. 1–12.

Casal, J. & Salla, J.M., 2006. Using liquid superheating energy for a quick estimation of overpressure in BLEVEs and similar explosions. *Journal of Hazardous Materials*, 137(3), pp.1321–1327.

CFD online, 2005. Favre averaged Navier-Stokes equations. Available at: https://www.cfd-online.com/Wiki/Favre_averaged_Navier-Stokes_equations [Accessed January 3, 2018].

Chang, C.H. & Liou, M.S., 2007. A robust and accurate approach to computing compressible multiphase flow: Stratified flow model and AUSM+-up scheme. *Journal of Computational Physics*, 225(1), pp.840–873.

Chen, N.H., 1979. An Explicit Equation for Friction Factor in Pipe. *Industrial and Engineering Chemistry Fundamentals*, 18(3), pp.296–297.

Cleaver, R.P., Cooper, M.G. & Halford, A.R., 1995. Further development of a model for dense gas dispersion over real terrain. *Journal of Hazardous Materials*, 40(1), pp.85–108.

Cleaver, R.P., Cumber, P.S. & Halford, 2003. Modelling outflow from a ruptured pipeline transporting compressed volatile liquids. *Journal of Loss Prevention in the Process Industries*, 16, pp.533–543. Available at: http://linkinghub.elsevier.com/retrieve/pii/S0950423003000883.

Cleaver, R.P. & Edwards, P.D., 1990. Comparison of an integral model for predicting the dispersion of a turbulent jet in a crossflow with experimental data. *Journal of Loss Prevention in the Process Industries*, 3(1), pp.91–96.

Conti, J. et al., 2016. *International Energy Outlook 2016 with projections to 2040*, Washington, D.C. Available at: www.eia.gov/forecasts/ieo/pdf/0484(2016).pdf.

Cosham, A. et al., 2012. The Decompression Behaviour of Carbon Dioxide in the Dense Phase. In *Proceedings of the 2012 9th International Pipeline Conference*. Calgary: ASME, pp. 1–18. Available at: http://proceedings.asmedigitalcollection.asme.org/proceeding.aspx?doi=10.1115/IPC2012-90461.

Cosham, A. & Eiber, R.J., 2008. Fracture propagation of CO_2 pipelines. *Journal of Pipeline Engineering*, 7(4), pp.281–292.

Cumber, P., 2007. Outflow from fractured pipelines transporting supercritical ethylene. *Journal of Loss Prevention in the Process Industries*, 20(1), pp.26–37. Available at: http://linkinghub.elsevier.com/retrieve/pii/S0950423006000490.

Daubert, T.E. & Danner, R.P., 1989. *Physical and thermodynamic properties of pure compounds: data compilation*, New York: Hemisphere.

Dinh, T.N., Nourgaliev, R.R. & Theofanous, T.G., 2003. Understanding the ill-posed two-fluid model. In *The 10th International Topical Meeting on Nuclear Reactor Thermal Hydraulics*. Seoul, pp. 1–37.

DNV, 2010. *Design and operation of CO2 pipelines*, Hovik.

Downar-Zapolski, P. & Bilicki, Z., 1996. The non-equilibrium relaxation model for one-dimensional flashing liquid flow. *International Journal of Multiphase Flow*, 22(3), pp.473–483. Available at: http://scholar.google.com/scholar?hl=en&btnG=Search&q=intitle:e+r+g+a+m+o+n#5 [Accessed October 31, 2014].

Drescher, M. et al., 2014. Experiments and modelling of two-phase transient flow during pipeline depressurization of CO_2 with various N_2 compositions. *Energy Procedia*, 63, pp.2448–2457. Available at: http://www.sciencedirect.com/science/article/pii/S1876610214020827.

Drew, D.A. & Lahey Jr, R.T., 1987. The virtual mass and lift force on a sphere in rotating and straining inviscid flow. *International Journal of Multiphase Flow*, 13(1), pp.113–121.

Elshahomi, A. et al., 2015. Decompression wave speed in CO_2 mixtures: CFD modelling with the GERG-2008 equation of state. *Applied Energy*, 140, pp.20–32. Available at: http://dx.doi.org/10.1016/j.apenergy.2014.11.054.

Ely, J.F., 2010. The corresponding-states principle. In *Applied thermodynamics of fluidsle*. Royal Society of Chemistry, pp. 135–171.

Embid, P. & Baer, M., 1992. Mathematical analysis of a two-phase continuum mixture theory. *Continuum Mechanics and Thermodynamics*, 4, pp.279–312.

Ferziger, J.H. & Peric, M., 2002. *Computational methods for fluid dynamics* 3rd ed., New York: Springer.

FlÅtten, T., Morin, A. & Munkejord, S.T., 2011. On solutions to equilibrium problems for systems of stiffened gases. *SIAM Journal on Applied Mathematics*, 71(1), pp.41–67. Available at: http://epubs.siam.org/doi/abs/10.1137/100784321.

Fossati, M. & Quartapelle, L., 2014. The Riemann problem for hyperbolic equations under a nonconvex flux with two inflection points. *arXiv:1402.5906*, pp.1–104. Available at: https://arxiv.org/abs/1402.5906 [Accessed May 30, 2017].

Friedel, L., 1979. Improved friction pressure drop correlations for horizontal and vertical two-phase pipe flow. In *European Two-Phase Flow Group Meeting*. Ispra.

Gant, S.E. et al., 2014. Evaluation of multi-phase atmospheric dispersion models for application to Carbon Capture and Storage. *Journal of Loss Prevention in the Process Industries*, 32, pp.286–298. Available at: http://linkinghub.elsevier.com/retrieve/pii/S0950423014001570 [Accessed November 27, 2014].

Gross, J. & Sadowski, G., 2001. Perturbed-Chain SAFT: An Equation of State Based on a Perturbation Theory for Chain Molecules. *Industrial & Engineering Chemistry Research*, 40(4), pp.1244–1260.

Gungor, K.E. & Winterton, R.H.S., 1987. Simplified general correlation for saturated flow boiling and comparisons of correlations with data. *Chemical Engineering Research and Design*, 65(2), pp.148–156.

Haida, M. et al., 2016. A modified homogeneous relaxation model for CO_2 two-phase flow in vapour ejector. *Journal of Physics: Conference Series*, 745(3), pp.1–8. Available at: http://stacks.iop.org/1742-6596/745/i=3/a=032159?key=crossref.e525fcd9d9b08690c6d3328a52b0facf.

Hammer, M., Ervik, A. & Munkejord, S.T., 2013. Method using a density-energy state function with a reference equation of state for fluid-dynamics simulation of vapor-liquid-solid carbon dioxide. *Industrial and Engineering Chemistry Research*, 52(29), pp.9965–9978.

Harper, P., Wilday, J. & Bilio, M., 2011. Assessment of the major hazard potential of carbon dioxide (CO_2). *Health and Safety Executive*. Available at: http://www.hse.gov.uk/carboncapture/assets/docs/major-hazard-potential-carbon-dioxide.pdf [Accessed December 20, 2016].

Hébrard, J. et al., 2016. Medium Scale CO_2 Releases. *Energy Procedia*, 86, pp.479–488. Available at: http://linkinghub.elsevier.com/retrieve/pii/S1876610216000515.

Hérard, J.M. & Hurisse, O., 2012. A fractional step method to compute a class of compressible gas–liquid flows. *Computers & Fluids*, 55, pp.57–69.

Hibiki, T. & Ishii, M., 2003. One-dimensional drift-flux model and constitutive equations for relative motion between phases in various two-phase flow regimes. *International Journal of Heat and Mass Transfer*, 46(25), pp.4935–4948.

International Energy Agency, 2017. Global carbon dioxide emissions, 1980-2016. Available at: https://www.iea.org/newsroom/news/2017/march/iea-finds-co2-emissions-flat-for-third-straight-year-even-as-global-economy-grew.html [Accessed March 25, 2017].

International Energy Agency, 2015. *Key World Energy Statistics*, Paris. Available at: http://www.iea.org/publications/freepublications/publication/key-world-energy-statistics-2015.html.

International Energy Agency, 2010. *Scenarios & Strategies To 2050*, Paris. Available at: http://www.oecd-ilibrary.org.ezproxy.library.uq.edu.au/energy/energy-technology-perspectives-2010_energy_tech-2010-en.

International Energy Agency, 2011. *World Energy Outlook*, Paris. Available at: http://www.iea.org/weo/docs/weo2011/WEO2011_GoldenAgeofGasReport.pdf.

Ishii, M., 1977. *One-dimensional drift-flux model and constitutive equations for relative motion between phases in various two-phase flow regimes*, Argonne.

Ishii, M. & Hikiki, T., 2006a. Basic relations in time averaging. In *Thermo-fluid dynamics of two-phase flow*. New York: Springer, pp. 89–92.

Ishii, M. & Hikiki, T., 2006b. Local instant formulation. In *Thermo-fluid dynamics of two-phase flow*. New York: Springer, pp. 11–20.

Ishii, M. & Hikiki, T., 2006c. Time-averaged balance equation. In *Thermo-fluid dynamics of two-phase flow*. New York: Springer, pp. 98-100, 103-105.

Ishii, M. & Hikiki, T., 2006d. Various methods of averaging. In *Thermo-fluid dynamics of two-phase flow*. New York, pp. 55–57.

Jacobson, M.Z., 2005. *Fundamentals of atmospheric modeling* 2nd ed., New York: Cambridge University Press.

Knoope, M.M.J. et al., 2014. The influence of risk mitigation measures on the risks, costs and routing of CO_2 pipelines. *International Journal of Greenhouse Gas Control*, 29, pp.104–124. Available at: http://dx.doi.org/10.1016/j.ijggc.2014.08.001.

Knudsen, J.G. et al., 1997a. Heat and mass transfer. In D. W. Green, ed. *Perry's Chemical Engineers' Handbook*. New York: McGraw-Hill, pp. 16–17.

Knudsen, J.G. et al., 1997b. Heat and mass transfer. In D. W. Green, ed. *Perry's Chemical Engineers' Handbook*. New York: McGraw-Hill, pp. 22–23.

Koornneef, J. et al., 2010. Quantitative risk assessment of CO_2 transport by pipelines-A review of uncertainties and their impacts. *Journal of Hazardous Materials*, 177(1–3), pp.12–27.

Kunz, O. et al., 2007. *The GERG-2004 wide-range equation of state for natural gases and other mixtures, Fortschr*, Düsseldorf: Ber. VDI, VDI-Verlag. Available at: http://www.gerg.eu/publications/technical-monographs.

Kunz, O. & Wagner, W., 2012. The GERG-2008 wide-range equation of state for natural gases and other mixtures: An expansion of GERG-2004. *Journal of Chemical & Engineering Data*, 57(11), pp.3032–3091. Available at: http://pubs.acs.org/doi/10.1021/je300655b.

Lemmon, E.W., Huber, M.L. & McLinden, M.O., 2010. NIST standard ReferenceDatabase 23: Reference fluid thermodynamic and transport properties - REFPROP.

Lemmon, E.W. & Tillner-Roth, R., 1999. A Helmholtz energy equation of state for calculating the thermodynamic properties of fluid mixtures. *Fluid Phase Equilibria*, 165, pp.1–21. Available at: http://linkinghub.elsevier.com/retrieve/pii/S0378381299002629.

LeVeque, R.J., 2002. *Finite Volume Methods for Hyperbolic Problems*, Cambridge: Cambridge University Press. Available at: http://ebooks.cambridge.org/ref/id/CBO9780511791253.

LeVeque, R.J., 1992. *Numerical Methods for Conservation Laws* 2nd ed., Basel: Birkhauser Verlag. Available at: http://www.jstor.org/stable/2938728?origin=crossref.

Liaw, H.J., 2016. Lessons in process safety management learned in the Kaohsiung gas explosion accident in Taiwan. *Process Safety Progress*, 35(3), pp.228–232.

Liiey, P.E. et al., 2008. Physical and chemical data. In R. H. Perry, D. W. Green, & J. O. Maloney, eds. *Perry's Chemical Engineers' Handbook*. New York: McGraw-Hill, pp. 2–335.

Linnitt, M., 2013. Average 250 pipeline accidents each year, billions spent on property damage. *Desmog Canada*. Available at: http://www.desmog.ca/2013/04/05/average-250-pipeline-accidents-each-year-billions-spent-property-damage [Accessed June 1, 2016].

De Lorenzo, M. et al., 2017. Homogeneous two-phase flow models and accurate steam-water table look-up method for fast transient simulations. *International Journal of Multiphase Flow*, 95, pp.199–219.

Lund, H., 2013. A hierarchy of relaxation models for two-phase flow. *J. Appl. Math.*, 72(6), pp.1713–1741.

Lydell, B.O.Y., 2000. Pipe failure probability—the Thomas paper revisited. *Reliability Engineering & System Safety*, 68(3), pp.207–217.

Mahgerefteh, H. & Atti, O., 2006. Modeling low-temperature–induced failure of pressurized pipelines. *AIChE Journal*, 52(3), pp.1248–1256. Available at: http://doi.wiley.com/10.1002/aic.10719.

Mahgerefteh, H., Atti, O. & Denton, G., 2007. An Interpolation Technique for Rapid CFD Simulation of Turbulent Two-Phase Flows. *Process Safety and Environmental Protection*, 85(B1), pp.45–50. Available at: http://linkinghub.elsevier.com/retrieve/pii/S095758200771385X.

Mahgerefteh, H., Brown, S. & Denton, G., 2012. Modelling the impact of stream impurities on ductile fractures in CO_2 pipelines. *Chemical Engineering Science*, 74, pp.200–210. Available at: http://linkinghub.elsevier.com/retrieve/pii/S0009250912001339 [Accessed April 20, 2012].

Mahgerefteh, H., Brown, S. & Martynov, S., 2012. A study of the effects of friction, heat transfer, and stream impurities on the decompression behavior in CO_2 pipelines. In *Greenhouse Gases: Science and Technology*. pp. 369–379.

Mahgerefteh, H., Brown, S. & Zhang, P., 2011. A dynamic boundary ductile-fracture-propagation model for CO_2 pipelines. *Journal of Pipeline Engineering*, 9(4), pp.265–276.

Mahgerefteh, H., Denton, G. & Rykov, Y., 2008. A hybrid multiphase flow model. *AIChE Journal*, 54(9), pp.2261–2268. Available at: http://www3.interscience.wiley.com/journal/120775034/abstract.

Mahgerefteh, H., Oke, A. & Atti, O., 2006. Modelling outflow following rupture in pipeline networks. *Chemical Engineering Science*, 61, pp.1811–1818.

Mahgerefteh, H., Saha, P. & Economou, I.G., 1997. A study of the dynamic response of emergency shutdown valves following full bore rupture of gas pipelines. *Process safety and environmental protection*, 75(4), pp.201–209. Available at: http://ac.els-cdn.com/S0957582097706815/1-s2.0-S0957582097706815-main.pdf?_tid=cfee6a70-544f-11e4-b658-00000aab0f6c&acdnat=1413366429_964b98c2be32902059114959a2d67f62.

Mahgerefteh, H., Saha, P. & Economou, I.G., 1999. Fast numerical simulation for full-bore rupture of pressurized pipelines. *AIChE Journal*, 45(6), pp.1191–1201. Available at: http://www3.interscience.wiley.com/journal/108067555/abstract.

Mahgerefteh, H., Saha, P. & Economou, I.G., 2000. Modeling fluid phase transition effects on dynamic behavior of ESDV. *AIChE Journal*, 46(5), pp.997–1006. Available at: http://doi.wiley.com/10.1002/aic.690460512.

Martynov, S. et al., 2014. Modelling three-phase releases of carbon dioxide from high-pressure pipelines. *Process Safety and Environmental Protection*, 92(1), pp.36–46. Available at: http://dx.doi.org/10.1016/j.psep.2013.10.004.

Martynov, S., Brown, S. & Mahgerefteh, H., 2013. An extended Peng-Robinson equation of state for carbon dioxide solid-vapor equilibrium. *Greenhouse Gases: Science and Technology*, 3(2), pp.136–147.

Martynov, S.B. et al., 2017. Assessment of fracture propagation in pipelines transporting impure CO_2 streams. *Energy Procedia*, 114, pp.6685–6697. Available at: http://linkinghub.elsevier.com/retrieve/pii/S1876610217319999.

Menikoff, R. & Plohr, B.J., 1989. The Riemann problem for fluid flow of real materials. *Reviews of Modern Physics*, 61(1), pp.75–130.

Menter, F.R., Kuntz, M. & Langtry, R., 2003. Ten years of industrial experience with the SST turbulence model. In K. Hanjalic, Y. Nagano, & M. Tummers, eds. *Turbulence Heat and Mass Transfer 4*. Begell House, Inc., pp. 625–632. Available at: http://cfd.mace.manchester.ac.uk/flomania/pds_papers/file_pds-1068134610Menter-SST-paper.pdf.

Molag, M. & Dam, C., 2011. Modelling of accidental releases from a high pressure CO_2 pipeline. *Energy Procedia*, 4, pp.2301–2307. Available at: http://dx.doi.org/10.1016/j.egypro.2011.02.120.

Moody, F.J., 1965. Maximum flow rate of a single component, two-phase mixture. *Journal of Heat Transfer*, 87(1), pp.134–141.

Munkejord, S.T., 2010. A numerical study of two-fluid models with pressure and velocity relaxation. *Advances in Applied Mathematics and Mechanics*, 2(2), pp.131–159.

Munkejord, S.T. et al., 2010. Thermo- and fluid-dynamical modelling of two-phase multi-component carbon dioxide mixtures. *International Journal of Greenhouse Gas Control*, 4(4), pp.589–596.

Munkejord, S.T., Evje, S. & FlÅtten, T., 2009. A MUSTA scheme for a nonconservative two-fluid model. *SIAM Journal on Scientific Computing*, 31(4), pp.2587–2622. Available at: http://epubs.siam.org/doi/10.1137/080719273.

Munkejord, S.T. & Hammer, M., 2015. Depressurization of CO_2-rich mixtures in pipes: Two-phase flow modelling and comparison with experiments. *International Journal of Greenhouse Gas Control*, 37, pp.398–411.

Munkejord, S.T., Hammer, M. & Løvseth, S.W., 2016. CO_2 transport: Data and models – A review. *Applied Energy*, 169, pp.499–523. Available at: http://linkinghub.elsevier.com/retrieve/pii/S0306261916300885.

Nakagawa, M., Berana, M.S. & Kishine, A., 2009. Supersonic two-phase flow of CO_2 through converging–diverging nozzles for the ejector refrigeration cycle. *International Journal of Refrigeration*, 32(6), pp.1195–1202.

National Transportation Safety Board, 2015. *Natural gas-fueled building explosion and resulting fire New York city, New York March 12, 2014*, Available at: http://www.ntsb.gov/investigations/dms.html.

Nouri-Borujerdi, A. & Shafiei Ghazani, A., 2017. Equilibrium and non-equilibrium gas–liquid two phase flow in long and short pipelines following a rupture. *AIChE Journal*, 63(7), pp.3214–3223.

Oke, A. et al., 2003. A transient outflow model for pipeline puncture. *Chemical Engineering Science*, 58, pp.4591–4604.

Olivier, J.G.J., Muntean, M. & Peters, J.A.H.W., 2015. *Trends in global CO_2 emissions: 2015 report*,

Paillère, H., Corre, C. & García Cascales, J.R., 2003. On the extension of the AUSM+ scheme to compressible two-fluid models. *Computers and Fluids*, 32(6), pp.891–916.

Patchigolla, K. & Oakey, J.E., 2013. Design overview of high pressure dense phase CO_2 pipeline transport in flow mode. *Energy Procedia*, 37, pp.3123–3130. Available at: http://linkinghub.elsevier.com/retrieve/pii/S1876610213004414.

Peng, D.Y. & Robinson, D.B., 1976. A new two-constant equation of state. *Industrial Engineering Chemistry Fundamentals*, 15, pp.59–64.

Pershad, H. et al., 2010. *CO_2 pipline infrastructure : An analysis of global challenges and opportunities*, Cambridge.

Pham, L.H.H.P. & Rusli, R., 2016. A review of experimental and modelling methods for accidental release behaviour of high-pressurised CO_2 pipelines at atmospheric environment. *Process Safety and Environmental Protection*, 104, pp.48–84. Available at: http://linkinghub.elsevier.com/retrieve/pii/S0957582016301665.

Pope, S.B., 2000a. Free shear flow. In *Turbulent Flows*. New York: Cambridge University Press, pp. 124–127.

Pope, S.B., 2000b. Gradient-diffusion and turbulent-viscosity hypotheses. In *Turbulent Flows*. New York: Cambridge University Press, pp. 92–94.

Pope, S.B., 2000c. Turbulent-viscosity models. In *Turbulent Flows*. New York: Cambridge University Press, pp. 373–384.

Powell, M.J.D., 1970. A hybrid method for non-linear equations. In P. Rabinowitz, ed. *Numerical methods for non-linear algebraic equations*. London: Gordon and Breach Science Publishers.

Ransom, V.H., 1987. Numerical benchmark test No. 2.1: Faucet flow. *Multiphase Science and Technology*, 3(1–4), pp.465–467. Available at: http://www.dl.begellhouse.com/journals/5af8c23d50e0a883,6b4442405c7a2bae, 3e915d316529ccc8.html.

Richards, P.J. & Norris, S.E., 2011. Appropriate boundary conditions for computational wind engineering models revisited. *Journal of Wind Engineering and Industrial Aerodynamics*, 99(4), pp.257–266. Available at: http://www.sciencedirect.com/science/article/pii/S0167610510001418.

Richardson, S. et al., 2006. Experimental determination of two-phase flow rates of hydrocarbons through restrictions. *Process Safety and Environmental Protection*,

84(1), pp.40–53. Available at: http://linkinghub.elsevier.com/retrieve/pii/S0957582006713039.

Richardson, S.M. & Saville, G., 1996. *Offshore technology report, OTH94 441, Isle of Grain pipeline depressurisation tests*, London.

Rocha, P.A.C. et al., 2014. *k-ω* SST (shear stress transport) turbulence model calibration: A case study on a small scale horizontal axis wind turbine. *Energy*, 65, pp.412–418. Available at: http://dx.doi.org/10.1016/j.energy.2013.11.050.

Sarkar, S. et al., 1991. The analysis and modelling of dilatational terms in compressible turbulence. *Journal of Fluid Mechanics*, 227, pp.473–493.

Shamsundar, N. & Lienhard, J.H., 1993. Equations of state and spinodal lines - A review. *Nuclear Engineering and Design*, 141, pp.269–287.

Soave, G., 1972. Equilibrium constants from a modified Redlich-Kwong equation of state. *Chemical Engineering Science*, 27(6), pp.1197–1203.

Sonin, A.A., 2001. Equation of motion for viscous Flow. pp.1–26. Available at: http://web.mit.edu/2.25/www/pdf/viscous_flow_eqn.pdf [Accessed March 21, 2017].

Stadtke, H., 2006. *Gasdynamic aspects of two-phase flow*, Weinheim: Wiley-VCH.

Steiner, D. & Taborek, J., 1992. Flow boiling heat transfer in vertical tubes correlated by an asymptotic method. *Heat Transfer Engineering*, 13(2), pp.43–69.

Taitel, Y. & Dukler, A.E., 1976. A theoretical approach to the Lockhart-Martinelli correlation for stratified flow. *International Journal of Multiphase Flow*, 2(5–6), pp.591–595.

Techo, R., Tickner, R.R. & James, R.E., 1965. An accurate equation for the computation of the friction factor for smooth pipes from the Reynolds number. *Journal of Applied Mechanics*, 32(2), pp.443–443.

Teng, L. et al., 2016. Decompression characteristics of CO_2 pipelines following rupture. *Journal of Natural Gas Science and Engineering*, 36, pp.213–223. Available at: http://dx.doi.org/10.1016/j.jngse.2016.10.026.

Thompson, K.W., 1990. Time-dependent boundary conditions for hyperbolic systems, II. *Journal of Computational Physics*, 89(2), pp.439–461.

Thompson, K.W., 1987. Time-dependent boundary conditions for hyperbolic systems. *Journal of Computational Physics*, 68(1), pp.1–24.

Tilton, J.N., 1997. Fluid and particle dynamics. In D. W. Green, ed. *Perry's Chemical Engineers' Handbook*. New York: McGraw-Hill, pp. 10–11.

Tokareva, S.A. & Toro, E.F., 2016. A flux splitting method for the Baer-Nunziato equations of compressible two-phase flow. *Journal of Computational Physics*, 323, pp.45–74. Available at: http://dx.doi.org/10.1016/j.jcp.2016.07.019.

Tokareva, S.A. & Toro, E.F., 2010. HLLC-type Riemann solver for the Baer-Nunziato equations of compressible two-phase flow. *Journal of Computational Physics*, 229(10), pp.3573–3604. Available at: http://dx.doi.org/10.1016/j.jcp.2010.01.016.

Toro, E.F., 2009a. Centred TVD Schemes. In *Riemann Solvers and Numerical Methods for Fluid Dynamics*. Heidelberg: Springer, pp. 511–514.

Toro, E.F., 2006. MUSTA: A multi-stage numerical flux. *Applied Numerical Mathematics*, 56(10–11 SPEC. ISS.), pp.1464–1479.

Toro, E.F., 2009b. Notions on hyperbolic partial differential equations. In *Riemann Solvers and Numerical Methods for Fluid Dynamics*. Heidelberg: Springer, pp. 44-45, 63-85.

Toro, E.F., 2009c. Random Choice and Related Methods. In *Riemann Solvers and Numerical Methods for Fluid Dynamics*. Heidelberg: Springer, pp. 244–245.

Toro, E.F., 2009d. Some properties of the Euler equations. In *Riemann Solvers and Numerical Methods for Fluid Dynamics*. Heidelberg: Springer, pp. 87–103.

Toro, E.F., 2009e. The HLL and HLLC Riemann Solvers. In *Riemann Solvers and Numerical Methods for Fluid Dynamics*. Heidelberg: Springer, pp. 293–311.

Toro, E.F., 2009f. The MUSCL-Hancock Scheme. In *Riemann Solvers and Numerical Methods for Fluid Dynamics*. Heidelberg: Springer, pp. 504–510.

Toro, E.F. & Billett, S.J., 2000. Centred TVD schemes for hyperbolic conservation laws. *IMA Journal of Numerical Analysis*, 20(1), pp.47–79.

Toro, E.F. & Siviglia, A., 2003. PRICE: primitive centred schemes for hyperbolic systems. *International Journal for Numerical Methods in Fluids*, 42(12), pp.1263–1291.

Toumi, I., Kumbaro, A. & Paillere, H., 1999. *Approximate Riemann solvers and flux vector splitting schemes for two-phase flow*, Paris.

Transportation Research Board, 2004. *Transmission pipelines and land use: A risk-informed approach*, Washington, D.C.: The National Academy of Sciences. Available at: http://www.nap.edu/openbook.php?record_id=11046&page=R1.

Vianellob, C., Macchiettoa, S. & Maschiob, G., 2013. Risk assessment of CO_2 pipeline network for CCS–A UK case study. *Chemical Engineering Transactions*, 31, pp.13–18.

Wen, J.X. et al., 2016. Further development and validation of CO_2FOAM for the atmospheric dispersion of accidental releases from carbon dioxide pipelines. *International Journal of Greenhouse Gas Control*, 52, pp.293–304. Available at: http://dx.doi.org/10.1016/j.ijggc.2016.07.006.

Witlox, H. et al., 2007. Flashing liquid jets and two-phase droplet dispersion. II. Comparison and validation of droplet size and rainout formulations. *Journal of Hazardous Materials*, 142(3), pp.797–809.

Witlox, H.W.M., Harper, M. & Oke, A., 2009. Modelling of discharge and atmospheric dispersion for carbon dioxide releases. *Journal of Loss Prevention in the Process Industries*, 22(6), pp.795–802. Available at: http://www.sciencedirect.com/science/article/pii/S0950423013001988.

Woolley, R.M. et al., 2014. An integrated, multi-scale modelling approach for the simulation of multiphase dispersion from accidental CO_2 pipeline releases in realistic terrain. *International Journal of Greenhouse Gas Control*, 27, pp.221–238. Available at: http://linkinghub.elsevier.com/retrieve/pii/S1750583614001583.

Woolley, R.M. et al., 2014. CO_2PipeHaz: Quantitative hazard assessment for next generation CO_2 pipelines. *Energy Procedia*, 63, pp.2510–2529.

Woolley, R.M. et al., 2013. Experimental measurement and Reynolds-averaged Navier–Stokes modelling of the near-field structure of multi-phase CO_2 jet releases. *International Journal of Greenhouse Gas Control*, 18, pp.139–149. Available at: http://linkinghub.elsevier.com/retrieve/pii/S1750583613002624.

Yeom, G.S. & Chang, K.S., 2013. A modified HLLC-type Riemann solver for the compressible six-equation two-fluid model. *Computers and Fluids*, 76, pp.86–104. Available at: http://dx.doi.org/10.1016/j.compfluid.2013.01.021.

Zuber, N. & Findlay, J.A., 1965. Average volumetric concentration in two-phase flow systems. *Journal of Heat Transfer*, 87(4), pp.453–468.

Zucrow, M.J. & Hoffman, J.D., 1976. *Gas Dynamics*, New York: Wiley.

Appendix

A1 Derivation of the Time-Averaged Conservation Equations

A1.1 General Conservation Equation for Fluid Dynamics

For an arbitrary flow Control Volume (CV), V_{CV}^k with a Control Surface (CS), S_{CV}^k, the general conservation equation of the k^{th} fluid phase is given by Ishii & Hikiki (2006):

$$\frac{d}{dt}\int_{V_{CV}^k} \rho_k \varphi_k dV = -\int_{S_{CV}^k} \boldsymbol{J}_k \cdot \boldsymbol{n}_k dS + \int_{V_{CV}^k} \varphi_k dV \qquad \text{A1.1}$$

where ρ_k is the density of the k^{th} fluid phase, φ_k is any quantity that is transported by the flow, the vectors, $\boldsymbol{J}_k$ and $\boldsymbol{n}_k$ respectively denote the outward flux (efflux) and surface normal of the CS. The remaining term, ψ_k is the volumetric source term in the CV.

The corresponding differential form is derived in the following. Throughout the derivation, two key mathematical theorems used, Leibniz rule and the Gauss' theorem are respectively given by:

$$\frac{d}{dt}\int_{V_{CV}^k} \mathrm{f} dV = \int_{V_{CV}^k} \frac{\partial}{\partial t}\mathrm{f} dV + \int_{S_{CV}^k} \mathrm{f}\boldsymbol{u}_k^S \cdot \boldsymbol{n}_k dS \qquad \text{A1.2}$$

$$\int_{V_{CV}^k} \nabla \cdot \boldsymbol{g} dV = \int_{S_{CV}^k} \boldsymbol{g} \cdot \boldsymbol{n}_k dS \qquad \text{A1.3}$$

Herein, f and $\boldsymbol{g}$ are (vector) functions that are to be integrated. The vector, $\boldsymbol{u}_k^S$ denotes the velocity of the movement of the CS. In the case where $\boldsymbol{u}_k^S$ is equal to the flow element velocity, $\boldsymbol{u}_k$ at the CS, Leibnitz rule reduces to the Reynolds transport theorem given by:

$$\frac{d}{dt}\int_{V_{CV}^k} \mathrm{f} dV = \int_{V_{CV}^k} \frac{\partial}{\partial t}\mathrm{f} dV + \int_{S_{CV}^k} \mathrm{f}\boldsymbol{u}_k \cdot \boldsymbol{n}_k dS \qquad \text{A1.4}$$

Applying equation A1.4 to the LHS of equation A1.1 gives:

$$\frac{d}{dt}\int_{V_{CV}^k}\rho_k\varphi_k dV=\int_{V_{CV}^k}\frac{\partial}{\partial t}\rho_k\varphi_k dV+\int_{S_{CV}^k}\rho_k\varphi_k\boldsymbol{u}_k\cdot\boldsymbol{n}_k dS \qquad \text{A1.5}$$

The surface integral term on the RHS can be converted to a volume integral via the Gauss's theorem:

$$\int_{S_{CV}^k}\rho_k\varphi_k\boldsymbol{u}_k\cdot\boldsymbol{n}_k dS=\int_{V_{CV}^k}\nabla\cdot\left(\rho_k\varphi_k\boldsymbol{u}_k\right)dV \qquad \text{A1.6}$$

Performing the same procedure for the surface integral term in equation A1.1 and substituting equation A1.5 to equation A1.1 leads to:

$$\int_{V_{CV}^k}\left(\frac{\partial}{\partial t}\rho_k\varphi_k+\nabla\cdot\left(\rho_k\varphi_k\boldsymbol{u}_k\right)\right)dV=\int_{V_{CV}^k}\left(-\nabla\cdot\boldsymbol{J}_k+\psi_k\right)dV \qquad \text{A1.7}$$

By taking the CV to be of infinitesimally small volume, the differential form of equation A1.7 reads:

$$\frac{\partial}{\partial t}\rho_k\varphi_k+\nabla\cdot\left(\rho_k\varphi_k\boldsymbol{u}_k\right)=-\nabla\cdot\boldsymbol{J}_k+\psi_k \qquad \text{A1.8}$$

The first term of equation A1.8 is the rate of change of φ_k per unit volume, the second term is the rate of convection of φ_k per unit volume.

It seems that, by directly solving equation A1.8, the solutions of the local instantaneous variations of φ_k can be readily obtained. However, the mathematical difficulties encountered in doing so are prohibitively great and beyond present computational capability (Ishii & Hikiki 2006d). These mathematical difficulties are: Existence of multiple fluid-fluid interfaces with unknown transient deformations; flow discontinuity at the interfaces; existence of turbulence flow. In particular, in the presence of turbulence, even for single-phase fluid without any interface, it has not been possible to obtain the exact solutions to local instantaneous variations.

Fortunately, these microscopic details of the flow are rarely needed for most practical engineering problems (Ishii & Hikiki 2006d). Rather, the corresponding macroscopic flow aspects are much more important. The variations of these macroscopic flow

properties can be represented by proper averaging the local instantaneous conservation equation A1.8.

In the following, the time-averaging of equation A1.8 is briefly discussed.

A.1.1.1 Basic Relations in Time-Averaging

In deriving the time-averaged general conservation equation, some useful relations are summarised following Ishii & Hikiki (2006a).

First, the time-averaging of a general function of the k^{th} fluid phase, f_k can be mathematically expressed as:

$$\bar{f}_k = \frac{1}{\Delta t}\int_{\Delta t} f_k dt \qquad \text{A1.9}$$

where Δt represents a fixed time interval.

In addition, the weighted time average of f_k can be obtained applying a non-zero scalar weight function, *w*:

$$\bar{f}_k^{\,w} = \frac{\overline{w f_k}}{\bar{w}} \qquad \text{A1.10}$$

In the case where *w* is the density function of the k^{th} fluid phase (denoted by M_k; $M_k = 1$ if the point of observation within CV is occupied by the k^{th} fluid phase, and $M_k = 0$ otherwise), the phase-weighted time average of f_k reads:

$$\bar{\bar{f}} = \frac{\overline{M_k f_k}}{\bar{M}_k} \qquad \text{A1.11}$$

Given that (Ishii & Hikiki 2006a):

$$\alpha_k = \frac{1}{\Delta t}\int_{\Delta t} M_k dt \qquad \text{A1.12}$$

where α_k is referred to as the probability of finding the k^{th} fluid phase at a given point in CV, equation A1.11 turns to:

$$\overline{\overline{\mathrm{f}_k}} = \frac{\overline{\mathrm{f}_k}}{\alpha_k} \qquad \text{A1.13}$$

From here on, α_k is called the volume fraction of the k^{th} fluid phase as mostly seen in the open literature.

w can also be the density of the k^{th} fluid phase. In this case, f_k is considered to be an extensive quantity (variable per unit volume). The extensive quantity is denoted by φ_k (firstly seen in equation A1.1) for consistency, and the resulting mass-weighted time average (also known as 'Favre average') is given by:

$$\underline{\varphi_k} = \frac{\overline{\rho_k \varphi_k}}{\overline{\overline{\rho_k}}} \qquad \text{A1.14}$$

Next, in view of equation A1.8, the time average of the time and space derivatives are presented.

Following Ishii & Hikiki (2006a), with Leibniz rule (defined in equation A1.2), the time average of the derivative can be linked to the derivative of average, such that:

$$\overline{\frac{\partial \mathrm{f}_k}{\partial t}} = \frac{\partial \overline{\mathrm{f}_k}}{\partial t} - \frac{1}{\Delta t}\sum_j \frac{1}{u_{ni}}\left(\mathrm{f}_k \boldsymbol{n}_k \cdot \boldsymbol{u}_k^S\right) \qquad \text{A1.15}$$

$$\overline{\nabla \mathrm{f}_k} = \nabla \overline{\mathrm{f}_k} - \frac{1}{\Delta t}\sum_j \frac{1}{u_{ni}}\left(\mathrm{f}_k \boldsymbol{n}_k\right) \qquad \text{A1.16}$$

with:

$$u_{ni} = -\frac{\left(\frac{\partial \mathrm{f}}{\partial t}\right)}{|\Delta \mathrm{f}|} \qquad \text{A1.17}$$

where:

$$\bar{\mathrm{f}} = \sum_k \overline{\mathrm{f}_k} \qquad \text{A1.18}$$

Note that the last term each in equations 1.15 and 1.16 is related to interface transfer at the j^{th} interface (Ishii & Hikiki 2006a).

Finally, the time average of the convection term in equation A1.8 is defined. For such purpose, ρ_k , u_k and φ_k are expressed as the sum between the corresponding weighted time averages and fluctuating components:

$$\rho_k = \overline{\overline{\rho_k}} + \rho_k' \qquad \text{A1.19}$$

$$\varphi_k = \underline{\varphi_k} + \varphi_k' \qquad \text{A1.20}$$

$$\boldsymbol{u}_k = \underline{\boldsymbol{u}_k} + \boldsymbol{u}_k' \qquad \text{A1.21}$$

with the following identities:

$$\overline{\overline{\rho_k'}} = 0 \qquad \text{A1.22}$$

$$\overline{\overline{\rho_k \varphi_k'}} = 0 \qquad \text{A1.23}$$

$$\overline{\overline{\rho_k \boldsymbol{u}_k'}} = 0 \qquad \text{A1.24}$$

By substituting equations A1.19 to A1.24, the phase-weighted time average of the convection term in equation A1.8 reads:

$$\overline{\overline{\rho_k \varphi_k \boldsymbol{u}_k}} = \overline{\overline{\rho_k}}\,\underline{\phi_k}\,\underline{\boldsymbol{u}_k} + \overline{\overline{\rho_k \varphi_k' \boldsymbol{u}_k'}} \qquad \text{A1.25}$$

where the last term is referred to as the turbulent flux, $\boldsymbol{J}_k^t$.

To this point, all the key relations that are required during the time-averaging of the local instantaneous general conservation equation A1.8 are given.

A.1.1.2 Time-Averaging

Returning to equation A1.8 and focusing on the LHS first, with the relations presented above, its time average is given by:

$$\overline{\frac{\partial \rho_k \varphi_k}{\partial t}} + \overline{\nabla \cdot \rho_k \varphi_k \boldsymbol{u}_k} = \tag{A1.26}$$

$$\frac{\partial \overline{\rho_k \varphi_k}}{\partial t} + \frac{1}{\Delta t}\sum_j \left(\frac{1}{u_{ni}} \boldsymbol{n}_k \cdot \rho_k \left(\boldsymbol{u}_k - \boldsymbol{u}_k^s \right) \varphi_k \right) + \nabla \cdot \left(\alpha_k \overline{\overline{\rho}}_k \underline{\phi}_k \underline{\boldsymbol{u}}_k \right) + \nabla \cdot \left(\alpha_k \boldsymbol{J}_k^t \right) =$$

$$\frac{\partial \alpha_k \overline{\overline{\rho}}_k \underline{\varphi}_k}{\partial t} + \frac{1}{\Delta t}\sum_j \left(\frac{1}{u_{ni}} \boldsymbol{n}_k \cdot \rho_k \left(\boldsymbol{u}_k - \boldsymbol{u}_k^s \right) \varphi_k \right) + \nabla \cdot \left(\alpha_k \overline{\overline{\rho}}_k \underline{\phi}_k \underline{\boldsymbol{u}}_k \right) + \nabla \cdot \left(\alpha_k \boldsymbol{J}_k^t \right)$$

Next, with regards to the RHS of equation A1.8, the corresponding time average simply reads:

$$-\overline{\nabla \cdot \boldsymbol{J}_k} + \overline{\psi_k} = -\nabla \cdot \alpha_k \overline{\overline{\boldsymbol{J}}}_k + \alpha_k \overline{\overline{\psi}}_k \tag{A1.27}$$

Finally, the time-averaged general conservation equation is derived:

$$\frac{\partial \alpha_k \overline{\overline{\rho}}_k \underline{\varphi}_k}{\partial t} + \nabla \cdot \left(\alpha_k \overline{\overline{\rho}}_k \underline{\phi}_k \underline{\boldsymbol{u}}_k \right) + \nabla \cdot \alpha_k \left(\boldsymbol{J}_k^t + \overline{\overline{\boldsymbol{J}}}_k \right) + \tag{A1.28}$$

$$\frac{1}{\Delta t}\sum_j \left(\frac{1}{u_{ni}} \boldsymbol{n}_k \cdot \rho_k \left(\boldsymbol{u}_k - \boldsymbol{u}_k^s \right) \varphi_k \right) - \alpha_k \overline{\overline{\psi}}_k = 0$$

To further simplify equation A1.28, the following definition for the interface exchange term is introduced:

$$I_k^{\varphi_k} = \frac{1}{\Delta t}\sum_j \left(\frac{1}{u_{ni}} \boldsymbol{n}_k \cdot \rho_k \left(\boldsymbol{u}_k - \boldsymbol{u}_k^s \right) \varphi_k \right) \qquad \text{A1.29}$$

Equation A1.28 hence becomes:

$$\frac{\partial \alpha_k \overline{\overline{\rho_k \varphi_k}}}{\partial t} + \nabla \cdot \left(\alpha_k \overline{\overline{\rho_k}} \underline{\underline{\phi_k}} \, \underline{\underline{\boldsymbol{u}_k}} \right) + \nabla \cdot \alpha_k \left(\boldsymbol{J}_k^t + \overline{\overline{\boldsymbol{J}_k}} \right) + I_k^{\varphi_k} - \alpha_k \overline{\overline{\psi_k}} = 0 \qquad \text{A1.30}$$

By specifying φ_k, $\boldsymbol{J}_k$, $\boldsymbol{J}_k^t$ and ψ_k, the time-averaged governing equations of mass, momentum and energy can be derived (Ishii & Hikiki 2006c).

A1.2 Mass Conservation Equation

In this case, $\varphi_k = 1$, $\boldsymbol{J}_k = \boldsymbol{0}$, $\boldsymbol{J}_k^t = \boldsymbol{0}$ and $\psi_k = 0$, and the time-averaged mass conservation equation for k^{th} fluid phase reads:

$$\frac{\partial \alpha_k \overline{\overline{\rho_k}}}{\partial t} + \nabla \cdot \left(\alpha_k \overline{\overline{\rho_k}} \underline{\underline{\boldsymbol{u}_k}} \right) + I_k = 0 \qquad \text{A1.31}$$

Here, I_k represents the rate of interface mass exchange per unit volume, given by (in its most common notation in the literature):

$$\Gamma_k = -I_k \qquad \text{A1.32}$$

The mass conservation equation in Cartesian coordinates is given by:

$$\frac{\partial \alpha_k \overline{\overline{\rho_k}}}{\partial t} + \frac{\partial}{\partial x}\left(\alpha_k \overline{\overline{\rho_k}} \underline{\underline{u_{x,k}}} \right) + \frac{\partial}{\partial y}\left(\alpha_k \overline{\overline{\rho_k}} \underline{\underline{u_{y,k}}} \right) + \frac{\partial}{\partial z}\left(\alpha_k \overline{\overline{\rho_k}} \underline{\underline{u_{z,k}}} \right) = \Gamma_k \qquad \text{A1.33}$$

where the subscripts, *x*, *y* and *z* respectively represent the x-, y- and z-axis directions.

A1.3 Momentum Conservation Equation

In this case, $\varphi_k = \boldsymbol{u}_k$, $\boldsymbol{J}_k = p_k \boldsymbol{I} - \boldsymbol{\tau}_k$, $\boldsymbol{J}_k^t = \overline{\rho_k \boldsymbol{u}_k' \boldsymbol{u}_k'} = -\boldsymbol{\tau}_k^t$ and $\psi_k = \boldsymbol{F}_k$, and the time-averaged momentum conservation equation is given by:

$$\frac{\partial \alpha_k \overline{\overline{\rho_k}}\, \underline{\underline{\boldsymbol{u}_k}}}{\partial t} + \nabla \cdot \left(\alpha_k \overline{\overline{\rho_k}}\, \underline{\boldsymbol{u}_k}\, \underline{\boldsymbol{u}_k} \right) + \nabla \cdot \left(\alpha_k \overline{\overline{p_k}} \boldsymbol{I} \right) - \nabla \cdot \alpha_k \left(\boldsymbol{\tau}_k^t + \overline{\overline{\boldsymbol{\tau}_k}} \right) + \boldsymbol{I}_k^{\boldsymbol{u}_k} - \alpha_k \overline{\overline{\boldsymbol{F}_k}} = 0 \qquad \text{A1.34}$$

where $\boldsymbol{\tau}_k$ and $\boldsymbol{\tau}_k^t$ are respectively the shear stress and the turbulence stress. $\boldsymbol{I}_k^{\boldsymbol{u}_k}$ represents the rate of fluid/fluid interface momentum exchange per unit volume.

In Cartesian coordinates, equation A1.34 in *x*-axis direction is given by:

$$\begin{aligned} &\frac{\partial \alpha_k \overline{\overline{\rho_k}}\, \underline{\underline{u_{x,k}}}}{\partial t} + \frac{\partial}{\partial x}\left(\alpha_k \overline{\overline{\rho_k}}\, \underline{u_{x,k}}\, \underline{u_{x,k}} \right) + \frac{\partial}{\partial y}\left(\alpha_k \overline{\overline{\rho_k}}\, \underline{u_{x,k}}\, \underline{u_{y,k}} \right) + \frac{\partial}{\partial z}\left(\alpha_k \overline{\overline{\rho_k}}\, \underline{u_{x,k}}\, \underline{u_{z,k}} \right) + \\ &\frac{\partial}{\partial x}\left(\alpha_k \overline{\overline{p_k}} \right) + \frac{\partial}{\partial y}\left(\alpha_k \overline{\overline{p_k}} \right) + \frac{\partial}{\partial z}\left(\alpha_k \overline{\overline{p_k}} \right) - \\ &\frac{\partial}{\partial x} \alpha_k \left(\overline{\overline{\tau_{xx,k}}} + \tau_{xx,k}^t \right) - \frac{\partial}{\partial y} \alpha_k \left(\overline{\overline{\tau_{xy,k}}} + \tau_{xy,k}^t \right) - \frac{\partial}{\partial z} \alpha_k \left(\overline{\overline{\tau_{xz,k}}} + \tau_{xz,k}^t \right) + \\ &I_k^{u_{x,k}} - \alpha_k \overline{\overline{F_{x,k}}} = 0 \end{aligned} \qquad \text{A1.35}$$

A1.4 Energy Conservation Equation

In this case, $\phi_k = E_k = e_k + u_k^2/2$, $\boldsymbol{J}_k = \boldsymbol{q}_k - \left(p_k \boldsymbol{I} - \boldsymbol{\tau}_k \right) \cdot \boldsymbol{u}_k$, $\boldsymbol{J}_k^t = \boldsymbol{q}_k^t = \overline{\rho_k \boldsymbol{u}_k'' E_k''} - \overline{\boldsymbol{\tau}_k \cdot \boldsymbol{u}_k''} + \overline{p_k \boldsymbol{I} \cdot \boldsymbol{u}_k''}$ and $\psi_k = \boldsymbol{F}_k \cdot \boldsymbol{u}_k + \dot{Q}_k$, and the time-averaged energy conservation equation is given by:

$$\begin{aligned} &\frac{\partial \alpha_k \overline{\overline{\rho_k}}\, \underline{\underline{E_k}}}{\partial t} + \nabla \cdot \left(\alpha_k \overline{\overline{\rho_k}}\, \underline{\boldsymbol{u}_k}\, \underline{E_k} \right) + \nabla \cdot \left(\alpha_k \overline{\overline{p_k}} \boldsymbol{I} \cdot \underline{\boldsymbol{u}_k} \right) - \\ &\nabla \cdot \left(\alpha_k \overline{\overline{\boldsymbol{\tau}_k}} \cdot \underline{\boldsymbol{u}_k} \right) + \nabla \cdot \alpha_k \left(\boldsymbol{q}_k^t + \overline{\overline{\boldsymbol{q}_k}} \right) + I_k^{E_k} - \alpha_k \overline{\overline{\boldsymbol{F}_k}} \cdot \underline{\boldsymbol{u}_k} = 0 \end{aligned} \qquad \text{A1.36}$$

where $\boldsymbol{q}_k$ and $\boldsymbol{q}_k^t$ are respectively the diffusion heat flux and the turbulence heat flux. For the modelling of the interface energy exchange term, $I_k^{E_k}$, it is essential to include

the term, $\overline{\overline{p}}\left(\partial\alpha_k/\partial t\right)$. According to Munkejord et al. (2009), this ensures the entropy conservation for k^{th} fluid phase. Hence:

$$\frac{\partial\alpha_k\overline{\overline{\rho_k}}\,\underline{\underline{E_k}}}{\partial t}+\nabla\cdot\left(\alpha_k\overline{\overline{\rho_k}}\,\underline{\underline{\boldsymbol{u}_k}}\,\underline{\underline{E_k}}\right)+\nabla\cdot\left(\alpha_k\overline{\overline{p_k}}\,\boldsymbol{I}\cdot\underline{\underline{\boldsymbol{u}_k}}\right)- \tag{A1.37}$$
$$\nabla\cdot\left(\alpha_k\overline{\overline{\boldsymbol{\tau}_k}}\cdot\underline{\underline{\boldsymbol{u}_k}}\right)+\nabla\cdot\alpha_k\left(\boldsymbol{q}_k^t+\overline{\overline{\boldsymbol{q}_k}}\right)+\overline{\overline{p}}\frac{\partial\alpha_k}{\partial t}+I_k^{E_k*}-\alpha_k\overline{\overline{\boldsymbol{F}_k}}\cdot\underline{\underline{\boldsymbol{u}_k}}=0$$

Also note that:

$$\underline{\underline{E_k}}=\underline{\underline{e_k}}+\frac{\left(\underline{\underline{\boldsymbol{u}_k}}\right)^2}{2}+\frac{\left(\boldsymbol{u}_k^{'}\right)^2}{2} \tag{A1.38}$$

The time-averaged energy conservation equation is also given in Cartesian coordinates:

$$\frac{\partial\alpha_k\overline{\overline{\rho_k}}\,\underline{\underline{E_k}}}{\partial t}+\frac{\partial}{\partial x}\left(\alpha_k\overline{\overline{\rho_k}}\,\underline{\underline{u_{x,k}}}\,\underline{\underline{E_k}}\right)+\frac{\partial}{\partial y}\left(\alpha_k\overline{\overline{\rho_k}}\,\underline{\underline{u_{y,k}}}\,\underline{\underline{E_k}}\right)+\frac{\partial}{\partial z}\left(\alpha_k\overline{\overline{\rho_k}}\,\underline{\underline{u_{z,k}}}\,\underline{\underline{E_k}}\right)+ \tag{A1.39}$$
$$\frac{\partial}{\partial x}\left(\alpha_k\underline{\underline{u_{x,k}}}\,\overline{\overline{p_k}}\right)+\frac{\partial}{\partial y}\left(\alpha_k\underline{\underline{u_{y,k}}}\,\overline{\overline{p_k}}\right)+\frac{\partial}{\partial z}\left(\alpha_k\underline{\underline{u_{z,k}}}\,\overline{\overline{p_k}}\right)-$$
$$\frac{\partial}{\partial x}\left(\alpha_k\underline{\underline{u_{x,k}}}\,\overline{\overline{\tau_{xx,k}}}\right)-\frac{\partial}{\partial y}\left(\alpha_k\underline{\underline{u_{x,k}}}\,\overline{\overline{\tau_{yx,k}}}\right)-\frac{\partial}{\partial z}\left(\alpha_k\underline{\underline{u_{x,k}}}\,\overline{\overline{\tau_{zx,k}}}\right)-$$
$$\frac{\partial}{\partial x}\left(\alpha_k\underline{\underline{u_{y,k}}}\,\overline{\overline{\tau_{xy,k}}}\right)-\frac{\partial}{\partial y}\left(\alpha_k\underline{\underline{u_{y,k}}}\,\overline{\overline{\tau_{yy,k}}}\right)-\frac{\partial}{\partial z}\left(\alpha_k\underline{\underline{u_{y,k}}}\,\overline{\overline{\tau_{zy,k}}}\right)-$$
$$\frac{\partial}{\partial x}\left(\alpha_k\underline{\underline{u_{z,k}}}\,\overline{\overline{\tau_{xz,k}}}\right)-\frac{\partial}{\partial y}\left(\alpha_k\underline{\underline{u_{z,k}}}\,\overline{\overline{\tau_{yz,k}}}\right)-\frac{\partial}{\partial z}\left(\alpha_k\underline{\underline{u_{z,k}}}\,\overline{\overline{\tau_{zz,k}}}\right)-$$
$$\frac{\partial}{\partial x}\alpha_k\left(\overline{\overline{q_{x,k}}}+q_{x,k}^t\right)-\frac{\partial}{\partial y}\alpha_k\left(\overline{\overline{q_{y,k}}}+q_{y,k}^t\right)-\frac{\partial}{\partial z}\alpha_k\left(\overline{\overline{q_{z,k}}}+q_{z,k}^t\right)+$$
$$\overline{\overline{p_k}}\frac{\partial\alpha_k}{\partial t}+I_k^{E_k*}-$$
$$\alpha_k\left(\overline{\overline{F_{x,k}}}\,\underline{\underline{u_{x,k}}}+\overline{\overline{F_{y,k}}}\,\underline{\underline{u_{y,k}}}+\overline{\overline{F_{z,k}}}\,\underline{\underline{u_{z,k}}}+\overline{\overline{\dot{Q}_k}}\right)=0$$

To this end, the full set of the time-averaged conservation equations are derived (both in coordinate free and Cartesian form). It can be seen that time-averaging over a fixed time interval gives rise to fluctuating terms (turbulence fluxes) and interface exchange terms (in presence of moving interfaces).

A1.5 Conservation Equations in Single-Fluid Flow

In the case of single-phase or homogeneous multi-phase flow, the previously derived conservation equations can be shown to reduce to (Ishii & Hikiki 2006c):

$$\frac{\partial}{\partial t}\bar{\rho} + \nabla \cdot \bar{\rho}\underline{\boldsymbol{u}} = 0 \qquad \text{A1.40}$$

$$\frac{\partial}{\partial t}\bar{\rho}\underline{\boldsymbol{u}} + \nabla \cdot \left(\bar{\rho}\underline{\boldsymbol{u}}\underline{\boldsymbol{u}} + \bar{p}\boldsymbol{I}\right) - \nabla \cdot \left(\bar{\boldsymbol{\tau}} + \boldsymbol{\tau}^{t}\right) = 0 \qquad \text{A1.41}$$

$$\frac{\partial}{\partial t}\bar{\rho}\underline{E} + \nabla \cdot \left(\bar{\rho}\underline{\boldsymbol{u}}\underline{E} + \bar{p}\boldsymbol{I} \cdot \underline{\boldsymbol{u}}\right) - \nabla \cdot \bar{\boldsymbol{\tau}} \cdot \underline{\boldsymbol{u}} - \nabla \cdot \left(\overline{\boldsymbol{q}_k} + \boldsymbol{q}_k^{t}\right) = 0 \qquad \text{A1.42}$$

Note that, as the entire CV is occupied by a single fluid phase or a homogeneous mixture of multiple fluid phases, the interface exchange terms are omitted.

For inviscid flow without energy diffusion, the above equations become:

$$\frac{\partial}{\partial t}\rho + \nabla \cdot \rho\boldsymbol{u} = 0 \qquad \text{A1.43}$$

$$\frac{\partial}{\partial t}\rho\boldsymbol{u} + \nabla \cdot \left(\rho\boldsymbol{u}\boldsymbol{u} + p\boldsymbol{I}\right) = 0 \qquad \text{A1.44}$$

$$\frac{\partial}{\partial t}\rho E + \nabla \cdot \left(\rho\boldsymbol{u}E + p\boldsymbol{I} \cdot \boldsymbol{u}\right) = 0 \qquad \text{A1.45}$$

The well-known Euler equations for fluid dynamics are derived.

In the case of viscous flow with turbulence, substitution of the definitions of the turbulence terms, $\boldsymbol{\tau}^{t}$ and $\boldsymbol{q}^{t}$ (given in Sections A1.3 and A1.4 respectively) into equations A1.40 to A1.42 gives:

$$\frac{\partial}{\partial t}\bar{\rho} + \nabla \cdot \bar{\rho}\underline{\boldsymbol{u}} = 0 \qquad \text{A1.46}$$

$$\frac{\partial}{\partial t}\bar{\rho}\underline{\boldsymbol{u}} + \nabla \cdot \left(\bar{\rho}\underline{\boldsymbol{u}}\underline{\boldsymbol{u}} + \bar{p}\mathrm{I}\right) - \nabla \cdot \left(\bar{\boldsymbol{\tau}} + \overline{\rho\boldsymbol{u}'\boldsymbol{u}'}\right) = 0 \qquad \text{A1.47}$$

$$\frac{\partial}{\partial t}\bar{\rho}\underline{\underline{E}}+\nabla\cdot\left(\bar{\rho}\underline{\underline{u}}\underline{\underline{E}}+\bar{p}\boldsymbol{I}\cdot\underline{\underline{u}}\right)-\nabla\cdot\left(\overline{\rho\boldsymbol{u}'E'}-\overline{\boldsymbol{\tau}\cdot\boldsymbol{u}}+\overline{p\boldsymbol{I}\cdot\boldsymbol{u}'}\right)=0 \qquad \text{A1.48}$$

The resulting equations are referred to as the Favre-averaged Navier-Stokes equations. It is known that, for most of flows encountered in engineering applications, the turbulence effect on fluid density can be safely neglected. In this case, Favre-averaging can be simply replaced with time-averaging, which leads to:

$$\frac{\partial}{\partial t}\bar{\rho}+\nabla\cdot\bar{\rho}\bar{\boldsymbol{u}}=0 \qquad \text{A1.49}$$

$$\frac{\partial}{\partial t}\bar{\rho}\bar{\boldsymbol{u}}+\nabla\cdot\left(\bar{\rho}\bar{\boldsymbol{u}}\bar{\boldsymbol{u}}+\bar{p}\boldsymbol{I}\right)-\nabla\cdot\left(\bar{\boldsymbol{\tau}}+\bar{\rho}\overline{\boldsymbol{u}'\boldsymbol{u}'}\right)=0 \qquad \text{A1.50}$$

$$\frac{\partial}{\partial t}\bar{\rho}\bar{E}+\nabla\cdot\left(\bar{\rho}\bar{\boldsymbol{u}}\bar{E}+\bar{p}\boldsymbol{I}\cdot\bar{\boldsymbol{u}}\right)-\nabla\cdot\left(\bar{\rho}\overline{\boldsymbol{u}'E'}-\overline{\boldsymbol{\tau}\cdot\boldsymbol{u}}+\overline{p\boldsymbol{I}\cdot\boldsymbol{u}'}\right)=0 \qquad \text{A1.51}$$

The classical Reynolds-averaged Navier-Stokes (RANS) equations are derived.

By observing equations A1.49 to A1.51, closure models are required for specifying $\bar{\boldsymbol{\tau}}$, $\bar{\rho}\overline{\boldsymbol{u}'\boldsymbol{u}'}$, $\bar{\rho}\overline{\boldsymbol{u}'E'}$, $\overline{\boldsymbol{\tau}\cdot\boldsymbol{u}}$ and $\overline{p\boldsymbol{I}\cdot\boldsymbol{u}'}$.

A1.5.1 Viscous Stress Model

$\bar{\boldsymbol{\tau}}$ is referred to as the stress tensor. For Newtonian fluid, it can be related to the mean strain rate (mean rate of change of the deformation), ***s*** of the fluid, given by:

$$\bar{\boldsymbol{\tau}}=\lambda\left(\nabla\cdot\bar{\boldsymbol{u}}\right)\mathrm{I}+2\mu\boldsymbol{s}=\lambda\left(\nabla\cdot\bar{\boldsymbol{u}}\right)\mathrm{I}+2\mu\left(\underbrace{\frac{\left(\nabla\bar{\boldsymbol{u}}\right)}{2}+\frac{\left(\nabla\bar{\boldsymbol{u}}\right)^{T}}{2}}_{\text{mean strain rate}}\right)= \qquad \text{A1.52}$$

$$\left(\lambda+\frac{2}{3}\mu\right)\left(\nabla\cdot\bar{\boldsymbol{u}}\right)\mathrm{I}+2\mu\left(\underbrace{\frac{\left(\nabla\bar{\boldsymbol{u}}\right)}{2}+\frac{\left(\nabla\bar{\boldsymbol{u}}\right)^{T}}{2}-\frac{1}{3}\left(\nabla\cdot\bar{\boldsymbol{u}}\right)\boldsymbol{I}}_{\text{trace-less mean strain rate}}\right)$$

where λ and μ are respectively the bulk viscosity and the dynamic viscosity. The first term in equation A1.52 is associated with the dilation of the fluid particles and usually negligible (even for compressible flow) (Sonin 2001).

A1.5.2 Turbulence Model

Returning to equations A1.49 to A1.51, the remaining unknowns, $\overline{\rho}\overline{\boldsymbol{u}'\boldsymbol{u}'}$, $\overline{\rho}\overline{\boldsymbol{u}'E'}$, $\overline{\boldsymbol{\tau}\cdot\boldsymbol{u}}$ and $\overline{p\boldsymbol{I}\cdot\boldsymbol{u}'}$ all contain fluctuating terms (the fluctuating terms in $\overline{\boldsymbol{\tau}\cdot\boldsymbol{u}}$ is shown below in equation A1.54). Additional turbulence modelling is required.

In specifying these unknown terms, they are manipulated in the following way:

$$\overline{\rho}\overline{\boldsymbol{u}'E'} + \overline{p\boldsymbol{I}\cdot\boldsymbol{u}'} = \overline{\rho}\overline{\boldsymbol{u}'\left(E-\overline{E}\right)} + \overline{p\boldsymbol{I}\cdot\boldsymbol{u}'} = \overline{\rho}\overline{\boldsymbol{u}'E} + \overline{p\boldsymbol{I}\cdot\boldsymbol{u}'} = \tag{A1.53}$$

$$\overline{\rho}\overline{\boldsymbol{u}'\left(e+\frac{1}{2}\boldsymbol{u}\cdot\boldsymbol{u}\right)} + \overline{\rho\frac{p}{\rho}\boldsymbol{I}\cdot\boldsymbol{u}'} =$$

$$\overline{\rho}\overline{\boldsymbol{u}'h} + \overline{\rho}\overline{\boldsymbol{u}'\frac{1}{2}(\boldsymbol{u}\cdot\boldsymbol{u})} = \overline{\rho}\overline{\boldsymbol{u}'h} + \overline{\rho}\overline{\boldsymbol{u}'\frac{1}{2}\left(\overline{\boldsymbol{u}}\cdot\overline{\boldsymbol{u}} + 2\overline{\boldsymbol{u}}\cdot\boldsymbol{u}' + \boldsymbol{u}'\cdot\boldsymbol{u}'\right)} =$$

$$\overline{\rho}\overline{\boldsymbol{u}'h} + \overline{\rho}\overline{\boldsymbol{u}'\frac{1}{2}\left(\boldsymbol{u}'\cdot\boldsymbol{u}'\right)} + \overline{\rho}\overline{\boldsymbol{u}'\left(\overline{\boldsymbol{u}}\cdot\boldsymbol{u}'\right)} =$$

$$\overline{\rho}\overline{\boldsymbol{u}'h} + \frac{\overline{\rho}\overline{\boldsymbol{u}'\left(\boldsymbol{u}'\cdot\boldsymbol{u}'\right)}}{2} + \overline{\boldsymbol{u}}\cdot\overline{\rho\left(\boldsymbol{u}'\boldsymbol{u}'\right)}$$

$$\overline{\boldsymbol{\tau}\cdot\boldsymbol{u}} = \overline{\boldsymbol{\tau}}\cdot\overline{\boldsymbol{u}} + \overline{\overline{\boldsymbol{\tau}}\cdot\boldsymbol{u}'} + \overline{\boldsymbol{\tau}'\cdot\overline{\boldsymbol{u}}} + \overline{\boldsymbol{\tau}'\cdot\boldsymbol{u}'} = \overline{\boldsymbol{\tau}}\cdot\overline{\boldsymbol{u}} + \overline{\boldsymbol{\tau}'\cdot\boldsymbol{u}'} \tag{A1.54}$$

Substitution of the above equations to the RANS equations A1.49 to A1.51 gives:

$$\frac{\partial}{\partial t}\overline{\rho} + \nabla\cdot\overline{\rho}\overline{\boldsymbol{u}} = 0 \tag{A1.55}$$

$$\frac{\partial}{\partial t}\overline{\rho}\overline{\boldsymbol{u}} + \nabla\cdot\left(\overline{\rho}\overline{\boldsymbol{u}}\overline{\boldsymbol{u}} + \overline{p}\boldsymbol{I}\right) - \nabla\cdot\left(\overline{\boldsymbol{\tau}} + \underbrace{\overline{\rho}\overline{\boldsymbol{u}'\boldsymbol{u}'}}_{(1)}\right) = 0 \tag{A1.56}$$

$$\frac{\partial}{\partial t}\overline{\rho}\overline{E}+\nabla\cdot\left(\overline{\rho}\overline{\boldsymbol{u}}\overline{E}+\overline{p}\boldsymbol{I}\cdot\overline{\boldsymbol{u}}\right) \qquad \text{A1.57}$$

$$-\nabla\cdot\left(\underbrace{\overline{\rho}\overline{\boldsymbol{u}'h'}}_{(2)}+\underbrace{\frac{\overline{\rho}\overline{\boldsymbol{u}'\left(\boldsymbol{u}'\cdot\boldsymbol{u}'\right)}}{2}}_{(3)}+\overline{\boldsymbol{u}}\cdot\underbrace{\overline{\rho}\overline{\left(\boldsymbol{u}'\boldsymbol{u}'\right)}}_{(1)}-\overline{\boldsymbol{\tau}}\cdot\overline{\boldsymbol{u}}-\underbrace{\overline{\boldsymbol{\tau}'\cdot\boldsymbol{u}'}}_{(4)}\right)=0$$

In the above equations, all terms containing the fluctuating parts are indexed from (1) to (4). Focusing on (1), it is referred to as the Reynolds (or turbulence) stress tensor, $\boldsymbol{\tau}^t$ (see also Section A1.3) which accounts for momentum transfer by the fluctuating velocity field. It can be split into the isotropic and anisotropic parts (respectively corresponding to the trace of $\boldsymbol{\tau}^t$ and the trace-less $\boldsymbol{\tau}^t$), given by:

$$\boldsymbol{\tau}^t=\overline{\rho}\overline{\boldsymbol{u}'\boldsymbol{u}'}=\underbrace{\overline{\rho}\frac{2}{3}k\boldsymbol{I}}_{\text{isotropic part}}+\underbrace{\overline{\rho}\left(\overline{\boldsymbol{u}'\boldsymbol{u}'}-\frac{2}{3}k\boldsymbol{I}\right)}_{\text{anisotropic part}} \qquad \text{A1.58}$$

where k is the turbulence kinetic energy defined as:

$$k=\frac{1}{2}\overline{\boldsymbol{u}'\cdot\boldsymbol{u}'} \qquad \text{A1.59}$$

Following the turbulent-viscosity (eddy-viscosity) assumption (see (Pope 2000b)), the anisotropic part of $\boldsymbol{\tau}^t$ can be related to the mean strain rate, $\boldsymbol{s}$ (defined in equation A1.52), directly analogous to the case of $\overline{\boldsymbol{\tau}}$:

$$\overline{\rho}\left(\overline{\boldsymbol{u}'\boldsymbol{u}'}-\frac{2}{3}k\boldsymbol{I}\right)=\overline{\rho}2\mu_t\boldsymbol{s} \qquad \text{A1.60}$$

where μ_t is the turbulent viscosity. The most frequently applied approach for specifying μ_t is the two-equation models (Pope 2000c). For example, the k-ε model is consisted of two transport equations for the turbulence quantities, k and ε (ε represents the rate of dissipation of k). The derivation of the k-ε model is briefly shown in the following (Pope 2000c).

The transport equation for $\boldsymbol{u}'$ can be derived from subtracting equation A1.50 from the Navier-Stokes equations, which gives:

$$\frac{\partial \boldsymbol{u}'}{\partial t} + \bar{\boldsymbol{u}} \cdot \nabla \boldsymbol{u}' = -\boldsymbol{u}' \cdot \nabla \bar{\boldsymbol{u}} + \nabla \cdot \overline{\boldsymbol{u}'\boldsymbol{u}'} + \nabla \cdot \left(\frac{\bar{\mu}}{\rho} \nabla \boldsymbol{u}' \right) - \frac{1}{\rho} \nabla p' \boldsymbol{I} \qquad \text{A1.61}$$

The transport equation for *k* (defined in equation A1.59) is thus:

$$\frac{\partial k}{\partial t} + \bar{\boldsymbol{u}} \cdot \nabla k = \underbrace{-\nabla \cdot \left(\frac{\overline{\boldsymbol{u}' \left(\boldsymbol{u}' \cdot \boldsymbol{u}' \right)}}{2} + \frac{\overline{\left(\boldsymbol{u}' p' \right)}}{\bar{\rho}} - 2 \frac{\bar{\mu}}{\rho} \overline{\boldsymbol{u}' \cdot \boldsymbol{s}^t} \right)}_{(1)} + \underbrace{-\overline{\boldsymbol{u}'\boldsymbol{u}'} : \nabla \bar{\boldsymbol{u}}}_{(2)} \underbrace{- 2 \frac{\bar{\mu}}{\rho} \overline{\boldsymbol{s}^t : \boldsymbol{s}^t}}_{(3)} \qquad \text{A1.62}$$

or in Cartesian coordinates:

$$\begin{aligned}
&\frac{\partial k}{\partial t} + \bar{u}_x \frac{\partial k}{\partial x} + \bar{u}_y \frac{\partial k}{\partial y} + \bar{u}_z \frac{\partial k}{\partial z} = \qquad \text{A1.63} \\
&-\frac{\partial}{\partial x} \left(\frac{\overline{u_x' u_x' u_x'}}{2} + \frac{\overline{u_y' u_y' u_y'}}{2} + \frac{\overline{u_z' u_z' u_z'}}{2} + \frac{\overline{\left(u_x' p' \right)}}{\bar{\rho}} - 2 \frac{\bar{\mu}}{\rho} \overline{u_x' s_{xx}^t} - 2 \frac{\bar{\mu}}{\rho} \overline{u_y' s_{xy}^t} - 2 \frac{\bar{\mu}}{\rho} \overline{u_z' s_{xz}^t} \right) \\
&-\frac{\partial}{\partial y} \left(\frac{\overline{u_x' u_x' u_x'}}{2} + \frac{\overline{u_y' u_y' u_y'}}{2} + \frac{\overline{u_z' u_z' u_z'}}{2} + \frac{\overline{\left(u_y' p' \right)}}{\bar{\rho}} - 2 \frac{\bar{\mu}}{\rho} \overline{u_x' s_{yx}^t} - 2 \frac{\bar{\mu}}{\rho} \overline{u_y' s_{yy}^t} - 2 \frac{\bar{\mu}}{\rho} \overline{u_z' s_{yz}^t} \right) \\
&-\frac{\partial}{\partial z} \left(\frac{\overline{u_x' u_x' u_x'}}{2} + \frac{\overline{u_y' u_y' u_y'}}{2} + \frac{\overline{u_z' u_z' u_z'}}{2} + \frac{\overline{\left(u_z' p' \right)}}{\bar{\rho}} - 2 \frac{\bar{\mu}}{\rho} \overline{u_x' s_{zx}^t} - 2 \frac{\bar{\mu}}{\rho} \overline{u_y' s_{zy}^t} - 2 \frac{\bar{\mu}}{\rho} \overline{u_z' s_{zz}^t} \right) \\
&-\left(\overline{u_x' u_x'} \frac{\partial \bar{u}_x}{\partial x} + \overline{u_y' u_x'} \frac{\partial \bar{u}_y}{\partial x} + \overline{u_z' u_x'} \frac{\partial \bar{u}_z}{\partial x} \right) \\
&-\left(\overline{u_x' u_y'} \frac{\partial \bar{u}_x}{\partial y} + \overline{u_y' u_y'} \frac{\partial \bar{u}_y}{\partial y} + \overline{u_z' u_y'} \frac{\partial \bar{u}_z}{\partial y} \right) \\
&-\left(\overline{u_x' u_z'} \frac{\partial \bar{u}_x}{\partial z} + \overline{u_y' u_z'} \frac{\partial \bar{u}_y}{\partial z} + \overline{u_z' u_z'} \frac{\partial \bar{u}_z}{\partial z} \right) \\
&-2 \frac{\bar{\mu}}{\rho} \left(\overline{s_{xx}^t s_{xx}^t} + \overline{s_{yx}^t s_{yx}^t} + \overline{s_{zx}^t s_{zx}^t} \right) \\
&-2 \frac{\bar{\mu}}{\rho} \left(\overline{s_{xy}^t s_{xy}^t} + \overline{s_{yy}^t s_{yy}^t} + \overline{s_{zy}^t s_{zy}^t} \right) \\
&-2 \frac{\bar{\mu}}{\rho} \left(\overline{s_{xz}^t s_{xz}^t} + \overline{s_{yz}^t s_{yz}^t} + \overline{s_{zz}^t s_{zz}^t} \right)
\end{aligned}$$

where:

$$\boldsymbol{s}^t = \left(\frac{\left(\nabla \boldsymbol{u}'\right)}{2} + \frac{\left(\nabla \boldsymbol{u}'\right)^T}{2} \right) \qquad \text{A1.64}$$

In the transport equation A1.62, the marked terms (1) to (3) respectively account for turbulent diffusion, production and dissipation. The turbulent diffusion term, which is responsible for the redistribution of k within CV, can be approximated by (Pope 2000c):

$$(1) \approx \frac{\mu_t}{\rho \mathrm{Pr}^t} \nabla k \qquad \text{A1.65}$$

where Pr^t is the turbulence Prandtl number (of 0.9 (Pope 2000c)). For the other turbulence quantity, ε, the corresponding transport equation is entirely empirical (Pope 2000c):

$$\frac{\partial \varepsilon}{\partial t} + \bar{\boldsymbol{u}} \cdot \nabla \varepsilon = -\nabla \cdot \left(\frac{\mu_t}{\rho \mathrm{Pr}^{\varepsilon}} \nabla \varepsilon \right) + C_{\varepsilon 1} \frac{\varepsilon}{k} \left(-\overline{\boldsymbol{u}' \boldsymbol{u}'} : \nabla \bar{\boldsymbol{u}} \right) - C_{\varepsilon 2} \frac{\varepsilon^2}{k} \qquad \text{A1.66}$$

where $\mathrm{Pr}^{\varepsilon} = 1.3$, $C_{\varepsilon 1} = 1.44$, $C_{\varepsilon 2} = 1.92$.

Finally, after obtaining k and ε, the turbulent viscosity is calculated as:

$$\mu^t = \bar{\rho} C_{\mu} \frac{k^2}{\varepsilon} \qquad \text{A1.67}$$

It should be pointed out here that the above derivation of the k-ε model is based on incompressible flow assumption (constant ρ). It can be easily extended to compressible flows by the addition of correction terms to the transport equations (see (Woolley et al. 2013) for example).

On a relevant note, following (Pope 2000a), the mean flow kinetic energy transport equation reads:

$$\frac{\partial \overline{K}}{\partial t}+\bar{\boldsymbol{u}}\cdot\nabla\overline{K}=\underbrace{-\nabla\cdot\left(\overline{\boldsymbol{u}\left(\boldsymbol{u}'\cdot\boldsymbol{u}'\right)}+\frac{\overline{\boldsymbol{u}(p)}}{\rho}-2\frac{\mu}{\rho}\bar{\boldsymbol{u}}\cdot\bar{\boldsymbol{s}}\right)}_{(1^*)}+\underbrace{\overline{\boldsymbol{u}'\boldsymbol{u}'}:\nabla\bar{\boldsymbol{u}}}_{(2^*)}-\underbrace{2\frac{\mu}{\rho}\overline{\boldsymbol{s}:\boldsymbol{s}}}_{(3^*)} \qquad \text{A1.68}$$

Each term on the RHS of equation A1.68 is again marked from (1*) to (3*). By comparing equations A1.68 and A1.62, terms (2) and (2*) are of opposite signs. It indicates that the turbulent kinetic energy, *k* is taken directly from the mean flow; the fluctuating motions (turbulences) gain its energy from the mean flow, while the mean flow loses its kinetic energy (hence leading to a lower mean velocity).

In addition, it is also noteworthy that the only from of energy exchange between mean flow internal energy, mean flow kinetic energy and turbulent kinetic energy is dissipation (terms (3) and (3*) respectively in equations A1.62 and A1.68). For virtually all flows encountered in practice, (3) >> (3*), that is, energy dissipation is mainly through turbulence.

Other two-equation turbulent-viscosity models are also available. In most of these, the transport equation of *k* is kept, but there are diverse choices for the second transport equation. For example, defining the specific dissipation rate as $\omega=\varepsilon/k$, the transport equation for ω is given by (Pope 2000c):

$$\frac{\partial \omega}{\partial t}+\bar{\boldsymbol{u}}\cdot\nabla\omega=-\nabla\cdot\left(\frac{\mu_t}{\rho\mathrm{Pr}^{\omega}}\nabla\omega\right)+C_{\omega 1}\frac{\omega}{k}\left(-\overline{\boldsymbol{u}'\boldsymbol{u}'}:\nabla\bar{\boldsymbol{u}}\right)-C_{\omega 2}\omega^2 \qquad \text{A1.69}$$

where Pr^{ω}, $C_{\omega 1}$ and $C_{\omega 2}$ are again model constants. It is noteworthy that, the addition of a diffusion term to equation A1.69 gives:

$$\frac{\partial \omega}{\partial t}+\bar{\boldsymbol{u}}\cdot\nabla\omega=-\nabla\cdot\left(\frac{\mu_t}{\rho\mathrm{Pr}^{\omega}}\nabla\omega\right)+C_{\omega 1}\frac{\omega}{k}\left(-\overline{\boldsymbol{u}'\boldsymbol{u}'}:\nabla\bar{\boldsymbol{u}}\right)-C_{\omega 2}\omega^2+\frac{2\mu_t}{\rho\mathrm{Pr}^{\omega}k}\nabla\omega\cdot\nabla k \qquad \text{A1.70}$$

It can be shown that equation A1.70 is essentially the transport equation of ε in the *k*-ε model (Pope 2000c).

Returning to equation A1.57, the term marked by (2) represents the turbulent transport of heat. A gradient approximation is usually applied, given by (Pope 2000b; CFD online 2005):

$$(2) \approx -C_p \frac{\mu_t}{\mathrm{Pr}^t} \nabla \bar{T} \qquad \text{A1.71}$$

where C_p is the constant pressure heat capacity of the mean flow.

(3) and (4) account for turbulent transport and diffusion of *k*, and they are modelled again by gradient approximation, given by (Pope 2000b; CFD online 2005):

$$(3) + (4) \approx -\left(\mu + \frac{\mu_t}{\sigma^k} \right) \nabla k \qquad \text{A1.72}$$

They can be neglected all together if $k << \bar{h}$, which is a reasonable assumption for most flows (CFD online 2005).

To this point, the closed form of the RANS equations is derived.

A2 Application of the Riemann Invariants and Rankine-Hugoniot Conditions in Solving a Hyperbolic PDE System Using the HEM Model as an Example

In Section 2.1.6.1.3, Chapter 2, the Riemann invariants and the Rankine-Hugoniot conditions for relating the variables across each wave in a hyperbolic PDE system are introduced. They form the basis of modern numerical solution schemes for hyperbolic PDE systems.

In order to demonstrate how the unknown variables in the star region, $\boldsymbol{V}_L^*$ and $\boldsymbol{V}_R^*$ (see figure 2.6, Chapter 2) can be solved by applying the Riemann invariants and Rankine-Hugoniot conditions, herein a degree of freedom analysis is performed for the Riemann problem defined by equation 2.161 in view of the HEM model.

Referring to figure 2.6, it is assumed that waves 1, 2 and 3 are respectively a shock wave, a rarefaction (decompression) wave, and a contact wave. Across the shock wave, with the Rankine-Hugoniot conditions, there are:

$$\rho_R \hat{u}_R = \rho_R^* \hat{u}_R^* \qquad \text{A2.1}$$

$$\rho_R \hat{u}_R^2 + p_R = \rho_R^* \hat{u}_R^{*2} + p_R^* \qquad \text{A2.2}$$

$$\hat{u}_R \left(\hat{E}_R + p_R\right) = \hat{u}_R^* \left(\hat{E}_R^* + p_R^*\right) \qquad \text{A2.3}$$

Note the change of the frame of reference in the Rankine-Hugoniot conditions (i.e. the shock wave speed, $c_{shock} = 0$), where:

$$\hat{u}_R = u_R - c_{shock} \qquad \text{A2.4}$$

$$\hat{u}_R^* = u_R^* - c_{shock} \qquad \text{A2.5}$$

$$\hat{E}_R = e_R + 1/2\left(\hat{u}_R\right)^2 \qquad \text{A2.6}$$

$$\hat{E}_R^* = e_R^* + 1/2\left(\hat{u}_R^*\right)^2 \qquad \text{A2.7}$$

Applying the Riemann invariants across the rarefaction wave and the contact wave, there are respectively:

$$I_1^{\lambda_2} = p_L - \int \rho_L c_L du = p_L^* - \int \rho_L^* c_L^* du \qquad \text{A2.8}$$

$$I_2^{\lambda_2} = s_L = s_L^* \qquad \text{A2.9}$$

and:

$$I_1^{\lambda_3} = p_R^* = p_L^* \qquad \text{A2.10}$$

$$I_2^{\lambda_3} = u_R^* = u_L^* \qquad \text{A2.11}$$

From the above, a total number of seven equations (equations A2.1 to A2.3 and A2.8 to A2.11) are identified corresponding to the assumed wave structure. Given that there are an equal number of unknowns (i.e. ρ_R^*, u_R^*, p_R^*, ρ_L^*, u_L^*, p_L^*, c_{shock}; note e_R^* and e_L^* can be obtained from an EoS), the algebraic system is closed.

A3 Derivation of the Harten-Lax-van Leer-Contact (HLLC) Scheme Following Toro (2009c)

The Euler equations 2.113 derived in Section 2.1.6.1.1, Chapter 2 (see also Section A1.5) reads:

$$\frac{\partial \boldsymbol{U}}{\partial t}+\frac{\partial \boldsymbol{F}(\boldsymbol{U})}{\partial x}=\boldsymbol{0} \qquad \text{A3.1}$$

where the vector, $\boldsymbol{U}$ and flux function, $\boldsymbol{F}$ are defined in Section 2.1.6.1.1. It is noted that equation A3.1 is in conserved form.

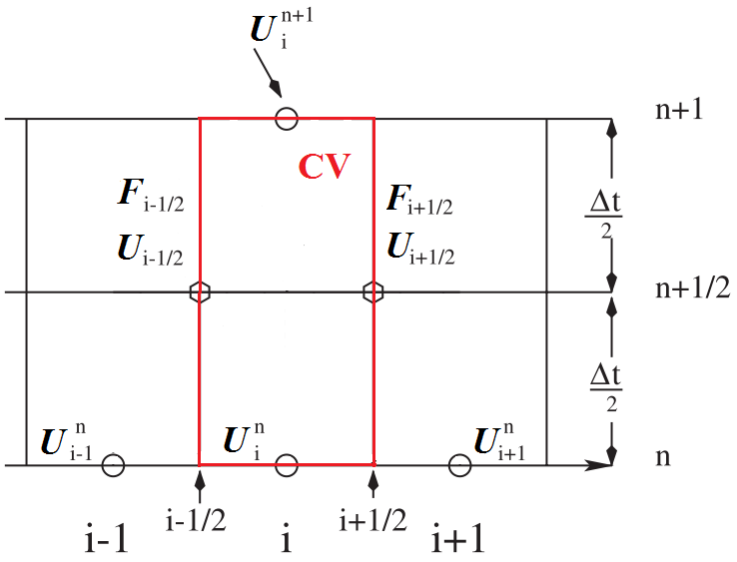

Figure A3.1: Schematic representation of the control volume of interest. The cell centres are denoted by i-1, i and i+1 (separated by Δx), while the cell interfaces are denoted by $i\pm1/2$. n stands for the n^{th} timestep of length of Δt.

Next, integration of equation A3.1 within the control volume of $\left[x_{i-1/2},x_{i+1/2}\right]\times\left[t_n,t_{n+1}\right]$ (shown in figure A3.1) gives (Toro 2009b):

$$\int_{x_{i-1/2}}^{x_{i+1/2}}\boldsymbol{U}\left(x,t_{n+1}\right)dx=\int_{x_{i-1/2}}^{x_{i+1/2}}\boldsymbol{U}\left(x,t_n\right)dx-\left[\int_{t_n}^{t_{n+1}}\boldsymbol{F}\left(x_{i-1/2},t\right)dt-\int_{t_n}^{t_{n+1}}\boldsymbol{F}\left(x_{i-1/2},t\right)dt\right] \qquad \text{A3.2}$$

Define the relevant space and time averages as:

$$\boldsymbol{U}_i^n = \frac{1}{\Delta x}\int_{x_{i-1/2}}^{x_{i+1/2}} \boldsymbol{U}\left(x,t_n\right)dx \qquad \text{A3.3}$$

$$\boldsymbol{F}_{i+1/2} = \frac{1}{\Delta t}\int_{t_n}^{t_{n+1}} \boldsymbol{F}\left(x_{i+1/2},t\right)dt \qquad \text{A3.4}$$

With the above definitions, equation A3.2 can be written as:

$$\boldsymbol{U}_i^{n+1} = \boldsymbol{U}_i^n - \frac{\Delta t}{\Delta x}\left[\boldsymbol{F}_{i+1/2} - \boldsymbol{F}_{i-1/2}\right] \qquad \text{A3.5}$$

It is clear that solving equation A3.1 is reduced to solving the fluxes, $\boldsymbol{F}$ at the cell interfaces (indexed as $i\pm1/2$). Here, the Harten-Lax-van Leer-Contact (HLLC) scheme (Toro 2009e) is presented (using $\boldsymbol{F}_{i-1/2}$ as an example).

To aid the derivation of the HLLC scheme, the wave structure corresponding to the Euler equations are displayed in figure A3.2.

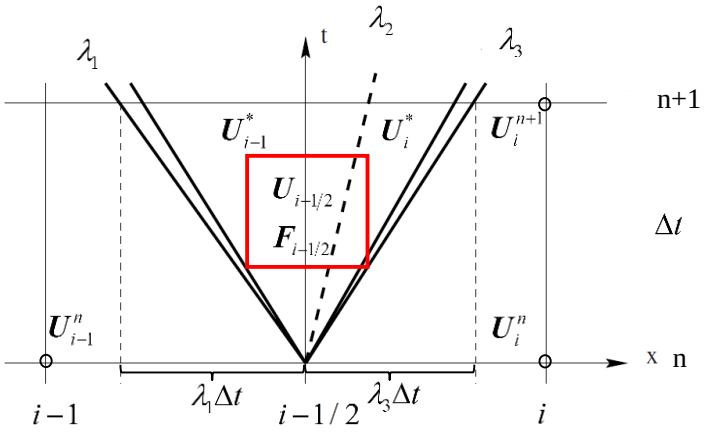

Figure A3.2: Schematic representation of the general wave structure of the Euler equations originating at a cell interface. The cell centres are denoted by i-1, i and i+1 (separated by Δx), while the cell interfaces are denoted by $i\pm1/2$. n stands for the n^{th} timestep of length of Δt.

Applying the Rankine-Hugoniot conditions (Section 2.1.6.1.3, Chapter 2) to all three waves in figure A3.2, there are:

$$\boldsymbol{F}_{i-1} - \boldsymbol{F}^*_{i-1} = \lambda_1 \left(\boldsymbol{U}_{i-1} - \boldsymbol{U}^*_{i-1} \right) \quad \text{A3.6}$$

$$\boldsymbol{F}^*_{i-1} - \boldsymbol{F}^*_i = \lambda_2 \left(\boldsymbol{U}^*_{i-1} - \boldsymbol{U}^*_i \right) \quad \text{A3.7}$$

$$\boldsymbol{F}^*_i - \boldsymbol{F}_i = \lambda_3 \left(\boldsymbol{U}^*_i - \boldsymbol{U}_i \right) \quad \text{A3.8}$$

where $\boldsymbol{F}_{i-1} = \boldsymbol{F}\left(\boldsymbol{U}_{i-1}\right)$, $\boldsymbol{F}^*_{i-1} = \boldsymbol{F}\left(\boldsymbol{U}^*_{i-1}\right)$, $\boldsymbol{F}^*_i = \boldsymbol{F}\left(\boldsymbol{U}^*_i\right)$ and $\boldsymbol{F}_i = \boldsymbol{F}\left(\boldsymbol{U}_i\right)$. It is noted that there are four unknown vectors ($\boldsymbol{U}^*_{i-1}$, $\boldsymbol{U}^*_i$, $\boldsymbol{F}^*_{i-1}$ and $\boldsymbol{F}^*_i$) in equations A3.6 and A3.8, and all other vectors are known from the previous timestep *n*. (The superscript, *n* is dropped for simplicity.)

In addition, the Riemann invariants (Section 2.1.6.1.3, Chapter 2) across the contact waves (marked by the dashed line in figure A3.2) are:

$$p^*_{i-1} = p^*_i = p^* \quad \text{A3.9}$$

$$u^*_{i-1} = u^*_i = \lambda_2 \quad \text{A3.10}$$

With equations A3.6, A3.8 (the first and second components) and A3.10, the following equations for p^*_{i-1} and p^*_i are derived:

$$p^*_{i-1} = p_{i-1} + \rho_{i-1}\left(\lambda_1 - u_{i-1}\right)\left(\lambda_2 - u_{i-1}\right) \quad \text{A3.11}$$

$$p^*_i = p_i + \rho_i\left(\lambda_3 - u_i\right)\left(\lambda_2 - u_i\right) \quad \text{A3.12}$$

With equations A3.11, A3.12 and A3.9, an expression for λ_2 is obtained:

$$\lambda_2 = \frac{p_i - p_{i-1} + \rho_{i-1}u_{i-1}(\lambda_1 - u_{i-1}) - \rho_i u_i\left(\lambda_3 - u_i\right)}{\rho_{i-1}(\lambda_1 - u_{i-1}) - \rho_i\left(\lambda_3 - u_i\right)} \quad \text{A3.13}$$

Note that (see Section 2.1.6.1.1, Chapter 2):

$$\lambda_1 = u_{i-1} - c_{i-1} \quad \text{A3.14}$$

$$\lambda_3 = u_i + c_i \qquad \text{A3.15}$$

where c is the speed of sound evaluated at cell centre i-1 or i.

Finally, rearranging equations A3.6 and A3.8 with p^*_{i-1} and p^*_i specified by equations A3.11 and A3.12 gives the expression for the interface fluxes, $\boldsymbol{F}_{i-1/2}$ (dependent on different wave configurations):

$$\boldsymbol{F}_{i-1/2} = \begin{cases} \boldsymbol{F}_{i-1}, & \text{if} \quad 0 \le \lambda_1 \\ \boldsymbol{F}_{i-1} + \lambda_1\left(\boldsymbol{U}^*_{i-1} - \boldsymbol{U}_{i-1}\right), & \text{if} \quad \lambda_1 < 0 < \lambda_2 \\ \boldsymbol{F}_i + \lambda_3\left(\boldsymbol{U}^*_i - \boldsymbol{U}_i\right), & \text{if} \quad \lambda_2 \le 0 < \lambda_3 \\ \boldsymbol{F}_i, & \text{if} \quad 0 \ge \lambda_3 \end{cases} \qquad \text{A3.16}$$

with the intermediate states given by:

$$\boldsymbol{U}^*_{i-1} = \rho_{i-1}\left(\frac{\lambda_1 - u_{i-1}}{\lambda_1 - \lambda_2}\right)\begin{bmatrix} 1 \\ \lambda_2 \\ \dfrac{E_{i-1}}{\rho_{i-1}} + \left(\lambda_2 - u_{i-1}\right)\left[\lambda_2 + \dfrac{p_{i-1}}{\rho_{i-1}\left(\lambda_1 - u_{i-1}\right)}\right] \end{bmatrix} \qquad \text{A3.17}$$

$$\boldsymbol{U}^*_i = \rho_i\left(\frac{\lambda_3 - u_i}{\lambda_3 - \lambda_2}\right)\begin{bmatrix} 1 \\ \lambda_2 \\ \dfrac{E_i}{\rho_i} + \left(\lambda_2 - u_i\right)\left[\lambda_2 + \dfrac{p_i}{\rho_i\left(\lambda_3 - u_i\right)}\right] \end{bmatrix} \qquad \text{A3.18}$$

A4 Derivation of the PRImitive CEntred Scheme of the First ORder CEntred Type (PRICE-FORCE) Following Toro & Siviglia (2003)

The general non-conservative form of hyperbolic PDEs reads (see also equation 2.129, Section 2.1.6.1.1, Chapter 2):

$$\frac{\partial \boldsymbol{V}}{\partial t} + \boldsymbol{A}(\boldsymbol{U})\frac{\partial \boldsymbol{V}}{\partial x} = 0 \qquad \text{A4.1}$$

where $\boldsymbol{V}$ is the vector of primitive variables and $\boldsymbol{A}$ is the coefficient matrix.

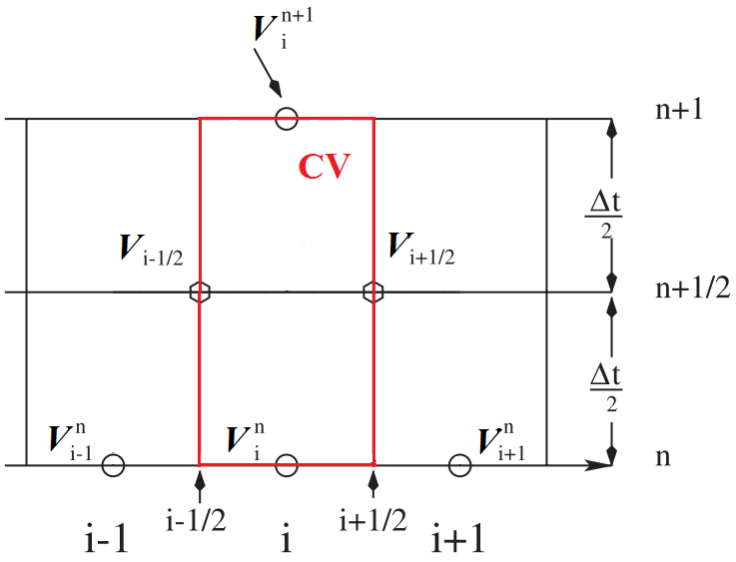

Figure A4.1: Schematic representation of the control volume of interest. The cell centres are denoted by *i*-1, *i* and *i*+1 (separated by Δx), while the cell interface is denoted by $i\pm1/2$. *n* stands for the n^{th} timestep of length of Δt.

By local linearisation with an appropriate constant matrix, $\hat{\boldsymbol{A}}_i$, integration within the control volume of $\left[x_{i-1/2}, x_{i+1/2}\right]\times\left[t_n, t_{n+1}\right]$ (shown in figure A4.1) gives:

$$\int_{x_{i-1/2}}^{x_{i+1/2}} \boldsymbol{V}\left(x,t_{n+1}\right)dx = \int_{x_{i-1/2}}^{x_{i+1/2}} \boldsymbol{V}\left(x,t_n\right)dx - \hat{\boldsymbol{A}}_i\left[\int_{t_n}^{t_{n+1}} \boldsymbol{V}\left(x_{i+1/2},t\right)dt - \int_{t_n}^{t_{n+1}} \boldsymbol{V}\left(x_{i-1/2},t\right)dt\right] \qquad \text{A4.2}$$

Define relevant space and time averages as:

$$\boldsymbol{V}_i^n = \frac{1}{\Delta x}\int_{x_{i-1/2}}^{x_{i+1/2}} \boldsymbol{V}(x, t_n)\,dx \qquad \text{A4.3}$$

$$\boldsymbol{V}_{i+1/2} = \frac{1}{\Delta t}\int_{t_n}^{t_{n+1}} \boldsymbol{V}(x_{i+1/2}, t)\,dt \qquad \text{A4.4}$$

Substitution of equations A4.3 and A4.4 to equation A4.2 gives:

$$\boldsymbol{V}_i^{n+1} = \boldsymbol{V}_i^n - \frac{\Delta t}{\Delta x}\hat{\boldsymbol{A}}_i\left[\boldsymbol{V}_{i+1/2} - \boldsymbol{V}_{i-1/2}\right] \qquad \text{A4.5}$$

where:

$$\hat{\boldsymbol{A}}_i = \boldsymbol{A}(\boldsymbol{V}_i) \qquad \text{A4.6}$$

The next task at hand is to compute the intermediate states denoted by $\boldsymbol{V}_{i\pm1/2}$ in figure A4.1.

For such purpose, the non-conservative versions of the Lax-Wendroff and the Lax-Friedrichs schemes are derived first. They are then used to construct the non-conservative version of the FORCE scheme employed in this thesis (Section 5.3.2.1, Chapter 5).

A4.1 PRICE-Lax-Wendroff Scheme

Integrating equation A4.1 within the control volume of $\left[x_{i-1/2}-1/2\,\Delta x, x_{i+1/2}+1/2\,\Delta x\right]\times\left[0,\theta\Delta t\right]$ (shown in figure A4.2; $\theta=\left[0,\,1\right]$) gives:

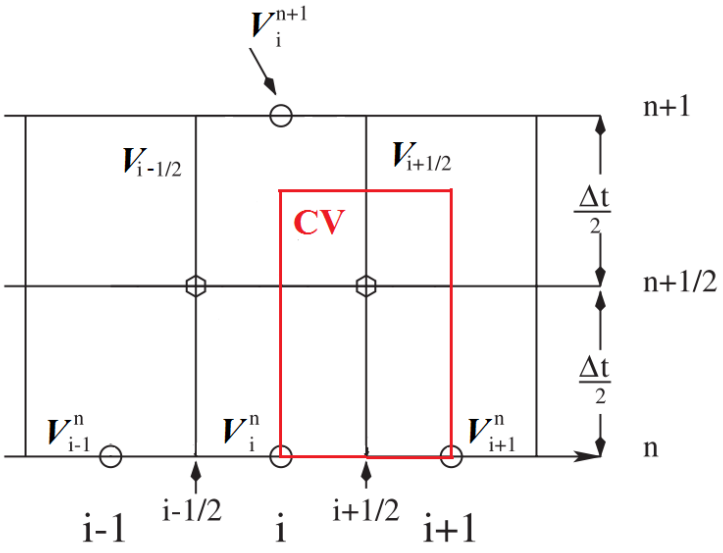

Figure A4.2: Schematic representation of the control volume for the derivation of the Lax-Wendroff scheme. The cell centres are denoted by *i*-1, *i* and *i*+1 (separated by Δx), while the cell interfaces are denoted by *i*±1/2. *n* stands for the n^{th} timestep of length of Δt.

$$\int_{x_{i-1/2}-1/2\Delta x}^{x_{i+1/2}+1/2\Delta x}\boldsymbol{V}\left(x,\theta\Delta t\right)dx=\int_{x_{i-1/2}-1/2\Delta x}^{x_{i+1/2}+1/2\Delta x}\boldsymbol{V}\left(x,0\right)dx \qquad \text{A4.7}$$
$$-\hat{\boldsymbol{A}}_{i+1/2}\left[\int_0^{\theta\Delta t}\boldsymbol{V}\left(x_{i+1/2}+1/2\,\Delta x,t\right)dt-\int_0^{\theta\Delta t}\boldsymbol{V}\left(x_{i+1/2}-1/2\,\Delta x,t\right)dt\right]$$

where:

$$\hat{\boldsymbol{A}}_{i+1/2}=\boldsymbol{A}\left(\frac{\boldsymbol{V}_{i+1}^n+\boldsymbol{V}_i^n}{2}\right) \qquad \text{A4.8}$$

Knowing that:

$$\boldsymbol{V}\left(x_{i+1/2}+1/2\,\Delta x,t\right)=\boldsymbol{V}_{i+1}^{n} \qquad \text{A4.9}$$

$$\boldsymbol{V}\left(x_{i+1/2}-1/2\,\Delta x,t\right)=\boldsymbol{V}_{i}^{n} \qquad \text{A4.10}$$

and recalling the definition of the space and time averages in equations A4.3 and A4.4, equation A4.7 can be recast into:

$$\boldsymbol{V}_{i+1/2}^{n+\alpha}=\frac{\boldsymbol{V}_{i+1}^{n}+\boldsymbol{V}_{i}^{n}}{2}-\frac{\theta\Delta t}{\Delta x}\hat{\boldsymbol{A}}_{i+1/2}\left[\boldsymbol{V}_{i+1}^{n}-\boldsymbol{V}_{i}^{n}\right] \qquad \text{A4.11}$$

With the choice of $\theta=1/2$, the intermediate state defined by equation A4.11 reads:

$$\boldsymbol{V}_{i+1/2}=\boldsymbol{V}_{i+1/2}^{n+1/2} \qquad \text{A4.12}$$

and the PRICE-Lax-Wendroff scheme is derived:

$$\boldsymbol{V}_{i}^{n+1}=\boldsymbol{V}_{i}^{n}-\frac{\Delta t}{\Delta x}\hat{\boldsymbol{A}}_{i}\left[\boldsymbol{V}_{i+1/2}^{n+1/2}-\boldsymbol{V}_{i-1/2}^{n+1/2}\right]=\boldsymbol{V}_{i}^{n}-\frac{\Delta t}{\Delta x}\boldsymbol{A}_{i}\left[\boldsymbol{V}_{i+1/2}^{PRICE-LW}-\boldsymbol{V}_{i-1/2}^{PRICE-LW}\right] \qquad \text{A4.13}$$

A4.2 PRICE-Lax-Friedrichs Scheme

Integration of equation A4.1 within the control volume of $\left[x_{i-1}, x_{i+1}\right]\times\left[0,1/2\,\Delta t\right]$ (shown in figure A4.3) gives (see (Toro 2009c) for the physical interpretation):

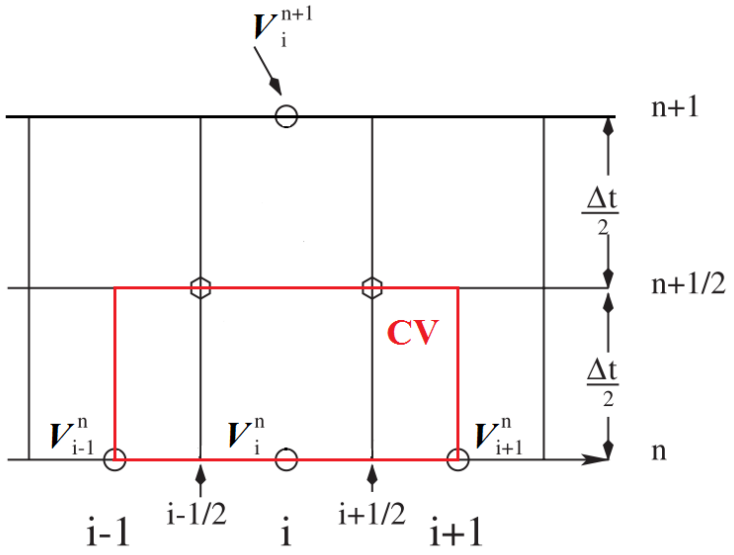

Figure A4.3: Schematic representation of the control volume for the derivation of the Lax-Friedrichs scheme. The cell centres are denoted by i-1, i and i+1 (separated by Δx), while the cell interfaces are denoted by $i\pm1/2$. n stands for the n^{th} timestep of length of Δt.

$$\int_{x_{i-1}}^{x_{i+1}} \boldsymbol{V}\left(x,\Delta t\right)dx = \int_{x_{i-1}}^{x_{i+1}} \boldsymbol{V}\left(x,0\right)dx - \hat{\boldsymbol{A}}_i\left[\int_0^{\Delta t/2} \boldsymbol{V}\left(x_{i+1},t\right)dt - \int_0^{\Delta t/2} \boldsymbol{V}\left(x_{i-1},t\right)dt\right] \qquad \text{A4.14}$$

where:

$$\hat{\boldsymbol{A}}_i = \boldsymbol{A}\left(\frac{\boldsymbol{V}_{i\text{-}1}+\boldsymbol{V}_{i+1}}{2}\right) \qquad \text{A4.15}$$

Combining with the definitions of space and time averages, equation A4.14 can be recast to:

$$\boldsymbol{V}_i^{n+1} = \frac{\boldsymbol{V}_{i-1}^n + \boldsymbol{V}_{i+1}^n}{2} - \frac{1}{2}\frac{\Delta t}{\Delta x}\hat{\boldsymbol{A}}_i\left[\boldsymbol{V}_{i+1}^n - \boldsymbol{V}_{i-1}^n\right] \qquad \text{A4.16}$$

or:

$$\boldsymbol{V}_i^{n+1} = \boldsymbol{V}_i^n - \frac{\Delta t}{\Delta x}\left[\boldsymbol{D}_{i+1/2} - \boldsymbol{D}_{i-1/2}\right] \qquad \text{A4.17}$$

where:

$$\boldsymbol{D}_{i+1/2} = \frac{1}{2}\hat{\boldsymbol{A}}_i\left(\boldsymbol{V}_i^n + \boldsymbol{V}_{i+1}^n\right) - \frac{1}{2}\frac{\Delta x}{\Delta t}\left(\boldsymbol{V}_{i+1}^n - \boldsymbol{V}_i^n\right) \qquad \text{A4.18}$$

$$\boldsymbol{D}_{i-1/2} = \frac{1}{2}\hat{\boldsymbol{A}}_i\left(\boldsymbol{V}_{i-1}^n + \boldsymbol{V}_i^n\right) - \frac{1}{2}\frac{\Delta x}{\Delta t}\left(\boldsymbol{V}_i^n - \boldsymbol{V}_{i-1}^n\right) \qquad \text{A4.19}$$

A4.3 PRICE-FORCE Scheme

The previously derived PRICE-Lax-Wendroff scheme can be rewritten as:

$$\boldsymbol{V}_i^{n+1} = \boldsymbol{V}_i^n - \frac{\Delta t}{\Delta x}\left[\boldsymbol{D}_{i+1/2}^{PRICE-LW} - \boldsymbol{D}_{i-1/2}^{PRICE-LW}\right] \quad \text{A4.20}$$

where:

$$\boldsymbol{D}_{i+1/2}^{PRICE-LW} = \hat{\boldsymbol{A}}_i\left(\boldsymbol{V}_{i+1/2}^{PRICE-LW}\right) \quad \text{A4.21}$$

From the previously derived PRICE-Lax-Lriedrichs scheme (equation A4.18), there is:

$$\boldsymbol{D}_{i+1/2}^{PRICE-LF} = \frac{1}{2}\hat{\boldsymbol{A}}_i\left(\boldsymbol{V}_i^n + \boldsymbol{V}_{i+1}^n\right) - \frac{1}{2}\frac{\Delta x}{\Delta t}\left(\boldsymbol{V}_{i+1}^n - \boldsymbol{V}_i^n\right) \quad \text{A4.22}$$

The algorithmic average between $\boldsymbol{D}_{i+1/2}^{PRICE-LW}$ and $\boldsymbol{D}_{i+1/2}^{PRICE-LW}$ gives the non-conservative version of the FORCE scheme (PRICE-FORCE scheme):

$$\boldsymbol{V}_i^{n+1} = \boldsymbol{V}_i^n - \frac{\Delta t}{\Delta x}\left[\boldsymbol{D}_{i+1/2}^{PRICE-FORCE} - \boldsymbol{D}_{i-1/2}^{PRICE-FORCE}\right] \quad \text{A4.23}$$

where:

$$\boldsymbol{D}_{i+1/2}^{PRICE-FORCE} = \frac{\boldsymbol{D}_{i+1/2}^{PRICE-LW} + \boldsymbol{D}_{i+1/2}^{PRICE-LF}}{2} \quad \text{A4.24}$$

It should be noted here that, by analogy, the conservative version of the FORCE scheme can be derived (see (Toro & Billett 2000)).

A5 Grid Convergence Test Results

A5.1 Modelling of CO_2 Decompression across the Triple Point

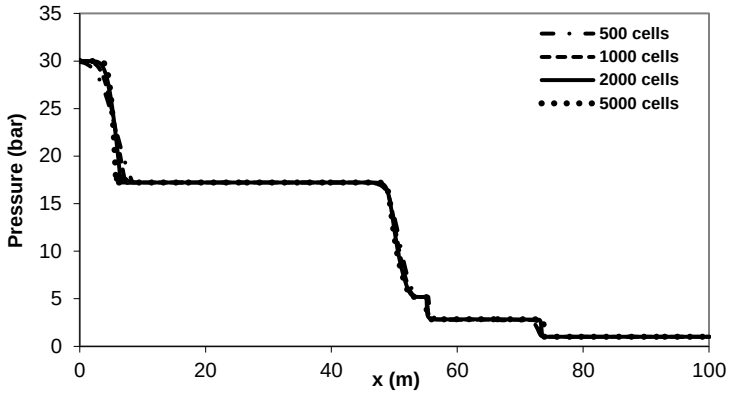

Figure A5.1: Grid convergence test results for the Riemann problem test, showing the predicted pressure profiles at 1 ms following the start of the simulations.

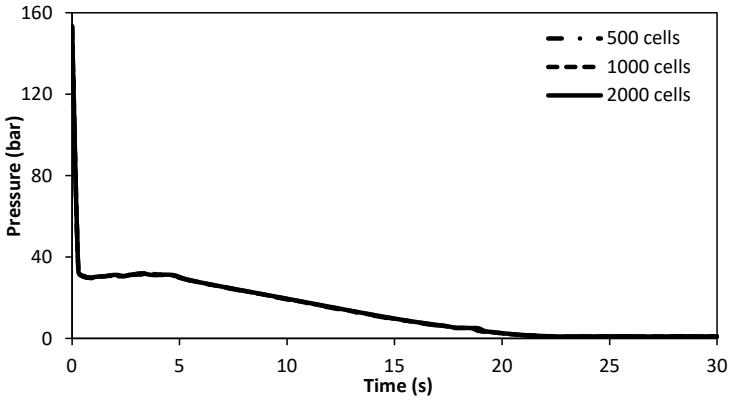

Figure A5.2: Grid convergence test results for CO_2 pipeline decompression simulations, showing the predicted pressure variations with time at the closed end of the test pipe during decompression.

A5.2 Modelling of Thermodynamic Non-Equilibrium during the Decompression of CO_2-Rich Mixtures

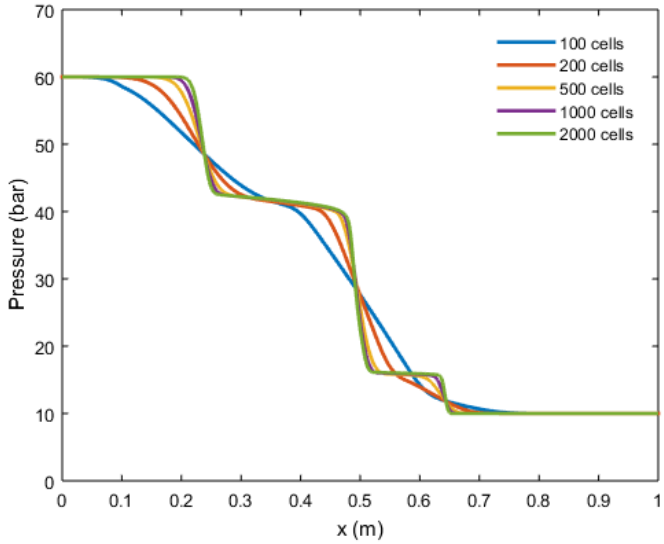

Figure A5.3: Grid convergence test results for the Riemann problem test, showing the predicted pressure profiles at 1 ms following the start of the simulations.

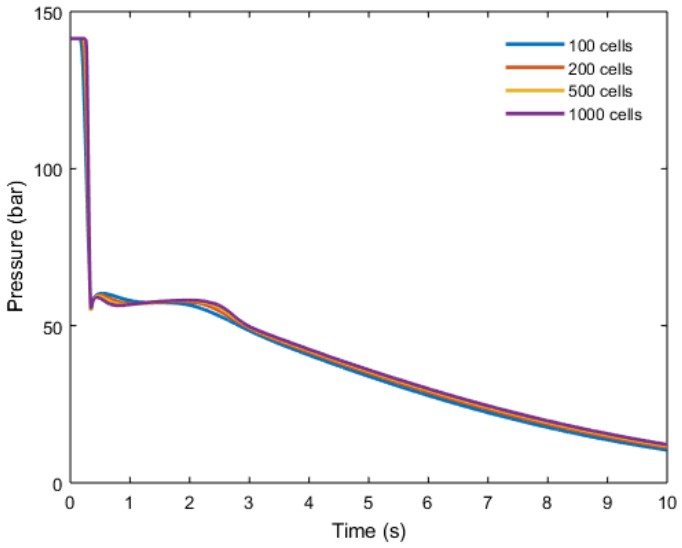

Figure A5.4: Grid convergence test results for the pipeline decompression simulations, showing the predicted pressure variations with time at the closed end of the test pipe during decompression for test 26.

A5.3 Modelling of Heterogeneous Flow during CO_2 Pipeline Puncture Decompression

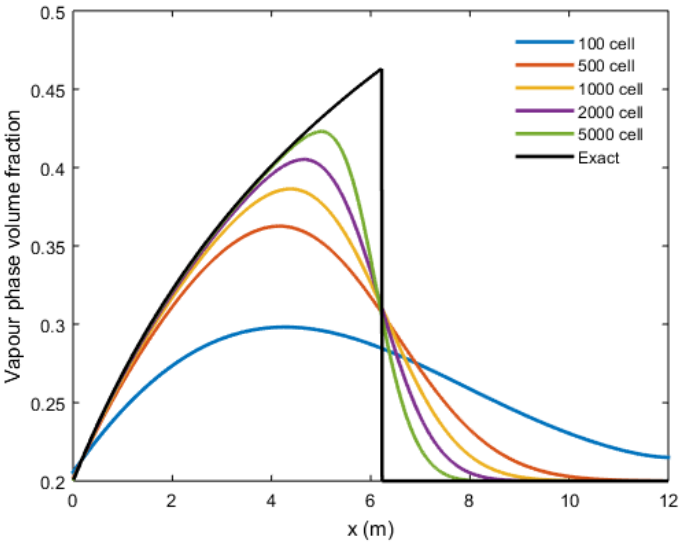

(a)

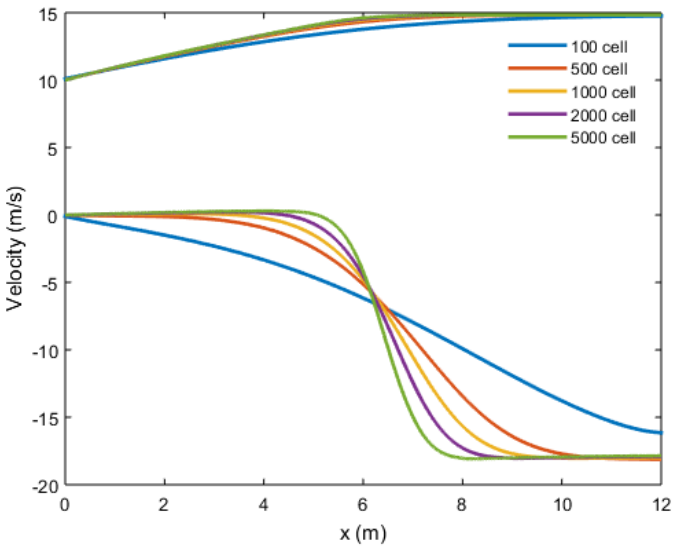

(b)

Figure A5.5: Grid convergence test results for the water faucet problem test, showing the predicted air volume fraction (a) and phasic velocity (b) profiles along the length of the computational domain at 0.5 s following the start of the simulations. Also included in (a) is the exact solution for reference.

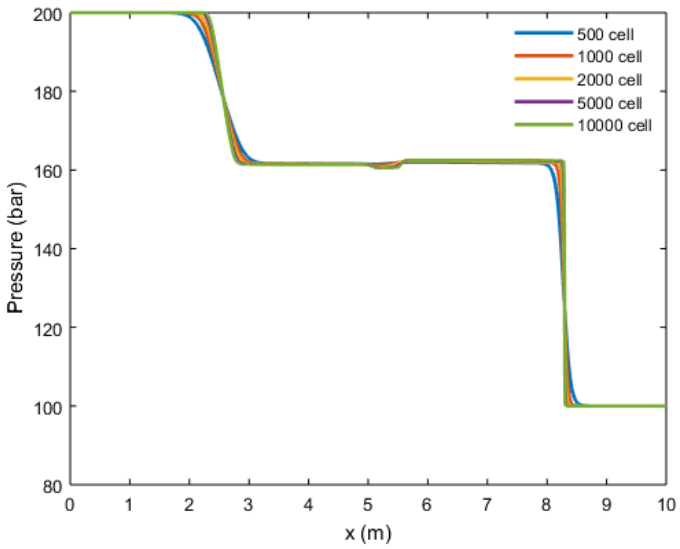

Figure A5.6: Grid convergence test results for the Toumi's shocktube problem test, showing the predicted pressure profiles along the length of the computational domain at 0.06 s following the start of the simulations.

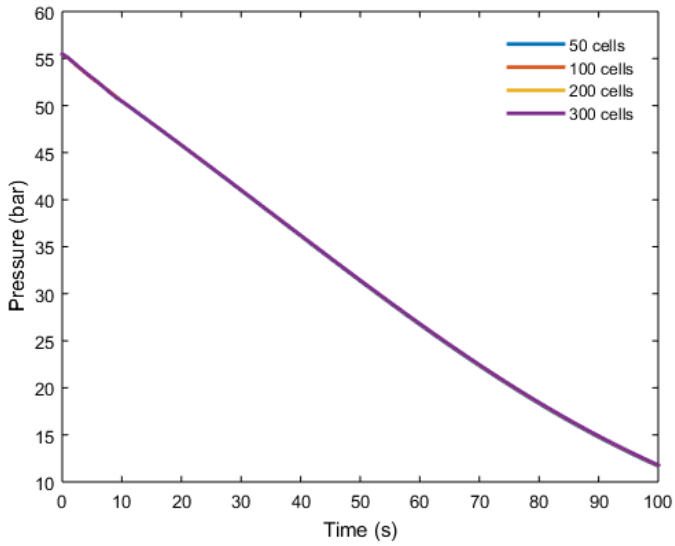

Figure A5.7: Grid convergence test for the CO_2 pipeline puncture decompression simulations, showing the predicted pressure variations with time at the closed end of the test pipe during decompression for the INERIS pipeline puncture decompression test.

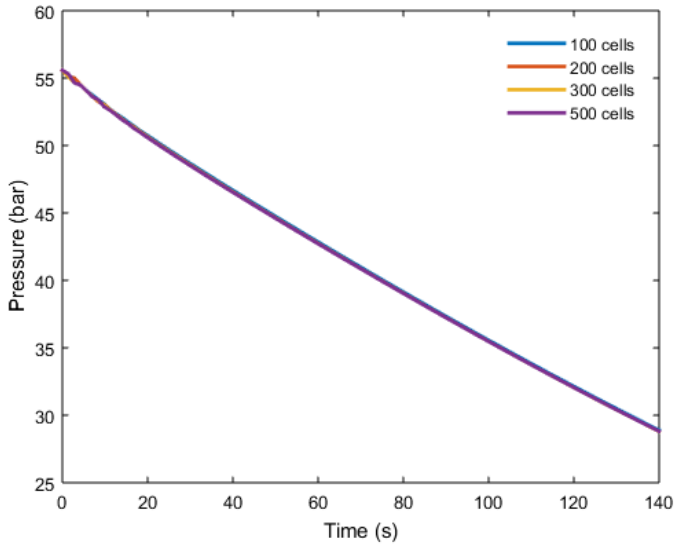

Figure A5.8: Grid convergence test for the CO_2 pipeline puncture decompression simulations, showing the predicted pressure variations with time at the closed end of the test pipe during decompression for the DUT pipeline puncture decompression test.

A5.4 Modelling of the Jet Expansion of outflows released from pressurised containments

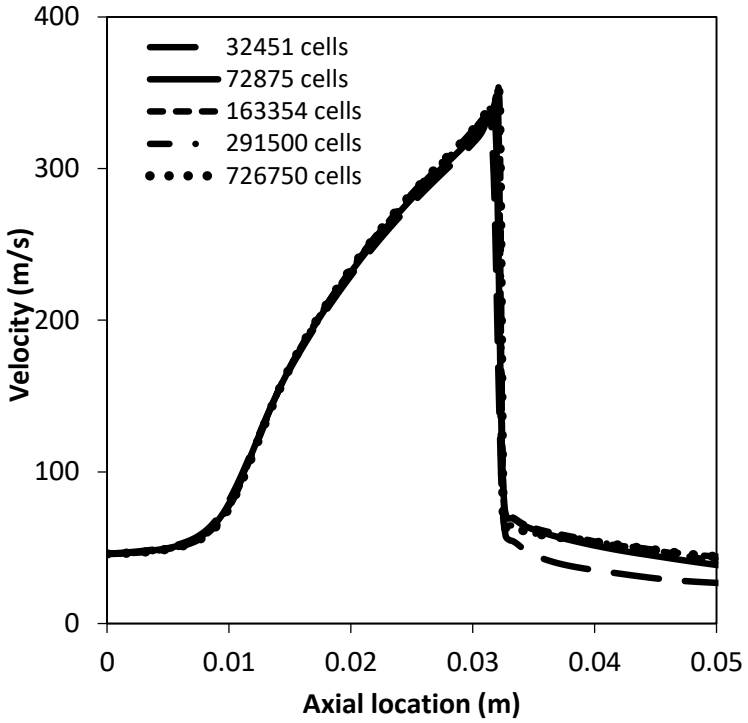

Figure A5.9: Grid convergence test results for the CFD jet expansion simulations, showing the predicted jet axial velocity profiles.